# Porosity and permeability evolution during calcite dissolution: numerical and experimental exploration of the (sub-)pore scale reactive transport processes

**P. Agrawal**

# Porosity and permeability evolution during calcite dissolution: numerical and experimental exploration of the (sub-)pore scale reactive transport processes

Evolutie van porositeit en permeabiliteit tijdens het oplossen van calciet: numerieke en experimentele verkenning van de reactive transportprocessen op (sub-) poriënschaal

(met een samenvatting in het Nederlands)

Proefschrift

ter verkrijging van de graad van doctor aan de Universiteit Utrecht op gezag van de rector magnificus, prof.dr. H.R.B.M. Kummeling, ingevolge het besluit van het college voor promoties  in het openbaar te verdedigen op vrijdag 21 mei 2021 des middags te 12.15 uur

door

**Priyanka Agrawal**

geboren op 25 november 1990 te Gangapur City, India

**Promotoren:**

Prof. dr. J.B.M. Middelburg
Prof. dr. N.H. de Leeuw

**Copromotoren:**

Dr. M. Wolthers
Dr. A. Raoof

To my beloved parents Suresh and Indra

To my dear sisters Monika and Neha

To my dear brother Pankaj

To love of my life Abhishek

# CONTENTS

# LIST OF TABLES

# LIST OF FIGURES

corresponding to Pe number 4.7 and pH value of (a) 3.1 corresponding to $pCO_2$ of 100.0 bar and (b) 3.9 corresponding to $pCO_2$ of 1.0 bar. The injection period for both cases is 15900 pore volumes (in reference to the original pore volumes at t = 0s). The inner white cylinder indicates the initial pore shape (i.e., at t=0s). The colored regions around the cylinder indicate zones dissolved during reaction. The colored rim around at the pore wall indicate the local reaction rates.   63

# Chapter

# 1. INTRODUCTION

## 1.1    Background

An increasing level of greenhouse gas emissions, especially $CO_2$ has posed a life-threatening risk to human society in the form of global warming and other climate changes (e.g., Keeling, 1997). Sequestration of $CO_2$ in its supercritical form (i.e. temperature and pressure higher than 31 ˚C and 74 atm), in geologic formations, is considered one of the most effective mitigation for decreasing $CO_2$ emissions into the atmosphere (Pacala and Socolow, 2004). For a long time, deep aquifers for $CO_2$ storage have been selected from the hydrocarbon reservoirs, in order to combine this operation with the enhanced oil recovery (EOR) operations. The injected $CO_2$ is capable of displacing oil from the pores of the reservoir rocks through several mechanisms out of which the main mechanism is mixing of $CO_2$ into the oil (Gaspar et al., 2009). The miscibility of $CO_2$ into oil is dependent on the presence of suitable conditions i.e., reservoir pressure and temperature (Gaspar et. al., 2009). This mixing leads to a reduction of oil viscosity and an increment in the mobility of oil. Recovering of trapped oil from the reservoirs helps companies to recover the $CO_2$ sequestration cost (Shaw and Bachu, 2002).

Carbonate formations are estimated to be 40% of the total hydrocarbon reservoirs present all over the world (Hawez and Ahmed, 2014). Dissolution of the injected $CO_2$ in resident brine results in chemical disequilibria and the initiation of various chemical reactions. The most important reaction in this system is the calcite dissolution reaction (Rathnaweera et al., 2016). This reaction can produce substantial changes in pore structure by altering pore geometry, connectivity, and tortuosity at the pore scale which at the macro scale contributes to properties like porosity and permeability. Accurate prediction of the behavior of $CO_2$ in the carbonate system is important to optimize the injection rate and to assess the long-term stability of stored $CO_2$ (Rochelle et al., 2004).

Injection of $CO_2$ or other acidic solutions into carbonate rocks triggers a series of hydro-chemical processes including calcite dissolution, reactive transport, and changes in the geometry of porous media (Fredd and Fogler, 1998; Hoefner and Fogler, 1988; Izgec et al., 2008; Luquot et al., 2014; Luquot and Gouze, 2009; Menke et al., 2018; Singurindy and Berkowitz, 2003). In the past, each of these processes has been studied in detail both as individual processes and coupled processes. The following sections provide a summary of the existing research on these processes:

### 1.1.1   Calcite dissolution kinetics

Confidence in the reaction rates is essential for reliable estimations of the $CO_2$-sequestration capacity. It is important, therefore, to comprehend the dissolution kinetics of calcite. Despite being the most researched mineral there is no consensus in the order of the dissolution rate of calcite ((Arvidson et al., 2003)). Subsequent sections summarize the existing findings on calcite dissolution kinetics which are relevant to this study.

Calcite dissolution rates are found to be a function of pH, $CO_2$ partial pressure ($P_{CO2}$), temperature, presence of divalent cations, ionic strength and organic molecules (Giudici, 2002; Gledhill and Morse, 2006; Morse et al., 2007; Morse and Arvidson, 2002; Plummer et al., 1978; Pokrovsky et al., 2009, 2005; Berner and Morse, 1974; Sjoberg and Rickard, 1984; Meldrum and Cölfen, 2008). In general, mineral dissolution includes three main steps: 1) transport of the reactants through solution to the solid surface, 2) reaction between the adsorbed reactant and solid, and 3) transport of the products away from the solid surface to the bulk solution. The dissolution rate is controlled by the slowest among these three steps. If Steps 1 and 3 are the slowest, then the reaction kinetics is diffusion-controlled and if Step 2 is the slowest, then the reaction kinetics is surface-controlled. Composition of the natural water determines the type of controlling reaction kinetics. In natural waters that are highly undersaturated with respect to

calcite, the rate of dissolution is generally controlled by the thickness of the diffusion boundary layer i.e., diffusion-controlled kinetics ( Berner and Morse, 1974; Boudreau et al., 2020; Morse and Arvidson, 2002; Sjoberg and Rickard, 1984). Accurate determination of the rate constant(s) in transport-controlled conditions is dependent on the maximum obtainable spin rate of the experimental set-up. In this regime and for solutions with pH ≤ 4, dissolution rate is strongly pH-dependent and independent of $P_{CO2}$ (Plummer et al., 1978). As the natural water approaches equilibrium with calcite, the dissolution kinetics show intermediate dependence on hydrodynamics and the observed rate constants show a non-linear dependency on the transport rate constant and chemical rate constant. This regime is referred as mixed kinetics (Morse and Arvidson, 2002). In this regime, for neutral-alkaline natural waters (pH >6), calcite dissolution rate depends on both pH and $P_{CO2}$ (Plummer et.al., 1978). Lastly, dissolution kinetics in natural waters that are (near) equilibrium with respect to calcite, is surface controlled. In this regime, the dissolution rate is independent of pH and $P_{CO2}$ (Plummer et.al., 1978) and the value of the chemical rate constant(s) reflects the architecture of the surface in the form of dislocation and point defect density (Rickard and Sjoberg, 1983). Findings from the investigations on the surface reactivity, generally observed under surface-controlled kinetics, is summarized in the last section.

The abovementioned controlling factors of calcite dissolution rate are applicable to the compositionally simple and generally diluted solutions. However, in general, formation brine relevant to the hydrocarbon reservoirs is much more chemically complex. Earlier, Hanor (1994) reported that the salinities of formation water can vary by five orders of magnitude from a few mg l$^{-1}$ (shallow meteoric flow regimes) to 400,000 mg l$^{-1}$ (Michigan Basin, USA). This also depends on whether reservoirs are water flooded and mixtures of formation and injection waters occur (Bergfors et al., 2020). The most common cation in formation water is Na$^+$, generally comprising 70 to 90% of total cation mass. With the increment in salinity, the proportion of Na$^+$ decreases and proportion of Ca$^{2+}$ increases. The amount of Ca$^{2+}$ can even exceed Na$^+$ at salinities higher than 300,000 mg l$^{-1}$ (Hanor, 1994). Several investigations have highlighted the influence of Ca$^{2+}$ ions on calcite dissolution kinetics (Buhmann and Dreybrodt, 1987; Gledhill and Morse, 2006; Gutjahr et al., 1996a; Sjöberg and Rickard, 1985), often with conflicting results. In some studies, Ca$^{2+}$ ions retarded calcite dissolution (Buhmann and Dreybrodt, 1987; Sjöberg and Rickard, 1985). The proposed mechanism responsible for the inhibition is the adsorption of Ca$^{2+}$ ions at the specific calcite surface sites through the Langmuir-Volmer model (i.e., reversible adsorption according to Langmuir adsorption isotherm) (Sjöberg, 1978). On the contrary, some studies reported positive impact of the increasing amount of Ca$^{2+}$ ions on the dissolution rate constants (Gledhill and Morse, 2006; Gutjahr et al., 1996a). Dwight and Morse (2006) suggested that the Ca$^{2+}$ ions affect the CO$_3^{2-}$ carrying capacity of the solution. They observed that, for a given saturation state of the solution, a raise in the amount of Ca$^{2+}$ reduces the relative amount of CO$_3^{2-}$ such that the solution becomes locally more undersaturated. Another controlling parameter for the calcite dissolution, from the perspective of the solution composition, is the ionic strength of the solution. While most experimental studies determining calcite dissolution rate models utilized diluted solution, only few studies investigated the dissolution kinetics in saline solutions comparable to formation brines (Gledhill and Morse, 2006; Pokrovsky et al., 2005). They observed an inhibiting impact of the salinity of the solution on dissolution rate constants.

The studies summarized above were based on bulk experiments of calcite dissolution, in which the rate constants were determined from the overall changes in the chemistry of the solution and surface area of the crystal. It is evident that for similar solutions (with respect to pH and $P_{CO2}$), existing rate models show over an order of magnitude of discrepancy in dissolution kinetics (Arvidson et.al., 2003). The observed incongruity is attributed to differences in

experimental setup, BET vs geometric area, textures of the substrate among possible factors. Correct estimation of crystal surface area has drawn considerable attention in the geochemical literature, and it has been shown that the measured surface area of the crystal is different than the reactive surface area. Lately, direct observations of dissolving calcite surfaces using atomic or near-atomic scale technology such as atomic force microscopy (AFM) and vertical scanning interferometry (VSI), have provided insights on the reaction rate variability of the different surface sites (Arvidson et al., 2003; Brand et al., 2017; Fischer et al., 2012; Lasaga and Luttge, 2001; Lüttge et al., 2003; Shiraki et al., 2000). These studies have shown that certain areas of the crystal surface are more reactive than other areas. Highly reactive areas are linked to high surface energy sites such as microdamage with in the crystal or lattice dislocations, namely, screw dislocations or point dislocations. Faster dissolution at these locations creates etch pits of different morphology, depending on the retreating velocity of the steps of the etch pit. The dissolution rate of these features was observed to be higher than of the flat surface. Due to the presence of these different surface sites and structures with different reactivity, Fischer et.al. (2012) suggested the utilization of rate spectra for defining the reactivity of surfaces, instead of a single value of a mean dissolution rate.

### 1.1.2 Reactive transport processes

Implementation of accurate reaction kinetics is the first step in building a realistic reactive transport model for simulation of processes related to $CO_2$ sequestration and injection of acidic solutions into carbonate rocks. Next aspect of these models is the transport of the reactants. In the context of this study, two modes of transport, namely, diffusion and convection/advection are considered. The advection rate is determined through the imposed flow boundary conditions while diffusion rate depends on the species-dependent diffusion coefficients and the concentration gradients of the species. In diffusion-controlled reaction kinetics corresponding to an acidic solution, which is far from equilibrium with respect to calcite, both transport rates are important. The fluid velocity controls the thickness of diffusion boundary layer, which means an increment in the injected fluid velocity leads to an increase in dissolution rate. The dissolution regime can be categorized based on the ratio of the reaction rate and the transport rate. This ratio is referred as Damköhler number (Da). Da number is defined in following two ways:

$$Da_I = \frac{k}{v} \tag{1.1}$$

$$Da_{II} = \frac{k \, l}{D} \tag{1.2}$$

where, $k$ is the reaction rate constant (m s$^{-1}$), $v$ is the fluid velocity (m s$^{-1}$), $l$ is the characteristic length (m) and $D$ is the diffusion coefficient (m$^2$ s$^{-1}$).

Da>1 indicates that a system is in a reaction dominated dissolution regime and Da<1 indicates a transport dominated regimes.

Relative strength of the advective flux compared to the diffusive flux, namely, Péclet number (Pe), is calculated as:

$$Pe = \frac{v \, l}{D} \tag{1.3}$$

Pe number determines the magnitude of the concentration gradient in the direction of the flow (longitudinal direction) and perpendicular to the direction of flow (transversal direction). In the case of advection dominated transport regimes (Pe>1), the transversal gradient is much stronger

than the longitudinal gradient whereas in case of diffusion dominated transport regimes (Pe<1), the longitudinal gradient is stronger than the transversal gradient. In the past, a number of studies have shown the importance of pore scale studies in unraveling the discrepancy observed between the lab and field scale experiments (e.g., Li et al., 2008; Molins et al., 2014). For example, Li. et.al. (2008) delineated the transport conditions under which a strong concentration gradient develops within a single pore and fracture. They observed that the development of a concentration gradient leads to significant difference in the reaction rate calculated when either a detailed reactive transport model was used or when a well-mixed system without pore-scale transport processes was assumed. Consequently, for these regimes, there will be scale dependency of the dissolution rate, thus, differences in lab rates *versus* field rates.

### 1.1.3   Changes in the geometry of the porous medium

Calcite dissolution leads to evolution of physical properties of the porous medium. The most affected properties are porosity and permeability. Porosity is directly related to the amount of dissolved solid volume therefore it is possible to estimate the changes in total porosity. Prediction of permeability is challenging as it is controlled by altering geometrical features at the detailed pore-scale structure. In general, modifying permeability is predicted from the evolving porosity. A multitude of experimental and numerical studies have presented the coupling of permeability and porosity as a function of the chemical and physical heterogeneities (e.g., Daccord et al., 1993a, b; Fredd and Fogler, 1998; Golfier et al., 2004; Gouze and Luquot, 2011; Hoefner and Fogler, 1988; Luquot and Gouze, 2009). For example, Fredd and Fogler (1998) performed acid dissolution experiments in carbonate rock and showed that the development of dissolution patterns is caused by the imposed specific flow and reaction conditions. For transport-controlled systems (transport time scale > reaction time scale) most of dissolution takes place in the injection region while for reaction-controlled systems (transport time scale < reaction time scale) dissolution occurs uniformly across whole porous medium. Between these two extreme regimes, there exist a combination of optimum flow and reaction conditions which leads to the development of wormholes (highly conductive fluid flow paths). Since, physical properties of rock respond to the developed dissolution pattern, a relationship between porosity and permeability is also dependent on the imposed flow and reaction regimes.

Porosity–permeability relations have been developed via different approaches: (i) through mathematical or (ii) geometrical derivations or (iii) through an upscaling of pore-scale simulations or (iv) through empirical fits to experiment dataset. Unfortunately, so far, no common relation exists that can be used for all carbonate rock types and dissolution conditions. Towards this effort, many studies have shown that, for a range of applications such as mineral dissolution, precipitation, biofilm accumulation, a Kozeny–Carman equation can be used to calculate changes in permeability due to changes in porosity (Kozeny, 1927; Carman, 1937). Originally, the Kozeny–Carman equation was developed to calculate the permeability for a system with constant porosity and permeability, but, now various forms of this equation are applied in models simulating changes in porosity and permeability (e.g., Pandey et al., 2015, 2014; Schneider et al., 1996; van Wijngaarden et al., 2013, 2011; Xie et al., 2015; Yasuhara et al., 2012). One of such modified versions of the Kozeny–Carman relation, a power law relation, calculates changes in permeability from changes in porosity as:

$$\frac{K_t}{K_o} = \left(\frac{\emptyset_t}{\emptyset_o}\right)^n \tag{1.4}$$

where, $K_t$ and $K_o$ are current and initial permeability, $\emptyset_t$ and $\emptyset_o$ are current and initial porosity and $n$ is a fitting factor. This relation is easy to implement at the Darcy scale since it requires porosity and fitting factor. At the Darcy scale, processes are described by *continuum models* in the context of averaged (i.e., effective or homogenized) porous media. These models are used for simulations at the scale of a few centimeters (e.g., plug), decimeters to meters (e.g., core) and up to hundreds of meters or kilometers (e.g., field). The models typically exploit the Darcy equation (or its extended form in case of evolving pore spaces) for modeling the flow, and advection-diffusion-reaction equations to describe the transport and reactions including dissolution and precipitation. Continuum models utilize either the asymptotic homogenization concept (Hornung, 1997), or the representative elementary volume (REV) concept where complex pore structures are averaged over REVs (Bear and Bachmat, 1991). For these averaged models, porosity-permeability relations are derived using following approaches:

  i)   fitting the experimental data to the empirical formula,
  ii)  numerically solving the so-called cell problems in volume averaging theory (e.g., Wood 2007) or in homogenization theory (Hornung, 1997),
  iii) fitting results from pore network model (or single pore) simulations to empirical formula (Nogues et al., 2013).

Several lab-scale experimental studies have demonstrated the dependency of exponent n (Equation 1.4) on the imposed dissolution conditions (e.g., Al-Khulaifi et al., 2017; Garing et al., 2015; Luhmann et al., 2014; Luquot et al., 2014; Menke et al., 2017, 2016, 2015; Noiriel et al., 2004; Rötting et al., 2015; Smith et al., 2013). For example, Luquot et.al. (2014) conducted four flow-through experiments to reproduce the *in-situ* acidic conditions during $CO_2$-brine injection in carbonate rocks developing at different distances from the injection well. They observed development of different dissolution patterns, depending on the $CO_2$ concentration such as localized dissolution for high $CO_2$ concentration and homogeneous dissolution for low $CO_2$ concentration. Subsequently, a higher value for exponent *n* was proposed for high $pCO_2$ conditions and a lower value for exponent *n* for lower $PCO_2$ experiments. This suggest that for each dissolution system a Kozeny-Carman equation should be fitted individually. However, performing a large range of experiments on $CO_2$ storage, to capture the differences between these classes of problems, is neither straightforward nor cheap. Therefore, another approach for determining the permeability is preferable here. Once the effective coefficients are known, specific problems related to $CO_2$ storage can be solved (e.g., André et al., 2010, 2007; Izgec et al., 2008).

Cell problems (see e.g., Hornung 1997; Wood 2007) can be solved using various numerical methods, such as Finite Volume Method (FVM), Finite Difference Method (FDM), Finite Element Method (FEM), Lattice-Boltzman Method (Chen et al., 2014b; Huber et al., 2014; Kang et al., 2006; X. Li et al., 2008) or mesh-free methods (Tartakovsky et al., 2007). Depending upon the discretization scheme, dissolution-induced pore geometry changes are considered through two basic approaches and the solution can be post-processed to calculate the permeability tensor. These approaches are briefly presented in the subsequent sections:

The numerical methods exploiting boundary-fitted grids either include different variants of remeshing techniques if FDM, FVM, FEM discretization techniques are used, or use grid free methods for discretization such as Smoothed Particle Hydrodynamics (SPH) (Tartakovsky et al., 2007). Numerical methods exploiting fixed grids, usually Cartesian ones, split to two subgroups of methods without and with front tracking.

Fixed grid methods without front tracking are robust and computationally very efficient but suffer from low accuracy. These methods handle the moving interface in the following way. A

voxel/pixel which is initially solid, during the solution procedure stores information about the accumulated amount of the substance dissolved from its reactive faces as a function of time. Once the accumulated amount is close to the original total amount in the voxel/pixel, the latter is transferred from solid to fluid phase to obtain a new solid-fluid interface (Bekri et al., 1995). A more accurate variant of this approach accounts for the change in the flow during the intermediate stages of the solid-fluid transition of voxel/pixel. In this case Navier-Stokes-Brinkman equations are solved, and at each time step the calculated solid volume fraction is used to calculate porosity, which is then used within the Kozeny-Carman formula to compute the permeability of the mixed (i.e., containing solid and fluid) voxels/pixels (Soulaine et al., 2017). Note that, because the reactive interface is very roughly represented in this group of methods (just stepwise functions between solid and fluid voxels/pixels), these methods are not very accurate for the simulation of surface reactions.

Fixed grid methods with front tracking include for example, the interface conditions, or level set method (X. Li et al., 2008) or Volume of Fluid (VOF) followed by interface reconstruction (Chen et al., 2014b; Kang et al., 2006), or the phase field method (Huber et al., 2014). The discretization on a fixed grid in the case of front tracking is usually based on one of the various immersed boundary methods and their modifications. These methods are computationally more expensive and less stable compared to the above-mentioned method. The immersed boundary techniques have to take care of the appearance of very small or strongly skewed cells. Further on, the discretization of transport problems in such cases may lead to unphysical oscillations, and more caution is necessary especially in the presence of reactions. Though, this group of methods allows for reasonable representations of the solid-fluid interface, and of near-interface velocities.

All of the above discussed methods are rigorous if the basic assumptions are satisfied (i.e., if an REV exists), but they usually require very intensive computations, in particular because the number of REV's in the case of reactive flow can be quite large, especially with increasing heterogeneity. Nowadays, tractable cell problems that can be solved having sizes of the order of millimeters, depending on the pore size distribution and tortuosity. This means that they have limited application in the case when heterogeneity is on the same or larger scale. In such cases, they have to be combined with other approaches.

Pore Network Modelling (PNM) (Raoof et al. 2012; Xiong et al. 2016; Algive et al. 2010; Varloteaux et al. 2013a and Varloteaux et al. 2013b) allows for the permeability to be calculated for significantly larger samples compared to solving cell problems, thus having a broader range of applicability. In pore network models, the void space of the porous medium is represented by an idealized geometry of pore-bodies joined by pore-throats. Samples of porous media containing several hundred thousand or even millions of pores can be represented in this case. These models represent the pore space by a set of pre-defined shapes for the bodies and the throats (most often capillaries with cylindrical, ellipsoidal, triangular or other cross-sectional shapes are used to describe the pore throats).

Several PNMs have been proposed to calculate permeability evolution for problems related to $CO_2$ or acid injection in carbonate rocks. For instance, Algive et al. (2010); Varloteaux et al. (2013a) and Varloteaux et al. (2013b), introduced dimensionless numbers to link microscopic wall deformation with changing porosity and permeability at the macroscopic level. Nogues et al. 2013 and Mehmani et al. 2012 treated the changing geometry problem due to precipitation/dissolution through modifying the throat conductivity by linking this to the changing volume of the pore. This way of evolving geometry assumes that the throat shape does not change during the dissolution process.

Simulations at the single pore scale can be used to improve the algorithms defined in PNM for reactive flow in evolving geometry and to investigate the nonlinearity of the reaction rate of calcite dissolution over the fluid composition as a function of advection, diffusion and the reaction rates. In the past, some pore-scale based simulations have been done to highlight the fluid composition control over the reaction rate in different flow regimes (e.g., Li et al., 2008; Molins et al., 2014). For example, Molins et al. (2014) performed a combination of experimental and modeling studies using a capillary tube filled with crushed calcite grain and an injecting solution at 4 bar $pCO_2$. Through a pore scale model, they showed the existence of mass-transfer limitations near the inlet region of the tube and inside pore spaces that were originally disconnected from the main flow path. They attributed the observed difference between the reaction rate from the continuum scale model (which assumes well-mixed conditions) and the pore scale model to these transfer controls. Further, they suggested that this pore-scale interplay of reaction and transport can become more significant for physically and chemically heterogeneous subsurface reservoirs selected for $CO_2$ sequestration.

## 1.2    Research objectives

The research in this thesis aims to identify optimum injection conditions such as injection rate and composition of the injecting solution (including pH, $pCO_2$, ionic strength, foreign divalent ions) for applications related to $CO_2$ sequestration and acid stimulation in carbonate reservoirs. To achieve this aim, we analyzed the impact of several injection parameters on the physical and chemical processes that govern the interaction of $CO_2$ or acidic solutions with calcite minerals at the single pore scale and at the pore-network scale through a combination of experimental and modeling methods. We initially represented the microscopic unit of the porous medium with a cylindrical shaped pore unit (or pore). In numerical simulations using this unit, namely pore scale simulations, the solid-fluid interface is defined explicitly as a moving boundary, and exact equations of the flow, transport, reaction, and geometry evolution are solved. Additionally, we perform microfluidic experiments using cylindrical pore units created in calcite crystals. The main focus of this pore-scale work is to comprehend the coupling of the reaction and transport time scales and its influence on the geometry evolution of the initially cylindrical pore. From the results of the single pore scale work, we derive new constitutive relationships for the changes in conductance during dissolution, which include information of the shape as a function of the imposed flow and reaction regimes. Further, the developed pore-scale model is used to investigate the existing assumption about the impact on hydrodynamic conditions on dissolution rate spectra in surface dissolution experiments using techniques such as AFM and VSI. Lastly, we perform micro-CT flow through experiments to explore the control of the solution impurity (i.e., salinity and divalent ions such as $Ca^{2+}$) on the calcite dissolution processes. In all chapters, we compared the numerical results with experimental observations. In this way, we access the limitations and validity of the utilized modeling techniques.

## 1.3    Outline of the thesis

This thesis is aimed at describing reactive transport processes corresponding to the injection of acidic solutions into carbonate rocks. We have achieved this objective through utilizing a combination of injection conditions (injection flow rate and solution composition) and combining simulations with experiments in the laboratory. This thesis contains four major themes and hence, each chapter is an independently readable article.

Chapter 2 of this thesis presents a single-pore scale model with the objective to investigate the impact of acidic-solution injection on pore-shape evolution within a calcite crystal. We have used the Stokes equation for fluid flow coupled with solute advection-diffusion equations and

multicomponent chemical reactions under evolving pore geometry and moving mesh. The developed reactive transport model is validated against microfluidic experiments conducted in single channels drilled through optical-grade calcite crystals. Depending on the flow and reaction regime, our results showed that the dissolution led to alteration of the original cylinder shape into a range of pore shapes. More specifically, under advection dominated and reaction-controlled regimes, the shape of the throat remains cylindrical throughout the dissolution period while under diffusion dominated and reaction dominated regimes, the cylindrical shape evolves into half-hyperboloid (~conical) shapes. The shape of the throat was found to directly control the conductance of the throat. We observed that ignoring the actual shape of the throat while calculating the conductance of the throat, can lead to an overestimation of the conductance of up to 76%. These results are important in the context of pore network modeling, where each throat in the pore network acquires its own dissolution regime and, subsequently, may undertake a specific shape modification, depending on the reactive-flow regime. Therefore, updating routines of throat conductance values should include the information about dissolution-induced shape changes.

Chapter 3 unravels the complex pore-scale hydrodynamic processes happening during experiments performed to obtain dissolution rates for calcite mineral surfaces. In this chapter, we implemented calcite surface topographies obtained experimentally using Vertical Scanning Interferometry (VSI), within an exemplary flow cell. We have first performed a series of simulations on the scale of the full flow cell utilized for calcite marble dissolution experiments. We show that commonly utilized flow rates and injected solution compositions in calcite dissolution experiments can result into accumulation of $Ca^{2+}$ ions in the boundary layer, leading locally to transport-controlled dissolution conditions inside the flow cell, contrary to the expected surface-controlled conditions. As a result, we observed dissolution rate heterogeneity at the flow-cell scale, but not at the microscopic scale of a typical field of view for VSI or Atomic Force Microscopy measurements. Next, we focused on the microscopic scale and investigated changes in hydrodynamics due to real (VSI-measured) surface roughness and the impact of the heterogeneity in the hydrodynamics on dissolution rate spectra. We show that hydrodynamics' heterogeneity at a rough calcite surface leads to much narrower rate spectra than measured experimentally. Moreover, when correcting the rates for actual specific surface area (and its changes), or when exaggerating the surface topography, we still do not obtain dissolution rate spectra as wide as observed in VSI experiments. Only when we impose rate spectra in our simulation from the beginning, then we produce the observed magnitude of reaction rate variability. Finally, through a systematic series of smaller scale simulations, which were performed for a range of flow and reaction regimes (i.e., denoted by Pe and Da numbers), we quantify the impact of the micro-scale surface roughness on the dissolution rates. Our results strongly suggest that the main control on dissolution rate heterogeneity that leads to observed dissolution rate spectra is the free energy landscape at the calcite surface, which is affected by (atomic scale) parameters such kink site and defect densities.

Chapter 4 takes forward the recommendations from Chapter 2 and presents a new formulation for updating the hydraulic conductance of individual throats in the pore network model (PNM). In the existing pore network models, utilization of the Hagen-Poiseuille relation for updating of conductance ignores the possibility of changes in the shape of throat during dissolution period. In this chapter, we derive the new relations for conductance, which account for the changing shape of the throat. In order to derive these relations, we performed additional single pore scale simulations, covering flow and reaction conditions relevant to the different throats of the pore networks used to model acid injection processes into carbonate rocks. For each simulated dissolution regime, we first find the dependency of the normalized conductance of the throat on the normalized volume of the throat. Subsequently, we determine the constitutive

functions between the imposed reactive-flow conditions and the geometry of the throat. The derived conductance relations are implemented in the pore network model.

In order to validate the modified pore network model, two sets of flow-through experiments on Ketton limestone samples were performed. These experiments utilized an injection of acidic solutions (pH 3.0) at two Darcy velocities i.e., $7.3 \times 10^{-4}$ and $1.5 \times 10^{-4}$ m s$^{-1}$. X-ray micro-CT images of the sample at the beginning and end of the experiment were collected. Extracted pore networks, obtained from the micro-CT images of the unreacted sample, were used for reactive transport PNMs. We observed that for the experimental conditions, most of the throats maintained their cylindrical shapes. Thus, both sets of the simulated reactive pore network models (i.e. one with the classical Hagen- Poiseuille relation and one with the new sets of conductance relations) predicted similar changes in the permeability of the sample. Next, we modelled a range of flow and reaction regimes using both types of reactive PNMs and compared the evolution of porosity-permeability. Our results revealed that in certain reactive-flow conditions, neglecting the evolution of the throat shape in the pore network can yield an overestimation of up to 27% in the predicted permeability values and an overestimation of over 50% in the fitted exponent for the porosity-permeability relations.

Chapter 5 explores the influence of brine composition, mainly calcium ions and NaCl-based salinity, on the development of dissolution patterns in carbonate rock. In this work, we conducted four flow-through experiments on the Ketton rock, through the injection of four different brine solutions at a constant flow rate of 0.26 ml min$^{-1}$. We show that the injection of solutions of varied corrosive nature leads different dissolution regimes corresponding to a range of Damköhler numbers. Increasing salinity and $Ca^{2+}$ amount in the injecting solution leads to a reduction in the corrosiveness of this solution. This is reflected in the developed dissolution patterns: the concentration of $Na^+$, $Cl^-$ and $Ca^{2+}$ ions in the injecting solution guides the dissolution regime from disseminated or microporous to wormhole dissolution. Furthermore, the composition of the injected solutions influenced the value of the fitting exponent for the porosity-permeability relationship.

Chapter 6 provides the summary of all four chapters and recommendations for the future work.

# Chapter

# 2. Evolution of pore-shape and its impact on pore conductivity during CO2 injection in calcite: Single pore simulations and microfluidic experiments

**Abstract**

Injection of $CO_2$ into carbonate rocks causes dissolution and alters rock transport properties. The extent of the permeability increases, due to the increased pore volume and connectivity, strongly depends on the regimes of transport and dissolution reactions. Identification of these regimes and their parametrization at the microscopic scale is required for an understanding of the injection processes, and, afterward, for calculating the effective macroscopic parameters for field-scale simulations. Currently, a commonly used approach for calculating the rock effective parameters is the Pore Network Method, PNM, but a better understanding of the validity of its basic assumptions and their areas of applicability is essential. Here, we performed a combined microscopic experimental and numerical study to explore pore-shape evolution over a wide range of transport and dissolution reaction regimes. Experiments were conducted by flowing an acidic solution through a microscopic capillary channel in a calcite crystal at two different flow rates. The effluent composition, as well as pore shape changes, were reproduced well by our pore-scale reactive transport model. Two key stages in pore shape evolution were observed, a transient phase and a quasi-steady-state phase. During the first stage, the shape of the single pore evolved very fast, depending on the flow regime. Under advective-dominant flow, the pore shape remained nearly cylindrical, while under diffusive-dominant transport, the pore shape developed into a half-hyperboloid shape. During the quasi-steady-state stage, the pore volume continued to increase, however, without or with diminutive change of the pore shape. In this stage, only a long period of injection may result in a significant deviation of the pore shape from the original cylinder shape, which is a common assumption in PNMs. Furthermore, we have quantitatively evaluated the impact of evolved pore shape spectrum on the conductance calculations and compared it to the formulations currently used for pore network modelling of reactive transport.

## 2.1    Introduction

Geological sequestration of $CO_2$ in carbonate reservoirs is considered to be a promising solution for mitigating the global warming problem caused by greenhouse gas emission (Hawez and Ahmed, 2014; Liao et al., 2012; Pacala and Socolow, 2004; Shaw and Bachu, 2002). Injection of $CO_2$ into such rocks triggers a series of chemical reactions, most importantly calcite dissolution, that may cause changes in pore shape, connectivity, and tortuosity (e.g., Rathnaweera et al., 2016). Accurate predictions of these changes are important in order to control the injection rate and to assess the long-term stability of the stored $CO_2$ (Rochelle et al., 2004).

Traditionally, the dissolution of carbonate rocks by acidic, $CO_2$-rich, solutions is simulated at the Darcy scale, which solves macroscopic equations over averaged porous media with the assumption that each spatial element of a porous medium is a well-mixed volume. However, the fluid transport processes and geochemical reactions occur at the pore-scale of the reservoir rock, where the solid-fluid interface are well defined. Therefore, confident prediction of rock transport properties from continuum scale models needs input from pore-scale models. Several research groups have utilized 3D micro-CT images or virtually generated geometries to simulate the coupled physical and chemical processes at the pore-scale, however, they are limited to a relatively small amount of pore volumes even with the existing computational power.

Another powerful approach to investigate these coupled subsurface processes at the pore scale is Pore Network Modelling (PNM) where the pore space is represented by a set of pre-defined shapes for pore bodies and throats. PNMs enable simulations on orders of magnitude

larger rock volumes compared to the full 3D pore-scale simulations, due to a simplified representation of pore geometries. Several reactive PNMs, capable of handling evolving geometries, have been proposed in the literature in the context of $CO_2$ related problems (Algive et al., 2010; Mehmani et al., 2012; Nogues et al., 2013; Raoof et al., 2012; Tansey and Balhoff, 2016; Varloteaux et al., 2013b, 2013a). For instance, microscopic pore wall evolution can be related to the change in porosity and permeability using dimensionless numbers (Algive et al., 2010; Varloteaux et al., 2013a, 2013b). In other available PNMs, the geometry modification assumes that pores open linearly, without changing shape, irrespective of reaction and transport regime (Mehmani et al., 2012; Nogues et al., 2013; Raoof et al., 2012). The validity of these assumptions can be tested using microfluidics experiments and detailed simulations at the single-pore scale.

Single-pore models, allow a detailed description of reactive transport processes (Chen et al., 2014a, 2014c; Kang et al., 2003; Kumar et al., 2011; L. Li et al., 2008; X. Li et al., 2008; Van Noorden, 2009). These models simulated coupled processes in the context of carbonate dissolution for fixed geometry (Li et al., 2008) and relatively simple chemical system or evolving geometry (Chen et al., 2014a, 2014c; Kang et al., 2003; Kumar et al., 2011; X. Li et al., 2008; Van Noorden, 2009). Recently, Gray et al., 2018 investigated a single channel drilled through solid calcite and a pristine Ketton Oolite core plug. They observed that the cylindrical pore evolves into a nonlinear half-hyperboloid shape. However, they did not investigate the flow and reactive transport regimes under which the nonlinear pore shape developed, and the influence of different transport and reaction parameters on the developed pore shape.

Here, we combine microscopic experiments with numerical simulations at the single-pore scale to investigate the impact of acidic-solution injection on pore-shape evolution in calcite. We have used the Stokes equation for fluid flow coupled with solute advection-diffusion equations and multicomponent chemical reactions. The evolution of the explicitly defined calcite solid-fluid interface is simulated using arbitrary-Lagrangian Eulerian (ALE) method. The developed model is validated by microfluidic experiments conducted in single pores drilled through optical-grade calcite crystals. Confocal laser microscope was used to track the pore shape evolution. Furthermore, the chemical composition of the effluent solution was measured to validate the overall calcite dissolution rate. Depending on flow-regime, our results showed an initial intense pore-shape change while the concentration gradients turn into a quasi-steady state. Once quasi-steady state was attained, the continued dissolution lead to an additional pore widening, with limited change of pore shape over time, which deviates from the original cylinder shape only for long periods of injection We have quantitatively evaluated the impact of our results on assumptions relating conductance evolution for PNM models that assume a linear pore opening. The goals of this paper are as follows:

(i)     Validate computer simulations by comparison with microfluidic lab experiments;

(ii)    Perform a systematic study of different flow, transport and reaction conditions in order to identify the regimes for which the currently used PNMs are providing reliable results and the regimes for which the usage of PNMs assuming constant cylindrical pore shapes can lead to significant errors.

(iii)   Calculate the pore conductance through the direct simulation algorithm presented here as well as using state of the art approaches used by PNMs, and compare the two methods.

## 2.2 Materials and Methods

### 2.2.1 Single pore simulations

To simulate pore evolutions, fluid flow and multi-complement transport processes were solved fully coupled with moving boundaries due to dissolution reactions (SI, Section A2.1). A Finite Element method was used (COMSOL Multiphysics®) and a Backward-Euler time stepping method was implemented for time discretization.

#### 2.2.1.1 Fluid Flow and Transport

We have solved Stokes equation since slow flow velocities with small Reynolds numbers are considered. Initialy, i.e., at time zero, it is assumed that the pore with calcite walls is in equilibrium with the steady-state flow. The simulation starts by dropping the pH of the injecting fluid via the inlet of the pore, which initiates the dissolution process leading to pore geometry evolution. During the simulation, the velocity field is updated to account for the pore geometry changes. To simulate the transport of each dissolved species, advection-diffusion-reaction equation is implemented. Details of simaultions are provided in Supplementary Information, Section A2.1.1.

#### 2.2.1.2 Geochemical Model

The injected solution into the carbonate rock reservoirs contains dissolved $CO_2$. This leads to the formation of the weak carbonic acid and its dissociation to establish new equilibria with $HCO_3^-$ and $CO_3^{2-}$ species. The reactions involving the dissolution of $CO_2$ in the water are much faster than any other fluid-mineral reactions (Rochelle et al., 2004), as long as the pH < 9 (Wolthers et al., 2008; Zeebe and Wolf-Gladrow, 2001) which is the situation for this study. Therefore, we can safely assume that solution-phase reactions are of equilibrium type (SI, Section A2.1.2). Calcite dissolution occurs at the fluid-solid interface which is represented by the lateral boundaries of the pore. The dissolution rate laws applied at these boundaries are based on the study by Busenberg and Plummer, 1986 (SI, Sections A2.1.2 and A2.3.1). Under acidic conditions, the overall dissolution rate strongly depends upon the activity of $H^+$ which becomes pH independent when values of pH are above 7. To calculate the activity coefficient of charged species, the Davies equation was applied.

#### 2.2.1.3 Pore shape evolution model

Calcite dissolution results in a moving fluid-solid interface problem. For such problems, the arbitrary Lagrangian-Eulerian (ALE) method is considered to be very precise as the solid-fluid boundary can be exactly tracked (Kumar et al., 2011; Soulaine et al., 2017; Van Noorden, 2009). (see Kumar et al., 2013 for more details on the ALE method in the context of reactive transport related problems).

A displacement rate, normal to the pore surface, is assigned to the reactive walls which depend on the amount of the dissolved calcite, and thus on the reaction rate of calcite dissolution. We should note that in the free boundary problem considered here, the displacement rate of the pore wall (i.e., the solid-fluid interface) is not a predefined constant value or function, instead, it is calculated at each time step and for each point along the pore length (SI, Section A2.1.3). This makes the dissolution rate a dynamic nonlinear parameter which depends on the solution composition.

#### 2.2.1.4 Physical-chemical parameters

The initial cylindrical pore geometry is representing a single pore located in a carbonate rock sample. The length and radius of the pore are L= $5 \times 10^{-4}$ m and r= $4 \times 10^{-5}$ m, respectively. The pore is initially filled with calcite-saturated water. The equilibrium concentration of species corresponding to this condition is listed in Table A2.1. Unless specified otherwise, the

diffusion coefficients for all species were assumed identical, with a value of $3.36 \times 10^{-9}$ m$^2$ s$^{-1}$ which is the average of the self-diffusion coefficient of species present in the reactive system (as listed in Table A2.1, hereafter this model is referred as Model I).

We performed several simulations by applying different flow velocities to cover a range of transport regimes, from diffusion dominated to advection dominated conditions. Moreover, by changing the chemical composition of the injecting solution we aimed to explore the impact of different reaction regimes. Five flow rates were imposed, including $2 \times 10^{-10}$, $2 \times 10^{-11}$, $2 \times 10^{-12}$, $2 \times 10^{-13}$, $2 \times 10^{-14}$ m$^3$ s$^{-1}$. This resulted in maximum velocity values of $8 \times 10^{-2}$, $8 \times 10^{-3}$, $8 \times 10^{-4}$, $8 \times 10^{-5}$ and $8 \times 10^{-6}$ m s$^{-1}$, in the center of the pore at the established parabolic velocity profiles. The injected solution is in equilibrium with a certain pCO2 value (pressure of CO2 gas). The concentration of all species with the target pCO2 values were obtained using PhreeqC (Parkhurst and Appelo, 2013) with the phreeqc.dat database. In this study, pCO2 values of 100.0, 10.0 and 1.0 bar were chosen to represent different reaction regimes. The corresponding values of the species concentrations in these solutions are listed in Table A2.1.

### 2.2.1.5 Parametrization of the flow and reaction regimes

In order to analyze the relative strength of advection, diffusion, and reaction, we use dimensionless Péclet number and Damkhöler number.

The Péclet number, $Pe$, compares the characteristic times of diffusion and advection transport processes as:

$$Pe = \frac{vr}{D} \tag{2.1}$$

where $v$ is the average velocity at the inlet boundary and $r$ is the radius of the channel at the inlet. Due to the dissolution, the radius at the inlet changes, and this leads also to the change of the inlet velocity. Both effects indicate that $Pe$ and $Da$ change with time.

The Damkhöler number, $Da$, measures the solution reactivity compared to the advection rate as:

$$Da = \frac{T_A}{T_R} \tag{2.2}$$

$$T_A = \frac{r}{v} \tag{2.3}$$

$$T_R = \frac{C_{Calcite}}{S_R} \tag{2.4}$$

$T_A$ and $T_R$ are the advection time scale and reaction time scale, respectively. $S_R$ is the surface reaction rate, noted at the end of the first stage from the inlet pore wall (mol m$^{-2}$ s$^{-1}$) and $C_{Calcite}$ is the density of surface sites of calcite at the start of dissolution (mol m$^{-2}$). This is calculated from the surface site density data i.e., 4.9 calcite molecules per nm$^2$ based on crystallographic data for the dominant cleavage plane of calcite (e.g., Wolthers et al., 2008) and Avogadro number ($6.023 \times 10^{23}$), providing $C_{Calcite}$ as $0.8 \times 10^{-5}$ mol m$^{-2}$.

As $Pe$ and $Da$ numbers change over time, we examine the results with respect to the initial $Pe$ and $Da$ numbers calculated at the inlet boundary of the pore. Table 2.1 provides the $Da$ and $Pe$ numbers corresponding to the numerical simulations i.e., Model I.

| Simulation No. | pH of the injecting solution | $Pe$ | $Da$ |
|---|---|---|---|
| | | | |

| | | | |
|---|---|---|---|
| 1 | 3.4 | 47.4 | 0.21 |
| 2 | 3.9 | 47.4 | 0.03 |
| 3 | 3.4 | 0.47 | 14.95 |
| 4 | 3.9 | 0.47 | 2.13 |
| 5 | 3.1 | 47.4 | 0.96 |
| 6 | 3.1 | 4.74 | 9.1 |
| 7 | 3.9 | 4.74 | 0.29 |

**Table 2.1: Simulations using different flow rates and reaction parameters to cover a range of *Da* and *Pe* numbers.**

### 2.2.2 Microfluidic experiments

To directly observe pore evolution and to validate our numerical model, microfluidic experiments were conducted using a capillary pore drilled in optical grade calcite crystal (Iceland spar). A laser fluorescence confocal microscopy (Nikon A1R confocal) was used to image the extent of dissolution and the pore shape change. For the fluorescent dye, fluorescein sodium salt (Lot No.: BCBM7214V; Sigma-Aldrich; emission wavelength – 515 nm) was used. The fluorescent dye solution (1mM) was mixed in a volumetric ratio of 1(dye solution): 100 (injecting solution volume), to prepare the fluorescent injecting solution. The sensitivity of this dye towards proton activity was tested for the pH range in these experiments. We tested inflow solutions of pH 1.98 and pH 3.04 (before adding dye) yielding pH 2.00 and 3.06 (after adding dye), respectively, confirming that used concentration of dye doesn't significantly modify the proton activity of the inflow solution. Additionally, solution measurements were done to obtain changes in pH and $Ca^{2+}$ concentration due to the dissolution of the calcite. Orion micro pH electrode was used for the pH measurement of the effluent solution. Inductively coupled plasma-optical emission spectrometer (ICP-OES, SPECTRO ARCOS) with a cross flow Nebulizer, was used for the $Ca^{2+}$ concentration measurement. The collected outflow samples for the period (0, T] were diluted with 2% $HNO_3$ solution to attain the minimum required sample volume of 6 ml for ICP-OES measurements. Measured $Ca^{2+}$ concentration from the outflow solution is compared to the flux-weighted averaged concentration of $Ca^{2+}$ at the pore outlet of the numerical model, calculated as:

$$cCa_{OUT} = \frac{\int_0^{r(T)} cCa(\acute{r})\, u(\acute{r})\, \acute{r} d\acute{r}}{\int_0^{r(T)} u(\acute{r})\, \acute{r} d\acute{r}} \qquad (2.5)$$

Here, $cCa(\acute{r})$ and $u(\acute{r})$ are the $Ca^{2+}$ concentration and velocity, at the radial distance of $\acute{r}$, respectively. $r(T)$ stands for the outlet radius of the pore at time t=T. Radial symmetry of the solution is assumed, thus no integration with respect to the angle φ in the cylindrical coordinates is needed.

Displacement of the calcite surface was quantified with reference to the position of the inert glass section attached to the inlet face of the channel. The details of material and methods are provided in SI, Section A2.2.

The experiments were conducted at two flow rates with one order of magnitude difference (i.e., 5 µl min$^{-1}$ and 50 µl min$^{-1}$) to inject solution with a pH value of 2. These flow rates yielded average velocities of $4.2 \times 10^{-4}$ m s$^{-1}$ and $4.2 \times 10^{-3}$ m s$^{-1}$, respectively. To implement the

experimental conditions as accurately as possible into the COMSOL model, the injecting solution composition was matched to the pH 2 using HCl acid in place of $pCO_2$. The details of this solution are given in Table A2.1.

## 2.3    Results and Discussion

### 2.3.1   Validation of the numerical model outcome with experiment results

Figure 2.1 shows the $Ca^{2+}$ concentration and the pH at the outflow obtained by measurements and using the numerical simulations. The agreement between modelling and measured data was good for Ca outflow concentrations and reasonably well for pH under both flow rates.
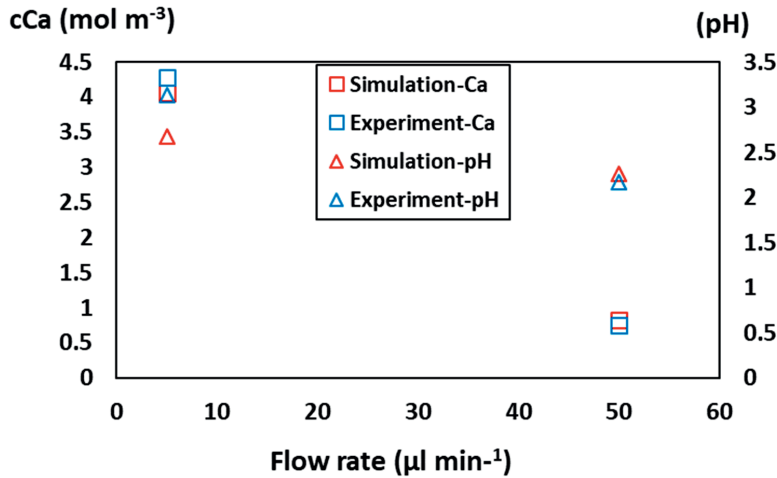


**Figure 2.1: Comparison of the measured $Ca^{2+}$ and pH at the outlet of the experiment with the flux-weighted average concentration of $Ca^{2+}$ and pH from the numerical simulations (Model-I).**

The simulation results for pore shape evolutions also showed a good agreement with the experimentally observed pore shape under both flow regimes (Figure 2.2). Under high flow rates, the channel evolved almost uniformly (with only minor curvatures of the pore wall near to the inlet) and almost retained the original cylindrical pore shape (Figure 2.2a and Figure 2.2c). Under low flow rate conditions, the channel evolved to a non-uniform half-hyperboloid shape, with a strong curvature developing close to the pore inlet (Figure 2.2b and Figure 2.2d). In the high flow rate experiment, we observed a similar magnitude of pore-wall displacement in the experiments (equal to 63 µm in Figure 2.2a) and simulations (equal to 61.44 µm in Figure 2.2c) after the same number of pore volumes. In contrast, under low flow rate, the magnitude of experimentally observed pore-wall displacement (with a value of 187 µm) was overestimated by the model which provide a value of 252 µm (Figure 2.2b and Figure 2.2d).
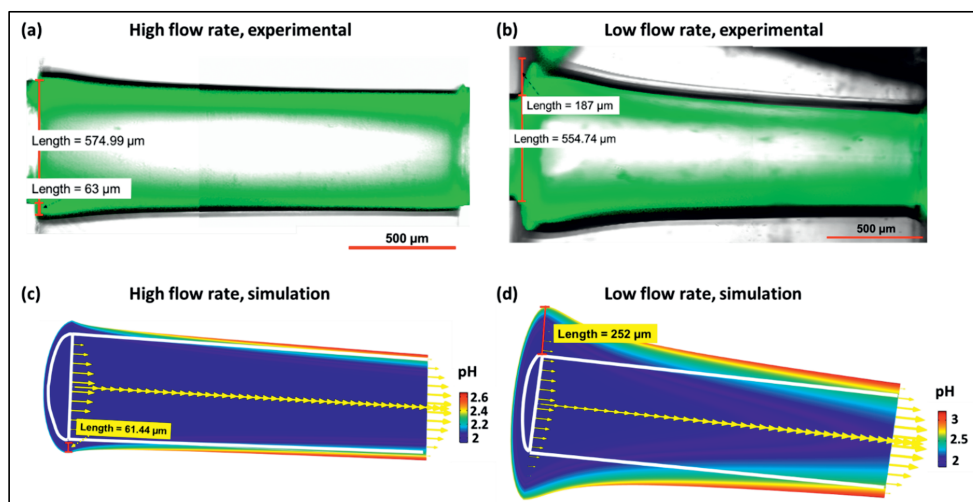
**Figure 2.2.** Comparison of high flow rate (50 µl/min corresponding to $Pe$=312.5) and low flow rate (5 µl/min corresponding to $Pe$=31.25) experimental observations with the numerical simulations. (a) and (c) show results under the high flow rate after injecting a solution of pH value of 2 for 3600s, and (b) and (d) show results under the low flow rate after injecting a solution of pH value of 2 for 36000s. Images in c and d plots were acquired by superimposing images from the transmitted detector and the fluorescein detector (Figure A2.2 and Figure **A2.3**). Simulation results are for the same flow rate and fluid composition and a similar number of pore volumes, with colours showing solution pH within the channel and, arrows indicating the velocity field. Arrow length is proportional to velocity. The inner white cylinder indicates the initial channel shape (i.e., at t=0s); the coloured regions located outside the cylinder indicate dissolved parts during the reaction**.**

For high flow rate, both effluent measurement and microscope image-based results are within the experimental error with the model utilizing a single diffusion coefficient for all aqueous species. Also, the agreement between the amount of dissolved calcite from the microscopic and the simulated image of the channel (Figure 2.2) indicates that the reactive-transport model appropriately captures the dissolution rate (i.e., the pore evolution). In the low flow rate experiment, the disagreement between the obtained calcite surface displacement value using modeling and experiments is within the range of the uncertainty of the input parameters, i.e., reaction rate constants and the choice of diffusion model (details are provided in SI, Sections 3.1-3.2). We also found that changing the diffusion coefficients or using species-specific diffusion coefficients would not improve the results. Therefore, as pore shape evolution under varying fluid velocity and composition is captured well by using a single diffusion coefficient model, we have applied Model I for the further analysis.

### 2.3.2 Initial stages of pore shape development

The pore fluid is initially at equilibrium with calcite proving a pH value of 9.9. Injection of an acidic solution with a pH of 3.9 and pCO2 value of 1.0 bar, shifts the equilibrium conditions of the pore fluid, differently under different flow regimes. The injection initiates calcite dissolution through a set of bulk reactions as well as surface reaction. The surface reaction products, i.e., $Ca^{2+}$ and $CO_3^{2-}$, accumulate within the boundary layer near the pore wall from where they move away towards the bulk fluid. The amount of reaction products strongly depends on the difference between pH of the injected solution and that of the initial pore fluid.

We observe a front propagation behavior along the pore at the initial stage of the reaction. In the advection-dominated flow regime ($Pe>1$), the $Ca^{2+}$ rich zone, that is initially near the pore wall at the pore inlet (Figure 2.3a, plot a), is predominantly transported downstream along the pore wall (Figure 2.3a, plots b and c) before reaching the central part of the pore. As such, the longitudinal gradient smoothens faster than the transversal (i.e., cross-sectional) gradient, yielding concentration profiles with a prominent transversal gradient (Figure 2.3a, plot d). Whereas in diffusion dominated flow regime ($Pe<1$), the $Ca^{2+}$ plume is shorter and more intensive (i.e., with a higher concentration of the reaction products) (Figure 2.3b, plot a). The reason is that at $Pe=0.47$, the flow velocity is slower, and more time is available to wash out the dissolution products. A stronger diffusive flux drives the transversal mixing as well, resulting in a concentration profile with a less prominent transversal gradient compared to the longitudinal gradient (Figure 2.3b, plots b-d).
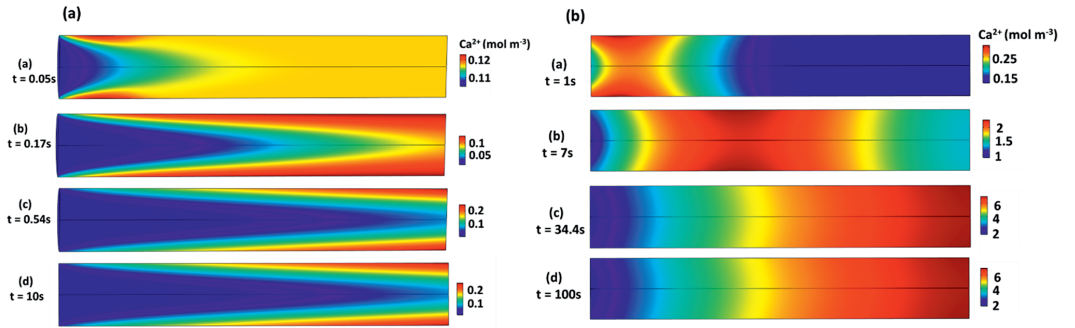


**Figure 2.3**. Concentration field of $Ca^{2+}$ over time inside pore space under flow rates corresponding to (a) **$Pe$**=47.4 (b) **$Pe$**=0.47. To improve the visualization of the concentration gradient, different scales have been used for all panels.

Although the low and high flow rate conditions lead to distinct concentration gradients, in both cases during the injection we observe two stages in the development of the concentration gradients. In the first stage, the concentration field changes significantly, leading to the establishment of a flow regime specific concentration field. Whereas in the second stage, referred to here as the quasi-steady stage, these changes become minute and the concentration gradients change only slowly. The quasi-steady state concentration gradient govern the dissolution and thus the pore wall evolution during the time. In the case when the concentration gradient along the wall is almost zero, the pore just expands in the normal direction without significant change of shape. In the case when there is a positive concentration gradient along the pore wall, the pore widens faster near the inlet compared to the outlet.

To quantify the pore shape evolution during these stages and to explicitly mark the duration of the first stage, the relative displacement rate of the pore wall was calculated as the ratio of the displacement rate of the pore inlet to the pore outlet. At any time, the value of the relative displacement rate indicates how faster the pore inlet is displaced compared to the pore outlet. For example, for $Pe$ number 0.47, initially inlet displacement rate is 8.5 times faster than the outlet displacement rate (Figure 2.4a). During the first stage, the displacement rate of the pore outlet decreases constantly, and at the end of this stage, the relative displacement rate reaches an asymptotic value of 2.3 (Figure 2.4a). Contrastingly, in the first stage for $Pe$ number 47.4, this rate attains an almost constant value of 1.27 (Figure 2.4b). Such evolution of relative displacement rate of the pore wall results into a rigorous modification of the pore wall shape. The continuous change in the relative displacement rate is related to the shape of the pore at

that time (shown in Figure A2.6 and Figure A2.7 for the example case of *Pe* number 0.47 and 47.4).
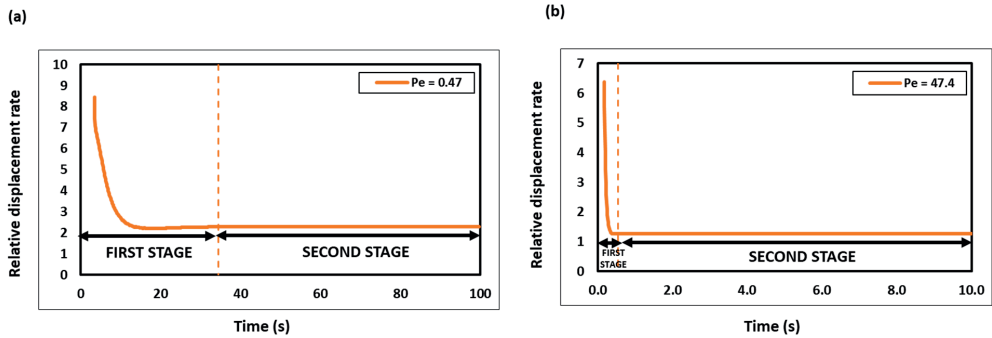


**Figure 2.4.** Relative displacement profiles of the pore wall inlet compared to the pore wall outlet for the *Pe* numbers of (a) 0.47 and (b) 47.4. Note that the start of these plots is from the time when pore outlet point has displaced at least 0.01 nm. The marking of the end of the first stage, as indicated by the dashed vertical line, is at the time when the change in the relative displacement rate with time is less than 0.01% and the changes into concentration gradients becomes minute i.e., t = 34.4s for *Pe*=0.47 and t = 0.54 for Pe=47.4.

In conclusion, during the first stage, the concentration field modifies intensively, resulting into the intensive evolution of the pore geometry and the end of this stage is marked by a nearly established concentration gradients along the pore wall, providing a basis to find a predictive rate for the pore shape evolution.

Although the first stage affects the pore shapes, based on the dissolution regimes, the impact of such developed pore shapes through the first stage is insignificant over the resulting pressure gradient (details are in SI, Section A2.3.3). This is due to the fact that the magnitude of the pore wall displacement in the short duration of the first stage is negligible compared to the overall aperture of the pore. Therefore, in the context of the simulated dissolution regimes and the pore dimensions, the geometry changes during the first stage of the dissolution can be neglected, which is in agreement with the theoretical evaluation of reactive transport regimes (Algive et al., 2010).

### 2.3.3 Evolution of the pore shapes under extended injection times

Although during the first stage the overall pore size would not increase considerably, the developed half-hyperboloid pore shapes indicate the dissolution pattern. The persisting longitudinal gradients in this stage imply that the pore inlet has higher dissolution rate compared to the pore outlet.

The overall pore opening takes place during the second stage. To explain the pore evolution, we choose the simulation corresponding to the *Pe* number of 0.47 and *Da* number of 2.13. As concentration gradients are established along the pore after the first stage and considering that the reaction rate depends on the concentration gradients, dissolution of the interface at the inlet and at the outlet will take place with different speeds, however, with a predictive manner (Figure A2.9). A remarkable observation was that for about 2,000,000s (nearly 23 days), the reaction rate showed larger values at the inlet compared to the outlet. As a result, during this period the pore widened faster at the inlet compared to the outlet, deviating to a greater extent from the initial cylindrical shape. Initially, the calcite near the inlet dissolves

about twice faster than close to the outlet (see also Figure 2.4a), while at time scales well beyond 23 days we observe lower, however similar, dissolution rates at both inlet and the outlet faces (Figure A2.9).

Figure 2.5 shows relative displacement rates modifying the pore shape during the second stage. The continued opening of the half-hyperboloid shape will eventually result in a development of a non-linear pressure profile. Figure 2.5 shows the shape of the pore at two different times. At the time of 1000s, when the inlet radius has increased with about 1.5% (40.6 vs 40) and the outlet radius has increased 0.67% (40.3 vs 40), the pressure along the pore remains linear, meaning that at each point along the pore, we have a constant pressure gradient (recall, that the constant pressure gradient along a pore is an essential assumption in pore network algorithms). However, at t=30000s, the pore shape develops so that the inlet radius has increased by 44% and the outlet radius by 18%, resulting in a non-linear pressure profile along the pore.

In contrast, for *Pe*=47, the relative displacement rate at the end of the first stage is close to one and the initially-cylindrical pore remains nearly cylindrical throughout the second stage and the pressure profile stays linear (Figure A2.10).
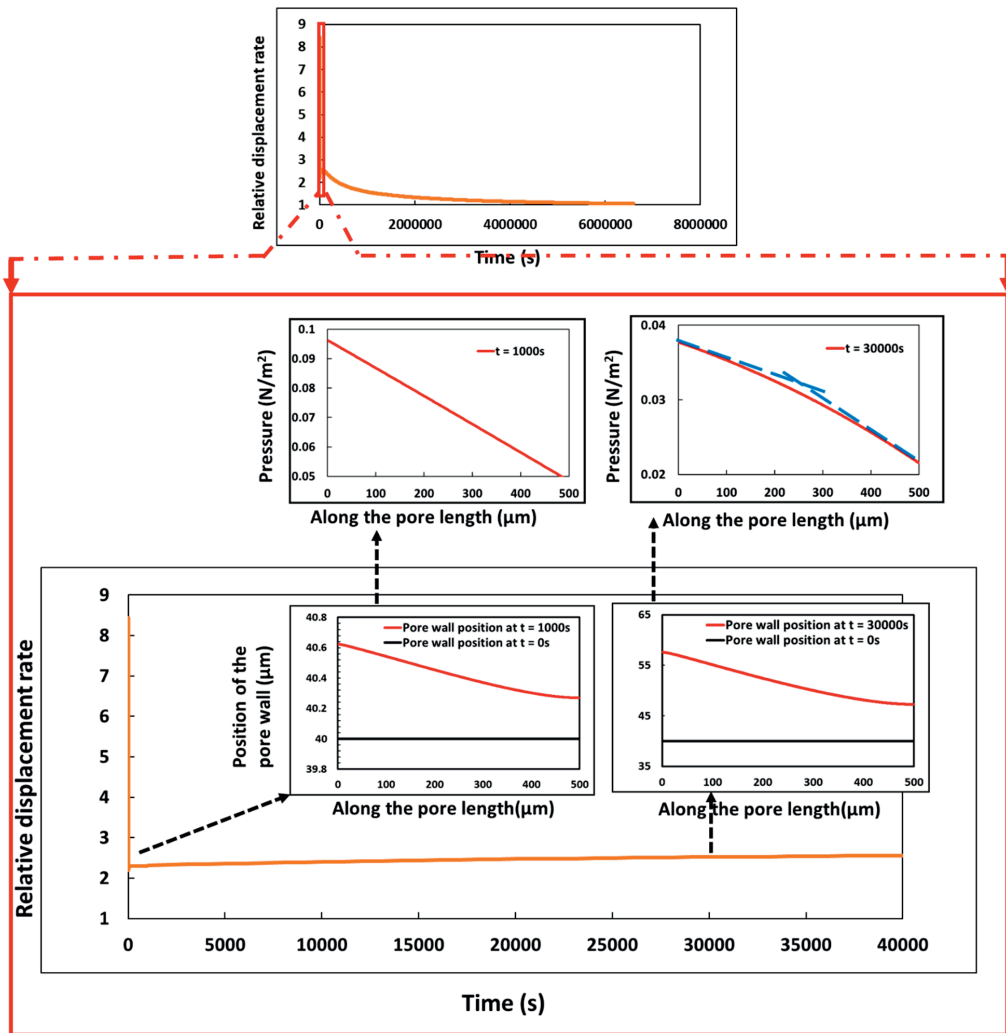
**Figure 2.5.** Evolution of the relative displacement rate during the second stage for the case when at the end of the first stage, the pore shape is hyperboloid (***Pe***=0.47, ***Da***=2.13). The evolved pore shapes and corresponding pressure profiles are shown in inset images, at t = 1000s, and 30000s. Note the different vertical axis scales in each inset image.

### 2.3.4  Flow rate effects on the pore shape evolution

To further explore the flow rate effects, we have performed several simulations by varying the Pe number while the pH of the inflowing solution was kept constant at a value of 3.9. At *Pe*<1, the reaction products effectively diffuse into the pore bulk fluid region before any substantial longitudinal transport takes place (Figure 2.3b). Near the inlet, strong diffusion of the reaction products toward the central parts of the pore facilitates calcite dissolution. At the same time, along the pore, the saturation index of the pore fluid with respect to calcite increases towards equilibrium, due to the buffering by the dissolution products, and dissolution rates decrease along the flow path. Consequently, dissolution reactions take place mainly close to the pore inlet, resulting in non-uniform pore widening and formation of a half hyperboloid-

shaped pore (Figure 2.2b, Figure 2.6a). For $Pe>1$, the transport is dominated by advection. Under this regime, the fast entering solution into the channel replaces the resident solution before the diffusion of the reaction products smoothens transversal gradients and buffers the pH of the solution. Therefore, the calcite pore wall is exposed to a reactive solution along the entire pore, resulting in an even dissolution rate and a nearly uniform evolution of the pore shape (Figure 2.2a, Figure 2.6b). Note that, at both flow rates, flow velocity increases towards the outlet face of the pore which reflects the constricted shape of the pore (Figure 2.6a).
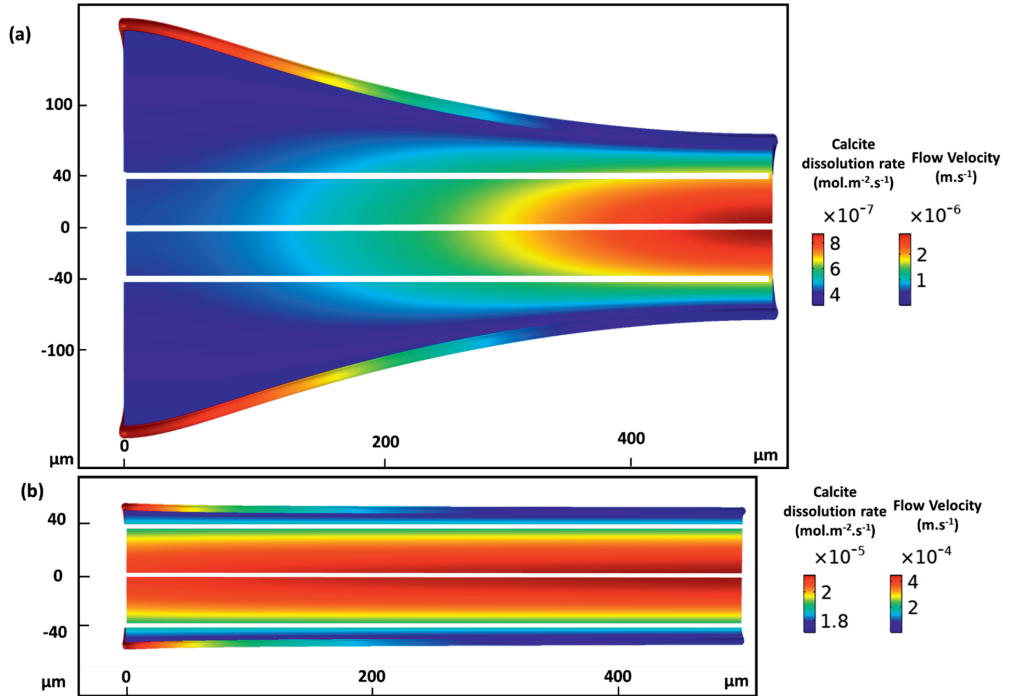


**Figure 2.6**. Simulation results showing the evolved pore shape and the distribution of the velocity field and the reaction rate for two flow regimes of (a) $Pe$=0.05 (b) $Pe$=4.74. The injection period is 15900 pore volumes for both cases with a pH value of 3.9 and pCO$_2$ value of 1.0 bar. The white lines indicate the initial pore shape and the coloured region outside of them indicates the dissolved zones during the reaction. The coloured rim at the pore wall shows the local calcite dissolution rates.

Besides a difference in the shape evolution (i.e., a localized difference in calcite dissolution rate), there is also a clear difference in the total amount of dissolved calcite per injected pore volume. The simulation under low flow rate resulted in a higher value of calcite surface displacement per pore volume injected, compared to the simulation under a fast flow rate. This is because the solution residence time is larger for the low flow rate simulation, and, therefore, reactants dissolve more calcite. However, when using time rather than injected pore volume, the low flow rate dissolves less calcite compare to a high flow rate over time. The evolution of the pore shape corresponding to all of the simulated flow rates is discussed in SI, Section A2.3.4.

### 2.3.5   Chemistry effects on the pore shape evolution

In addition to the flow rate, the chemistry of the injecting fluid affects the pore shape. To explore chemistry effects further, we performed simulations with two injecting solutions at pH values of 3.1 and 3.9, corresponding to pCO$_2$ of 100.0 bar and 1.0 bar, respectively. Evolution of the pore shape depends on the reactivity of the pore wall towards the injecting solution. Expectedly, the pH=3.1 solution results in the stronger displacement of the pore wall than the pH=3.9 solution. This results in increased concentrations of the reaction products near the pore wall, driving the local solution chemistry towards equilibrium with respect to calcite. This buffering of fluid is also reflected by a change of the fluid pH, in the case of the pH=3.1 inflow solution at $Pe$=4.74, the transversal average pH increases from 4.71 to 4.82 corresponding to the dissolution rate from 1.70 x 10$^{-4}$ [mol m$^2$ s$^{-1}$] to 0.49 x 10$^{-4}$ [mol m$^2$ s$^{-1}$] from inlet to outlet boundaries, respectively. The result of this alteration in the pore fluid chemistry is ultimately reflected by the evolved pore shape. In this case, the pore widens non-uniformly along the pore length (Figure A2.12a). However, injecting a pH=3.9 solution at $Pe$=4.74 provides a transversal average pH that changes from 4.09 to 5.10 and dissolution rate from 2.12 x 10$^{-5}$ [mol m$^2$ s$^{-1}$] to 1.72 x 10$^{-5}$ [mol m$^2$ s$^{-1}$], from the inlet to outlet boundaries, respectively. In this case, fluid buffering during dissolution is relatively weaker and a more uniform pore shape develops (Figure A2.12b).

To cover a range of values for Damkhöler numbers, i.e., reaction regimes, we have chosen a combination of flow rates and injecting fluid chemistries (Figure 2.7). Table 2.1 provides details of these simulations. By increasing $Da$ number, the reaction time scale decreases compared to the advection time scale and the system approaches being transport limited instead of surface-rate limited. The normalized displacement profiles after injecting 1590 pore volumes, provided in Figure 8, show that there is a monotonic relation between pore shape and $Da$, under the considered reaction regimes.

For $Da$<1 and $Pe$=47.4, reaction time scale is higher than the advection time scale, and at the same time advection dominates the diffusion. In such advection-dominated transport regimes, the chemistry of the injecting fluid has less control on pore shape evolution and adjusting inflow pH from 3.4 to 3.9 has a negligible impact over the pore shape (Figure 2.7a, $Da$ numbers 0.03 and 0.21). Whereas in the $Da$>1 and $Pe$=0.47 regime, which is overall reaction-dominated while transport is diffusion-dominated, the same shift of inlet pH causes a profound change in pore shape (Figure 2.7a, $Da$ number 2.13 and 14.95).
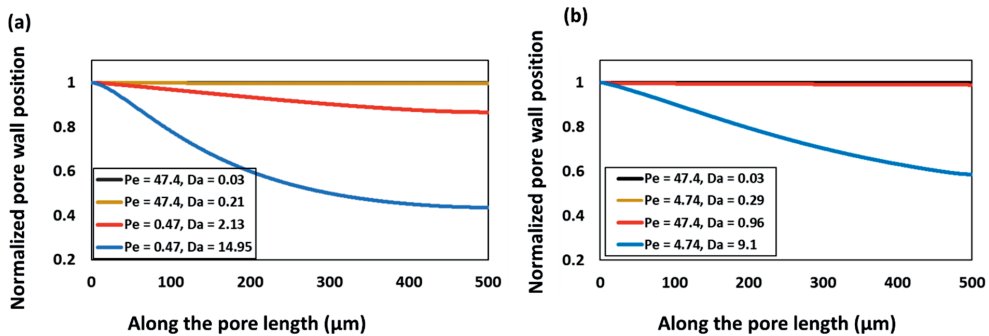


**Figure 2.7.** The normalized position of the reacting pore wall under different reaction and flow regimes denoted by $Da$ and $Pe$ numbers respectively. In all cases, 1590 pore volumes were injected. (a) The pH of the injecting solution, reflected by high $Da$ (see Table 2.1),

impacts the pore shape more prominently for simulations with low $Pe$ number (b) Injection flow rate impacts the pore shape more prominently for simulations using more acidic solutions.

The dissolution regime corresponding to $Da<1$ and $Da>1$, can also be obtained by changing the pH of the injecting fluid. If the pH=3.9 solution is injected, i.e., $Da<1$, the impact of changing flow rate is less prominent over the pore shape and the pore shape remains nearly uniform (Figure 2.7b, $Da$=0.03 $Pe$=47.4 versus $Da$=0.29, $Pe$=4.74). For a regime of $Da>1$ using a reactive fluid with pH=3.1, a shift of $Pe$ number causes a significant change of the pore shape (Figure 2.7b, $Da$ number 0.96 and 9.1).

In reaction-limited dissolution regimes ($Da<1$), control of flow rate and reactive strength of the injecting fluid becomes marginal over the shape of the pore. The reason is that the time necessary for dissolution-reaction (i.e., generating the reaction products and consuming protons) may dominate rather than the fluid mixing scale when analyzing the fluid buffering state. And in these regimes, dissolution is spatially homogeneous leading to uniformly developed pore shapes. Whereas in transport-limited dissolution regimes ($Da>1$), fluid mixing strength exerts control over the chemical gradient inside pore space. This leads to heterogeneous dissolution process in which both flow rate and chemistry of the injecting fluid govern the pore shape.

To summarize, we can conclude that both injection parameters such as flow rate and fluid chemistry impart control over the pore shape. Figure 2.8 provides a spectrum of pore shapes based on changes in transport and reaction regimes shown by $Pe$ and $Da$ numbers. The marking of the regimes in this study aligns well with the previously reported pore-scale work specific to the calcite dissolution for e.g., Soulaine et al., 2017. They have also observed the boundary between the uniform and non-uniform type of dissolution at $Da$ number 1. In the subsequent section, we compare the conductance of a single pore after long injection period, calculated here with using fully coupled pore-scale model utilizing ALE method, and the approximate calculation of the conductance discussed in Pore Network algorithms, and investigate the related error depending on the dimensionless process parameters $Pe$ and $Da$.
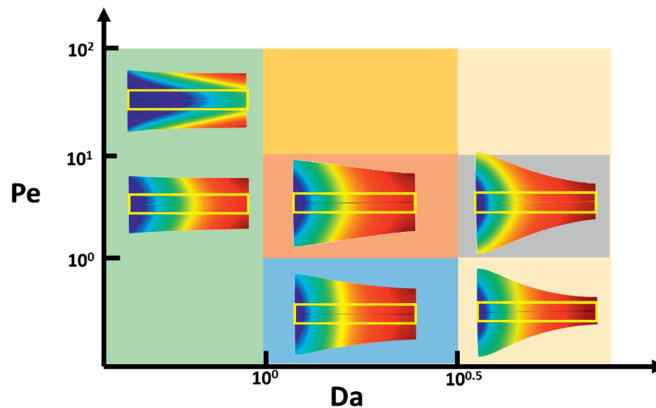


**Figure 2.8.** Pore evolution after several hours of acid injection, based on changes in transport and reaction regimes shown by $Pe$ and $Da$

### 2.3.6   Implication of the pore shapes on the pore conductance

Evolution of conductance in dissolution simulations is implemented in existing pore network algorithms (e.g., Raoof et al., 2012, Mehmani et al., 2012 and Nogues et al., 2013). A significant underlying assumption in this implementation is that the shape of the pore remains uniform, where the evolved pore shape still results in a linear pressure drop along the pore. The results presented here show that this assumption is valid under the advection-dominated flow regimes with $Pe>1$ and transport-dominated reaction regimes with $Da<1$. However, as we observed in the case of the $Pe=0.47$, the changes of the shape start to influence the pressure profile in a time scale of 30000 second which is within the time scale of injection period in a reservoir.

   The pressure profile along a pore is directly related to the conductance calculated in PNM. Taking the commonly assumed laminar flow, when the pore changes are uniform along its length, the pressure drops linearly (Figure A2.10). This is not the case when the pore shape deviates from the cylindrical one. In such a case the pressure gradient is not constant and changes along the pore (Figure 2.5). Such pressure nonlinearity affects the pore conductance, and, therefore, the rock permeability. Hence, we need to quantify the impact of such modified shapes on the conductance of the pore.

The definition of conductance, $K$, is given via the flow rate, $Q$ (m$^3$ s$^{-1}$) and the pressure drop $\Delta P$ (N m$^{-2}$) along the pore as:

$$Q = K\Delta P \tag{2.6}$$

   For a rounded cylindrical pore (with a constant diameter along the pore) with a parabolic velocity profile (i.e., Hagen - Poiseuille flow) the conductance, $K$ (m$^5$ N$^{-1}$ s$^{-1}$), is known and it is given by:

$$K = \frac{\pi(2r)^4}{128\mu L} \tag{2.7}$$

   Here $L$ is the length of the pore (called also pore throat length in the PNM literature) given in meters, (m), $r$ is the radius of the pore (m). In dissolution experiments, as the radius $r=r(t)$ (and eventually, the shape of the pore changes), the pore conductance is no longer constant, K=K(t). We calculated the apparent pore conductance (i.e., overall conductance of the pore) using Equation 2.6. For Figure 2.9, the conductance and pore volume is normalized with respect to the initial pore conductance and the initial pore volume, respectively.
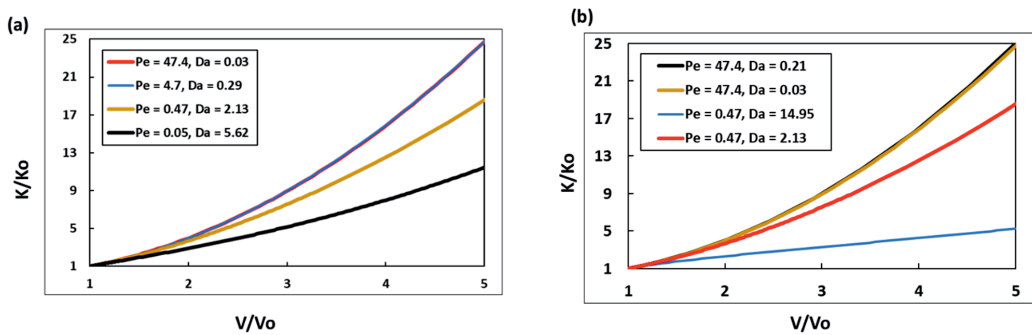


**Figure 2.9**. Conductance of the pore as a function of pore volume for (a) different **Pe** numbers and constant fluid pH value of 3.9 (b) different **Da** numbers and two of the **Pe** number sets

The half-hyperboloid pore shape leads to a changing pressure gradient along the pore (Figure 2.9a, black line). The narrowness of the pore aperture towards the outlet provides small contributions to the overall volume changes of the pore; however, this section of the pore controls the overall conductance of the pore. Consequently, pore volume increases considerably (near the pore inlet), while pore conductance changes marginally during hyperboloid pore shape formation (Figure 2.9a, black line). This means that, as non-uniformity of the pore shape increases, the change of conductance becomes smaller for the same amount of volume change (Figure 2.9). Therefore, at the pore scale, the change of the pore conductance in time in certain cases cannot be described just as a function of the pore volume, the pore shape may play a significant role. The implication of this observation for macroscale simulations is that formulae which provide permeability only as a function of porosity are not always suitable, and they are accurate only over a certain flow and reactive transport regime for which they have been developed.

In most of the existing pore network models, the conductance of the pore throat is updated at each time step in response to the changing volume of the pore only, without accounting for the pore shape evolution. And, such a conductance is obtained by utilizing either the volume of the connecting pore bodies (Nogues et al. 2013) or the volume of the pore throat (Raoof et al. 2012). We calculated the conductance of the simulated pore geometry in a similar method as used by Raoof et al. 2012. At each time step, the volume of the pore provides the uniform radius of the pore which is further utilized in calculating the conductance. Figure 2.10 shows the comparison of this conductance with the one calculated from the actual geometry of the pore, for two of the dissolution regimes.
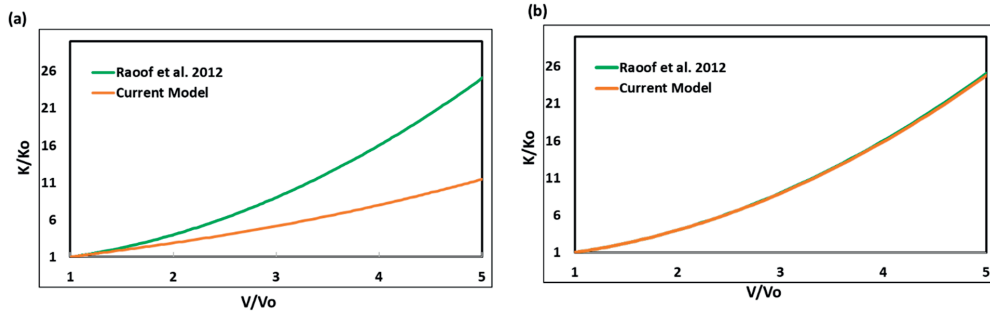


**Figure 2.10**. Comparison of the pore conductance calculated from the actual shape of the pore vs an exemplary method from the existing pore network model for (a) $Pe$=0.05 and $Da$=5.62 (b) $Pe$=47.4 and $Da$=0.03

We observe that if the dissolution process maintains the cylindrical shape of the pore, then the conductance is only a function of the volume of the pore, as assumed in PNMs (Figure 2.10b). Whereas, for the dissolution regime corresponding to $Pe$<1 and $Da$>1, the conductance of the pore does not remain a function only of the volume of the pore, but it depends also on the shape of the pore. In the latter case, ignoring the dependence of the conductance from the pore shape results in an error. The conductance calculated from the volume of the pore (PNM approach) overestimates by 38% the conductance calculated from the actual hyperboloid pore shape when the volume of the dissolved calcite is equal to the original volume of the pore. This overestimation is 76% when the volume of the dissolved calcite is equal to two times the original volume of the pore and may increase further with dissolution (Figure 2.10a).

Note that the pore conductance evolution during the dissolution process depends not only on the flow and reaction regimes, as shown here (Figure 2.9), but also on the length of the pore, on the initial radius of the pore, on the equilibrium pH and on the pH of the injected fluid. For the pH, radius and length of the pore investigated here, Figure 2.11 summarizes the regimes in which the conductance can be calculated as in PNM only by the volume of the pore vs the regimes where this method fails to capture the correct conductance. This figure presents a moment during the dissolution process at which the change in the pore volume is 100% (i.e., $V/V_0 = 2$). For the reaction-controlled regimes ($Da<1$), irrespective of the flow rate, the volume-based conductance is within 1% range of the actual conductance. This difference increases significantly for the transport-controlled regimes, where the diffusion-dominated flow regimes yielding up to 76% of the difference. Note that the difference increases further with dissolving larger volume of the calcite. This result illustrates the limitation of the existing assumption in the pore network model, however, the work for deriving a more defined relationship for conductance remains a topic for future work.
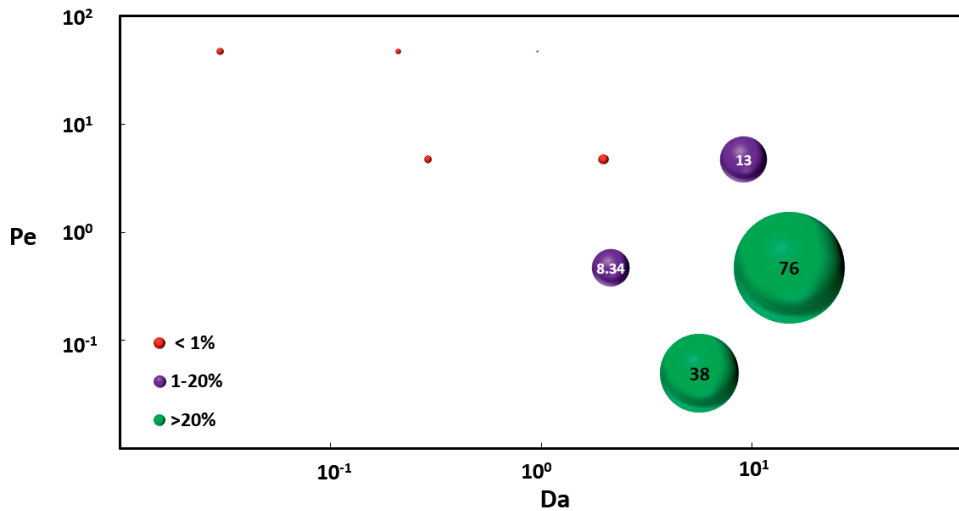


**Figure 2.11**. *Pe-Da* phase diagram showing the % difference in the conductance based on the volume of the pore with the one from the actual pore geometry.

## 2.4    Conclusions

1. The simulation results of reactive transport processes through single calcite pore and the results from the respective microfluidic experiments were found to be in good agreement at both investigated flow rates. The validated computational algorithm was used to perform a thorough and detailed study of the dissolution processes for a range of hydrochemical parameters.

2. It was observed that the calcite dissolution process can be divided into two stages with respect to the concentration field development and pore shape evolution. During the first, very short (in the order of seconds) and intrinsically transient stage, the reactive-transport processes rapidly change the concentration field inside the pore, and at the end of this stage, the pore has attained a characteristic shape and concentration gradient. Only the latter plays a critical role in the longer-term dissolution process. These numerical results are a justification of the statements of other authors that the pore shape development during the first stage can be

ignored, while the concentration gradient should be accurately calculated. The second stage is long (days or longer) and corresponds to real injection times in reservoirs. At this stage, the flow and transport are at a quasi-steady state. The pore shape changes slowly, but for large concentration gradients, significant deviation from the original cylindrical shape can be observed for certain dissolution regimes.

3. Generally, lower flow rates result in significant concentration gradients in the longitudinal direction and thus in a non-uniform change of the pore shape. As a result, the pressure gradient is no longer constant along the pore. An increase in solution reactivity (lowering in pH) provides the same effect; it drives reactions towards equilibrium over a shorter distance from the inlet, and, therefore, results in non-uniform pore shapes. Injecting fluid with a high flow rate, or lower reactivity yields a more uniform pore volume increase. We also observe that the impact of flow rate and fluid reactivity on the pore shape are more significant when dissolution is transport controlled ($Da>1$).

4. For certain flow and reaction regimes, a significant difference is observed between the pore conductance computed here and pore conductance computed according to PNM (assuming constant pore shape). Further research is needed to understand if and how PNM can be used for dissolution regimes for which the basic PNM assumption leads to significant error in conductance evaluation.

## Appendix 2

### A2.1 Mathematical Model Set-up

The numerical solutions are sensitive to the mesh refinement. Based on the mesh sensitivity study, we choose the starting mesh size in the range of 0.01-2 μm near the boundary and 0.05-3 μm in the bulk part of the model. Dissolution induced mesh deformation did not deteriorate the mesh a lot as such the mesh quality remained acceptable throughout the simulation time window. (see Agrawal et al., 2017 for more details on the meshing method).

### A2.1.1 Fluid Flow and Transport

In this study we have considered slow fluid velocity only (i.e., Reynolds number Re ≪ 1). Therefore, the inertial terms can be neglected in the momentum equations and the Stokes equation may be used to compute the velocity field and the pressure in the single pore:

$$\rho \frac{\partial u}{\partial t} + \nabla.p = \mu \Delta u \qquad (A2.1)$$
$$\nabla.u = 0 \qquad (A2.2)$$

where, $p$ is pressure, $\rho$ is the fluid density and $\mu$ is the fluid viscosity. The density and dynamic viscosity of water were 998.25 kg m$^{-3}$ and 8.96 × 10$^{-4}$ Pa s, respectively. The concentration of the dissolved species is assumed to be low enough so that the fluid density and the viscosity changes are negligible.

For transport of aqueous species, the advection-diffusion-reaction equation is implemented. as:

$$\frac{\partial c_i}{\partial t} + \nabla.(-D_i.\nabla c_i) + \nabla.(u.c_i) = R_i \qquad (A2.3)$$

Where, $D_i$, $c_i$ and $R_i$ are diffusion coeffcient (m$^2$ s$^{-1}$), concentration (mol m$^{-3}$) and reaction input of species $i^{th}$ (mol m$^{-3}$ s$^{-1}$), respectively.

At the inlet, a constant mass flux condition is imposed, and constant pressure of 1.0 bar is applied at the outlet. At the lateral boundaries of the pore no-slip condition boundary conditions are imposed, i.e., the tangential velocity is zero there. The normal velocity at the lateral pore boundaries is continuous, i.e., the normal fluid velocity at the interface is equal to the normal velocity with which the solid wall moves due to dissolution.

At the pore inlet we implemented a flux-based boundary condition (Starchenko et al., 2016). This flux depends upon the fluid velocity and the concentration values specified.

$$n.(-D_i.\nabla c_i + u.c_i) = u_n.c_{oi} \qquad (A2.4)$$

where, $c_{oi}$ is the inlet (injected) concentration of species $i^{th}$ and $u_n$ is the normal velocity at the inlet. The concentration for each aqueous species is given in Table A2.1. The outlet boundary is exposed to zero gradient condition for all species. To conserve the mass across the solid-fluid interface, the total (diffusive plus convective) flux for species involved in the surface reactions. i.e., Ca$^{2+}$ and CO$_3$$^{2-}$ equals the reactive flux at the interface. This reads:

$$-n.(-D_i.\nabla c_i + u.c_i) = R_{Calcite} \qquad (A2.5)$$

where, $R_{Calcite}$ [mol m$^{-2}$ s$^1$] is the surface reaction rate as discussed in subsequent Section A2.1.2.

| Species | Injecting Solution - I (mol m$^{-3}$) | Injecting Solution - 2 (mol m$^{-3}$) | Injecting Solution - 3 (mol m$^{-3}$) | Injecting Solution – 4 (Solution corresponding to experiment) | Initial solution inside pore (mol m$^{-3}$) | Diffusion coeffecient (m$^2$ s$^{-1}$) [a]from Li and Gregory, 1974 and |
|---|---|---|---|---|---|---|

| | | | | (mol m$^{-3}$) | | [b]from Liu et al., 2011 |
|---|---|---|---|---|---|---|
| H$^+$ | 1.1 | $5.02 \times 10^{-1}$ | $1.63 \times 10^{-1}$ | $1.26 \times 10^{1}$ | $1.27 \times 10^{-7}$ | [a]$9.31 \times 10^{-9}$ |
| OH$^-$ | $1.58 \times 10^{-8}$ | $3.54 \times 10^{-8}$ | $1.09 \times 10^{-7}$ | $1.43 \times 10^{-9}$ | $8.35 \times 10^{-2}$ | [a]$5.27 \times 10^{-9}$ |
| CO$_2$(aq) | $1.51 \times 10^{3}$ | $3.07 \times 10^{2}$ | $3.23 \times 10^{1}$ | $1.07 \times 10^{-2}$ | $2.27 \times 10^{-5}$ | [a]$1.19 \times 10^{-9}$ |
| HCO$_3^-$ | 1.04 | $4.74 \times 10^{-1}$ | $2.01 \times 10^{-2}$ | $6.7 \times 10^{-7}$ | $8.35 \times 10^{-2}$ | [a]$1.19 \times 10^{-9}$ |
| CO$_3^{2-}$ | $1.34 \times 10^{-7}$ | $1.34 \times 10^{-7}$ | $1.34 \times 10^{-7}$ | $7.68 \times 10^{-15}$ | $3.38 \times 10^{-2}$ | [a]$0.92 \times 10^{-9}$ |
| Ca$^{2+}$ | 0 | 0 | 0 | 0 | 0.12 | [a]$0.79 \times 10^{-9}$ |
| Na$^+$ | $2.00 \times 10^{2}$ | $2.00 \times 10^{2}$ | $2.00 \times 10^{2}$ | $2.0 \times 10^{2}$ | 0 | [b]$1.34 \times 10^{-9}$ |
| Cl$^-$ | $2.00 \times 10^{2}$ | $2.00 \times 10^{2}$ | $2.00 \times 10^{2}$ | $2.13 \times 10^{2}$ | 0 | [b]$1.86 \times 10^{-9}$ |
| pH | 3.1 | 3.4 | 3.9 | 2 | 9.91 | - |
| pCO$_2$ | 100 | 10 | 1 | $3.31 \times 10^{-4}$ | $6.76 \times 10^{-7}$ | - |

**Table A2.1.** Concentrations and self-diffusion coeffcients of aqueous species in the injecting solution and in the initial solution inside pore.

### A2.1.2 Geochemical Model

The injected acidic solution in the carbonate reservoir initates a number of chemical reactions:

$$K_1: CO_2(aq) = H^+ + HCO_3^- \tag{A2.6}$$
$$K_2: HCO_3^- = H^+ + CO_3^{2-} \tag{A2.7}$$
$$K_w: H_2O = H^+ + OH^- \tag{A2.8}$$

Correspondingly, the mass action laws providing non-linear relations are:

$$K_1 = \frac{a_{H^+} \; a_{HCO_3^-}}{a_{CO_2(aq)}} \tag{A2.9}$$

$$K_2 = \frac{a_{H^+} \; a_{CO_3^{2-}}}{a_{HCO_3^-}} \tag{A2.10}$$

$$K_w = a_{H^+} \; a_{OH^-} \tag{A2.11}$$

where, $K_1$, $K_2$, and $K_w$ are equilibrium constants of the reactions. At 25°C, $K_1 = 4.5 \times 10^{-7}$, $K_2 = 4.78 \times 10^{-11}$ (Plummer and Busenberg, 1982), $K_w = 1 \times 10^{-14}$. $a_i$ is the activity of the $i^{th}$ species. The activity ($a_i$) and the concentration ($c_i$) are related by:

$$a_i = \gamma_i \frac{c_i}{c_o} \tag{A2.12}$$

where, $c_o$ is the standard concentration i.e., 1000 mol m$^{-3}$ (IUPAC 1982), $c_i$ is the concentration of the $i^{th}$ species in mol m$^{-3}$ and $\gamma_i$ is the activity coefficient of the $i^{th}$ species. The standard concentration is used in order to make both, the activity and the activity coefficient, unitless.

Davies equation as:

$$\log \gamma_i = -A \, z_i^2 \left( \left[ \frac{\sqrt{I}}{1 + \sqrt{I}} \right] - [0.3I] \right) \tag{A2.13}$$

where, $z_i$ is the charge of the $i^{th}$ species and $I$ is the ionic strength of the solution. As the reactions progress, the ionic strength is calculated at each time step. In this study the value of the constant $A$ is taken as 0.5085 at 25°C (Stumm and Morgan, 1996). The activity coefficient of the neutral species i.e., H$_2$O and CO$_2$(aq) is assumed to be equal to 1. Ionic strength of the solution is calculated as (Stumm and Morgan, 1996):

$$I = 0.0005 \left( \sum_{i=1}^{7} c_i z_i^2 \right)$$

(A2.14)

Plummer et al., 1978, studied the calcite dissolution process for a pure calcite crystal and observed three main pathways for the dissolution of calcite:

$k_1$: $CaCO_3(s) + H^+(aq) = Ca^{2+}(aq) + HCO_3^-(aq)$ (A2.15)

$k_2$: $CaCO_3 + CO_2(aq) = Ca^{2+}(aq) + 2HCO_3^-(aq)$ (A2.16)

$k_3$: $CaCO_3(s) = Ca^{2+}(aq) + CO_3^{2-}(aq)$ (A2.17)

The rates of these reversible reactions were combined into a single dissolution rate law:

$$R_{Calcite} \text{ [mol m}^{-2}\text{ s}^{-1}] = (k_1 \, a_{H^+} + k_2 \, a_{CO_2(aq)} + k_3 \, a_{H_2O}) \, (1 - 10^{0.67 SI})$$

(A2.18)

where, $k_1 = 8.64 \times 10^{-5}$, $k_2 = 4.78 \times 10^{-7}$ and $k_3 = 2.34 \times 10^{-9}$ at 25°C are the reaction rate constants (Busenberg and Plummer, 1986). The choice of this rate model is explained in the Section A2.3.1. SI is the saturation index of the fluid defined as the ratio of the ion activity product (product of $a_{Ca^{2+}}$ and $a_{CO_3^{2+}}$) and the solubility constant of the calcite, taken here as $10^{-8.48}$ (Plummer and Busenberg, 1982)

### A2.1.3 Pore geometry evolution model

The conventional methods to solve the partial differential equations are either the Lagrangian, i.e., a material-coordinate-based system, or Eulerian, i.e., spatial-coordinate-based system. The pure Eulerian method is challenging to be used for moving domain problems because of the requirement for the continuous update in the value of the independent variables with time. Arbitrary Lagrangian Eulerian (ALE) method is an intermediate of these two methods, in which the flow and transport equations are defined in a fixed reference domain and this fixed domain is linked to the time-dependent moving domain. The displacement rate is defined as:

$$w_n = R_{Calcite} \, MV$$
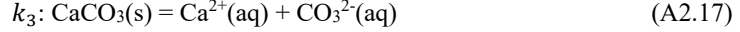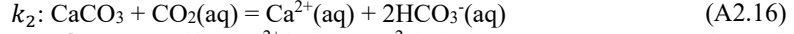
(A2.19)

where, $w_n = u_n$ is the displacement rate defined at lateral boundary of pore, $R_{Calcite}$ (see Equation A2.18) is the reaction rate of calcite [mol m$^{-2}$ s$^{-1}$] and $MV$ is molar volume of calcite i.e., $3.69 \times 10^{-5}$ m$^3$ mol$^{-1}$.

### A2.2 Microfluidic Experiment

### A2.2.1 Microfluidic Device

The microfluidic set-up was created by drilling a channel through the calcite crystal. Initially, the calcite crystal was cut into blocks of different sizes. This crystal was later placed between two glass plates, of a thickness of 4 mm, using 3M™ Scotch-Weld DP-100 clear epoxy. The purpose of the glass plates was to keep the inlet and outlet connections intact, during the calcite dissolution experiments. In this crystal-glass assembly, a channel of diameter 0.5mm and length 10mm, was drilled using ultrasonic CNC (computer numerical control) milling machine. The center of the channel was maintained at 0.45mm from the crystal surface. This distance was chosen so that the channel can be later visualized under the confocal microscope. The inlet and outlet connections, used in this device were, stainless dispensing tips with internal diameter 0.25 mm, outer diameter 0.51 mm and length 6.35 mm (Figure A2.1).

### A2.2.2 Injection solution composition and injection flow rates

The injection solutions were prepared using deionized water equilibrated with atmospheric $CO_2$ and adjusted to desired pH with 1M stock solution of HCl acid. To ensure the sufficiently constant ionic activity of solutions, 0.2M equivalent NaCl salt (Lot No.: K48328204648) was added. At the start of each experiment, $CaCO_3$ saturated water is injected in the channel, to attain the approximate carbonate reservoir initial conditions. The solutions were injected with the use of a syringe pump (11 Pico Plus Elite, Harvard Apparatus) and a 5 ml Gastight syringe

(Hamilton 1700 series) at the desired flow rates. The experimental set-up and micro-fluidic device are presented in Figure A2.1.
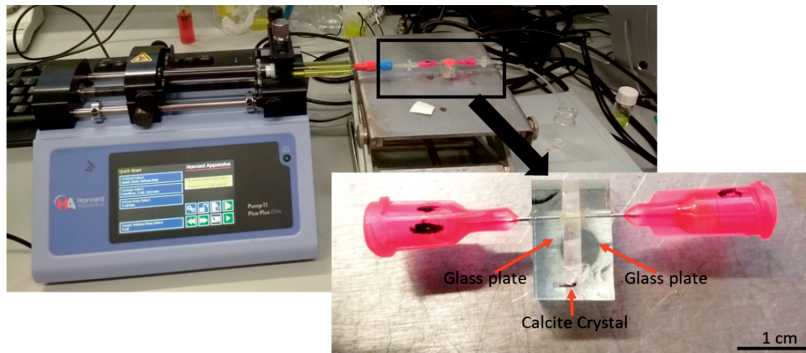


**Figure A2.1.** Microfluidics experimental setup showing pump, syringe (filled with fluorescent dye mixed acid solution) and calcite crystal – glass – needle assembly.

### A2.2.3 Experiment datasets

To ensure that the equal numbers of acid pore volumes injected in these two different flow rate experiments, the duration of experiment was kept at one hour for high flow rate and ten hours for low flow rate.

The confocal microscope can obtain Z-direction focused planar information from a 3D specimen, i.e., cylindrical channel in this experiment. This microscopic imaging was enhanced by utilizing fluorescent salt. Images were acquired under the following microscopic settings: Objective - x10 magnification, 0.45-numerical aperture without immersion lens (Plan-Apochromat), 512 x 512 images, 2.46µm/px resolution, Laser emitting 488 nm excitation wavelength, two detector tubes (tube 1: Emission wavelength band 500-550 nm – suitable with fluorescein sodium salt dye (Fluorescein detector), tube 2: transmitted detector (TD)), scanning mode – Resonant line scan. For both experiments, channel images were obtained prior and after the injection of equal number of acid solution pore volumes. Three types of images are obtained: 1) through transmitted detector, 2) through fluorescein detector and 3) By superimposing images of these two detectors i.e., transmitted detector and fluorescein detector. All of the images are focused around the middle of the channel.
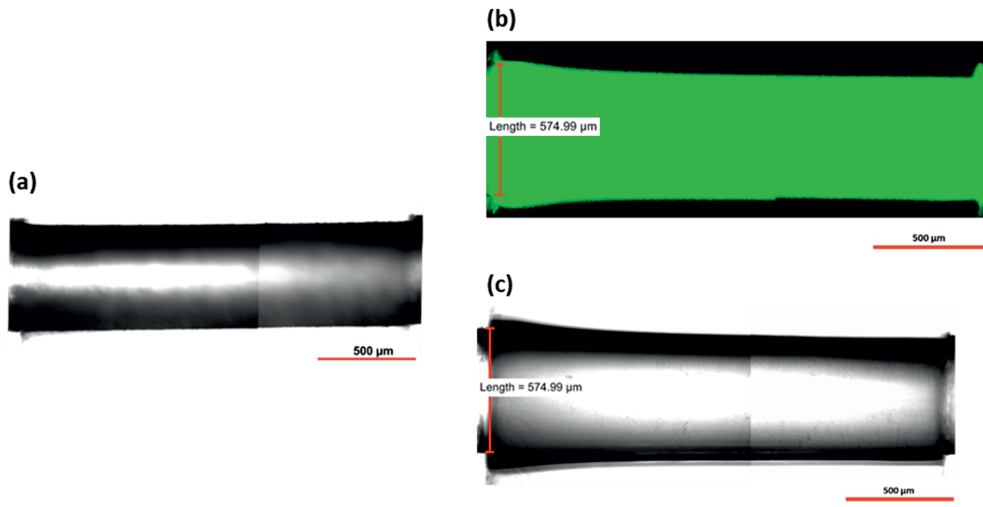
**Figure A2.2.** Confocal images of the channel from the high flow rate experiment (a) at t = 0s from transmitted detector (b) After one hour of acid flushing from fluorescein detector (c) After one hour of acid flushing from transmitted detector
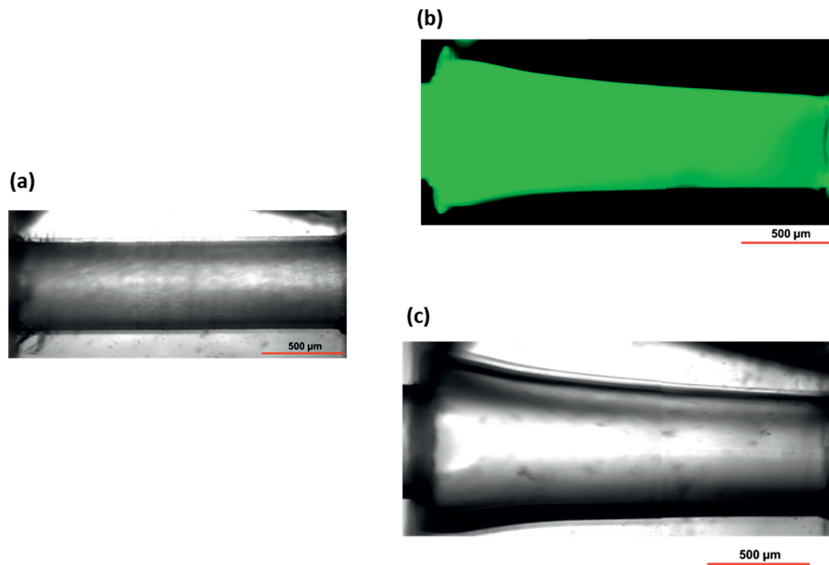


**Figure A2.3.** Confocal images of the channel from the Low flow rate experiment (a) at t = 0s from transmitted detector (b) After one hour of acid flushing from fluorescein detector (c) After one hour of acid flushing from transmitted detector

## A2.3 Results

### A2.3.1 Imposed reaction rate vs other available reaction rates in the literature

Figure A2.4 summarizes some of the available reaction rate laws for calcite dissolution process. For similar solution conditions (pH), there is more than one order of magnitude difference in the absolute value of the reaction rate. This difference is attributed to the different experimental

conditions e.g., the type of the experiment setup, speed of the rotating disc, crystal vs powdered calcite, $pCO_2$ and ionic strength.
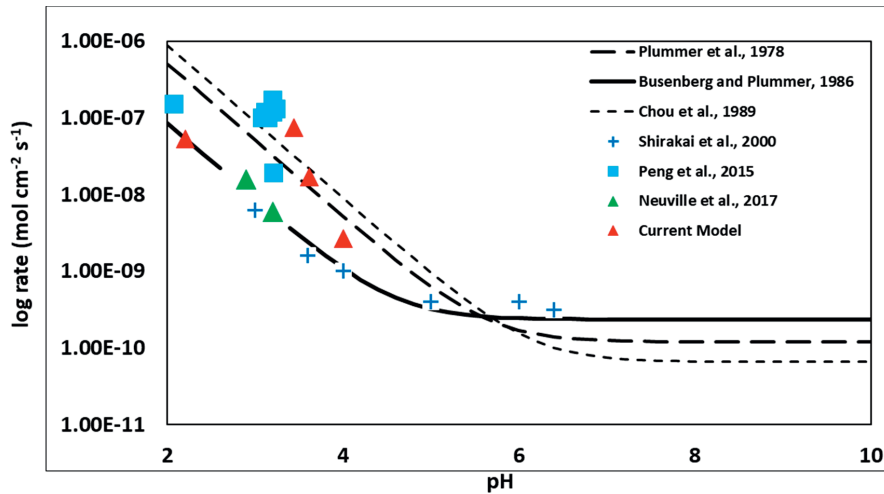


**Figure A2.4.** Implemented rate model vs existing rate models for calcite dissolution process.

The current model imposes the reaction rates from Busenberg and Plummer (1986). This choice of the rate law is found to be in better agreement with the microfluidic experiments. For the similar single calcite-channel based microfluidic experiments, Neuville et al. (2017) also noted the calcite dissolution rates in agreement with this rate model.

### A2.3.2 Sensitivity analysis of the numerical model against diffusive flux

The presented model (Model I) is using a single value of the diffusion coefficient for all the species i.e., $3.36 \times 10^{-9}$ $m^2s^{-1}$. To examine the model sensitivity towards diffusive fluxes, we compared the $Ca^{2+}$ concentrations of the outflow solution of the experiment with the current model alongside with three alterations of this model through different diffusive flux considerations: a) Model II - Single value of the diffusion coefficient i.e., $1 \times 10^{-9}$ $m^2s^{-1}$ b) Model III - Single value of the diffusion coefficient i.e., $5.6 \times 10^{-9}$ $m^2s^{-1}$ (Gray et al., 2018) c) Model IV - Species-specific diffusion coefficient (without electrochemical migration).
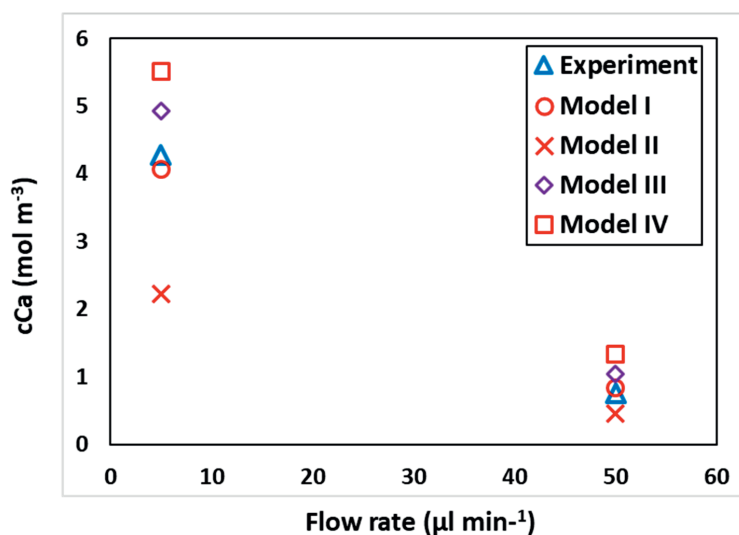
**Figure A2.5.** Comparison of $Ca^{2+}$ concentration measured at the outlet in the experiment with the flux-weighted average concentration of $Ca^{2+}$ from different numerical simulations such as Model I – Single diffusion coefficient for all species i.e., $3.36 \times 10^{-9}$ $m^2s^{-1}$, Model II - Single diffusion coefficient for all species i.e., $1 \times 10^{-9}$ $m^2s^{-1}$, Model III - Single diffusion coefficient for all species i.e., $5.6 \times 10^{-9}$ $m^2s^{-1}$ (Gray et al., 2018), Model IV – Species-specific diffusion coefficient.

From Figure A2.5, it is obvious that the simplified models based on a fixed diffusion coefficient are closer to the experimental results if the utilized value of the diffusion coefficient is the average of the self-diffusion coefficient of all the species. Whereas, if the species-dependent diffusion coefficient is included in the model while neglecting the charge balance and electrochemical migration, there is a large discrepancy between modelled and measured $Ca^{2+}$ concentrations. This illustrates the importance of charge balance in dilute solutions such as the one used in the current experiment (0.2M NaCl) as also noted by Li et al., 2007. Thus, the implementation of charge-coupled diffusion (Nernst-Plank equation) (Gray et al., 2018) or Poisson-Nernst-Plank equation developed to handle charge separation in nano-pores (Yang et al., 2018), may further improve the match between model and measurement. However, our goal was to investigate pore shape evolution for varying fluid velocity and composition, and it may be concluded that model I captures the pore shape evolution and outflow composition well.

**A2.3.3 Initial stages of pore shape development process:**
Figure A2.6 and Figure A2.7, shows the pore shapes at different time moments of the dissolution process in correspondence with the relative displacement rate.

In order to demonstrate the implication of the geometry modification during the first stage, we simulated another set of models under the same external environment conditions such as the flow rate and fluid chemistry of the injecting fluid, but with no geometry evolution during the first stage of the dissolution. For this testing, the fixed simulation conditions across two sets are: flow regime corresponding to the Pe number 0.47, injecting fluid with a pH value of 3.9. At each time step, the pressure gradient calculated from this model is compared with the one coupled with the evolving geometry from the start of the simulation. We observed that at the

end of the first stage, the evolved shape of the pore induced a difference of less than 0.1% in the value of the pressure gradient, indicating that pore shape evolution during the first stage almost does not impact the pore conductance (Figure A2.8).
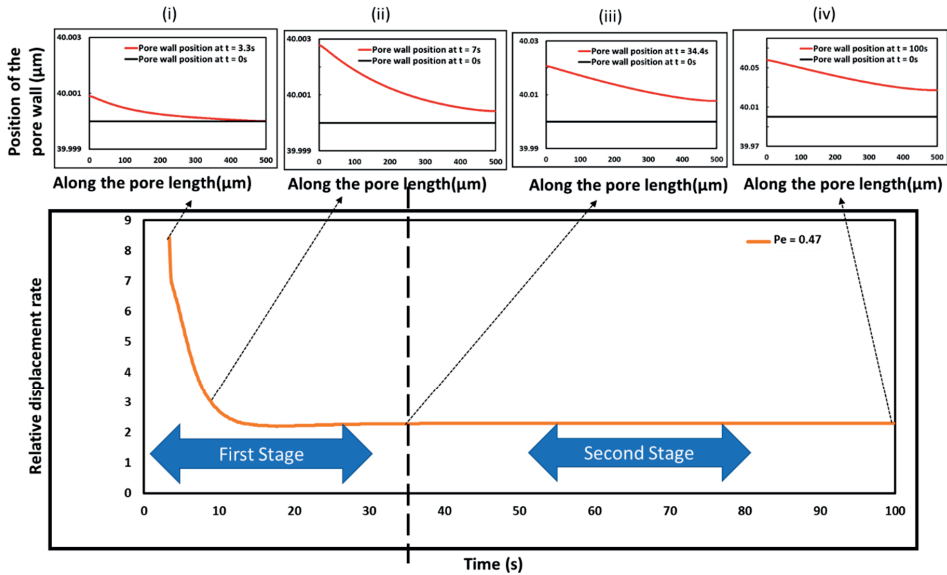


**Figure A2.6:** Evolution of the pore shape during the first stage of the calcite dissolution process is presented in the perspective of the relative displacement rate, for the Pe number 0.47. The end of the transient stage is marked with the dashed line at 34.4s. Note the different vertical axis scales in each inset image.
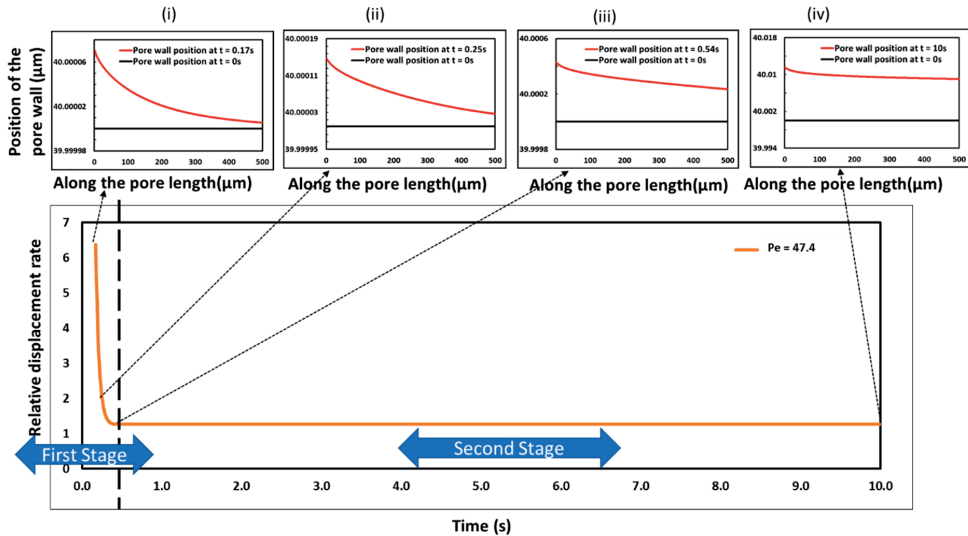


**Figure A2.7:** Evolution of the pore shape during the first stage of the calcite dissolution process is presented in the perspective of the relative displacement rate, for the Pe number 47.4. The

end of the transient stage is marked with the dashed line at 0.54s. Note the different vertical axis scales in each inset image.
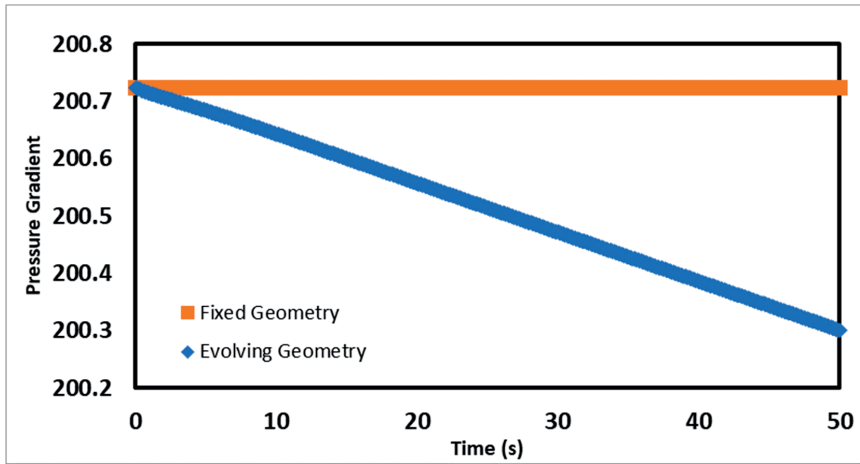


**Figure A2.8:** Comparison of the pressure gradient for the model with evolving geometry vs the one with the fixed geometry for Pe=0.47 and Da=2.13.

Figure A2.9 and Figure A2.10 below are illustration of the discussion in Section 2.3.3 in the main paper.
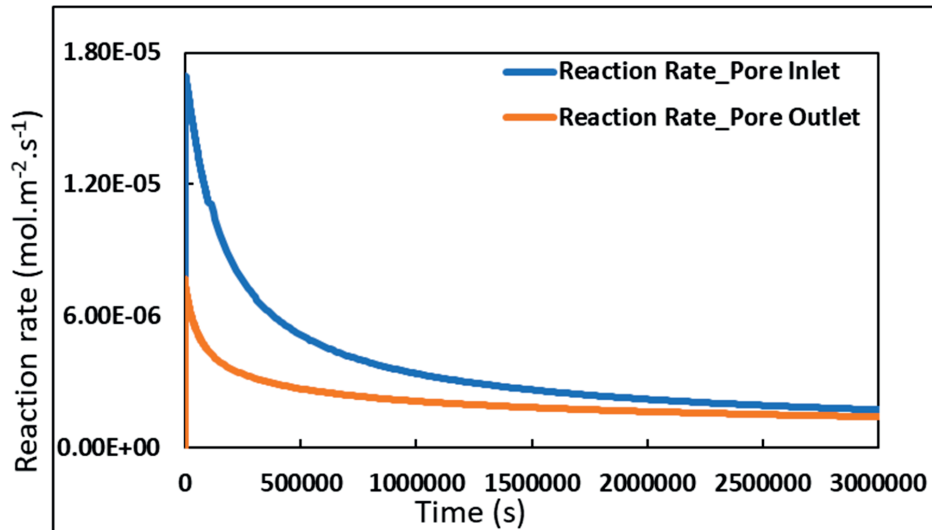


**Figure A2.9:** Evolution of the reaction rate at the pore inlet and at the pore outlet points for the hyperboloid shaped pore (Pe=0.47, Da=2.13).
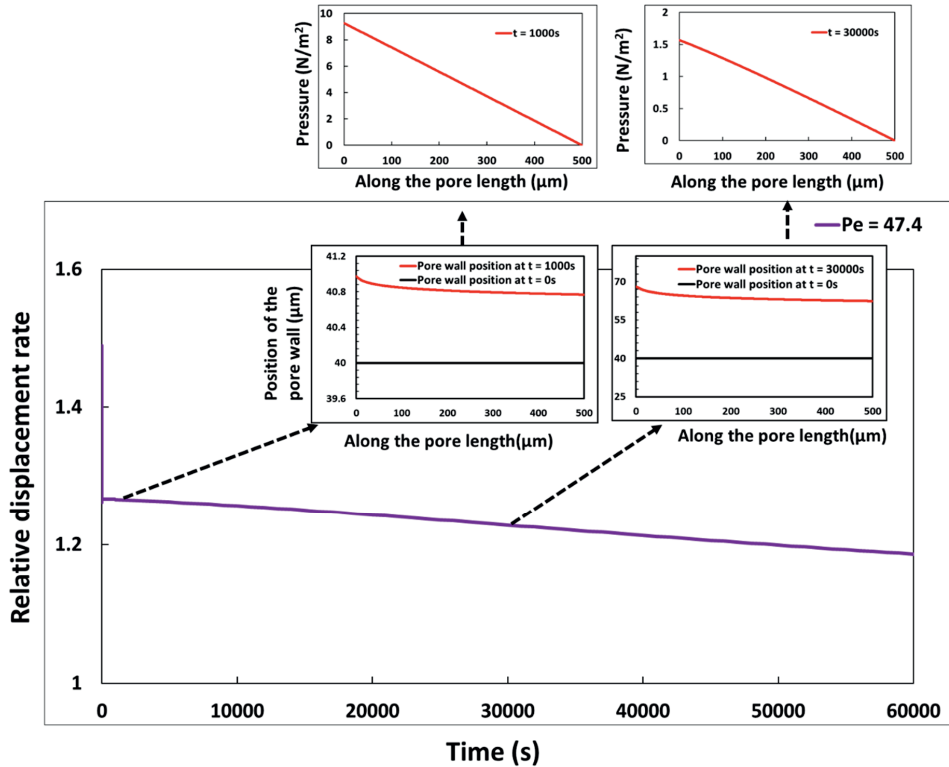
**Figure A2.10:** Evolution of the relative displacement rate during the second stage for the case when at the end of the first stage, the pore shape is almost cylindrical (Pe=47). The evolved pore shape and corresponding pressure profile is shown in inset images, at t = 1000s and 30000s. Note the different vertical axis scales in each inset image.

### A2.3.4 Flow rate effects on the evolution of the pore shape

Figure A2.11 shows the relative displacement profile for the range of the simulated flow rates. For all advection-dominated flow regimes, the relative displacement rate at the end of the first stage is close to one which means that initially, the cylindrical pore can remain almost cylindrical throughout the second stage, and as a consequence, the pressure profile remains linear (Figure A2.10). For the flow regime corresponding to the Pe number 0.05, a very high value of the relative displacement rate at the end of the first stage indicates a strong non-uniformity in the developed pore shape (Figure A2.11b-ii). As a result, the interplay of reaction, advection, and diffusion becomes more and more dynamic and pore shape evolution becomes more complex, as indicated by the constantly modifying value of the relative displacement rate (Figure A2.11b-i).
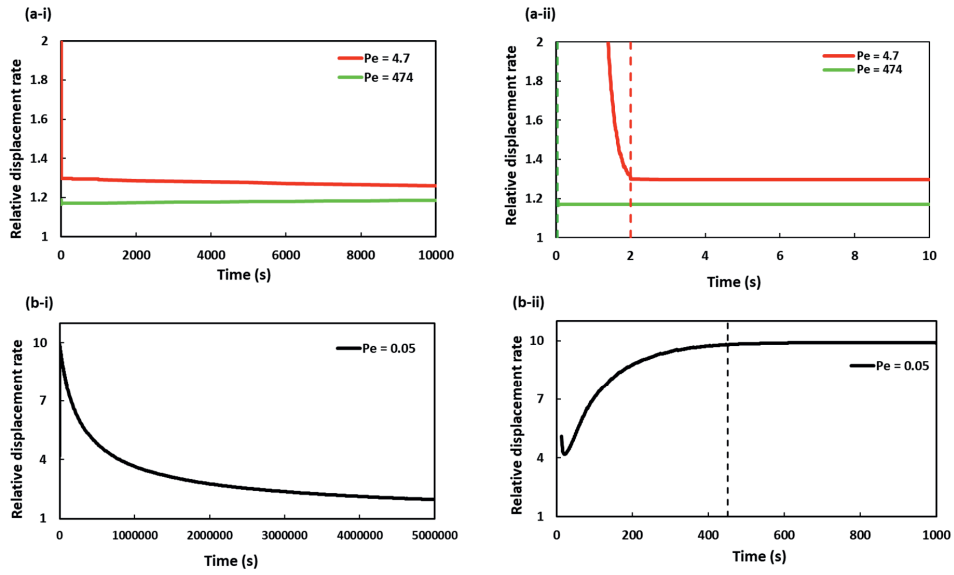
**Figure A2.11:** Evolution of the relative displacement rate for cases when at the end of the first stage, the pore shape is (a) almost cylindrical (b) half-hyperboloid. The initial part of the plots a-i and b-i is zoomed into separate plots i.e., a-ii and b-ii, respectively. The dashed vertical lines in the same color as the color of the plots marks the end of the first stage for the different simulations.

Figure A2.12 below is illustration of the discussion in Section 2.3.5 in the main paper.
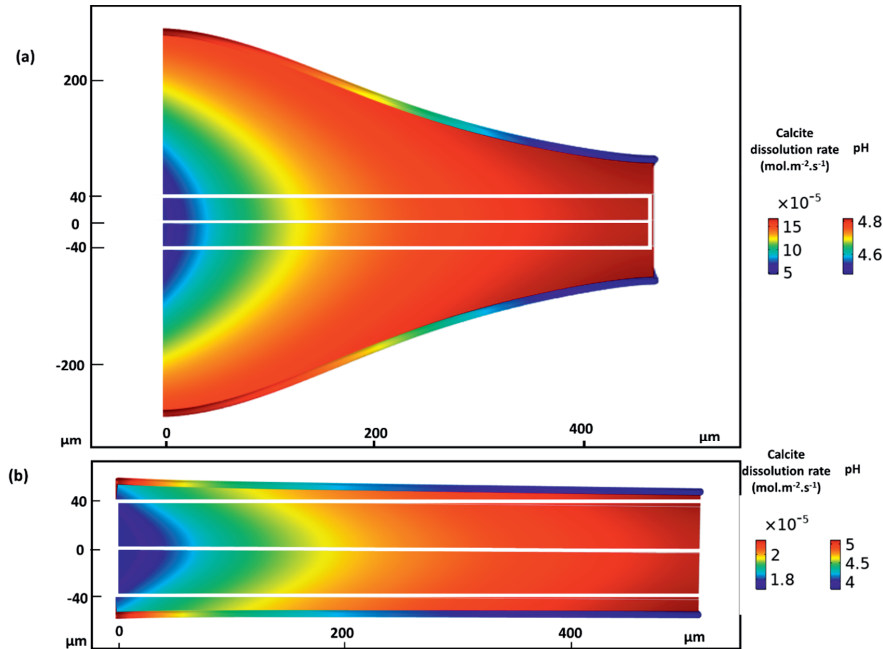


**Figure A2.12.** Simulation results showing the evolved pore shape and distribution of velocity field and reaction rate for two reaction regimes. Injecting a solution with flow rate corresponding to Pe number 4.7 and pH value of (a) 3.1 corresponding to $pCO_2$ of 100.0 bar and (b) 3.9 corresponding to $pCO_2$ of 1.0 bar. The injection period for both cases is 15900 pore volumes (in reference to the original pore volumes at t = 0s). The inner white cylinder indicates the initial pore shape (i.e., at t=0s). The colored regions around the cylinder indicate zones dissolved during reaction. The colored rim around at the pore wall indicate the local reaction rates.

Chapter 2

# Chapter

# 3. The contribution of hydrodynamic processes to calcite dissolution rates and rate spectra

## ABSTRACT

Recent studies on the dissolution rate of microscopically rough calcite surfaces have shown lateral variations in dissolution rate, which can be described as rate spectra. In order to examine the contribution of hydrodynamic effects during such experiments towards the observed average rate and rate spectra, we have simulated the dissolution of a rough calcite surface at the micrometer scale, using measured surface topographies and the geometries of an exemplary flow-through cell, and compare the resulting rate spectra to the measured rate spectra.

Before investigating rate spectra at the microscopic scale, the hydrodynamics and dissolution rate heterogeneity on a flat calcite surface at the scale of the entire flow cell were explored. The numerical results suggest that, for commonly utilized flow rates (i.e., $6 \times 10^{-8}$ $m^3$ $s^{-1}$) and injected solution composition (pH 8.8, alkalinity 4.4 meq/kg-$H_2O$ and $pCO_2$ $10^{-3.48}$ bar), a significant amount of $Ca^{2+}$ ions accumulate near the calcite surface within the diffusive boundary layer. Moreover, this accumulation varied depending on the location of the investigated area relative to the flow field within the cell and was non sensitive of increasing the flow rates. Due to the accumulation of calcium ions, the solution close to the reacting surface became less undersaturated with respect to calcite compared to the bulk flowing solution. As a result, the numerical outcomes predicted an average calcite dissolution rate that is up to an order of magnitude lower than the one expected from the injected solution, depending on the position within the flow field.

Simulations of the microscopically rough calcite did not produce similarly wide dissolution rate spectra like those observed experimentally when only flow heterogeneity near the rough calcite surface was considered or when the real crystal topography (specific surface area) was included. Simulated and measured rate spectra agreed only when rate spectra were imposed explicitly into the simulations. This study therefore confirms that, for the reactive-flow regimes considered here, which correspond to microscopic experiments, the heterogeneity and topography of the crystal surface and the resulting heterogeneity in the free energy landscape at the surface play a major role in controlling the dissolution rate spectra. Only when more reactive (i.e., more acidic) solutions are injected at higher velocities, the hydrodynamics-induced rate variability could contribute towards the dissolution rate spectra.

## 3.1 Introduction

In past three decades, ample experiments have been conducted aiming at understanding the controlling processes for calcite dissolution at both the macroscopic bulk scale (Busenberg and Plummer, 1986; Chou et al., 1989; Plummer et.al., 1978; Pokrovsky et al., 2005; Sjoberg and Rickard, 1984) and at the microscopic scale (Arvidson et al., 2003; Brand et al., 2017; Fischer et al., 2012; Lüttge et al., 2003; Shiraki et al., 2000). Yet, the reported rate equations provide different results for similar state of the solution with discrepancies over several orders of magnitude (Arvidson et al., 2003). Several explanations have been suggested for this discrepancy including i) different laboratory settings leading to flow heterogeneity within the reactor, e.g. fluidized bed reactors (Chou et al., 1989) or disk-shaped flow cells (Arvidson et al., 2003) or mixed-flow reactors (Pokrovsky et al., 2005), or rotating disk batch reactors (Pokrovsky et al., 2005; Sjoberg and Rickard, 1984), ii) the texture of the reacting substrate i.e., single crystals (Busenberg and Plummer, 1986; Sjoberg and Rickard, 1984), powder (Chou et al., 1989; Plummer et.al., 1978; Pokrovsky et al., 2005), single crystal surfaces with defect structures and variation in dissolution mechanism such as the step-wave model (Lasaga and Luttge, 2001), and iii) dissolution rate spectra (Brand et al., 2017; Fischer et al., 2012; Noiriel et al., 2020). Mineral surface area has also been suggested as a source of uncertainty related to reason (ii) and (iii) above, since bulk experiments rely on the value of the surface area of the

substrate (crystal/powder) to calculate normalized rate values that can be compared across different investigations. Therefore, accurate parameterization of mineral surface area becomes critical. Three definitions for the surface area have been discussed in the literature including a) geometric surface area, GSA, which assumes microscopically smooth crystal surfaces, b) specific surface area, SSA, which corrects for smoothness assumption and takes care of surface roughness, and c) reactive surface area, RSA, which is often related to the SSA using a constant factor often set between one and three with no clear basis for this choice (Steefel et al., 2015).

Dissolution experiments at the microscopic scale, such as those using Atomic Force Microscopy (AFM), Vertical Scanning Interferometry (VSI) and X-ray Computer Tomography (XCT) approaches obtain dissolution rates directly from the evolution of the exact crystal surface area (Shiraki et al., 2000; Arvidson et al., 2003; Fischer et al., 2012; Brand et al., 2017). These methods capture the temporal evolution of crystal surface morphology at nano- to micro-scale without any assumptions about surface reactivity and surface area normalization via rate map measurements and calculations (Emmanuel and Levenson, 2014; Fischer et al., 2012; Kahl et al., 2020; Noiriel et al., 2020; Yuan et al., 2019). The topography evolution information combined with the molar volume of calcite dissolved provides the dissolution rate average and/or the lateral heterogeneity. In the past, such studies have revealed that the molecular-scale crystal structures, such as point defects, etch pits, steps and faces significantly influence the calcite dissolution rate and mechanism (Fischer et.al., 2012; Brand et.al., 2017; Noiriel et al., 2020). These studies have shown that in the case of crystal heterogeneity (particularly, crystal surface heterogeneity) a rate spectrum for the surface reactivity more adequately describes dissolution, in comparison with using a single value for the reaction rate (Fischer et al., 2012). Furthermore, molecular level modelling with kinetic Monte Carlo algorithms have shown that the kink site density, modified by both the defect density and the surface nano-topography is critically controlling the reaction kinetics (e.g., Fischer et al., 2018; Kurganskaya and Rohlfs, 2020).

Flow-through experiments rely on certain assumptions regarding the hydrodynamic effects. A key assumption is related to the mass transfer conditions at the surface section under investigation. One of the prerequisites of AFM and VSI experiments is the prevalence of surface-controlled conditions. Constraints about fluid residence time etc. are discussed in detail in literature, exemplified by the observations on calcite surface step movement as a function of distance from equilibrium during dissolution reaction at different flow-through rates (Liang and Baer, 1997). In general, the demanded value of the flow rate emanates from a sensitivity test where the mean dissolution rate of the observed calcite surface section levels off as flow rate increases (e.g., Figure 1 in Liang and Baer, 1997). Eventually, the onset of a steady state reaction rate, independent of flow rate, gives a cut-off flow rate above which the reactive transport system of flow cell is assumed to be kinetically/surface controlled. However, several reactive transport simulations of AFM fluid cells, particularly for gypsum dissolution, have previously revealed that the transport conditions in cells are often more complex (Gasperino et al., 2006; Peruffo et al., 2016). For example, Peruffo et al. (2016), inspected the impact of mass transfer conditions over the assumed kinetics-controlled reaction regime. They found that the flow rate value of $5 \times 10^{-8}$ m$^3$ s$^{-1}$ is termed to produce reaction-controlled regime, based on the sensitivity test. However, in reality this flow rate leads to a build-up of calcium and sulfate in the order of 7mM near the gypsum surface. This indicates the prevalence of a mixed surface-transport controlled regime at higher flow rates depending on the solubility of the solid under investigation.

Surface roughness is a factor which may contribute to an enhancement of a boundary layer where dissolution products can accumulate. For calcite dissolution, it has been shown that the

microscale surface roughness influences the hydrodynamic interactions between fluid and crystal surface through the development of the non-uniform diffusion boundary layer (DBL, Deng et al., 2018). Such a non-uniform diffusive boundary layer results into localized stagnant/immobile zones on top of the crystal surface which attain lower values for the reaction rate (Jeschke and Dreybrodt, 2002). In the context of calcite dissolution, hydrodynamics of micro scale roughness has been explored either with 2D synthetic fracture profiles with a minimum amplitude of 10 µm (Deng et al., 2018) or using actual calcite surface, however, only under surface-controlled kinetics (Levenson et al., 2015; Levenson and Emmanuel, 2013). For example, Deng et al. (2018), presented an explicit control of the surface roughness over the hydrodynamics for a range of transport and reaction regimes and upscaled these pore scale processes to estimate a correlation factor for the reactive and specific surface areas. However, this study utilized fracture profiles with much higher roughness magnitude than the generally observed roughness magnitude in VSI and AFM experiments. Levenson et al., 2013, simulated the crystal surfaces obtained from AFM experiments and showed that for a given roughness magnitude of the crystal and under surface-controlled dissolution conditions, the diffusion boundary layer remains uniform. However, they also noted that the choice of the chemistry model might influence this observation. This motivates the current study to utilize a detailed reactive transport model for delineating the fluid hydrodynamics at the microscopic scale for both reaction and transport-controlled dissolution regimes.

The main goal of this paper is to determine the contribution of hydrodynamics to the lateral heterogeneity in dissolution rates (rate spectra) observed at the microscopic scale. First, a comprehensive study was carried out to explore possible processes responsible for variation in the (absolute) average measured reaction rates observed macroscopically versus microscopically. For this purpose, a series of computations at the scale of an exemplary flow cell utilized for calcite and marble dissolution experiments was performed to explore the impact of the experiment setting (in particular flow rate, but also solution composition) and to investigate the influence of the surface roughness of the crystal on the dissolution under surface-controlled regimes. Secondly, we performed a series of smaller-scale, higher resolution simulations to investigate the impact of µm surface roughness on the dissolution rate under transport-controlled regimes. In all simulations, we used surface topographies that were measured experimentally using VSI. In summary, this study aims to answer if either the hydrodynamics or the calcite surface or their coupled consideration can explain the observations of surface-direct measurements including dissolution rate spectra.

## 3.2    Materials and Methods

 In this study, micrometer (pore) scale reactive transport including fluid flow, transport of the solute species, and chemical reactions was simulated by solving a coupled system of non-linear equations using COMSOL Multiphysics®. The following sections provide the modelling formulation. Further details of the numerical method can be found in (Agrawal et al., 2020).

### 3.2.1  Mathematical Model

#### 3.2.1.1   Fluid Flow and Transport

  Fluid flow corresponding to the laminar flow (i.e. resulting in a Reynolds number Re < 100) and incompressible fluid was simulated using the Navier - Stokes equations:

$$\rho \left( \frac{\partial u}{\partial t} + u.\nabla u \right) = -\nabla p + \mu \nabla^2 u \qquad (3.1)$$

$$\nabla.u = 0 \qquad (3.2)$$

where, $p$ is pressure, $u$ is velocity, $\rho$ is the fluid density and $\mu$ is the fluid viscosity. Initially, i.e., at the time of zero, steady state flow field conditions were maintained in the domain. Flow

equations were solved along with the boundary conditions i.e., inlet was maintained either at constant flux in case of Model G1-Flat-1R and related variants OR constant average velocity in case of Model G2-Flat-1R and related variants. At the outlet, atmospheric pressure conditions were maintained. Remaining boundaries of the models were treated as no-slip boundaries.

Transport of the aqueous species was modelled using the advection-diffusion-reaction equation:

$$\frac{\partial c_i}{\partial t} + \nabla.(-D.\nabla c_i) + \nabla.(u.c_i) = R_i \tag{3.3}$$

where, $D$ is the diffusion coeffcient i.e., $3.36 \times 10^{-9}$ ($m^2$ $s^{-1}$), $c_i$ and $R_i$ are concentration (mol $m^{-3}$) and reaction input of $i^{th}$ species (mol $m^{-3}$ $s^{-1}$), respectively.

We assumed that calcite dissolution takes place only at the fluid-solid boundary. The mass-balance equation related to the surface reaction yields:

$$-n.(-D.\nabla c_i + u.c_i) = R_{Calcite} \tag{3.4}$$

where, $R_{Calcite}$ (mol $m^{-2}$ $s^1$) is the calcite dissoluiton rate calculated from Equation 3.8. Transport equations are solved along with the boundary conditions i.e., Danckwerts flux condition at the inlet, zero flux condition at the outlet and no-flux condition at the remaining boundaries except the calcite boundary (Agrawal et.al., 2020).

We used consistent initialization in the numerical model. This option reduces the computational times needed to reach steady state. We observed that there is no impact of keeping this option on/off over the steady state-based dissolution rates (Figure A3.1).

### 3.2.1.2 Geochemical Model
The aqueous complexation reactions corresponding to the dissolution of $CO_2$ in the water, are implemented as equilibrium reactions, i.e. they are assumed to occur instantaneously, which under the simulated conditions may be considered a valid approximation (Zeebe and Wolf-Gladrow, 2001) and provided in Table 3.1 together with their corresponding equilibrium constant values.

Dissolution of calcite is simulated by applying three pathways (Plummer et al., 1978):

$$k_1: CaCO_3(s) + H^+(aq) = Ca^{2+}(aq) + HCO_3^-(aq) \tag{3.5}$$
$$k_2: CaCO_3 + CO_2(aq) = Ca^{2+}(aq) + 2HCO_3^-(aq) \tag{3.6}$$
$$k_3: CaCO_3(s) = Ca^{2+}(aq) + CO_3^{2-}(aq) \tag{3.7}$$
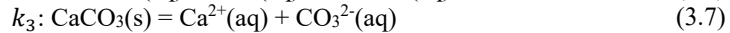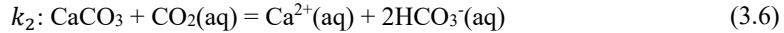
where, $k_1 = 8.64 \times 10^{-5}$ (m $s^{-1}$), $k_2 = 4.78 \times 10^{-7}$ (m $s^{-1}$) and $k_3 = 2.34 \times 10^{-9}$ (m $s^{-1}$) at 25°C are the reaction rate constants (Busenberg and Plummer, 1986). The rates of these reversible reactions can be combined into a single dissolution rate law:

$$R_{Calcite} \text{ [mol } m^{-2} s^{-1}] = R_I R_E \tag{3.8}$$
$$R_E \text{ [mol } m^{-2} s^{-1}] = (k_1 a_{H^+} + k_2 a_{CO_2(aq)} + k_3 a_{H_2O})(1 - 10^{0.67SI}) \tag{3.9}$$

where, $R_I$ denotes the intrinsic rate factor derived from molecular scale roughness of the calcite surface (Fischer et. al., 2012), $R_E$ is the extrinsic rate factor derived from the composition of the solution. $SI$ is the saturation index of the solution calculated as $(a_{Ca^{2+}} a_{CO_3^{2-}})/(K_{eq})$, where $K_{eq} = 10^{-8.48}$ (Plummer and Busenberg, 1982). $a_i$ is the activity of the $i^{th}$ species calculated from the concentration of the $i^{th}$ species and ionic strength of the solution using Davies equation. In Equation 3.9, the expression in the first brackets is the driving force while the second term determines the distance from the equilibrium state. Calcite dissolution rate is a

strong function of $H^+$ activity under acidic conditions and becomes pH independent when pH passes a value of 7.

For this study, we have implemented two types of calcite dissolution rate models through variations in $R_I$. In the first type, the reactivity of the calcite surface was assumed to be controlled only by the composition of the solution and therefore had $R_I = 1$. Models with a single value of $R_I$ include 1R in the nomenclature (Table 3.2). The second type of models included location dependent values for $R_I$ and these values were calculated from the reaction rate map obtained experimentally in a VSI setup. This reaction rate map was obtained using a dissolution time frame obtained from time periods of 2h-6h. For more information on the reaction rate map see (Bollermann and Fisher, 2020). Calculation of $R_I$ was performed on the reaction rate map $0.021 \times 0.021$ mm. The rate factor, $R_I(x, y)$, was calculated as:

$$R_I(x, y) = \frac{R_{VSI}(x, y)}{R_{VSI,m}} \qquad (3.10)$$

where, $R_{VSI}(x, y)$ is the reaction rate recorded in VSI experiment and $R_{VSI,m}$ is the mode of the $R_{VSI}(x, y)$ of the extracted area. Models with location specific value of $R_I$ include RS in the nomenclature (Table 3.2).

**Table 3.1:** Implemented bulk phase reactions and their corresponding equilibrium rate constants.

| Reactions | Equilibrium rate constant |
|---|---|
| $CO_2(aq) = H^+ + HCO_3^-$ | [a]$4.5 \times 10^{-7}$ |
| $HCO_3^- = H^+ + CO_3^{2-}$ | [a]$4.78 \times 10^{-11}$ |
| $H_2O = H^+ + OH^-$ | $1 \times 10^{-14}$ |

[a]Equilibrium rate constants are taken from Plummer and Busenberg, 1982

### 3.2.2 Physical-chemical parameters

### 3.2.2.1 Numerical models of physical domains/Geometry

Two numerical models of physical domains are utilized in the current study as base models. *Model G1-Flat-1R* is geometrically identical to a flow cell used to perform calcite marble dissolution experiments in Bollermann and Fischer, 2020. *Model G2-Flat-1R* is a small parallelepiped sub-volume of *Model G1-Flat-1R*, requiring relatively less computational time than *Model G1-Flat-1R*, used to perform sensitivity analyses. The two base models and their several variations are clustered in two sets depending on their usage purpose. *Set I* consist of *Model G1-Flat-1R* and four additional variants, where computer simulations done on this set aim at studying different surface topographies and different kinetics of the dissolution processes. *Set II* consists of *Model G2-Flat-1R* and one more variant, where these two are used in parametric and sensitivity studies of dissolution processes under different topographies, flow rate, and solution composition. A more detailed description of the considered numerical models/geometries reads as follows. Table 3.2 and Table 3.3 provide details of all the variants of *Model G1-Flat-1R* and *Model G2-Flat-1R* and Figure A3.2 and Figure A3. 3 provides conceptual pictures of all the variants of *Model G1-Flat-1R* and *Model G2-Flat-1R*.

### *Set I.*

*Model G1-Flat-1R* represents the whole disk-shaped flow cell with a diameter of 15 mm and a thickness value of 1.75 mm as shown in Figure 3.1. Details regarding the experimental setup is available in Bollermann and Fischer, 2020. A polished marble (calcite) surface served as the base surface of the flow cell. In the experiment, part of the marble surface was masked using an inert material (with thickness ~ 550 nm) so that it can be used as the reference point after

the experiments. *Model G1-Flat-1R* includes all these settings to be consistent with the experiments. Furthermore, for postprocessing of the results, we have chosen four areas, each with a size of 0.021 × 0.021 mm, namely areas A, A', B, and C that are on the surface of the crystal in order to observe mass transfer during dissolution. Area A corresponds to the location used for surface topography and rate data collection in Bollermann and Fischer, 2020, area B was placed near the inlet of the flow cell and area C was at the same distance from the inlet as the area A but on the opposite edge of the flow cell, in a zone with different flow characteristics compared to the one in A. The locations of the areas A, B and C are shown in Figure 3.1. Area A' is a shift of area A in a direction away from the mask (perpendicular to the edge of the mask), and the distance between the centres of the two areas A and A' is 0.03 mm. Area A' is not shown on Figure 3.1 because at the scale of the full flow cell it is visibly not distinguishable from area A.

Four further variants of *Model G1-Flat-1R* were considered to investigate the influence of the crystal surface topography and the kinetics of the dissolution process. Due to the computational challenges, fine resolution for the surface topography was used only for area A and area A' in these four variants.

*Model G1A-HE-1R (*HE: Height-from-Experiment and 1R: Single value of $R_I$ in Equation 3.8) is a variation of *Model G1-Flat-1R*, where the flat calcite surface of the area A is replaced with the topography data, $h(x,y)$, obtained from a calcite crystal which had been dissolved for a duration of ten hours (Bollermann and Fischer, 2020).

In order to extend the current study to a range of topographic features, we have constructed variations of *Model G1-Flat-1R* - i.e., *Model G1A-HS-1R* and *Model G1A-P-1R*. In *Model G1A-HS-1R*, area A and A' are imposed with an amplified surface topography $h_1(x,y)$ and $h_2(x,y)$, respectively. These surface topographies are calculated as:

$$h_1(x,y) = 5.0[h(x,y) - h_m] \tag{3.11}$$

$$h_2(x,y) = -5.0[h(x,y) - h_m] + 2.0h_m \tag{3.12}$$

where, $h_m$ is the reference (equal to the mean height value) datum of the topography data $h(x,y)$ i.e., -0.4 mm. Height difference of each point of the surface $h(x,y)$ with respect to the reference datum ($h_m$) is exaggerated by a factor of five.

In *Model G1A-P-1R*, six pillars of calcite of size 0.002 × 0.002 × 0.020 mm, with an alternative facing direction, upward or downward, are placed at 0.004 mm, at otherwise flat area A of *Model G1-Flat-1R* to investigate the hydrodynamic control of magnified surface roughness. Figure A3.2 shows topographic variations incorporated in *Model G1A-HS-1R* and *Model G1A-P-1R*.

*Model G1A-HE-RS* is a variation of *Model G1A-HE-1R*, where instead of a single value of $R_I$ in Equation 3.8, location specific values of $R_I$ were implemented (see Section 3.2.1.2 for more details).

**Table 3.2:** Variants of the base Model G1 i.e., Full flow cell for marble dissolution experiment used in this study and their main properties. [1]topography $h(x,y)$ from (Bollermann and Fischer, 2020); [2] $h_1(x,y)$ for A from Equation (3.11) and $h_2(x,y)$ for A' from Equation (3.12); [3]from Equation 3.8.

| Model | Highlight surface | Kinetics |
|---|---|---|

| | | |
|---|---|---|
| *Model G1-Flat-1R* | **Flat** reactive surface | Single value of $R_I$ in Equation 3.8 |
| *Model G1A-HE-1R* | *Area A:* topography and **H**eight from **E**xperiment[1] | Single value of $R_I$ in Equation 3.8 |
| *Model G1A-HS-1R* | *Area A: Height is* **S**ynthetic: exaggerated topography[2] | Single value of $R_I$ in Equation 3.8 |
| *Model G1A-P-1R* | *Area A:* six **P**illars | Single value of $R_I$ in Equation 3.8 |
| *Model G1A-HE-RS* | *Area A:* topography **H**eight from **E**xperiment[1] | Location **S**pecific value of $R_I$ [3] |

### Set II

The Model *G1* series is computationally demanding. Therefore, for the sensitivity analyses presented in Sections 3.2.3 and 3.2.4, a new model, *Model G2 – Flat-1R*, was developed. This model contains a rectangular flow cell with a dimension of 1 mm (length) × 0.3 mm (width) × 1.75 mm (depth). At 0.8 mm from the inlet boundary and 0.13mm from the lateral boundary of the domain, *Area A''* (0.021 × 0.021 mm) was either kept as flat surface (*Model G2 – Flat-1R*) or replaced with the same experimental topography as in *Model G1A-HE-1R* (*Model G2A'' – HE-1R*). Boundary conditions were set to ascertain that A'' in *Model G2 – Flat-1R* has similar flow conditions as Area A in *Model G1-Flat-1R.*

**Table 3.3:** Variants of the base *Model G2* i.e., small parallelepiped used in this study and their main properties. [1] topography $h(x, y)$ from (Bollermann and Fischer, 2020);

| Model | Highlight surface | Kinetics |
|---|---|---|
| *Model G2 – Flat-1R* | **flat** reactive surface | **S**ingle value of $R_I$ in Equation 3.8 |
| *Model G2 – HE-1R* | topography and **H**eight from **E**xperiment[1] | **S**ingle value of $R_I$ in Equation 3.8 |

#### 3.2.2.2 Chemical compositions and flow rates

For this study, five sets of injecting solutions with different compositions, solutions Sol. #1, Sol. #2, Sol. #3, Sol. #4, Sol. #5, were considered. The first solution, Sol. #1, corresponds to the commonly applied solutions in VSI experiments i.e., pH 8.8 and alkalinity of 4.4 meq/kg-$H_2O$ (Bibi et al., 2018) except the added amount of $Ca^{2+}$ species with an amount of $1 \times 10^{-6}$ mol m$^{-3}$. This slight addition of $Ca^{2+}$ species in the injecting solutions did not affect the steady state based mean dissolution rates, however it was needed for convergence of the computer simulations (explained in Figure A3.1). The composition of all solutions with the target pH values and target pCO2 conditions were defined using PhreeqC program (Parkhurst and Appelo, 2013) with the phreeqc.dat database. Except Sol. #2, all other solutions were prepared as if open to the atmospheric. The corresponding values of the species concentrations in these solutions are provided in Table A3.1.

In all models, the flow cell was considered to be filled with the injecting solution from the start of the simulation. For *Model G1-Flat-1R*, three sets of flow rates were imposed: $6 \times 10^{-8}$, $1 \times 10^{-8}$, and $1 \times 10^{-7}$ m$^3$ s$^{-1}$ (corresponding to mean inlet velocities of 0.08, 0.013 and 0.13 m s$^{-1}$ respectively). The first and the third flow rates lie in the range of commonly applied flow rates in VSI experiments (Bollermann and Fischer 2020; Bibi et al., 2018). For *Models G1A-HE-1R, G1A-HS-1R, G1A-P-1R* and *G1A-HE-RS*, a flow rate of $6 \times 10^{-8}$ m$^3$ s$^{-1}$, corresponding to mean inlet velocity equal to 0.08 m s$^{-1}$ was applied. For *Model G2 – Flat-1R* and *Model G2 – HE-1R*, a set of four average velocities were imposed:

0.002, 0.04, $4.75 \times 10^{-4}$ and $4.75 \times 10^{-6}$ m s$^{-1}$. The first of these average velocities corresponds to the average velocity at observed in the simulations of area A in *Model G1-Flat-1R* if the injected flow rate is $6 \times 10^{-8}$ m$^3$ s$^{-1}$.

### 3.2.3 Parametrization of the flow and reaction regimes

The Péclet number, $Pe$, is defined as:

$$Pe = \frac{vh}{D} \tag{3.13}$$

where $v$ is the location specific average velocity, $h$ is the height of the investigated volume (disk or rectangle, depending on the model run) and D is the diffusion coefficient i.e., $3.36 \times 10^{-9}$ m$^2$ s$^{-1}$.

For the investigated systems, we defined two Damköhler numbers. The first Damköhler number, $Da_I$, compares the reaction time scale with the diffusion time scale as:

$$Da_I = \frac{h^2 * S_R}{D * C_{Calcite}} \tag{3.14}$$

$C_{Calcite}$ is the density of surface sites of calcite at the start of dissolution (mol m$^{-2}$) i.e., $0.8 \times 10^{-5}$ mol m$^{-2}$. $S_R$ is the mean dissolution rate (mol m$^{-2}$ s$^{-1}$) calculated from observed reaction rates at a surface of size (0.021 × 0.021 mm) i.e., Area A, B and C in *Model G1-Flat-1R*. and Area A'' in *Model G2 – Flat-1R*; unless otherwise noted. Mean dissolution rate is calculated as:

$$S_R = \frac{\sum_{i=1}^{N_i} R_{Calcite}(x, y)}{N_i} \tag{3.15}$$

Where, $N_i$ is the total numbers of grid points from which dissolution rate is utilized in calculation. In a surface size of 0.021 × 0.021 mm, a total of 144 grid points is utilized such that the distance between each grid point is $0.148 \times 10^{-3}$ mm.

The second Damköhler number, $Da_{II}$, compares the reaction time scale with the advection time scale as:

$$Da_{II} = \frac{h * S_R}{v * C_{Calcite}} \tag{3.16}$$

Table A3. 2 and Table A3.3 provides the Pe, $Da_I$ and $Da_{II}$ numbers at the examined locations in *Model G1* and *Model G2*, respectively.

### 3.3    Results

Section 3.3.1 addresses the hydrodynamics and dissolution rate heterogeneity at the scale of the whole flow-through cell. Section 3.3.2 addresses the results related with the main objective of this study i.e., investigating the contribution of heterogeneity in hydrodynamics due to micro scale surface roughness towards dissolution rate spectra.

### 3.3.1   Hydrodynamics and calcite dissolution rates at the Flow-Cell scale

#### 3.3.1.1   Velocity field
The velocity field inside the flow cell is shown in Figure 3.1. This velocity field corresponds to the flow rate value of $6 \times 10^{-8}$ m$^3$ s$^{-1}$, which falls in the range of flow rates usually chosen for microscopic surface dissolution experiments (Bollermann and Fischer, 2020). Pe and Da numbers of this numerical experiment are provided in Table A3. 2. The heterogeneity in the

velocity field is evident in a horizontal cross-section located at a distance of 100 μm from the bottom surface of the cell and varies up to one order of magnitude i.e., between $1 \times 10^{-4}$ (dark read, at the center) and $1 \times 10^{-5}$ m s$^{-1}$ (dark blue, at the rims of the flow cell) (Figure 3.1). All these velocities yield low Reynolds number, thus laminar flow, while the flow streamlines show the development of horizontal vorticity in the flow field.
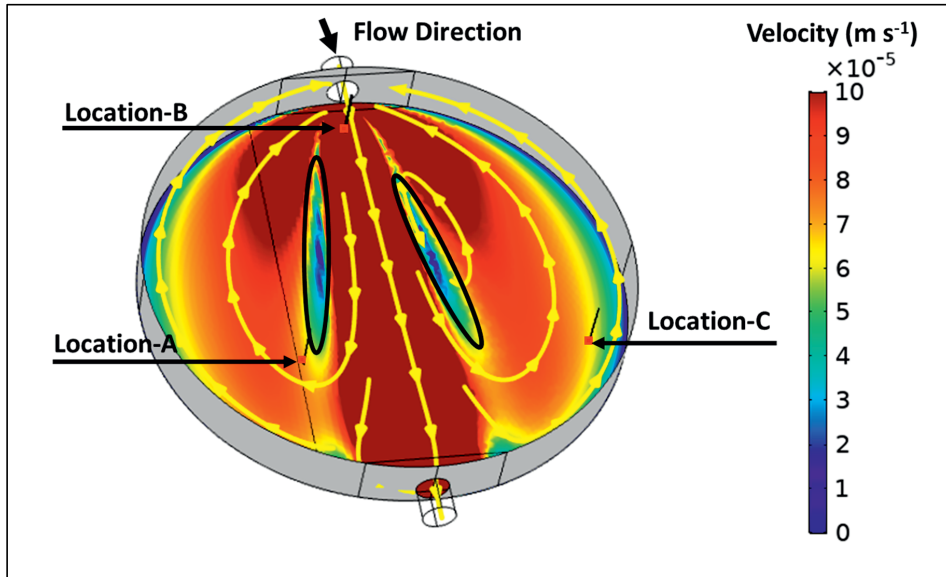


**Figure 3.1.** The simulated domain for the whole disk-shaped flow cell, with 15 *mm* diameter and 1.75 *mm* thickness, showing the velocity field and flow streamlines at a planar surface positioned at a distance of 100μm from the bottom of the flow cell. Regions where the magnitude of the velocity is lower than the surrounding locations are marked using black outlines.

### 3.3.1.2 Dissolution rates

The breakthrough curve of the Ca$^{2+}$ species shows that the reactive system attains a quasi-steady state within 100 seconds of the dissolution period (Figure A3.4). Figure 3.2 shows the observed spatial distribution of Ca$^{2+}$ concentration, $\Omega$ ($\Omega = 10^{SI}$ and reflects the saturation state of solution with respect to calcite) and reaction rate at the calcite surface, after 200s (so, after 100s quasi-steady state dissolution) in *Model G1-Flat-1R* with Sol. #1 (pH 8.8 and alkalinity of 4.4 meq/kg-H$_2$O). The Ca$^{2+}$ concentration field reflects the heterogeneity of the flow regime. For example, the high velocity belt between inlet and outlet accumulates the lowest amount of Ca$^{2+}$ ions near the calcite surface. Contrastingly, the low velocity zones towards the boundary of the flow cell and on both sides of the high velocity belt (highlighted in the Figure 3.1), show a significantly higher accumulation of Ca$^{2+}$ ions near the calcite surface. Despite such significant accumulation of the Ca$^{2+}$ ions near the calcite surface, the composition of solution away from calcite surface remains unaffected (vertical 2D slices in Figure 3.2a and Figure 3.2b), resulting into a significant concentration gradient in the transversal direction. This build-up of Ca$^{2+}$ ions near the calcite surface changes the saturation state of the fluid that is in contact with the calcite surface (Figure 3.2b). Since this build-up of Ca$^{2+}$ ions at the calcite surface has a horizontal heterogeneity, consequently, the dissolution rate varies up to one order of magnitude over the

calcite surface (Figure 3.2c): the zones with high reaction rates overlap with the high velocity zones (Figure 3.2c).
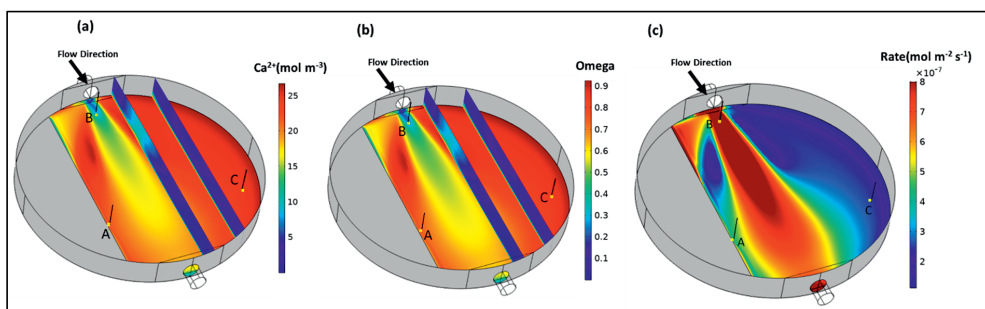


**Figure 3.2.** The simulated flow cell showing steady state fields at the calcite surface for (a) $Ca^{2+}$ concentration (b) saturation state of solution with respect to calcite ($\Omega = 10^{SI}$); (c) computed surface reaction rate map based on Equation 3.8 at calcite surface. Vertical 2D slices in plots a-b show vertical profiles of the respective variables. Simulation conditions are $6 \times 10^{-8}$ $m^3$ $s^{-1}$ flow rate, Sol. #1 (pH 8.8 and alkalinity of 4.4 meq/kg-$H_2O$).

While the mean dissolution rate of the whole calcite surface in the flow cell is of an order of $5 \times 10^{-8}$ mol $m^2$ $s^{-1}$, there is strong local heterogeneity in dissolution rates (Figure 3.2c). This heterogeneity is examined further at three selected locations, namely location A, B and C (Figure 3.2). For these locations, the average velocity, surface and bulk concentrations of $Ca^{2+}$ species and mean dissolution rate are provided in Table A3.4 and Table A3.5. Figure 3.3a shows the evolution of the mean dissolution rate as computed from Equation 3.15 at locations A, B and C. At time $t=0$ (i.e., first time step of the simulation), at all three locations, the mean dissolution rate is of an order of $1.96 \times 10^{-8}$ mol $m^2$ $s^{-1}$ which is around 13% lower than the expected dissolution rate as per the composition of the injected solution i.e., $2.26 \times 10^{-6}$ mol $m^{-2}$ $s^{-1}$ (orange line in Figure 3.3a). As the dissolution simulation evolves, and the concentration fields establish, the dissolution rate changes from the initial value to values of $4.70 \times 10^{-7}$, $1.45 \times 10^{-6}$ and $2.90 \times 10^{-7}$ mol $m^{-2}$ $s^{-1}$ at locations A, B and C, respectively. Location B shows a smaller shift in the dissolution rate from the initial dissolution rate value compared to locations A and C (Figure 3.3a). The variability in dissolution rates due to the established flow and concentration fields in the entire flow cell can be plotted as rate spectrum in Figure 3.3b.
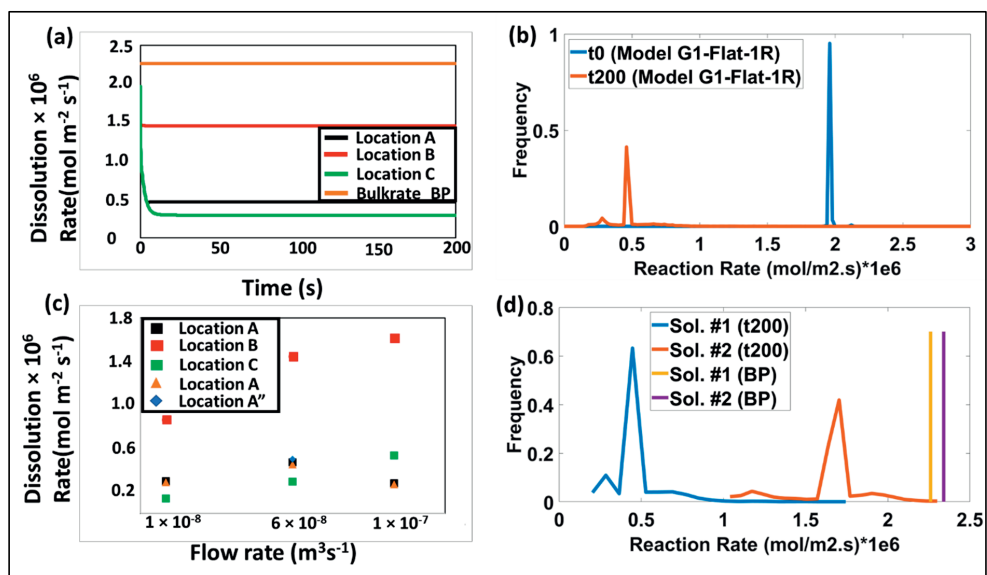
**Figure 3.3**. (a) Temporal evolution of the mean dissolution rate obtained at locations A, B and C. The orange line provides the dissolution rate value from Busenberg and Plummer, 1986 who used the bulk concentrations. (b) the simulated rate spectra based on the whole calcite surface at time $t$ = 0s and $t$ = 200s. Plots (a) and (b) are based on *Model G1- Flat-1R*, with a flow rate of $6 \times 10^{-8}$ m$^3$ s$^{-1}$, Sol. #1 (pH 8.8 and alkalinity of 4.4 meq/kg-H$_2$O) (c) the mean dissolution rate as a function of injection rate for locations A, B and C (square symbols indicate *Model G1-Flat-1R and* triangle symbols indicate *Model G1A-HE-1R*). Comparison of the mean dissolution rate at location A from *Model G1-Flat-1R* and *Model G1A-HE-1R* shows that the imposition of the surface roughness in the model does not have a significant effect on the mean value of the dissolution rate. The blue rhomb denotes the mean dissolution rate at location A'' in *Model G2-Flat-1R* simulation using Sol. #1 (pH 8.8 and alkalinity of 4.4 meq/kg-H$_2$O) (d) rate spectra from simulations utilizing Sol. #1 and 2. Vertical lines on the right section of the plot correspond to the dissolution rate model provided by Busenberg and Plummer (1986). Both solutions were injected using a flow rate of $6 \times 10^{-8}$ m$^3$ s$^{-1}$.

### 3.3.1.3 Varying flow rate

To showcase the impact of the flow rate on the hydrodynamics of the flow cell, we varied the flow rate in simulations on *Model G1-Flat-1R* to values of $1 \times 10^{-7}$ and $1 \times 10^{-8}$ m$^3$ s$^{-1}$, while keeping the solution composition fixed to the Sol. #1. At $1 \times 10^{-8}$ m$^3$ s$^{-1}$, parallel streamlines in a relatively more homogeneous flow field established resulting in lower lateral heterogeneity in dissolution rates (Figure A3.6 – b1 and b2). At $1 \times 10^{-7}$ m$^3$ s$^{-1}$ more pronounced heterogeneity in the velocity and reaction rate fields were observed (Figure A3.6 – a1 and a2) with more intense and larger low velocity zones than at $6 \times 10^{-8}$ m$^3$ s$^{-1}$ (Figure 3.1). Figure 3.3c presents the impact of varying flow rate conditions over the mean dissolution rates observed at locations A, B and C. With increasing flow rate, the mean dissolution rate increases at locations B and C and decreases at location A. At $1 \times 10^{-7}$ m$^3$ s$^{-1}$ location A is situated in one of the expanded low velocity zones (Figure A3.6).

### 3.3.1.4 Varying solution composition

Next, we explored the impact of composition of the injecting solution on the hydrodynamics of the flow cell using *Model G1-Flat-1R*. Results presented thus far were obtained with

Sol. #1. Sol. #2, which has same value of pH but without any $CO_3^{2-}$ species (system closed to the atmosphere; Table A3.1 shows composition). Comparison of the rate spectra based on Sol. #1 and 2 is shown in Figure 3.3d. We observed that at t=0 both solutions yield similar dissolution kinetics (yellow and purple vertical plots in Figure 3.3d) and at the monitoring time t =200 s, Sol. #2 showed a smaller decrease in the reaction rate as well as smaller amount of rate heterogeneity (blue and orange plots in Figure 3.3d).

### 3.3.2   The rough calcite surface

### 3.3.2.1 Comparison of rate spectra at location A

In order to unravel the impact of hydrodynamics near rough surfaces on measured dissolution rates, we now focus on location A (Figure 3.2), which is of similar size to fields of view generally used in VSI surface dissolution experiments that have revealed dissolution rate spectra. Simulations were performed with a solution with a pH value of 8.8 (Sol. #1) and a flow rate value of $6 \times 10^{-8}$ m$^3$ s$^{-1}$; Pe and Da numbers of this numerical experiment are provided in Table A3. 2.

Reaction rate maps were obtained for location A with a smooth surface (*Model G1-Flat-1R*) and with the experiment-based topography (*Model G1A-HE-1R*) imposed (Figure 3.4a and b). When location A is flat, a constant solution composition (i.e., no horizontal gradient) is observed at steady state, resulting in a homogenous constant dissolution rate of $4.69 \times 10^{-7}$ mol m$^{-2}$ s$^{-1}$ (Figure 3.4a). Imposition of surface topography in location A introduces heterogeneity in the flow field and concentration field and therefore also in the reaction rates (Figure 3.4b). As a result, a 4% lower mean±2σ dissolution rate of $4.52\pm0.16 \times 10^{-7}$ mol m$^{-2}$ s$^{-1}$ is obtained (Figure 3.4b). Fig. 4c and 4d show vertical slices with the $Ca^{2+}$ concentration in the first 5µm above the rough calcite surface, along the line PQ as shown in Figure 3.4b. While the smooth calcite surface results into homogeneous accumulation of the $Ca^{2+}$ concentration, the deeper (etch pit) parts at the rough calcite surface are found to be enriched in $Ca^{2+}$ (Figure 3.4c and Figure 3.4d). Due to this accumulation of $Ca^{2+}$, the etch pits show lower dissolution rates (Figure 3.4b) and a general depth dependency of dissolution rate was observed (Figure A3.7, but see detailed description in SI Section A3.1) from which the rate spectra were calculated.

The rate spectrum observed in the simulations of the rough calcite surface obtained after 10 hours of dissolution when deeper etch pits have evolved, falls within the experimental rate spectra (Figure 3.5) but shows a narrower range: the rate spectrum obtained from the simulations varies within a factor of two (Figure 3.5), while the rate spectrum measured experimentally shows more than two orders of magnitude variation i.e., mean±2σ dissolution rate is $4.56\pm5.56 \times 10^{-7}$ mol m$^{-2}$ s$^{-1}$. Recall that in these simulations (*Model G1-HE-1R*) a single dissolution rate was imposed, irrespective of the surface topography. Exaggerating the surface topography within the meshing limits of the COMSOL approach and using a single fixed dissolution rate also did not yield dissolution rate spectra at quasi steady state that reproduce the experimentally observed rate spectra (Figure A3.8, SI Section A3.2)
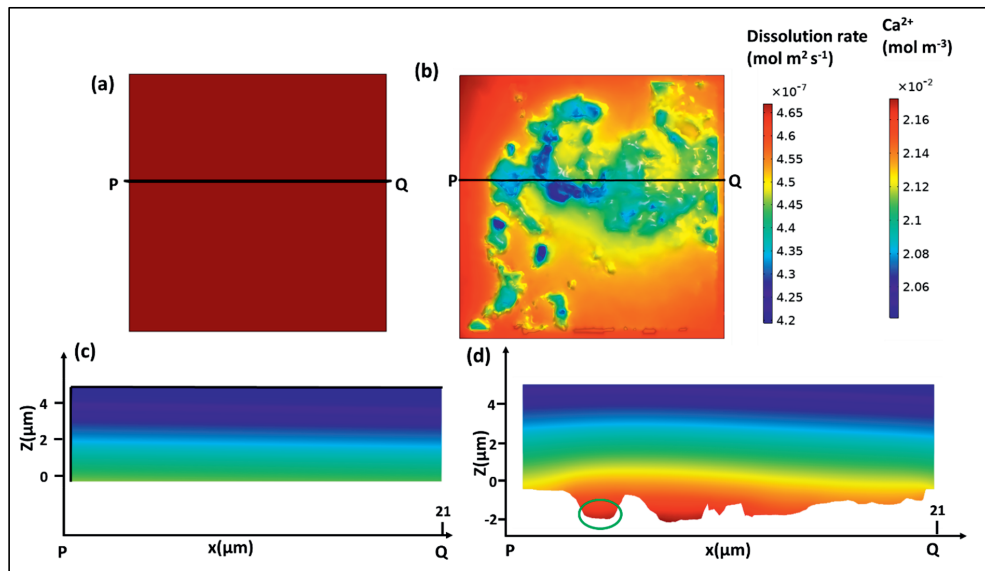
**Figure 3.4.** Reaction rate maps of Area A, after 200s of solution injection using (a) *Model G1-Flat-1R* (b) *Model G1A-HE-1R*. Vertical concentration slices of $Ca^{2+}$ are extracted along profile PQ from (c) *Model G1-Flat-1R* (d) *Model G1A-HE-1R*. The green color marker highlights $Ca^{2+}$ enriched pockets. Simulation are based on a flow rate of $6 \times 10^{-8}$ $m^3$ $s^{-1}$ and using Sol. #1 (pH 8.8 and alkalinity of 4.4 meq/kg-$H_2O$).
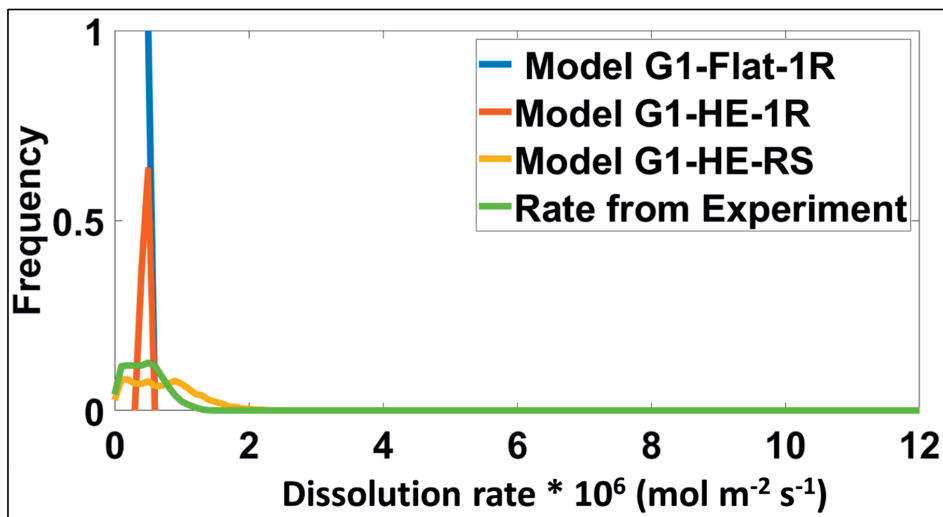


**Figure 3.5.** Comparison of the simulated rate spectra against the experimentally observed rate spectra. Simulation conditions include a flow rate of $6 \times 10^{-8}$ $m^3$ $s^{-1}$ using Sol. #1 (pH 8.8 and alkalinity of 4.4 meq/kg-$H_2O$).

In order to represent surface-controlled heterogeneity in dissolution rates, we also utilized a model in which we imposed location specific values of $R_I$ to Location A (*Model G1A- HE-RS*). While the *Model G1-Flat-1R* yielded a single dissolution rate and *Model G1A-HE-1R* a very

narrow dissolution spectrum in the quasi steady state, *Model G1A- HE-RS* showed a wider dissolution rate spectrum with an optimum width comparable to the dissolution rate spectrum measured experimentally (Figure 3.5, yellow and green line). The rate spectrum obtained from the simulations with imposed rate spectra extends over more than two orders of magnitude, similar to the rate spectrum measured experimentally.

### 3.3.2.2 Varying reaction and flow regime

Above findings are derived from *Model G1-Flat-1R* and its variants. This section investigates the impact of flow and reaction regimes on the hydrodynamics of the rough surface through simulation of *Set II* models, namely, *Model G2-Flat-1R and Model G2-HE-1R* which are parallelepiped sub-volumes of *Model G1-Flat-1R* (Figure A3. 3).

For a given flow velocity, lowering the pH value of the injecting solution results into increased reactivity towards calcite surface and thus increased production of the reaction products. As a result, the rate of removal of these products becomes the limiting factor in determining the dissolution rate and the reaction regime moves toward transport-controlled kinetics. This shift of the reaction regime is reflected through the increasing value of the Da number. Table A3.3 summarizes the Pe, $Da_I$ and $Da_{II}$ numbers and other solution parameters for all simulated flow and reaction regimes.

Injection of a solution with a pH value of 2 at an average velocity of 0.002 m s$^{-1}$ results in a mean±2σ dissolution rate at quasi steady state of an order of $1.10 \pm 0.07 \times 10^{-4}$ mol m$^2$ s$^{-1}$ (*Model G2-HE-1R*). This mean dissolution rate reflects the modified solution composition at the calcite surface i.e., at Location A: the pH of the solution in the diffusive boundary layer is around 2.8 (Figure 3.6b) and SI = -7.42/Ca concentration = 5.13 mol m$^{-3}$. Calculation of the $Da_I$ and $Da_{II}$ number based on the steady-state mean dissolution rate (Equation 3.14 and 3.16), instead of based on the composition of the injected solution, allows for analysis of rate heterogeneity due to local factors only (such as local surface topography) independent of other factors that affect this rate (e.g. size and shape of the numerical flow cell and location of the studied area with respect to the inlet). The vertical slice of pH (Figure 3.6b) shows that the pH of the deeper (etch pit) parts at the surface has a somewhat higher pH (+ 0.05 units) as compared to the flat parts. Like for *Model G1A-HE-1R* (Figure 3.4b) Ca accumulation was also observed in the deeper parts of the surface profile. As a result, these etch pits attain up to 12% lowered dissolution rate (Figure 3.6a).

Figure 3.7 presents the reaction rate heterogeneity for all simulated reaction and flow regimes. We observed the highest heterogeneity in dissolution rates (± 12%, due only to hydrodynamics) for the given surface roughness at $Da_I$= 12572 (i.e. pH 2 Sol. #4) and further increase of $Da_I$ number (i.e. decrease in pH) does not increase the rate heterogeneity any further (Figure 3.7 and Figure A3.9). For inflow solutions that are closer to equilibrium with respect to calcite, the relationship between flow rate, solution reactivity and dissolution rate heterogeneity becomes more complex: we observed higher amount of rate heterogeneity for solutions with lower reactivity regimes (Figure 3.7a - Pe=1041 and $Da_I$=201 (purple colored plot) vs Pe=1041 and $Da_I$=51(yellow colored plot) ). For the case where the dissolution reaction time scale is 3 orders of magnitude higher than the diffusion time scale, further increase in the reactivity by lowering pH does not impact the rate heterogeneity (Figure 3.7b - Pe=20833 and $Da_I$=30664 (red colored plot); Pe=1041 and $Da_I$=12572 (green colored plot)). Contrastingly, when reaction time scales are less than 3 orders of magnitude higher than diffusion time scale, increased rate heterogeneity is observed with decreasing pH (Figure 3.7b - Pe=20833 and $Da_I$=420 (magenta colored plot); Pe=1041 and $Da_I$=304 (orange colored plot)). This range of $Da_I$ number covers the state of solutions from being transport controlled (pH > 5) to surface controlled kinetics (pH<5) (Table A3.3).
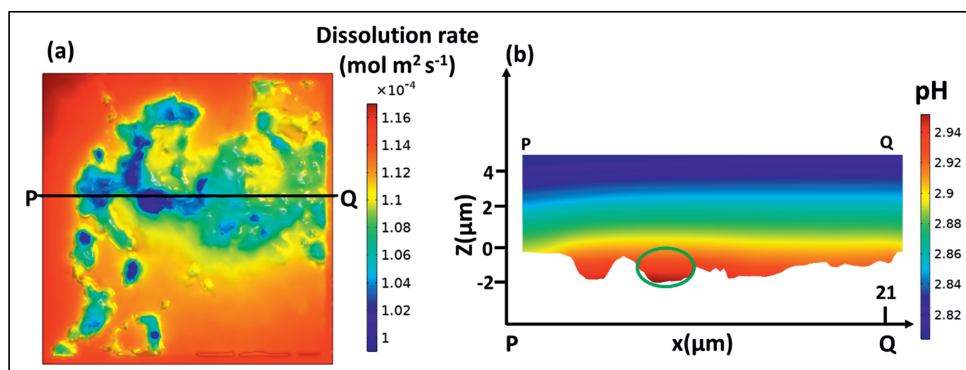
**Figure 3.6.** (a) Steady state reaction rate map in location A" in *Model G2-HE-1R* (b) Vertical concentration slice for pH obtained along profile PQ. Green oval points to the less acidic pockets. Simulation conditions are 0.002 m s$^{-1}$ average velocity using Sol. #4 (pH 2).
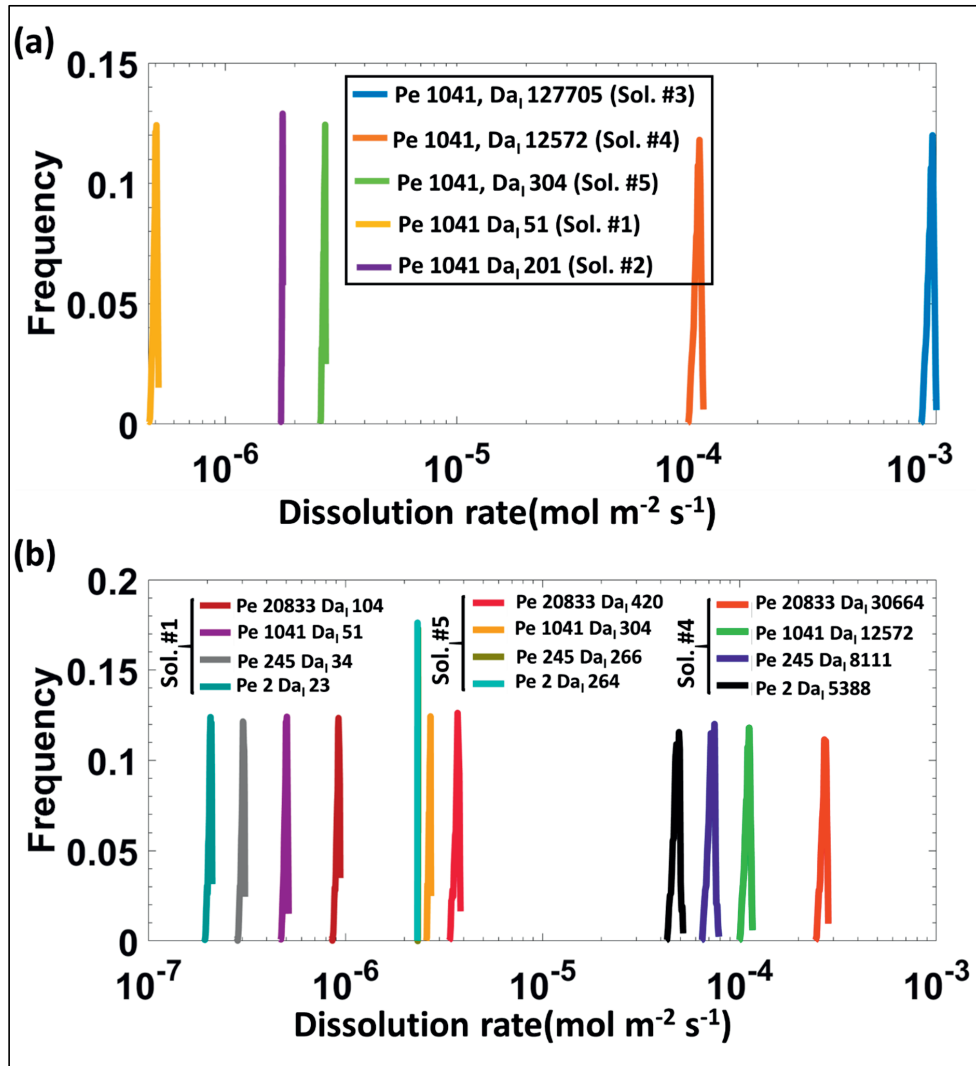
**Figure 3.7.** Rate spectra for simulations corresponding to (a) fixed Pe number and different $Da_I$ numbers, and (b) different Pe numbers corresponding to $Da_I$ numbers.

## 3.4 Discussion

### 3.4.1 Controls on dissolution rate heterogeneity at the flow cell scale

We observed that the flow rate value of $6 \times 10^{-8}$ m$^3$ s$^{-1}$, which is commonly utilized for surface experiments, developed a heterogeneous velocity field inside the circular flow cell (Figure 3.1) in contrast to, e.g., slit cells. In general, the thickness of the diffusion boundary layer is inversely related to velocity, because a higher value of velocity leads to an increased transport rate of aqueous species in both transversal and longitudinal directions. For example, highest average flow velocity led to a maximum rate of removal of the reaction products from the

calcite surface at location B as well as to a maximum rate of longitudinal transport of the removed reaction products. In contrast, the flow velocity at locations A and C was lower, so the rate of removal of reaction products from the calcite surface was lower while transversal mixing of the removed products was higher. Therefore, lowest near-surface and bulk $Ca^{2+}$ concentration was observed at location B compared to locations A and C.

The observed heterogeneity of velocity and $Ca^{2+}$ concentration field suggests that the imposed boundary conditions of the flow cell led locally different magnitudes of transport (i.e., advection and diffusion) and reaction time scale. The attainment of a steady state dissolution rate at any location of the flow cell thus depends on the relative strength of these two transport-time scales. Therefore, the injection of Sol. #1 (pH 8.8 and alkalinity 4.4 meq $Na_2CO_3$/kg-$H_2O$) led to over an order of magnitude heterogeneity in the dissolution rates observed in a circular flow cell (Figure 3.2c). As a result, we observed that the locations such as B that are in the high velocity zones of the cell are most close to the surface-controlled conditions while most of the remaining part of the flow cell pertains to transport-controlled conditions.

The implications of the variability in transport-controlled conditions inside the flow cell are twofold: a) the observed mean dissolution rate in the flow cell was up to one order of magnitude lower than expected based on the composition of the injected solution and b) the size and location of the study window will affect observations made during surface experiments. We observed that a flow rate higher than $1 \times 10^{-7}$ $m^3$ $s^{-1}$ is required for establishing surface-controlled regimes inside the entire flow through cell (Figure 3.5). These findings suggest that the prevalence of a certain reaction regime is a function of the choice of the examined location and the flow rate, beside the composition of the solution and the shape of the flow cell.

The solution composition, and in particular the capacity of the solution to buffer against changes in the equilibration state of the solution with respect to calcite, also affects the dissolution rate heterogeneity observed at the scale of the flow cell. Sol. #1, with a pH 8.8 and concentration of $CO_3^{2-}$ ions is 0.2 mol $m^{-3}$ is regularly chosen for microscopic dissolution experiments, because it offers slow dissolution kinetics. This solution has a considerable buffer capacity compared to Sol. #2 (same pH, no dissolved inorganic carbon at the inflow) (Figure A3.10). The high pH of these solutions enables $H^+$ independent kinetics (Plummer et.al., 1978) and the amount of $CO_3^{2-}$ controls the distance of the solution from the equilibrium state (Equation 3.9). The fact that we observed a lower amount of buffering by the Sol. #2 that by Sol. #1 indicates that the amount of $CO_3^{2-}$ species in the Sol., # 1, which contributes into SI of the solution, is responsible for the observed buffering. This effect has been explained in detail in SI Section A3.3. In summary, solutions with high pH value (of around 8.8) and lower amount of DIC (dissolved inorganic carbon) experience lower amount of buffering, therefore a lower amount of rate heterogeneity than solutions with the same pH but higher DIC. Therefore, the former seems to be a better choice for experiments at surface-controlled kinetics at an injection rate of $6 \times 10^{-8}$ $m^3$ $s^{-1}$, in microscopic surface experiments.

Such detailed analysis of the optimum flow rate and the solution composition could only be possible through the findings of the reactive transport processes occurring inside the flow cell. In past, similar impact of the experiment setting on the mixing conditions was noted for gypsum dissolution (Gasperino et al., 2006 and Peruffo et al, 2016). For example, Peruffo et al, 2016 observed that complex hydrodynamics near the tip holder and the tip in an AFM fluid cell lowers the mass transport rate in the vicinity, which further leads to the accumulation of the $Ca^{2+}$ and $SO_4^{2-}$ ions near the crystal surface in the field of view. Based on their findings they suggested that either an entire micro-crystal lying on an otherwise inert crystal surface should be investigated to avoid dissolution processes happening outside the region of interest affecting dissolution processes within the field of view, or a detailed hydrodynamic model of the whole

AFM cell is needed to account for dissolution processes happening outside the region of interest. In the context of calcite dissolution, the current study also encourages detailed investigation of the reactive transport processes inside flow cells. Such information will help in optimizing the design of a flow cell and injection parameters and/or identification and quantification of the impact of the transport-controlled conditions over observed dissolution rates.

### 3.4.2 Controls on dissolution rate heterogeneity at the microscopic scale

At the microscopic scale, i.e. the scale of commonly utilized fields of view for dissolution experiments using VSI or AFM, the solution near the flat calcite surface was well-mixed thus a single dissolution rate was observed (Location A Figure 3.4a and Figure A3.5) and no impact of the flow-cell-scale rate heterogeneity was observed. Furthermore, the imposition of the real crystal topography in location A (Figure 3.7b) results in the development of a rate spectrum. This rate spectrum is an explicit consequence of the surface roughness on local hydrodynamics, since for *Model G1A-HE-1R*, a single reaction rate law was implemented. Although the dissolution corresponding to the injected solution of a pH value of 8.8 results into nearly $H^+$ independent kinetics, the rate of removal of the reaction products i.e, $Ca^{2+}$ and $CO_3^{2-}$ is controlled by diffusive transport. Therefore, the non-uniform diffusive boundary layer determines how much of these reaction products accumulates near the calcite surface.

The observed rate spectrum at the microscopically rough calcite surface (*Model G1-HE-1R*) is much narrower than the experimentally observed rate spectrum (Figure 3.5). This indicates that the hydrodynamics in combination with just surface roughness is not enough to explain the overall experimentally observed dissolution rate heterogeneity, even until 10 hours of dissolution when deeper etch pits have evolved. In our simulations, the magnitude of roughness induced in this dissolution period is not developing significant non-uniformity in the diffusive boundary layer. Consequently, for this roughness and flow regime, the diffuse boundary layer can be considered of a uniform thickness. This confirms that under surface-controlled dissolution conditions, the experimentally observed rate spectra cannot be explained purely by heterogeneity in hydrodynamics induced by surface topography.

Once rate spectra are imposed in our simulations of the microscopically rough calcite surface (*Model G1-HE-RS)*, only then rate spectra of similar width to those observed experimentally are obtained. The fact that we cannot obtain similarly wide rate spectra without imposing rate spectra from the start of the simulations is a strong indication that rough calcite surfaces intrinsically show local variability in dissolution rate. These findings are in the agreement with the observation made by Levenson et.al, 2003 for surface-controlled kinetics. To summarize, rate spectra can be attributed to atomic-scale surface heterogeneities such as surface structure, kink densities and defect distribution at or near the crystal surface, which result in a free-energy landscape at the dissolving surface (Shiraki et al., 2000; Arvidson et al., 2003; Lüttge et.al., 2003; Fischer et al., 2012; Brand et al., 2017). This means that, irrespective of the location of the observation area within the flow cell, the local atomic-scale surface heterogeneities most likely determine the measured dissolution rate spectra.

The sensitivity analysis performed for a range of transport and reaction regimes showed that the hydrodynamics induced rate heterogeneity became more pronounced with the increasing acidity of the injected solution and with the increasing injection fluid velocity (Figure 3.7 and Figure A3.9). For the simulated roughness magnitudes, we observed that the highest noted variability in the dissolution rate due to hydrodynamics only is around 12%, which is lower than the previously observed variability for fractures with roughness of a magnitude higher than 10μm (Deng et.al., 2018).

## 3.5    Conclusions

1. Computer simulations of calcite marble dissolution experiments were performed at the scale of an entire flow-through cell and at a scale equal to fields of view in microscopic dissolution experiments.

2. Simulations at the scale of full flow cell show that due to the no slip velocity at the surface of the crystal a vertical gradient in the concentration of the dissolved components is observed, even at equilibrium. As a result, the equilibrium composition at the surface of the crystal inside the flow cell differs from the composition of the injected solution. The difference depends on the shape of the flow cell, the flow regime, and the location within the cell.

3. Significant horizontal heterogeneity of the flow and the concentration within the considered flow cell is observed. Together with the building of a vertical diffusion layer, this leads to significant discrepancy between the reactivity calculated on the base of the mass outflow from the flow cell using the composition of the injected fluid, and the real local reactivities within the flow cell. Consequently, selection of the location for a small observation area for surface measurements is very important: differences of up to an order of magnitude can be observed due to the horizontal flow and composition heterogeneity in a circular flow cell in contrast to, e.g., slit cells. However, at the small scale within the observation area for e.g. AFM or VSI measurements, this horizontal heterogeneity of the fluid composition is negligible.

4. The simulations at conditions corresponding to the reaction and flow regime of microscopic surface dissolution experiments show that the roughness of a crystal surface (as from VSI experiments) does not influence the hydrodynamics and vice versa, no significant variations in the composition near the surface are observed due to the roughness.

5. It is concluded that neither flow regimes (cell geometry) nor consideration of the rough sample topography (specific surface area) and the resulting variability in hydrodynamics can explain experimentally observed dissolution rate spectra if a constant dissolution rate is used. Sensitivity studies show this is true also for increased surface roughness.

6. Considering the variability of surface reactivity via imposed dissolution rate spectra allows to explain experimentally observed dissolution rate spectra. This means that the heterogeneity of a crystal surface and the free energy on the surface play an important if not determining role for dissolution rate spectra for the considered flow and reactivity regimes.

7. The impact of surface roughness on hydrodynamics was observed to rise with the increased reactivity (acidity) of the injected solution and with the increasing injection fluid velocity. The highest limit of rate heterogeneity, observed in this study, for the simulated roughness magnitudes, is lower than the observed impact for the much higher roughness of a fracture (Deng et.al., 2018) where the roughness is of (>10μm) higher magnitude.

## Appendix 3
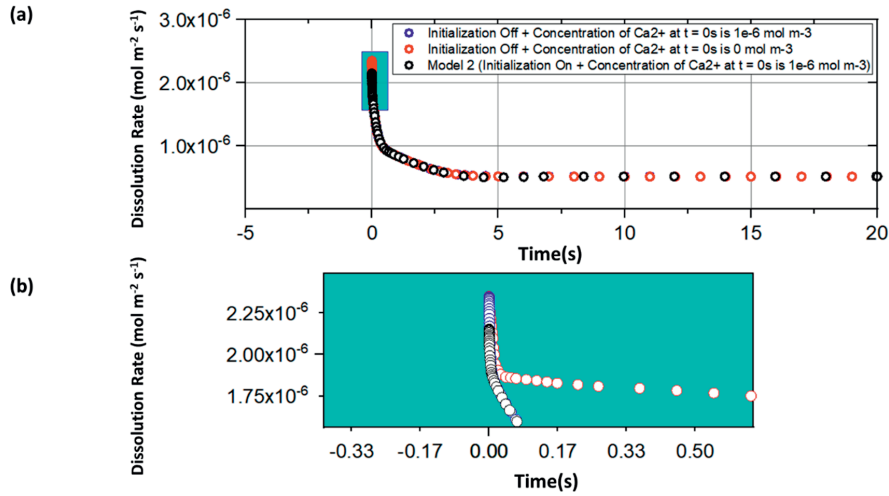


**Figure A3.1**. (a) Impact of initialization of COMSOL Model and initial addition of $Ca^{2+}$ species in the injecting solution, over mean dissolution rate. Blue rectangle covered area of plot a is zoomed out in plot (b)



**Figure A3.2**. Sketch of the *Model G1-Flat-1R* and its 4 variants through the variations in surface topography and kinetic rates at Area A and A'.

The table shows Model G2 with variants:

| | Model Nomenclature | Surface Topography | Kinetics |
|---|---|---|---|
| Model G2 (with Flow Direction, Z, Y, X axes) | Model G2-Flat-1R | Area A'' (green square) | Single value of $R_I$ in Equation 8 |
| Variants of Model G2 through variations in the surface topography at an Area A'' (Studied Area A'', Flow Direction, X, Y) | Model G2-HE-1R | Area A'' (topographic map image) | Single value of $R_I$ in Equation 8 |

**Figure A3. 3**. Sketch of the *Model G2-Flat-1R* and its 4 variants through the variations in surface topography and kinetic rates at Area A''.

**Table A3.1**: **Concentration of all aqueous species corresponding to all five injecting solutions.**

| Species | Injecting Solution – Sol.#1 (Solution corresponding to the experiment) (mol m$^{-3}$) | Injecting Solution – Sol. #2 (mol m$^{-3}$) | Injecting Solution – Sol. #3 (mol m$^{-3}$) | Injecting Solution – Sol. #4 (mol m$^{-3}$) | Injecting Solution – Sol. #5 (mol m$^{-3}$) |
|---|---|---|---|---|---|
| H$^+$ | $1.42 \times 10^{-6}$ | $1.26 \times 10^{-3}$ | $1.28 \times 10^{2}$ | $1.26 \times 10^{1}$ | $1.26 \times 10^{-1}$ |
| OH$^-$ | 0.01 | $1.42 \times 10^{-5}$ | $1.50 \times 10^{-10}$ | $1.43 \times 10^{-9}$ | $1.42 \times 10^{-7}$ |
| CO$_2$(aq) | 0.01 | $1.08 \times 10^{-2}$ | $1.05 \times 10^{-2}$ | $1.07 \times 10^{-2}$ | $1.08 \times 10^{-2}$ |
| HCO$_3^-$ | 4.01 | $6.67 \times 10^{-3}$ | $6.92 \times 10^{-8}$ | $6.70 \times 10^{-7}$ | $6.67 \times 10^{-5}$ |
| CO$_3^{2-}$ | 0.18 | $7.53 \times 10^{-7}$ | $8.83 \times 10^{-17}$ | $7.68 \times 10^{-15}$ | $7.53 \times 10^{-11}$ |
| Ca$^{2+}$ | $1 \times 10^{-6}$ | 0 | 0 | 0 | 0 |
| Na$^+$ | 4.4 | 200 | 200 | 200 | 200 |
| Cl$^-$ | - | 200 | 328 | 213 | 200 |
| pH | 8.8 | 8.8 | 1 | 2 | 4 |

**Table A3. 2. Pe, $Da_I$ and $Da_{II}$ numbers at the examined locations in base *Model G1* and its variants for all simulated flow and reaction regimes. The highlighted cells correspond to the experimental conditions. $V_i$ = Flow rate; $V_{avg}$ = Average flow velocity; $R_{avg}$ = Average dissolution rate**

| Model | Area | $V_i$ (m³ s⁻¹) | Sol. # | $V_{avg}$ (m s⁻¹) | $R_{avg}$ (mol m² s⁻¹) | Pe | $Da_I$ | $Da_{II}$ |
|---|---|---|---|---|---|---|---|---|
| G1-Flat-1R | A | $6 \times 10^{-8}$ | 1 | $2 \times 10^{-3}$ | $4.69 \times 10^{-7}$ | 1041 | 53 | 0.051 |
| | B | $6 \times 10^{-8}$ | 1 | $6 \times 10^{-2}$ | $1.45 \times 10^{-6}$ | 31250 | 165 | 0.005 |
| | C | $6 \times 10^{-8}$ | 1 | $1.8 \times 10^{-3}$ | $2.90 \times 10^{-7}$ | 937 | 33 | 0.035 |
| | A | $1 \times 10^{-7}$ | 1 | $4 \times 10^{-3}$ | $2.74 \times 10^{-7}$ | 2083 | 31 | 0.015 |
| | B | $1 \times 10^{-7}$ | 2 | $9.8 \times 10^{-2}$ | $1.62 \times 10^{-6}$ | 51041 | 184 | 0.004 |
| | C | $1 \times 10^{-7}$ | 2 | $5 \times 10^{-3}$ | $5.30 \times 10^{-7}$ | 2604 | 60 | 0.023 |
| | A | $1 \times 10^{-8}$ | 2 | $4.8 \times 10^{-4}$ | $2.95 \times 10^{-7}$ | 247 | 33 | 0.136 |
| | B | $1 \times 10^{-8}$ | 2 | $5 \times 10^{-3}$ | $8.64 \times 10^{-7}$ | 2604 | 98 | 0.038 |
| | C | $1 \times 10^{-8}$ | 3 | $2.7 \times 10^{-4}$ | $1.34 \times 10^{-7}$ | 139 | 15 | 0.110 |
| G1-HE-1R | A | $6 \times 10^{-8}$ | 4 | $2 \times 10^{-3}$ | $4.52 \times 10^{-7}$ | 1041 | 51 | 0.049 |
| G1-HS-1R | A | $6 \times 10^{-8}$ | 4 | $2 \times 10^{-3}$ | $3.76 \times 10^{-7}$ | 1041 | 42 | 0.041 |
| G1-HS-1R | A' | $6 \times 10^{-8}$ | 4 | $2 \times 10^{-3}$ | $4.36 \times 10^{-7}$ | 1041 | 49 | 0.048 |
| G1-P-1R | A | $6 \times 10^{-8}$ | 4 | $2 \times 10^{-3}$ | $3.02 \times 10^{-7}$ | 1041 | 34 | 0.033 |
| G1-HE-RS | A | $6 \times 10^{-8}$ | 5 | $2 \times 10^{-3}$ | $7.33 \times 10^{-7}$ | 1041 | 83 | 0.080 |
| G1-Flat-1R | A | $6 \times 10^{-8}$ | 5 | $2 \times 10^{-3}$ | $1.67 \times 10^{-6}$ | 1041 | 190 | 0.182 |
| G1-Flat-1R | B | $6 \times 10^{-8}$ | 5 | $6 \times 10^{-2}$ | $2.29 \times 10^{-6}$ | 31250 | 261 | 0.008 |
| G1-Flat-1R | C | $6 \times 10^{-8}$ | 5 | $1.8 \times 10^{-3}$ | $1.20 \times 10^{-6}$ | 937 | 136 | 0.146 |

**Table A3.3**: Pe, $Da_I$ and $Da_{II}$ numbers at the examined locations in base *Model G1* and its variants for all simulated flow and reaction regimes. $V_{avg}$ = Average flow velocity; $R_{avg}$ = Average dissolution rate; $SI_{avg}$ = Average saturation index; $pH_{avg}$ = Average pH

| Sol. # | $V_{avg}$ (m s$^{-1}$) | $R_{avg}$ (mol m$^2$ s$^{-1}$) | $SI_{avg}$ | $pH_{avg}$ | Pe | $Da_I$ | $Da_{II}$ |
|---|---|---|---|---|---|---|---|
| *Model G2-flat-1R and Area A''* | | | | | | | |
| 1 | 0.04 | $9.47 \times 10^{-7}$ | -0.34 | 8.88 | 20833 | 107 | 0.01 |
| 1 | 0.002 | $5.18 \times 10^{-7}$ | -0.16 | 8.89 | 1041 | 59 | 0.06 |
| 1 | $4.70 \times 10^{-4}$ | $3.13 \times 10^{-7}$ | -0.09 | 8.90 | 244 | 35 | 0.15 |
| 1 | $4.70 \times 10^{-6}$ | $2.13 \times 10^{-7}$ | -0.06 | 8.90 | 2 | 24 | 9.89 |
| 2 | 0.04 | $2.19 \times 10^{-6}$ | -1.77 | 9.38 | 20833 | 249 | 0.01 |
| 2 | 0.002 | $1.79 \times 10^{-6}$ | -0.94 | 9.63 | 1041 | 203 | 0.20 |
| 2 | $4.70 \times 10^{-4}$ | $1.58 \times 10^{-6}$ | -0.73 | 9.63 | 244 | 179 | 0.73 |
| 2 | $4.70 \times 10^{-6}$ | $1.08 \times 10^{-6}$ | -0.40 | 9.77 | 2 | 122 | 50.15 |
| 3 | 0.002 | $1.19 \times 10^{-3}$ | -7.52 | 1.74 | 1041 | 135451 | 135452 |
| 4 | 0.04 | $2.83 \times 10^{-4}$ | -8.46 | 2.37 | 20833 | 32267 | 1.55 |
| 4 | 0.002 | $1.17 \times 10^{-4}$ | -7.48 | 2.76 | 1041 | 13339 | 12.81 |
| 4 | $4.70 \times 10^{-4}$ | $7.55 \times 10^{-5}$ | -7.00 | 2.96 | 244 | 8605 | 35.16 |
| 4 | $4.70 \times 10^{-6}$ | $5.04 \times 10^{-5}$ | -6.57 | 3.16 | 2 | 5741 | 2345.42 |
| 5 | 0.04 | $3.85 \times 10^{-6}$ | -7.63 | 4.64 | 20833 | 438 | 0.02 |
| 5 | 0.002 | $2.72 \times 10^{-6}$ | -6.36 | 5.26 | 1041 | 310 | 0.30 |
| 5 | $4.70 \times 10^{-4}$ | $2.34 \times 10^{-6}$ | -3.32 | 7.02 | 244 | 266 | 1.09 |
| 5 | $4.70 \times 10^{-6}$ | $2.31 \times 10^{-6}$ | -2.56 | 7.29 | 2 | 262 | 107.36 |
| *Model G2-HE-1R and Area A''* | | | | | | | |
| 1 | 0.04 | $9.17 \times 10^{-7}$ | -0.32 | 8.90 | 20833 | 104 | 0.01 |
| 1 | 0.002 | $4.52 \times 10^{-7}$ | -0.16 | 8.92 | 1041 | 51 | 0.05 |
| 1 | $4.70 \times 10^{-4}$ | $3.01 \times 10^{-7}$ | -0.09 | 8.93 | 244 | 34 | 0.14 |
| 1 | $4.70 \times 10^{-6}$ | $2.06 \times 10^{-7}$ | -0.06 | 8.93 | 2 | 23 | 9.57 |
| 2 | 0.04 | $2.18 \times 10^{-6}$ | -1.72 | 9.39 | 20833 | 248 | 0.01 |
| 2 | 0.002 | $1.77 \times 10^{-6}$ | -0.91 | 9.63 | 1041 | 201 | 0.19 |
| 2 | $4.70 \times 10^{-4}$ | $1.56 \times 10^{-6}$ | -0.71 | 9.63 | 244 | 177 | 0.73 |
| 2 | $4.70 \times 10^{-6}$ | $1.07 \times 10^{-6}$ | -0.40 | 9.77 | 2 | 121 | 49.80 |
| 3 | 0.002 | $1.12 \times 10^{-3}$ | -7.46 | 1.76 | 1041 | 127705 | 122.60 |
| 4 | 0.04 | $2.69 \times 10^{-4}$ | -8.39 | 2.51 | 20833 | 30664 | 1.47 |
| 4 | 0.002 | $1.10 \times 10^{-4}$ | -7.42 | 2.78 | 1041 | 12572 | 12.07 |
| 4 | $4.70 \times 10^{-4}$ | $7.12 \times 10^{-5}$ | -6.93 | 2.99 | 244 | 8111 | 33.14 |
| 4 | $4.70 \times 10^{-6}$ | $4.73 \times 10^{-5}$ | -6.51 | 3.31 | 2 | 5388 | 2201.44 |
| 5 | 0.04 | $3.69 \times 10^{-6}$ | -7.51 | 4.81 | 20833 | 420 | 0.02 |
| 5 | 0.002 | $2.68 \times 10^{-6}$ | -6.22 | 5.44 | 1041 | 304 | 0.29 |
| 5 | $4.70 \times 10^{-4}$ | $2.34 \times 10^{-6}$ | -3.27 | 7.04 | 244 | 266 | 1.09 |
| 5 | $4.70 \times 10^{-6}$ | $2.32 \times 10^{-6}$ | -2.78 | 7.07 | 2 | 264 | 108.21 |
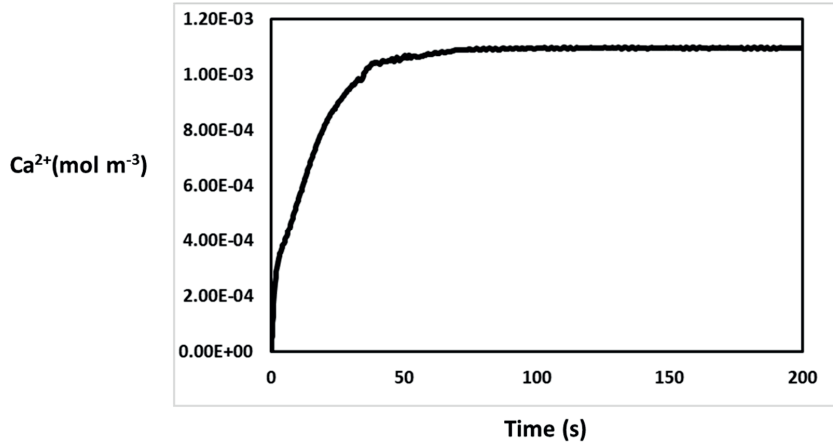
**Figure A3.4.** Breakthrough curve of the $Ca^{2+}$ species shows that the system corresponding to the flow rate value of $6 \times 10^{-8}$ $m^3$ $s^{-1}$ attained the quasi-steady-state in approximately 100s.

**Table A3.4**: Statistics related to the flow regime and solution composition at areas A, B and C in *Model G1-Flat-1R,* after injection of the fluid for 200s. Simulation conditions are $6 \times 10^{-8}$ $m^3$ $s^{-1}$ flow rate, Sol. #1 (pH 8.8 and alkalinity of 4.4 meq/kg-$H_2O$). $V_{avg}$ = Average flow velocity; $R_{avg}$ = Average dissolution rate; $cCa_s$ = Surface average $Ca^{2+}$ concentration, calculated at the calcite surface; $cCa_b$ = Bulk average $Ca^{2+}$ concentration calculated from the vertical slice of height 1.75 mm positioned at the respective location.

| Area | $V_{avg}$ (m $s^{-1}$) | $cCa_s$ (mol $m^{-3}$) | $cCa_b$ (mol $m^{-3}$) | $R_{avg}$ (mol $m^{-2}$ $s^{-1}$) |
|---|---|---|---|---|
| A | $2 \times 10^{-3}$ | 0.022 | 0.002 | $4.69 \times 10^{-7}$ |
| B | $6 \times 10^{-2}$ | 0.009 | $4.92 \times 10^{-4}$ | $1.45 \times 10^{-6}$ |
| C | $1.8 \times 10^{-3}$ | 0.024 | 0.004 | $2.90 \times 10^{-7}$ |

**Table A3.5**: Concentration and activity of all aqueous species which are part of the calcite dissolution system, at the calcite surface, at areas A, B and C in *Model G1-Flat-1R*. Simulation conditions are $6 \times 10^{-8}$ $m^3$ $s^{-1}$ flow rate, Sol. #1 (pH 8.8 and alkalinity of 4.4 meq/kg-$H_2O$).

| Species | Area A Concentration (mol $m^{-3}$) | Activity (mol $m^{-3}$) | Area B Concentration (mol $m^{-3}$) | Activity (mol $m^{-3}$) | Area C Concentration (mol $m^{-3}$) | Activity (mol $m^{-3}$) |
|---|---|---|---|---|---|---|
| $H^+$ | $1.28 \times 10^{-6}$ | $1.19 \times 10^{-6}$ | $1.36 \times 10^{-6}$ | $1.26 \times 10^{-6}$ | $1.27 \times 10^{-6}$ | $1.18 \times 10^{-6}$ |
| $OH^-$ | 0.009 | 0.008 | 0.009 | 0.008 | 0.009 | 0.008 |
| $CO_2(aq)$ | 0.010 | 0.010 | 0.010 | 0.010 | 0.010 | 0.010 |
| $HCO_3^-$ | 4.018 | 3.739 | 4.016 | 3.738 | 4.018 | 3.739 |
| $CO_3^{2-}$ | 0.200 | 0.150 | 0.188 | 0.142 | 0.202 | 0.152 |

| Ca$^{2+}$ | 0.022 | 0.016 | 0.009 | 0.007 | 0.024 | 0.018 |
|---|---|---|---|---|---|---|
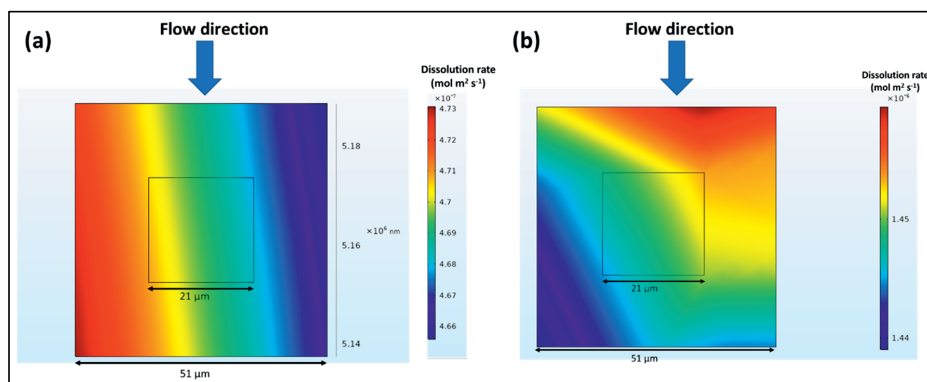


**Figure A3.5**. Dissolution rate map at locations (a) A and (b) B in *Model G1-Flat-1R*. Simulation conditions are $6 \times 10^{-8}$ m$^3$ s$^{-1}$ flow rate, Sol. #1 (pH 8.8 and alkalinity of 4.4 meq/kg-H$_2$O).
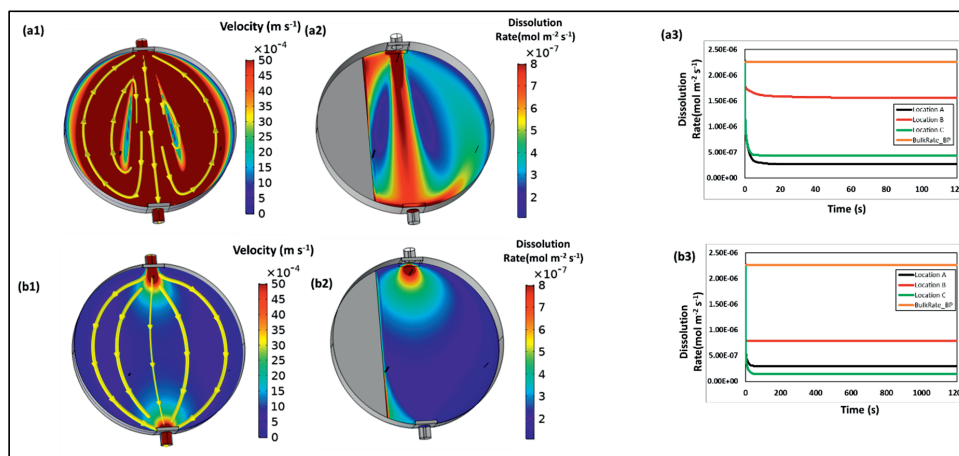


**Figure A3.6**. Simulated flow cell corresponding to the flow rate value of $1 \times 10^{-7}$ m$^3$ s$^{-1}$ showing quasi-steady-state (a1) velocity field with streamlines (a2) quasi-steady-state reaction rate map and (a3) temporal evolution of the mean dissolution rate at locations A, B, and C. Panels b1-b3 show the same for the simulation with the flow rate value of $1 \times 10^{-8}$ m$^3$ s$^{-1}$. Note that velocity fields in panels a1 and b1 are plotted for the same velocity range and reaction field in panels a2 and b2 are plotted for the same reaction rates range.

## A3.1 The dependency of dissolution rates on roughness magnitude

Quantification of the rate heterogeneity was performed using height and dissolution rate profiles, extracted along line PQ in Fig. 4 in the main document, perpendicular to the flow direction. A comparison of the depth and dissolution rate of each point along these profiles, using point P as reference, revealed a complex dependency of the dissolution rate over the depth (Figure A3.7). In general, the dissolution rate shows a linear dependency over the depth

magnitude (Figure A3.7c) although there are some differences. The plot corresponding to the two consecutives etch pits (highlighted by the blue outline in Figure A3.7b) shows that a difference of 1.5µm in the depth compared to the flat part of the surface can lead to a 6% difference in the dissolution rate, whereas, the part in the plot that corresponds to the area with a less steep topography at the same depth (~ 1.5µm highlighted by the green outline in Figure A3.7b) shows a difference of only 4% in their respective dissolution rates. Moreover, in two small sections on the surface dissolution rate has no dependency over the depth magnitude (highlighted by the black outline in Figure A3.7b). The complex relationship between surface depth/steepness and dissolution rate (along a line perpendicular to the flow direction) suggests that non-local effects related to the surface heights also play a role in determining the dissolution rate. This is further illustrated by the different curves for dissolution rate versus depth difference Figure A3.7c) for the deeper steeper etch pits (blue line) and the less steep areas at the same depth (green line).
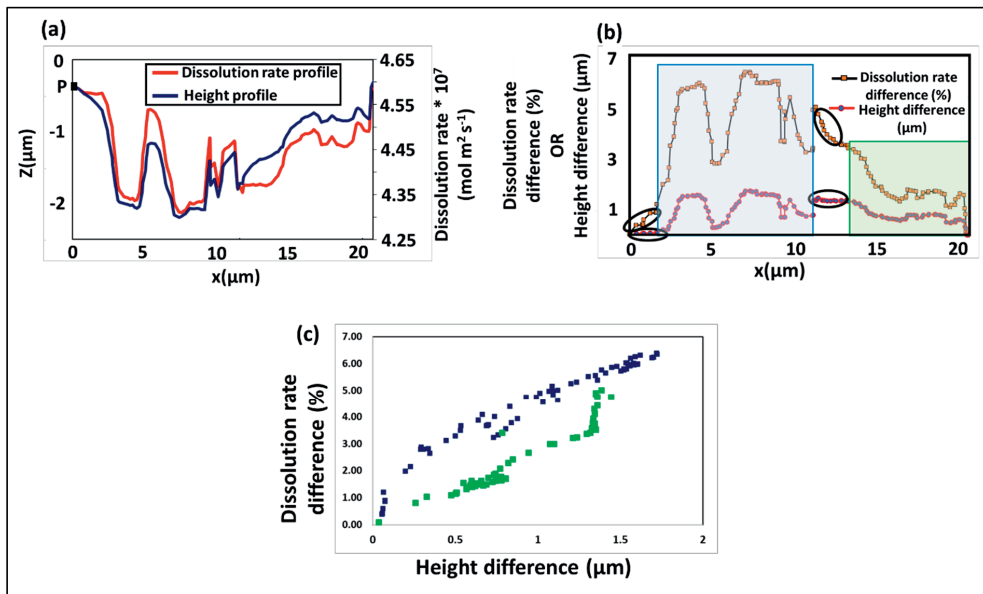


**Figure A3.7.** (a) Height and dissolution rate profiles extracted along profile PQ in Fig. 4 in the main document, perpendicular to the flow direction. (b) difference in height (µm) and dissolution rate (%) compared to reference point P_ for each point along line PQ. Regions marked with different colored boxes show the variety in the dependency of the rate heterogeneity over the height difference (c) difference in the dissolution rate (%) vs height difference (µm) for the blue and green boxes in Figure A3.7b. Simulation conditions are 6 × $10^{-8}$ m$^3$ s$^{-1}$ flow rate, Sol. #1 (pH 8.8 and alkalinity of 4.4 meq/kg-H$_2$O).

## A3.2 Varying roughness magnitude

To find out which level of roughness evolution during surface experiments impacts mass transport so much that the formation of a diffusion boundary layer leads to numerical dissolution rate spectra that equal the experimentally observed dissolution rate spectra, we exaggerated the experimentally observed surface roughness of *Model G1A-HE-1R*, by a factor of five (*Model G1A-HS-1R*). This exaggeration was limited to a factor of five, in order to preserve meshing quality of the resultant narrow topographic features (Figure A3.8b). We observed that the surface composed of peaks and troughs of an amplitude of around 7µm

yielded a variation in rate heterogeneity of about half-an-order (Figure A3.8a). *Model G1A-P-1R*, which included a more exaggerated surface roughness imposed as pillars with a height of 20µm, showed a rate heterogeneity of one order (Figure A3.8a and c). This suggests that presence of such elongated topographic features, which are in general more than what is observed in experiments, will have a hydrodynamic impact on the observed rate spectra, in particular at the lower side end of the spectrum. However, overall, these exaggerated surface topographies do not result in a match with the wide rate spectra observed experimentally (purple line in Figure A3.8a).
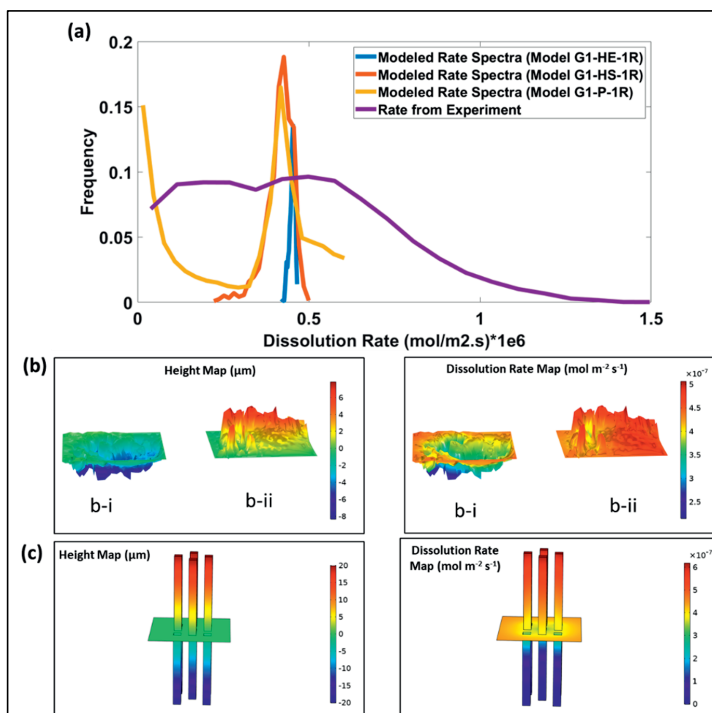


**Figure A3.8.** (a) Impact of surface roughness over rate spectra is presented for two types of roughness models i.e., *Model G1A-HS-1R* and *Model G1A-HP-1R*. Height and reaction rate maps are provided corresponding to (b) *Model G1A-HS-1R* and (c) *Model G1A-HP-1R*.
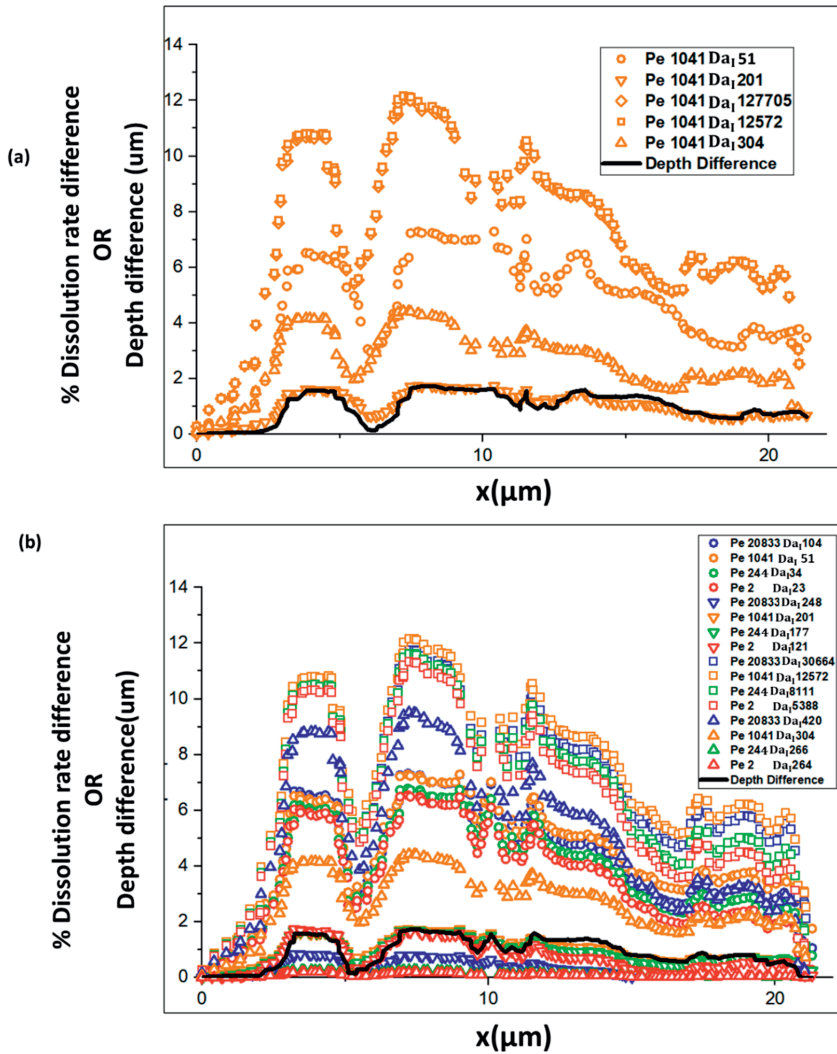
**Figure A3.9**. Calculated % difference in the dissolution rate along line PQ (marked in Fig. 6) for simulations with (a) fixed Pe number and different $Da_I$ numbers (b) Different Pe number and corresponding $Da_I$ numbers.

**A3.3 How the composition of the inflow solution affects buffering capacity of the solution due to the dissolution processes:**

In order to illustrate the impact of the composition of the inflow solution on the buffering capacity of the solution, we have performed batch calcite dissolution reactions using Sol. #1 (pH 8.8 and 4.2 mM DIC) and Sol. #2 (same pH but no any initial DIC), in PhreeqC using the phreeqC.dat database. At the first-time step, the magnitude of dissolution rate, and the amount of $Ca^{2+}$ and $CO_3^{2-}$ species released into solution due to dissolution, is higher for Sol. #2 than Sol. #1 (Figure A3.10d). Higher amounts of dissolution products followed by addition of reaction products for Sol. #2 might be expected to result in a higher shift in the saturation state

of this solution. On the contrary, the saturation index of the Sol. #1 dropped more sharply than the Sol. #2 (Figure A3.10c). This can be explained by the initial solution composition: Sol. # 1, with some initial DIC, buffers more strongly against any pH changes (Figure A3.10a) than Sol. # 2. Also, upon minor generation of dissolution products, it reaches near-equilibrium conditions more rapidly (Figure A3.10b) than Sol. #2. Subsequently, the dissolution rate corresponding to the Sol. #1 was observed to decline more strongly (Figure A3.10d).
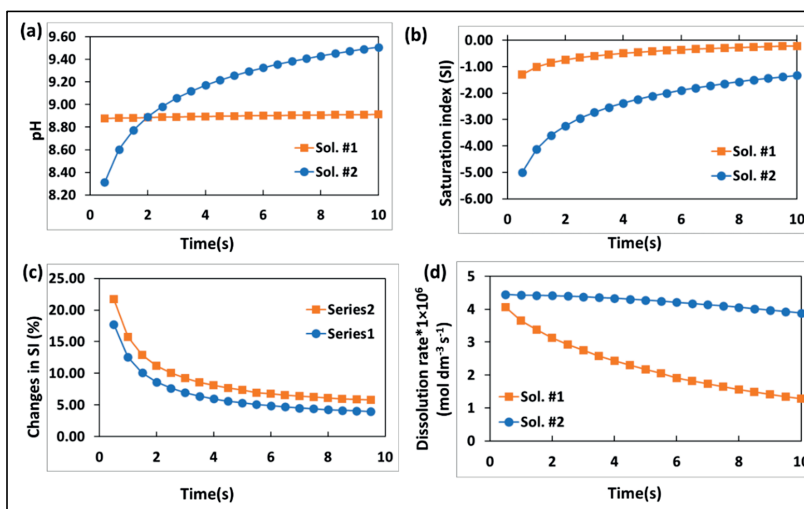


**Figure A3.10.** Evolution of (a) pH (b) saturation index (SI) (c) changes in SI (%), and (d) dissolution rate, with respect to time.

Chapter 3

# Chapter

## 4. A new formulation of conductance evolution in pore network models for calcite dissolution

**ABSTRACT**

Pore network model (PNM) simulation is an important method to simulate reactive transport processes in porous media and to investigate constitutive relationships between permeability and porosity that can be implemented in continuum-scale reactive-transport modelling. Existing reactive transport pore network models (rtPNM) assume that the initially cylindrical pore throats maintain their shape and pore throat conductance is updated using the Hagen-Poiseuille relation. However, in the context of calcite dissolution, earlier studies have shown that during dissolution, pore throats can attain a spectrum of shapes, depending upon the imposed reactive-flow conditions (Agrawal et al., 2020). In the current study, we have performed reactive transport simulations on the scale of a single capillary for a range of flow and reaction regimes. These numerical simulations yielded new constitutive relations for the calculation of conductance as a function of pore throat volume and imposed flow and reaction conditions. These relations are implemented in new PNMs (nrtPNM) and results about porosity-permeability changes were compared against the existing PNMs.

In order to validate the reactive transport pore network model, we conducted two sets of flow-through experiments on two Ketton limestone samples. Acidic solutions (pH 3.0) were injected at two Darcy velocities i.e., $7.3 \times 10^{-4}$ and $1.5 \times 10^{-4}$ m s$^{-1}$ while performing X-ray micro-CT scanning. Experimental values of the changes in sample permeability were estimated in two independent ways: through PNM flow simulation and through Direct Numerical Simulation. Both approaches used images of the samples from the beginning and end of the experiments. Extracted pore networks, obtained from the micro-CT images of the sample from the beginning of the experiment, were used for reactive transport PNMs (rtPNM and nrtPNM).

We observed that for the experimental conditions, most of the pore throats maintained the initially prescribed cylindrical shape such that both rtPNM and nrtPNM showed a similar evolution of porosity and permeability. This was found to be in reasonable agreement with the observed porosity and permeability changes in the experiment. Next, for a range of flow and reaction regimes, we have performed a comparison of permeability evolution between rtPNM and nrtPNM. We found that for certain dissolution regimes, neglecting the evolution of the pore throat shape in the pore network can lead to an overestimation of up to 27% in the predicted permeability values and an overestimation of over 50% in the fitted exponent for the porosity-permeability relations. In summary, this study showed that at certain conditions, rtPNM is fine to be used, but at other conditions it will give an overestimation of the permeability evolution.

## 4.1    Introduction

Numerous applications require an understanding of fluid interactions with porous solid phases. Examples include optimization of the recovery from hydrocarbon reservoirs and prediction of the long-term consequences of $CO_2$ injection in subsurface. Calcite dissolution is an important reaction in subsurface reservoirs. Several studies have demonstrated that during calcite dissolution, a multitude of physical and chemical processes operate at the pore scale which govern the evolution of the porous medium. Such modification of the porous medium and the related porosity-permeability relations is a function of the initial heterogeneity of the rock and of the dissolution conditions i.e., the injection rate and chemistry of the injected fluid (e.g. Agrawal et al., 2020; Golfier et al., 2002; Hoefner and Fogler, 1988; Li et al., 2008; Luquot et al., 2014; Luquot and Gouze, 2009; Meile and Tuncay, 2006; Molins et al., 2014). One approach to comprehend the complexity of calcite dissolution process is through using pore-scale computational models such as pore network models (PNMs).

Several pore network formulations have been developed to present porous media topology and angular pore geometries (Acharya et al., 2005; Al-Gharbi and Blunt, 2005; Ghanbarian B., Hunt A. G., 2016; Raoof et al., 2013; Raoof and Hassanizadeh, 2012, 2009). Some studies have used pore throats with varying shapes, such as sinusoidal or other converging-diverging shapes (Acharya et al., 2005; Al-Gharbi and Blunt, 2005), for which analytical expressions can be applied to calculate pore conductance (Acharya et al., 2005; Ghanbarian B., Hunt A. G., 2016; Raoof and Hassanizadeh, 2012). Correct estimation of the hydraulic conductance values of the pores throats is required to obtain an accurate permeability for the sample.

In the context of calcite dissolution, the existing pore network models use a network of spherical pores bodies and cylindrical pore throats to simulate the related reactive transport processes (Mehmani et al., 2012; Nogues et al., 2013; Raoof et al., 2012). These pore network models provide porosity-permeability relations as a function of the specific dissolution condition, which is a key input for continuum scale models. An important consideration in the existing pore network models is related to the way conductance of the pore throat is updated during the calcite dissolution.

Most pore network models assume that pore throats, having initially a uniform circular cross section along their length, preserve their form throughout dissolution, irrespective of the flow and reaction regimes. Consequently, in response to dissolution, pore conductance values can be calculated using the Hagen-Poiseuille relation. However, it has been shown that initially uniform pore throat structures can develop into a spectrum of pore throat shapes with circular cross sections of variable diameter along their length depending on the flow and reaction regimes (e.g. Agrawal et.al., 2020). For example, under diffusion and reaction dominated dissolution regimes, the pore throat structure changes into a half-hyperboloid (~conical) shape. Under this condition, the Hagen-Poiseuille equation would result in an overestimation of pore throat conductance. Agrawal et al. (2020) showed that the conductance evolution in the pore network models should include information on pore throat shape evolution that takes the reaction regime into account. As mentioned earlier, some PNMs have been developed with originally non-uniform shapes of pore throats, however, no pore network-based study has incorporated the dissolution induced evolution of pore throat shapes.

In this study, we link the evolving shape of pore throats, under a wide range of conditions, to the resulting pore throat conductance values using reactive transport simulations. We implemented the constitutive relations for the evolution of conductance as a function of pore throat shape and volume (Agrawal et.al., 2020) in a pore network extracted from experimental micro-CT data, to simulate reactive transport across the rock sample in a modified PNM. The outcome was compared to the Hagen-Poiseuille PNM approach and to the permeability evolution determined experimentally experimental micro-CT. Finally, the impact of the new conductance evolution relationship on porosity-permeability relations was tested for a range of flow and reaction regimes.

## 4.2    Experimental Method

In this study, we used an oolitic limestone sample, Ketton Limestone, quarried from the Upper Lincolnshire Limestone Formation (village of Ketton in Rutland, England). Two plugs with a diameter of 6*mm* and an approximate length of 12*mm* were extracted from the homogeneous oolitic block. Hereafter, these samples are referred as K1 and K2. Two sets of reactive transport experiments were conducted on these samples. The injecting solution contained HCl acid with a pH value of 3.0, applied with two flow rates provided in Table 4.1. The environmental micro-CT (EMCT) scanner (Bultreys et al., 2016) at the Centre for X-ray Tomography (www.ugct.ugent.be) was used to image the progress of calcite dissolution with a reconstructed

voxel size of $6\mu m$. Each dynamic scan consisted of 2200 projections recorded in a total scan time of ~15 minutes. The sample was scanned at the beginning and at the end of the experiment. Data from raw projections were reconstructed into a 3D stack volume using the filtered back-projection method implemented in Octopus Software (Vlassenbroeck et al., 2007).

**Table 4.1: Parameters for both of the micro-CT experiments**

| Experiment | Porosity | Flow rate $(m^3\ s^{-1})$ | Darcy velocity $(m\ s^{-1})$ | pH of injected solution | Injection duration (Minutes) |
|---|---|---|---|---|---|
| E1-HQ | 0.18 | $2.05 \times 10^{-8}$ | $7.3 \times 10^{-4}$ | 3.0 | 102 |
| E2-LQ | 0.13 | $4.33 \times 10^{-9}$ | $1.5 \times 10^{-4}$ | 3.0 | 330 |

Next, 3D datasets were filtered using a non-local means filter and segmented with the watershed segmentation method (Avizo 9.5.0, Thermo Fischer Scientific). Table 4.1 provides the porosity values computed from the segmented image volumes of the sample from the beginning of the experiments. We observed that the computed porosity values in this study fall within the range of earlier reported segmentation images-based porosity values of Ketton rock (e.g., Table 3 in Menke et al., 2017) which differs from the measured true bulk porosity (e.g., Table 1 in Menke et al., 2017). This indicates that the segmentation contains the similar (unavoidable) difference from the measured bulk porosity values. For both experiments, the size of the segmented 3D volume was $1318 \times 1316 \times 2494$ voxels from which smaller sub-volumes were used in this study as discussed in Section 4.3.2.1.

## 4.3    NUMERICAL METHODS

We performed pore-scale modeling at three different levels: i) single pore scale (where we simulated reactive transport for an evolving pore space under different conditions, cf Agrawal et al. 2020), ii) pore network scale (where rock dissolution is simulated using PNM), and iii) Direct Numerical Simulations (DNS) using 3D imaged pore structures (where the detailed flow field is obtained by simulating incompressible flow in the rock images). The single pore-scale model provided insight on the evolution of the conductance of a pore throat for a range of physiochemical conditions and was previously validated against experimental microfluidic experiments (Agrawal et al., 2020). In the current work, we developed constitutive relationships for dissolution-induced conductance based on results from this systematic single pore model. The evolution of porosity and permeability observed in the pore network model was validated against a Direct Numerical Solution of flow across the sample. Next, for a range of flow and reaction regimes, pore network models were run with and without the new improved conductance relationships and the permeability results of both models were compared. Table 4.2 summarizes key details of various simulations used in this study.

**Table 4.2: Overview of the various simulations performed in this study. [1]following method of Aslannejad et al. (2018); [2]following method from Raoof et al. (2012).**

| Model | Label | Program | Obtains |
|---|---|---|---|
| **Single-pore, reactive transport** | | | |
| | - | COMSOL Multiphysics® | Relationship describing impact of pore shape evolution on conductance evolution |
| **3D pore space, flow only** | | | |

|  | DNS | OpenFOAM | Permeability changes from experimental images[1] |
|--|-----|----------|---------------------------------------------------|
|  | foPNM | PoreFlow | Permeability change from the pore network extracted from experimental images[2] |
| **3D pore space, reactive transport** | | | |
|  | rtPNM | PoreFlow | Simulation of porosity and permeability evolution[2] |
|  | nrtPNM | PoreFlow | Determine impact of pore shape evolution on simulated permeability evolution |

### 4.3.1  Single pore-scale model

Pore-scale reactive transport models utilizing a single capillary geometry were simulated by solving the Stokes equations for fluid flow and advection-diffusion-reaction equations for reactive transport of aqueous species (COMSOL Multiphysics®). Readers are referred to Agrawal et al. (2020) for details of the simulations and their validation against microscopic experiments of reactive transport in calcite crystals. The modeled range of boundary conditions (i.e., injection rate, composition of injecting solution, and pore throat geometry) correspond conditions relevant to injection of $CO_2$ or acidic solution into carbonate rocks. Details of the simulated flow regimes, reaction regimes and pore throat geometries are provided in Table A4.1.

To investigate the control of the reaction and flow regimes over the evolution of pore throat conductance, we calculated three dimensionless parameters, namely, the Péclet number, the Damköhler number, and the Geometry Factor at the beginning of each simulation. The Péclet number (Pe) was defined as:

$$Pe = \frac{vr}{D} \tag{4.1}$$

where, $v$ is the average velocity at the inlet boundary, $r$ is the radius of the pore throat (m) and D is the diffusion coefficient i.e., $3.36 \times 10^{-9}$ m$^2$ s$^{-1}$.

The Damköhler number (Da) was defined as:

$$Da = \frac{r\,k}{v * C_{Calcite}} \tag{4.2}$$

where, $C_{Calcite}$ is the density of surface sites of calcite i.e., $0.8 \times 10^{-5}$ mol m$^{-2}$ and $k$ (mol m$^{-2}$ s$^{-1}$) is obtained based on the forward rate constant in the kinetic rate law for calcite dissolution (i.e., the reaction rate constant $k_1$ in Equation 4.11 in Section 4.3.3.2) and the activity of H$^+$ ions (i.e., $aH^+$ in Equation 4.11 in Section 4.3.3.2) in the injected solution.

The Geometry Factor, $GF$, was defined as:

$$GF = \frac{l}{r} \tag{4.3}$$

where, $l$ is the length of the pore throat.

The conductance $g$ (m$^5$ N$^{-1}$ s$^{-1}$) of the pore throat was calculated from the imposed volumetric flux, F (m$^3$ s$^{-1}$), and the pressure drop across the pore throat, $\Delta P_{sp}$ (N m$^{-2}$), as:

$$F = g\Delta P_{sp} \tag{4.4}$$

In the case of a cylindrical pore throat geometry and laminar flow, Equation 4.4 is equivalent to the following definition of conductance, $g$:

$$g = \frac{\pi r^4}{8\mu l} \tag{4.5}$$

where, $\mu$ is the viscosity of water, 0.001 Pa s at about 25 °C.

Section 4.4.2 provides the modified relations for the calculation of the pore throat conductance for a range of flow and reaction regimes.

### 4.3.2   Pore Network Generation

### 4.3.2.1 Pore networks extracted from the digital rock volumes
A total of five pore networks were generated from the micro-CT images of Ketton using the maximal ball algorithm (Raeini et al., 2017). Two subsets of size 700 × 700×700 voxels, K1S1 and K1S2, were obtained from the digital volumes of the sample K1 at two different times i.e., t = 0 and t = 102 minutes. Similar sized subsets, K2S1 and K2S2, were extracted from the digital volumes of the sample K2 at the two experiment times i.e., t = 0 and t = 330 minutes, respectively. These subsets were utilized for the purpose of validation of the pore network model such that networks K1S1 and K2S1 were the starting pore networks for the reactive transport simulation. Note that the selected time duration for both experiments leads to injection of comparable pore volumes i.e., 2442 in the experiment E1-HQ and 1996 in the experiment E2-LQ.

Another subset of size 300 × 300 × 300 voxel, namely, K1S3, was extracted from the digital volume of the sample K1 at an experiment time step t = 0 minutes. This subset was utilized for the sensitivity study of the modified conductance model presented in Section 4.4.4.

The position of these subsets with reference to the full volumes of the Ketton sample is shown in Figure 4.1 and Figure A4.1. Figure 2.2 shows the frequency distribution of properties of the extracted pore networks such as pore body radius, pore throat radius, pore throat length and coordination number. Table 4.3 provides the statistics of each extracted pore network.

**Table 4.3: Statistics of all five pore networks extracted from the imaged rock samples. [1]Porosity of the extracted pore network; [2] Permeability from single phase flow simulation on the extracted pore networks.**

|  | K1S1 | K1S2 | K2S1 | K2S2 | K1S3 |
|---|---|---|---|---|---|
| Number of pore bodies | 2088 | 1787 | 2015 | 1960 | 184 |
| Number of pore throats | 3794 | 3108 | 3324 | 3293 | 316 |
| Mean coordination number | 3.63 | 3.48 | 3.30 | 3.36 | 3.43 |
| Mean pore body radius(m) | $48.38\times 10^{-6}$ | $53.55\times 10^{-6}$ | $46.51\times 10^{-6}$ | $48.67\times 10^{-6}$ | $48.22\times 10^{-6}$ |
| Mean pore throat radius(m) | $26.23\times 10^{-6}$ | $31.22\times 10^{-6}$ | $24.80\times 10^{-6}$ | $26.52\times 10^{-6}$ | $25.94\times 10^{-6}$ |
| Mean pore throat length(m) | $112.41\times 10^{-6}$ | $118.40\times 10^{-6}$ | $107.29\times 10^{-6}$ | $110.14\times 10^{-6}$ | $117.78\times 10^{-6}$ |
| [1]Porosity | 0.15 | 0.16 | 0.12 | 0.13 | 0.19 |

| $^2$Permeability $(k_{foPNM})$ (mD) | 2809.6 | 6511.6 | 1226.1 | 2865.5 | 5515.6 |
|---|---|---|---|---|---|
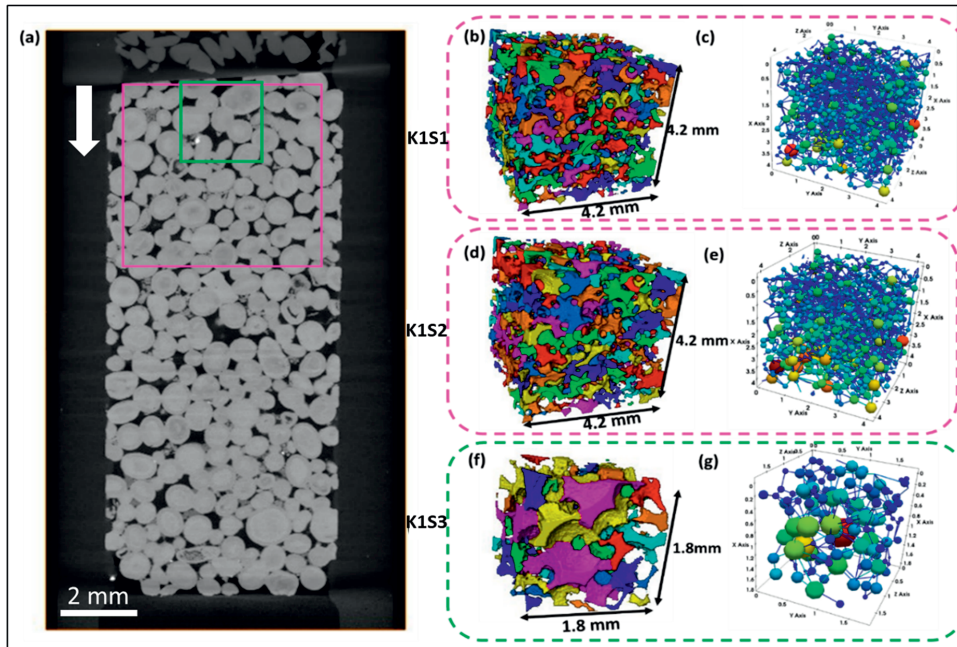


**Figure 4.1: pore structures and sub volumes.** (a) a vertical slice obtained using the micro-CT volume of the sample K1 showing the position and sizes of the extracted sub-volumes K1S1 (t =0), K1S2 (t = 102 min) (magenta color lines) and K1S3 (t =0) (green color line). The white arrow shows the flow direction (image is rotated 180° compared to experimental position, where flow was upward). Panels (b), (d) and (f) indicate the digital subsets, K1S1, K1S2 and K1S3, respectively. Panels (c), (e) and (g) are the extracted pore networks from the corresponding sub-volumes.
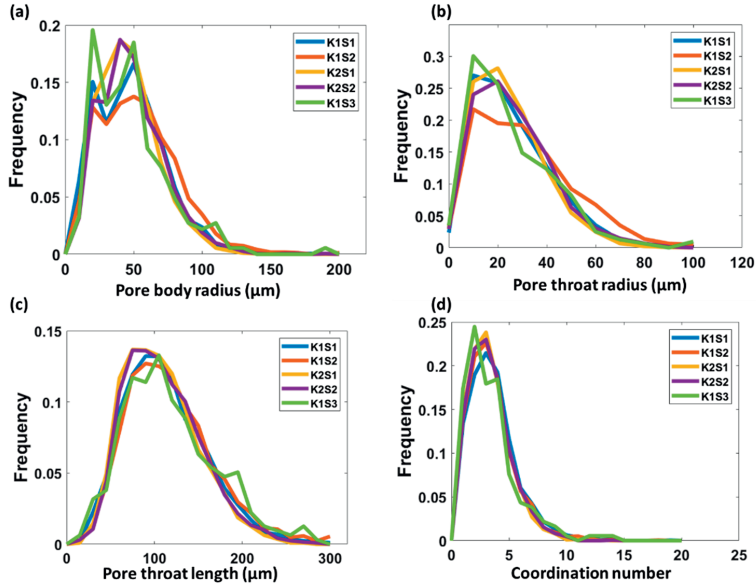
**Figure 4.2: pore sizes**. Pore size distribution for (a) pore body radius (b) pore throat radius, and (c) pore throat length. (d) the distribution of pore coordination numbers.

### 4.3.3 Pore Network Model

The pore network model utilized in this study is an adaptation of the previously developed pore-scale model by Raoof et al. (2012). Here, this model is discussed briefly:

**4.3.3.1 Flow and Solute transport**

For this study, single phase flow was established across the pore network. This was achieved by assuming laminar flow along each pore throat of the network (i.e., Reynolds number is less than 1). Flux through a pore throat was described by the Hagen-Poiseuille equation as:

$$q_{ij} = g_{ij}(p_j - p_i) \qquad (4.6)$$

where $q_{ij}$ is total volumetric flux through the pore throat $ij$, $g_{ij}$ is the conductance of the pore throat $ij$, and $p_i$ and $p_j$ are the pressures in pore bodies i and j, respectively. The simulated pore network models in this study utilized the Hagen-Poiseuille relation (i.e., Equation 4.5) and modified conductance relations (i.e., Equations 4.18) for calculation of the pore throat conductance.

For incompressible, saturated flow conditions, the sum of fluxes of all pore throats connected to a pore body was equated to zero. This implies that the amount of flux going to a pore body should be equal to the amount of flux coming out of that pore body:

$$\sum_{j=1}^{N_k} q_{ij} = 0; \; j = 1,2, \dots N_k \qquad (4.7)$$

here $N_k$ is the coordination number of pore body $k$.

Equation 4.7 is valid for all pore bodies of the network except those present at the inlet and outlet face of the network. Combination of Equations 4.6 and 4.7 resulted in a linear system of

equations, to be solved for the pressure of the pore bodies and the volumetric flux through the pore throats. We have used a constant Darcy velocity boundary condition at the inlet face, a constant pressure (i.e., atmospheric pressure) boundary condition at the outlet face, and no-slip boundary conditions was applied at the lateral faces of the network.

From the imposed Darcy velocity ($u_D$) and pressure difference between the inlet and outlet faces ($\Delta P_{PNM}$), the absolute permeability of the pore network is calculated from:

$$k_{PNM} = \frac{\mu \, u_D \, L}{\Delta P_{PNM}} \tag{4.8}$$

where, $L$ is the length of the pore network along the flow direction.

All the chemical components are transported through the pore network by advection and diffusion processes. For a given pore body $i$ and for the flow conditions under which fluid flowing from pore body $j$ towards pore body $i$, through pore throat $ij$, we can define the transport of the $k^{th}$ chemical component as:

$$V_i \frac{d}{dt}(c_{k,i}) = \sum_{j=1}^{N_{in}^{throat}} q_{ij} c_{k,ij} - Q_i c_{k,i} + \sum_{j=1}^{z_i} D A_{ij} \frac{(c_{k,ij} - c_{k,i})}{l_{ij}} - R_{k,i} \tag{4.9}$$

where, $V_i$ , $Q_i$ and $c_{k,i}$ are the volume, volumetric flow rate and concentration of $k^{th}$ component in pore body $i$, respectively. The left-hand side (L.H.S) of the Equation 4.9 calculates the rate at which the concentration of the $k^{th}$ component should be updated in the pore body $i$. This rate is a combined output of the advective, diffusive and reactive rates. The first term on the right hand side (R.H.S) of the Equation 4.9 calculates the total amount of the incoming flux of each component through $N_{in}^{throat}$ upstream pore throats. This calculation utilizes the volumetric flow rate ($q_{ij}$) and concentration ($c_{k,ij}$) in pore throat $ij$. The second term on the R.H.S calculates the total outflux of the $k^{th}$ component. The third term on the R.H.S calculates the diffusion rate of the $k^{th}$ component through $z_i$ connected pore throats. This calculation utilizes the molecular diffusion coefficient ($D$) and the cross-sectional area of the throat ($A_{ij}$). The last R.H.S term, $R_{k,i}$, defines changes due to chemical reactions of the $k^{th}$ component taking place inside the pore body.

Similarly, the mass balance equation for pore throat $ij$ and for the case when the fluid is flowing from pore body $j$ to pore throat $ij$, can be written as:

$$V_{ij} \frac{d}{dt}(c_{k,ij}) = q_{ij} c_{k,j} - q_{ij} c_{ij} + D A_{ij} \frac{(c_{k,j} - c_{k,ij})}{l_{ij}} + D A_{ij} \frac{(c_{k,i} - c_{k,ij})}{l_{ij}} - R_{k,ij} \tag{4.10}$$

where $V_{ij}$ , $q_{ij}$ and $c_{k,ij}$ are the volume, volumetric flow rate and concentration of $k^{th}$ component in pore throat $ij$, respectively. $R_{k,ij}$ provides feedback from reactions of the $k^{th}$ component taking place inside the pore throat.

### 4.3.3.2 Reactions and rate laws
To describe the calcite dissolution system, we have incorporated a total of four reactions. Out of those four reactions, three reactions involving only aqueous species are described using equilibrium relationships, whereas the dissolution of calcite is described by a kinetic rate law. Details of equilibrium reactions are provided in Table 4.4.

Plummer et. al. (1978) has identified three main mechanisms through which calcite dissolution takes place. Accordingly, we have defined the calcite dissolution rate as:

$$Rate = A\left(k_1 a_{H^+} + k_2 a_{H_2CO_3^*} + k_3\right)\left(1 - \frac{a_{Ca^{2+}} a_{CO_3^{2-}}}{K_{eq}}\right) \tag{4.11}$$

where, A is the reactive surface area of calcite and $a_i$ is the activity of species $i$. $k_1 = 8.64 \times 10^{-5}$ (m s$^{-1}$), $k_2 = 4.78 \times 10^{-7}$ (m s$^{-1}$) and $k_3 = 2.34 \times 10^{-9}$ (m s$^{-1}$) are reaction rate constants at 25°C (Plummer and Busenberg, 1982). $K_{eq} = 10^{-8.48}$ is the equilibrium constant for calcite dissolution (Plummer and Busenberg, 1982).

**Table 4.4: Equilibrium rate laws of $CO_2$-$H_2O$ system and respective equilibrium constants**

| Reactions | Equilibrium rate constant from Plummer and Busenberg, 1982 |
|---|---|
| $CO_2(aq) = H^+ + HCO_3^-$ | [a]$4.5 \times 10^{-7}$ |
| $HCO_3^- = H^+ + CO_3^{2-}$ | [a]$4.78 \times 10^{-11}$ |
| $H_2O = H^+ + OH^-$ | $1 \times 10^{-14}$ |

### 4.3.3.3 Modeling parameters

We have utilized two sets of flow and chemical conditions for pore network modeling. The first set is derived from the experimental parameters (Table 4.1) and the second set covers the range of reaction and flow regimes which are relevant to acid stimulation experiments in carbonate reservoirs.

In the experiments, we injected the solutions at a fixed flow rate. Table 4.5 provides the magnitude of the calculated Darcy velocity for the experiments E1-HQ and E2-LQ. Models corresponding to these experiments utilized the respective value of the Darcy velocity for injecting a solution with the pH value of 3.0. Additional sets of utilized Darcy velocities and pH of the injected solutions are provided in Table 4.5. Lower pH values of the injected acid are relevant to acid stimulation applications in carbonate reservoirs (Janbumrung and Trisarn, 2017). The composition of these solutions was calculated using PhreeqC (Parkhurst and Appelo, 2013) and phreeqc.dat database (Table A4.2).

**Table 4.5: Statistics related to the simulated pore networks**

| Sample | Experiment | Darcy Velocity (m s$^{-1}$) | pH of injecting solution | Simulation Duration (Minutes) | Injected Pore Volumes | $\widetilde{Pe}$ | $\widetilde{Da_I}$ | $\widetilde{Da_{II}}$ |
|---|---|---|---|---|---|---|---|---|
| K1S1 | E1-HQ | $7.3 \times 10^{-4}$ | 3.0 | 35.5 | 2442 | 974 | $5.82 \times 10^4$ | $5.98 \times 10^1$ |
| K2S1 | E2-LQ | $1.5 \times 10^{-4}$ | 3.0 | 115 | 1996 | 192 | $5.82 \times 10^4$ | $3.03 \times 10^2$ |
| K1S3 | | $1.5 \times 10^{-4}$ | 1.0 | 100 | 56 | 1.70 | $1.04 \times 10^6$ | $6.13 \times 10^5$ |
| K1S3 | | $8.3 \times 10^{-5}$ | 1.0 | 20 | 56 | 8.50 | $1.04 \times 10^6$ | $1.23 \times 10^5$ |
| K1S3 | | $15 \times 10^{-4}$ | 1.0 | 10 | 56 | 17.00 | $1.04 \times 10^6$ | $6.13 \times 10^4$ |
| K1S3 | | $30 \times 10^{-4}$ | 1.0 | 5 | 56 | 34.00 | $1.04 \times 10^6$ | $3.07 \times 10^4$ |
| K1S3 | | $75 \times 10^{-4}$ | 1.0 | 2 | 56 | 85.00 | $1.04 \times 10^6$ | $1.23 \times 10^4$ |
| K1S3 | | $1.5 \times 10^{-4}$ | 3.0 | 3000 | 1670 | 1.70 | $1.07 \times 10^4$ | $6.30 \times 10^3$ |
| K1S3 | | $8.3 \times 10^{-5}$ | 3.0 | 600 | 1670 | 8.50 | $1.07 \times 10^4$ | $1.26 \times 10^3$ |
| K1S3 | | $15 \times 10^{-4}$ | 3.0 | 300 | 1670 | 17.00 | $1.07 \times 10^4$ | $6.30 \times 10^2$ |
| K1S3 | | $30 \times 10^{-4}$ | 3.0 | 150 | 1670 | 34.00 | $1.07 \times 10^4$ | $3.15 \times 10^2$ |

| K1S3 | $75 \times 10^{-4}$ | 3.0 | 60 | 1670 | 85.00 | $1.07 \times 10^{4}$ | $1.26 \times 10^{2}$ |
|------|------|-----|------|------|-------|------|------|
| K1S3 | $1.5 \times 10^{-4}$ | 5.0 | 3000 | 1670 | 1.70 | $3.87 \times 10^{2}$ | $2.28 \times 10^{2}$ |
| K1S3 | $8.3 \times 10^{-5}$ | 5.0 | 600 | 1670 | 8.50 | $3.87 \times 10^{2}$ | $4.56 \times 10^{1}$ |
| K1S3 | $15 \times 10^{-4}$ | 5.0 | 300 | 1670 | 17.00 | $3.87 \times 10^{2}$ | $2.28 \times 10^{1}$ |
| K1S3 | $30 \times 10^{-4}$ | 5.0 | 150 | 1670 | 34.00 | $3.87 \times 10^{2}$ | $1.14 \times 10^{1}$ |
| K1S3 | $75 \times 10^{-4}$ | 5.0 | 60 | 1670 | 85.00 | $3.87 \times 10^{2}$ | 4.56 |

In order to categorize the simulated flow and reaction regimes, we have defined the macroscopic Peclet number ($\widetilde{Pe}$) and Damköhler numbers ($\widetilde{Da_I}$ and $\widetilde{Da_{II}}$) as:

$$\widetilde{Pe} = \frac{u_D\,L}{D} \tag{4.12}$$

$$\widetilde{Da_I} = \frac{L^2\,k_1\,a_{H^+}}{D\,C_{Calcite}} \tag{4.13}$$

$$\widetilde{Da_{II}} = \frac{L\,k_1\,a_{H^+}}{U_D\,C_{Calcite}} \tag{4.14}$$

where, $u_D$ is the Darcy velocity (m s$^{-1}$) and $L$ is the length of the pore network along the flow direction. Table 4.5 provides $\widetilde{Pe}$, $\widetilde{Da_I}$ and $\widetilde{Da_{II}}$ numbers for all the simulated models.

### 4.3.4 Direct flow simulation of pore-scale images

In order to compare the permeability values obtained from PNM results, we have performed pore-scale flow DNS. We have used the Volume of Fluid (VOF) method implemented in OpenFOAM Computational Fluid Dynamic (CFD) package to solve incompressible flow using a semi-implicit method for pressure (Aslannejad et al., 2018; Bedram and Moosavi, 2011).

Numerical three-dimensional simulation of incompressible linear-viscous flow was done by solving the Navier-Stokes equations:

$$\rho\left(\frac{\partial u}{\partial t} + u.\nabla u\right) = -\nabla p + \mu\nabla^2 u \tag{4.15}$$

$$\nabla.u = 0 \tag{4.16}$$

where, $p$ is pressure, $u$ is velocity, $\mu$ is the viscosity of water ($\mu = 0.001$ Pa.s) and $\rho$ is the density of water ($\rho = 1000$ kg m$^{-3}$).

The flow equations are solved by applying a constant pressure difference between inlet and outlet faces ($\Delta P_I$) and no-slip boundary condition on the remaining faces. This yielded the velocity and pressure for each voxel in the domain. The flow rate, $Q$ (m$^3$ s$^{-1}$) was calculated as $Q = \int u_x\,A_x$, where $A_x$ (m$^2$) is the cross-sectional area of the inlet face perpendicular to the direction of flow $x$ and $u_x$ is the inlet face velocity component in the direction of flow. From the flow rate ($Q$) and the imposed pressure difference ($\Delta P_{DNS}$), absolute permeability of the 3D XMT image, $k_{DNS}$ (m$^2$) is calculated using Darcy equation:

$$k_{DNS} = \frac{\mu \, Q \, L_x}{\Delta P_{DNS} \, L_y \, L_z} \tag{4.17}$$

where, $L_x$, $L_y$ and $L_z$ are the domain lengths in each direction.

## 4.4     Results and Discussions

Section 4.4.1 presents comparison of the pore network models against observations from micro-CT experiments. Next, using simulation results on a single-pore model, we derived constitutive relationships for the conductance of pore throats in Section 4.4.2. These relationships were implemented in the new PNM (nrtPNM). Section 4.4.3 provides comparison of permeability evolution from nrtPNM *versus* rtPNM for the experimental conditions. Section 4.4.4 extends this comparison for a range of transport and reaction regimes. In Section 4.4.5 we present the impact of flow and reaction conditions over the porosity-permeability relations obtained from nrtPNM *versus* rtPNM.

### 4.4.1 Validation of the reactive transport pore network model (rtPNM) with the micro-CT experiments

Two rock pore networks i.e., K1S1 and K2S1 were simulated with similar initial and boundary conditions to the experiments E1-HQ and E2-LQ, respectively. At time t =0, samples were filled with a fluid solution equilibrated with calcite. In the experiment E1-HQ, injection of a solution with a pH value of 3.0 initiated calcite dissolution which shows itself as a decreasing amount of calcite in Figure 4.3e. Figure 4.3a-d shows the corresponding time-based evolution of the average chemical species concentrations. The pH of the solution inside the sample decreased continuously as a larger number of pores were penetrated by the acidic solution (Figure 4.3a-d). The acid penetration time for each pore throat depends on its distance from the inlet boundary and its connectivity with the dominant flow channels. The inlet area of the sample reaches a steady state in shorter times compared to the outlet area (Figure A4.2). Moreover, the steady state pH of the inlet area is lower than the outlet area (Figure A4.2). This indicates that within the simulation time, a significant number of pore throats in the outlet area were not yet filled with the inflow solution. From the distribution of pH of the solution inside the sample, after injection of around 2442 pore volumes, we observed that more than 40% of pore throats were filled with the inflow solution pH value of 3.0, while ~ 1% pore throats retained the calcite equilibrated solution (Figure A4.3a). Compared to experiment E1-HQ, the lower injection rate in experiment E2-LQ further delayed the attainment of steady state for different part of the sample (Figure A4.4). Consequently, after around 1996 pore volumes of acid injection in the experiment E2-LQ, a significant fraction of pore throats was filled with solutions having pH values larger than 7 (Figure A4.3b).

Figure 4.4 compares the evolution of porosity and permeability in the reactive transport model (rtPNM) against the experimental porosity and permeability data, obtained from the time-lapse micro-CT images. Experimental data of changes in porosity were calculated from the porosities of the extracted pore networks that were derived from the digital images of the sample belonging to the start and end of the experiment (Table 4.3). The model showed a smaller amount of dissolved calcite compared to the measured values from the experiment (Figure 4.4a). One of the probable reasons could be the deviation of applied rates implemented in models from rate values generated in the experiments. Such deviation can cause, for example, slower penetration rate of the acid in the pore network model than in the experiment. For the model related to the experiment E1-HQ, 2442 pore volumes of acid injection were not sufficient to attain a complete steady state pH in the system (Figure 4.3e).

For both experiments, we observed a fairly good agreement between the permeability evolution in the reactive transport model ($k_{rtPNM}$) and in the dissolution experiments ($k_{foPNM}$ and $k_{DNS}$) (Figure 4.4b). Additionally, we observed that for the experiment E2-LQ, $k_{foPNM}$ agrees well with $k_{DNS}$, while for the experiment E1-HQ, the two values differ significantly (Figure 4.4b). The difference between permeabilities obtained through foPNM and DNS is likely due to the simplification of the pore-scale geometrical features during extraction of pore network (de Boever et al., 2016).
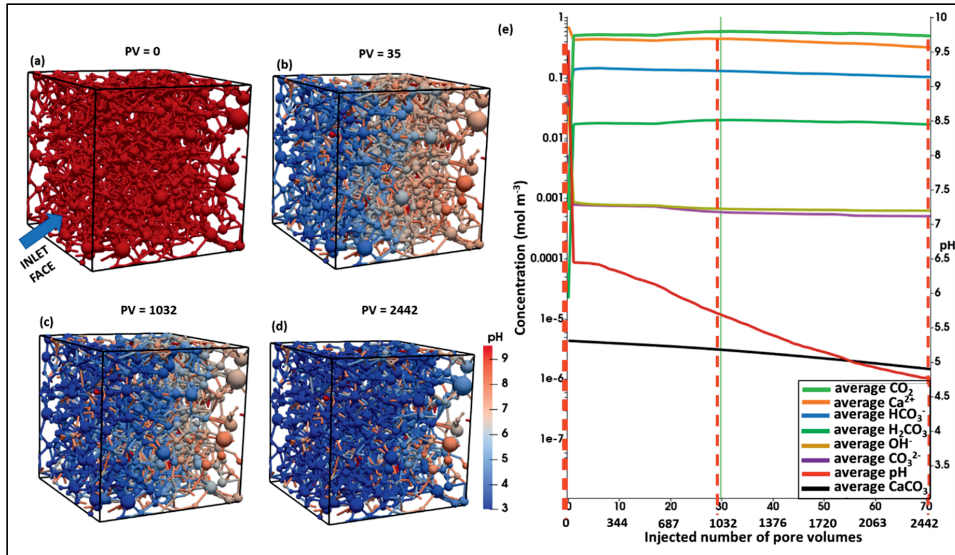


**Figure 4.3: concertation fields.** (a-d) show 3D distribution of pH within the reactive transport pore network model (rtPNM) corresponding to the experiment E1-HQ at times corresponding to pore volumes of (a) 0, (b) 35, (c) 1032, and (d) 2442. (e) evolution of the concentration of aqueous species with the injected number of pore volumes. Note: to obtain the 1D time plot, the 3D concentration fields are averaged within the entire sample at different times.
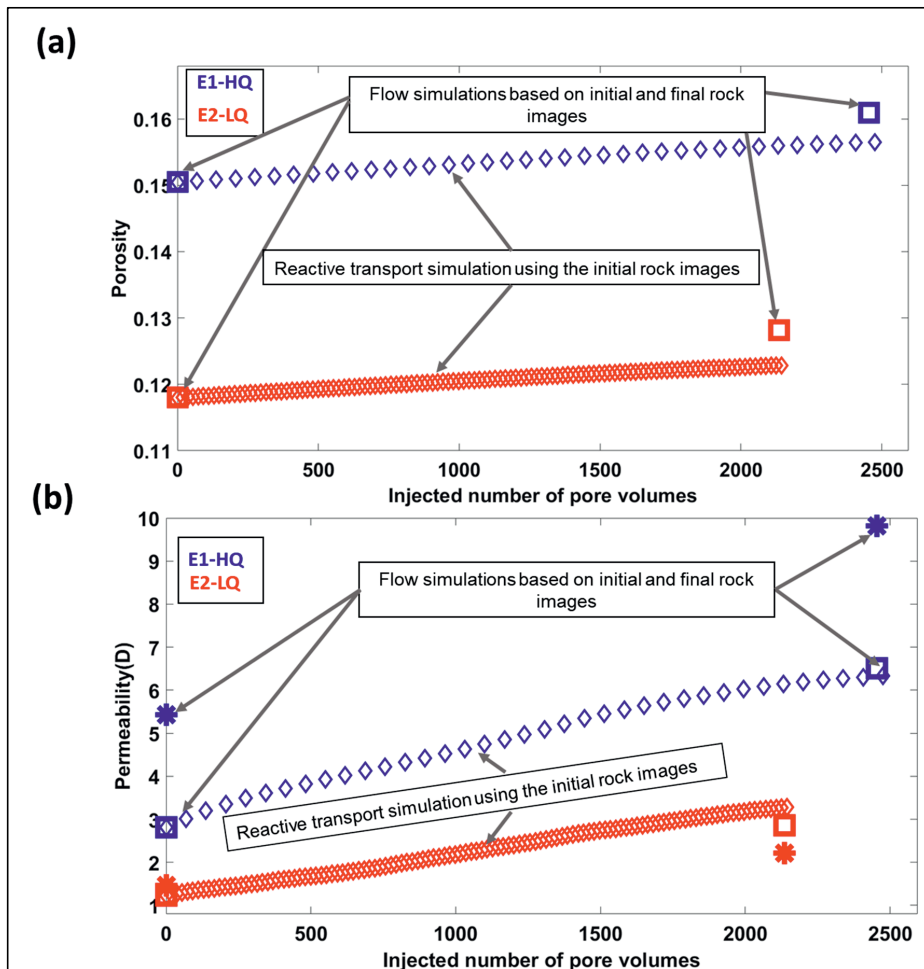
**Figure 4.4:** (a) Porosity evolution and (b) permeability evolution against the injected pore volumes for experiments E1-HQ (high flow rate) and E2-LQ (low flow rate). Diamond markers correspond to rtPNM which use the initial sample pore structure as their initial condition and perform reactive transport to calculate and predict evolution of samples over time. Asterisks and squares show results of flow only simulations performed on the 3D image of the sample from the beginning and end of the experiments: asterisks show results from DNS and squares show results from foPNM simulations.

### 4.4.2 Derivation of the constitutive relations for calculation of pore throat conductance

Agrawal et.al. (2020) have shown that the imposed flow and reaction regimes determine the evolution of the pore throat shape and subsequent evolution of conductance during calcite dissolution. Figure 4.5 and Figure A4.5 present the dependency of the conductance of a pore throat on the volume of that pore throat for the simulated flow and reaction regimes while the length and initial radius of the pore throat are fixed at a value of $500 \times 10^{-6}$ and $40 \times 10^{-6}$ m, respectively.
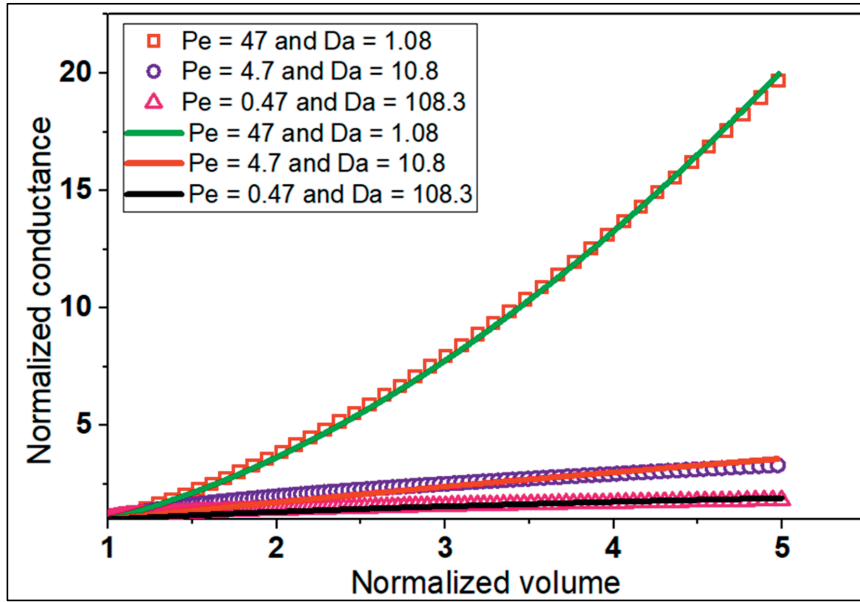
**Figure 4.5:** pore conductance relations. Normalized values of pore throat conductance as a function of normalized volume of pore throat for some of the simulated flow and reaction regimes (pore throat length and initial radius are fixed at $500.0 \times 10^{-6}$ m and $40.0 \times 10^{-6}$ m, respectively). For each dataset, markers represent the data points and the solid lines represent the fitted curves (Equation 4.18).

We observe that, at any time during calcite dissolution, the updated pore conductance can be related to the modified volume of the pore throat using an exponent, b:

$$\frac{g_t}{g_o} = \left(\frac{V_t}{V_o}\right)^b \tag{4.18}$$

where $g_t$ and $g_o$ are the conductance of the pore throat, calculated from Equation 4.4, $g_o$ at time t=0s and $g_t$ at time t during the course of the dissolution; similarly, $V_t$ and $V_o$ are the volume of pore throat at time t=0s and at time t. Exponent **b** represents the distinctiveness and topology of the evolved pore shape. Since the evolution of the pore throat shape is guided by a number of parameters such as initial geometry of the pore throat and imposed flow and reaction regimes, b is a function of these parameters (Figure 4.6a).

Figure 4.6a shows that under advection dominated regimes, indicated by Pe>1, and reaction-controlled regimes, indicated by Da<1, the b coefficient approaches a value of 2.0. Under these regimes, the shape of the pore throat remains cylindrical throughout the dissolution period (Agrawal et al., 2020; Figure 4.7a). Under this condition (i.e., b=2.0), our relation (Equation 4.14) becomes equal to the Hagen Poiseuille relation (Equation 4.5). For diffusion dominated regimes, when Pe<1, and reaction dominated regimes, when Da>1, the cylindrical shape evolves into half-hyperboloid shapes (Agrawal et al., 2020; Figure 4.7b). For these cases, the value of b becomes smaller than 2.0 and the accurate pore conductance can be calculated from Equation 4.14. It should be noted that here, shape evolution implies that the profile of the shape along the flow path changes from cylinder to half-hyperboloid longitudinal while cross-section of the pore throat, i.e. perpendicular to the flow path, remains circular.
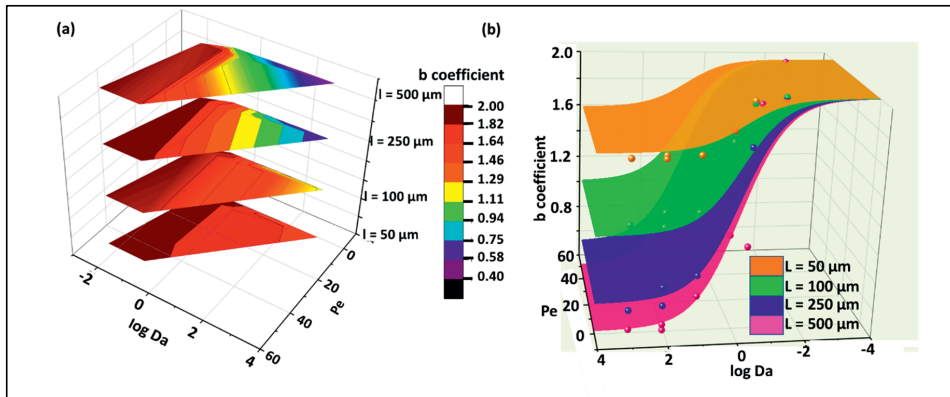
**Figure 4.6: pore conductance parameters.** (a) Dependency of the *b* coefficient (using the color legend) on the strength of reaction and flow regime (the horizontal axes) and pore throat lengths (shows a segregated color. i.e., each surface corresponds to a certain pore throat length). Higher values of *b* coefficient correspond to higher *Pe* numbers and lower *Da* numbers. Pore throat length of value of $500.0 \times 10^{-6}$ m shows a higher range for the *b* coefficient compared to a smaller pore throat length with a value of $250.0 \times 10^{-6}$ m. (b) the fitted curved surface together with the data points used to obtain the best fit (SI Section A4.1; Table A4.1)
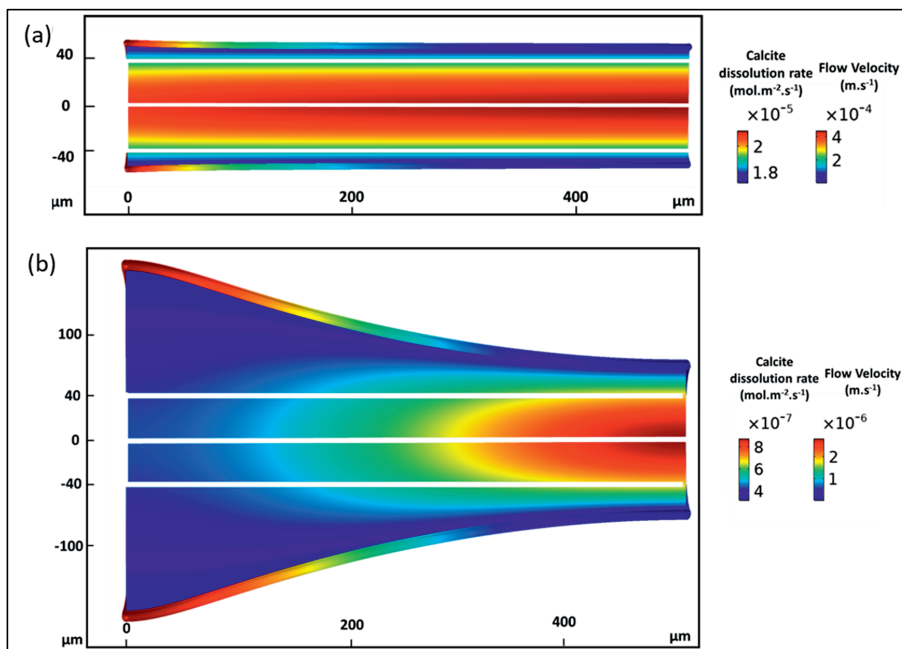


**Figure 4.7:** pore shape evolution. The key simulation results from Agrawal et.al., 2020, showing the evolved pore shape and the distribution of the velocity field and the reaction rates for two different flow regimes of (a) ***Pe***=4.74 and (b) ***Pe***=0.05. The injection period was 15900 pore volumes for both cases using a pH value of 3.9 and a $pCO_2$ value of 1.0 bar. White lines indicate the initial pore shape, and, therefore, the coloured regions outside of these white lines

indicate the dissolved zones during the reaction. The outer-coloured rim, located at the pore wall, shows the local calcite dissolution rate.

The relation for coefficient b can be expressed as:

$$b = A_1 + \frac{2 - A_1}{1 + \frac{Da^{p_3}}{Pe^{p_4}}} \tag{4.19}$$

$$A_1 = p_1 * GF^{-p_2} \tag{4.20}$$

Values of fitting parameters ($p_1$, $p_2$, $p_3$ and $p_4$) were obtained using nonlinear least squares method (SI Section A4.1, Figure A4.6a). We have obtained a R-square value of 0.94 indicating that the fitted relationship and its parameters are able to describe data points (Figure A4.6b). Figure 4.6b shows the 3D plot of the fitted relation and the corresponding data points. In general, for reaction regimes corresponding to Da> 1 and Da<1, the fitted relationship captures the dependency of b over Pe number, Da number and GF (Figure A4.6b). Figure A4.7 shows the sensitivity of the derived model over the testing data set. For most of the test data points, the % difference in the value of b calculated from the fitted model vs that obtained from numerical simulation is within 10% (Figure A4.7b). This assures the predictive capacity of the proposed model.

Next, along with Hagen Poiseuille's relation, we have used our developed relation to perform pore network model simulations. Hereafter, these two pore network models will be referred as rtPNM and nrtPNM (i.e., new model). In nrtPNM, at each time step of the simulation, using the updated Pe number, Da number, and GF, the b value was calculated for each pore throat of the pore network. Subsequently, for each pore throat of the pore network, the modification in conductance was calculated. In Sections 4.4.3 and 4.4.4, we compare the impact of these two pore network modeling approaches on the evolution of the permeability of the sample.

### 4.4.3   nrtPNM under flow and reaction regimes of micro-CT experiments

For the experiment E1-HQ, diffusion dominated pore throats are highlighted in red in Figure A4.8a after injection of around 2442 pore volumes. These pore throats either have Pe<0.0001 (i.e., diffusion is practically the only transport mechanism) or 0.0001<Pe<1 (i.e., both diffusion and low velocity convection are controlling the transport). Part of the diffusion dominated pore throats, mostly pore throats with Pe<0.0001, have a Da number greater than 1 (highlighted in green color in Figure A4.8b). These pore throats will transform into non-uniform pore shapes, and a value of b smaller than 2.0 is obtained for the calculation of conductance using Equation 4.14 (highlighted in yellow color in Figure A4.8c). In the experiment E1-HQ, the fraction of such diffusion dominated, and reaction dominated pore throats is ~8%, whereas in the experiment E2-LQ, this fraction is ~11% (Figure A4.8d-Figure A4.8f).

We observed that both rtPNM and nrtPNM provide porosity and permeability evolutions that are so similar that the results would overlap in Figure A4.9. This is because the flow conditions for both experiments, which were selected to trigger visible porosity changes within the time frame of the micro-CT experiments, lead predominantly to advection dominated regimes as indicated by large $\widetilde{Pe}$ numbers (Table 4.5). Therefore, under these flow conditions, 89-92% pore throats keep their cylindrical shape during dissolution and nrtPNM agrees equally well as rtPNM with the experimentally determined porosities and permeabilities.

### 4.4.4   nrtPNM under different flow and reaction regimes

This section explores the influence of the injection velocity and pH value of the injected solution over the calcite dissolution processes and subsequent evolution of the petrophysical properties of the sample. Calcite dissolution is a combination of three processes: i) transport of the reactants towards the calcite surface, ii) interaction of reactants with the calcite surface and iii) removal of the products away from the calcite surface. The fluid velocity inside the pore throat determines the transport rate for the first and the last steps. The pH of the solution controls the rate of the second step. Calcite dissolution rate is observed to increases when a solution with a lower pH value is injected or the injection rates are increased. Figure 4.8 shows the impact of changing the injection rate, resulting in a different $\widetilde{Pe}$ number, on the evolution of porosity while the pH of the injected solution is fixed at a value of 1.0. For the injection of the same number of pore volumes, lowering of the acid injection rates leads to dissolution of a higher amount of calcite (Figure 4.8) as it increases the residence time of acid within the sample. Comparing results from nrtPNM and rtPNM, we observed similarity in the porosity evolution but dissimilarity in the permeability evolution (Figure 4.8). Figure A4.10 and Figure A4. 11 provide the evolution of porosity and permeability for remaining simulated cases.

Differences in the evolution of permeability in these models are proportional to the number of pore throats transforming into non-uniform shapes during dissolution. As mentioned earlier, these sets of pore throats belong to a diffusion dominated transport regime and a reaction dominated dissolution regime. For each of the simulated boundary conditions, we have identified the fraction of pore throats which fulfils this criterion (Table A4.3, Figure A4. 12). For example, for a simulated network S5, injection of a solution with pH of 1.0 and a Darcy velocity of $3.17 \times 10^{-6}$ m s$^{-1}$ results into development of a non-uniform shape for around 60% of pore throats (Figure 4.8: $\widetilde{Pe} = 1.70$ and $\widetilde{Da_{II}} = 6.13 \times 10^5$). Consequently, for this case, we observed that rtPNM overestimates the permeability by around 27% as compared to nrtPNM. For all simulated boundary conditions, Figure 4.9 summarizes the % difference in the predicted value of permeability from these two models. This shows that, for flow and reaction regimes corresponding to $\widetilde{Da_{II}}$ greater than 100, the two pore network models start to deviate and for $\widetilde{Da_{II}}$ greater than $10^3$, significant differences evolve the permeability prediction of the sample.
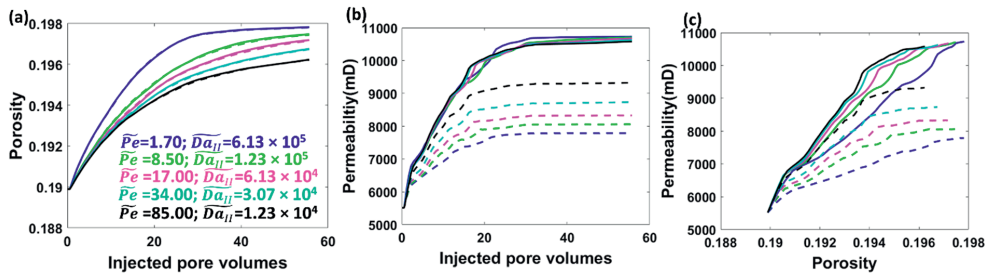


**Figure 4.8: Evolution of porosity and permeability.** (a) Porosity vs injected pore volumes (b) Permeability vs injected pore volumes and (c) Permeability vs Porosity, from rtPNM (solid lines) and nrtPNM (dotted lines). The inflow solution had a pH value of 1.0 and was injected using five different Darcy velocities. Note that the legend provided in panel (a), is color coordinated with the plotted line colors and applicable for panels (b) and (c), as well.
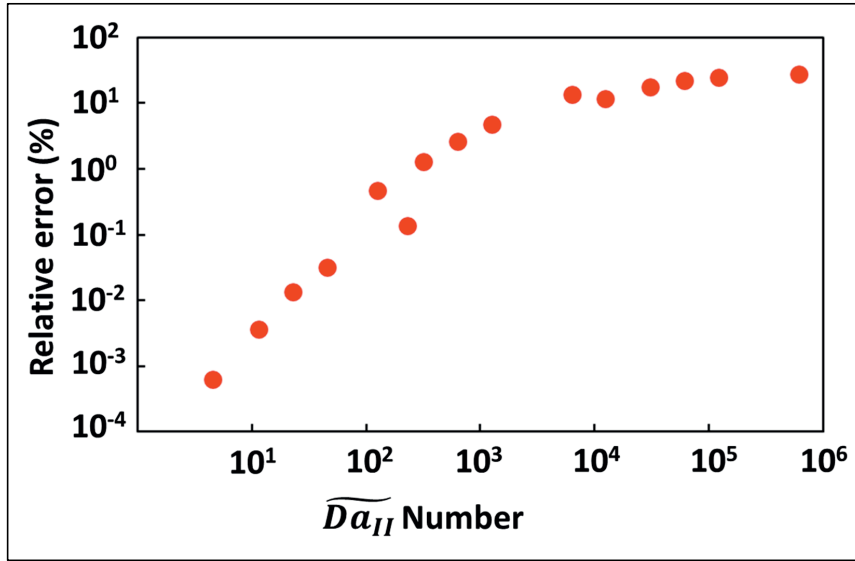
**Figure 4.9: the obtained accuracy.** Relative percentage difference in the final permeability value of the sample simulated using the new conductance relation, nrtPNM, and the Hagen Poiseuille relation, rtPNM, under different $\widetilde{Da_{II}}$ numbers.

### 4.4.5 Implications for porosity-permeability relationship used at the field scale

Many continuum-scale models use a power law relation to determine the evolution of permeability from the changes in porosity (e.g. Hommel et al., 2018):

$$k_t = k_o \left( \frac{\emptyset_t}{\emptyset_o} \right)^{\alpha} \tag{4.21}$$

where $k_o$ and $\emptyset_o$ are the initial permeability and porosity of a sample. The fitting parameter, $\alpha$, depends on the initial properties of the rock and on the processes controlling the changes in the pore geometry (e.g. Parvan et al., 2020). The $\alpha$ value can either be obtained through theoretical derivation or through fitting of experiments and models. In this study, we observed that for a very similar rock sample, $\alpha$ is a function of the injection parameters such as Darcy velocity and acidity of the injected solution (Figure 4.10) (see also Nogues et al., 2013). Moreover, we observed a temporal variation in $\alpha$ which indicates different phases of dissolution (Figure 4.10).

Figure 4.10 shows $\alpha$ as a function of the porosity of our samples for a set of simulations. First, for some of the injection conditions, rtPNM provided larger $\alpha$ values, by a factor of over 50%, as compared to the nrtPNM (Figure 4.10: $\widetilde{Pe}$=1.70 and $\widetilde{Da_{II}}$ = 6.13×10⁵).

The initially large $\alpha$ value suggests that the first target of the acid reactions are the highly conductive paths where a small increment in the porosity results in large increment in permeability (Bernabé et al., 2003; Nogues et al., 2013). We observed that the increment in the injection velocity or in the pH of the injected solution leads to a consistent increase of $\alpha$ (Figure 4.10), irrespective of which model was used (rtPNM or nrtPNM). This can be explained by the fact that, in advection dominated regimes or in reaction-controlled regimes, the dissolution

takes place more uniformly in the sample. Figure 4.10 again shows that at certain conditions, rtPNM is fine to be used, but at other conditions it will give an overestimation.
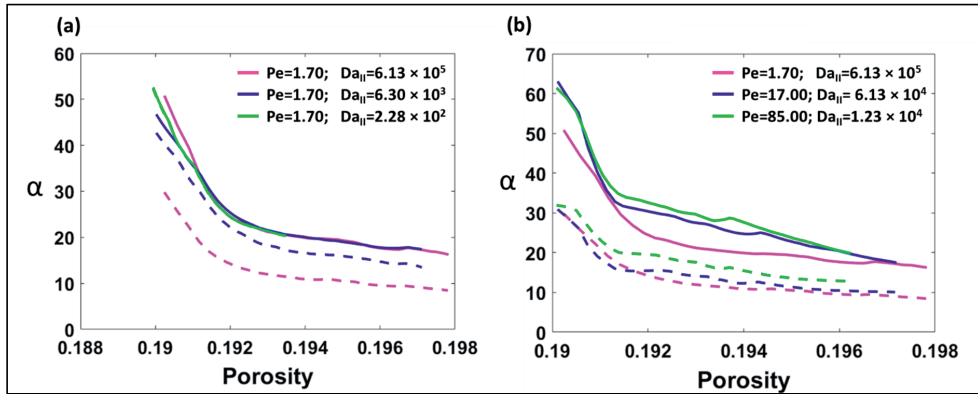


**Figure 4.10: Permeability coefficient α.** Power law exponent coefficient α as a function of porosity change for simulations with (a) constant injection velocity (i.e., constant $\widetilde{Pe}$ number = 1.70) using different solution pH values, and (b) injection of a solution with a constant pH value of 1.0 using three different velocities. Note that the solid lines correspond to rtPNM and the dotted lines correspond to nrtPNM.

## 4.5    Conclusions

In the context of pore network models for calcite dissolution, we have presented new constitutive relations to update pore throat conductance, which takes care of the evolving pore throat shape as per the imposed flow and reaction regimes. This was achieved through numerical simulation of reactive transport processes on a scale of single capillary/pore throat and later extraction of the evolution of conductance of the capillary. We observed that, for the advection dominated and reaction-controlled dissolution regimes, the conductance can be updated using the Hagen-Poiseuille relation, since the initial cylindrical pore throat shape is maintained during dissolution. On the contrary, for the diffusion dominated and reaction-dominated dissolution regimes, the pore throat shape changes to the half-hyperboloid (~conical) shape and the proposed new conductance relations provides an improved description of the impact on conductance evolution of the pore throat.

Next, the derived conductance relations were implemented in pore network simulations and the prediction of permeability was compared with the existing pore network models. We observed that corresponding to the micro-CT experimental conditions i.e., $\widetilde{Pe}$=974, $\widetilde{Da_{II}}$ = 59.8 and $\widetilde{Pe}$=192, $\widetilde{Da_{II}}$ = 303, only around 11% of total pore throats were subjected to the conditions which are responsible for the development of the non-uniform pore throat shapes. Consequently, estimated permeability from the pore network model remained indifferent to the relations used for updating of conductance of individual pore throats. As a result, new and existing PNM provided equally good agreement with the permeability of the reacted sample image obtained after the experiment.

Finally, we performed a sensitivity study of the new conductance relations across a range of flow and reaction regimes. This revealed that the injection of highly acidic solutions with a pH value of 1.0 and at an injection velocity of $3.17 \times 10^{-6}$ m s$^{-1}$ caused 60% of total pore throats to modify their initially cylindrical shapes into non-uniform shapes due to dissolution. We observed that, compared to the newly modified PNM, utilization of existing PNM can lead to

an overestimation of 27% in the predicted permeability value and an overestimation of over 50% in the fitted exponent $\alpha$ for the porosity-permeability relationship. In the context of applications such as the injection of $CO_2$ or acidic solution into carbonate rocks, pore network models are the most promising tool for the prediction of porosity-permeability relations at the representative elementary volume level. Depending on the reactive-flow regime, incorporation of the dissolution induced changes of the pore throat shape may be required in order to enhance the prediction capacity of existing pore network models and possibly bring the modeled outcomes closer to field observations.

Appendix 4

| pH of the injecting solution | Pe Number | Da Number | log10(Da) | Throat Length (μm) | Throat Width (μm) | GF | b_Observed | b_Calculated | %Difference |
|---|---|---|---|---|---|---|---|---|---|
| 2 | 0.47619 | 108.2936 | 2.0346 | 250 | 40 | 6.25 | 0.58081 | 0.66449 | -14.4086 |
| 2 | 0.04762 | 1082.958 | 3.03461 | 250 | 40 | 6.25 | 0.56048 | 0.63046 | -12.48527 |
| 3 | 47.61905 | 0.11094 | -0.95492 | 250 | 40 | 6.25 | 1.90274 | 1.91938 | -0.8749 |
| 3 | 4.7619 | 1.10937 | 0.04507 | 250 | 40 | 6.25 | 1.31174 | 1.45372 | -10.82386 |
| 3 | 0.47619 | 11.09366 | 1.04507 | 250 | 40 | 6.25 | 0.79223 | 0.79851 | -0.793 |
| 3 | 0.04762 | 110.939 | 2.04508 | 250 | 40 | 6.25 | 0.71851 | 0.64509 | 10.21783 |
| 5 | 47.61905 | 0.00402 | -2.39613 | 250 | 40 | 6.25 | 1.98704 | 1.99198 | -0.2486 |
| 5 | 4.7619 | 0.04017 | -1.39613 | 250 | 40 | 6.25 | 1.97975 | 1.91959 | 3.03891 |
| 5 | 0.47619 | 0.40167 | -0.39613 | 250 | 40 | 6.25 | 1.67938 | 1.45459 | 13.38496 |
| 2 | 0.47619 | 108.2936 | 2.0346 | 500 | 40 | 12.5 | 0.40353 | 0.45675 | -13.18677 |
| 2 | 0.04762 | 1082.958 | 3.03461 | 500 | 40 | 12.5 | 0.42146 | 0.41742 | 0.95828 |
| 3 | 47.61905 | 0.11094 | -0.95492 | 500 | 40 | 12.5 | 1.86532 | 1.90684 | -2.22586 |
| 3 | 4.7619 | 1.10937 | 0.04507 | 500 | 40 | 12.5 | 1.03482 | 1.36874 | -32.26863 |
| 3 | 0.47619 | 11.09366 | 1.04507 | 500 | 40 | 12.5 | 0.64293 | 0.61161 | 4.87102 |
| 3 | 0.04762 | 110.939 | 2.04508 | 500 | 40 | 12.5 | 0.4486 | 0.43433 | 3.18283 |
| 3.3 | 4.7619 | 0.57065 | -0.24363 | 500 | 40 | 12.5 | 1.38609 | 1.53737 | -10.91436 |
| 3.4 | 4.7619 | 0.45932 | -0.33788 | 500 | 40 | 12.5 | 1.43803 | 1.58634 | -10.31334 |
| 3.8 | 4.7619 | 0.20054 | -0.69781 | 500 | 40 | 12.5 | 1.9411 | 1.74057 | 10.33054 |
| 5 | 47.61905 | 0.00402 | -2.39613 | 500 | 40 | 12.5 | 1.99274 | 1.99074 | 0.10056 |
| 5 | 4.7619 | 0.04017 | -1.39613 | 500 | 40 | 12.5 | 1.90444 | 1.90708 | -0.13847 |
| 5 | 0.47619 | 0.40167 | -0.39613 | 500 | 40 | 12.5 | 0.98857 | 1.36975 | -38.55887 |
| 2 | 0.47619 | 108.2936 | 2.0346 | 100 | 40 | 2.5 | 1.2418 | 1.1124 | 10.42013 |
| 2 | 0.04762 | 1082.958 | 3.03461 | 100 | 40 | 2.5 | 1.1668 | 1.08978 | 6.60108 |
| 3 | 47.61905 | 0.11094 | -0.95492 | 100 | 40 | 2.5 | 1.90297 | 1.94642 | -2.28342 |
| 3 | 4.7619 | 1.10937 | 0.04507 | 100 | 40 | 2.5 | 1.686 | 1.63693 | 2.91035 |
| 3 | 0.47619 | 11.09366 | 1.04507 | 100 | 40 | 2.5 | 1.239 | 1.20147 | 3.02933 |

| | | | | | | | | | |
|---|---|---|---|---|---|---|---|---|---|
| 3 | 0.04762 | 110.939 | 2.04508 | 100 | 40 | 2.5 | 1.14495 | 1.09951 | 3.96879 |
| 5 | 47.61905 | 0.00402 | -2.39613 | 100 | 40 | 2.5 | 1.96697 | 1.99467 | -1.4082 |
| 5 | 4.7619 | 0.04017 | -1.39613 | 100 | 40 | 2.5 | 1.98617 | 1.94656 | 1.99477 |
| 5 | 0.47619 | 0.40167 | -0.39613 | 100 | 40 | 2.5 | 1.97307 | 1.63751 | 17.00671 |
| 2 | 0.47619 | 108.2936 | 2.0346 | 50 | 40 | 1.25 | 1.63279 | 1.65909 | -1.61114 |
| 2 | 0.04762 | 1082.958 | 3.03461 | 50 | 40 | 1.25 | 1.61871 | 1.65041 | -1.95842 |
| 3 | 47.61905 | 0.11094 | -0.95492 | 50 | 40 | 1.25 | 1.87112 | 1.97942 | -5.78816 |
| 3 | 4.7619 | 1.10937 | 0.04507 | 50 | 40 | 1.25 | 1.76244 | 1.86055 | -5.56726 |
| 3 | 0.47619 | 11.09366 | 1.04507 | 50 | 40 | 1.25 | 1.63128 | 1.6933 | -3.80191 |
| 3 | 0.04762 | 110.939 | 2.04508 | 50 | 40 | 1.25 | 1.61196 | 1.65414 | -2.61708 |
| 5 | 47.61905 | 0.00402 | -2.39613 | 50 | 40 | 1.25 | 1.93604 | 1.99795 | -3.19811 |
| 5 | 4.7619 | 0.04017 | -1.39613 | 50 | 40 | 1.25 | 1.97335 | 1.97947 | -0.31019 |
| 5 | 0.47619 | 0.40167 | -0.39613 | 50 | 40 | 1.25 | 1.98963 | 1.86078 | 6.47624 |
| 2 | 23.80952 | 0.54147 | -0.26643 | 500 | 20 | 25 | 1.9387 | 1.66613 | 14.05962 |
| 2 | 2.38095 | 5.41468 | 0.73357 | 500 | 20 | 25 | 1.03585 | 0.76077 | 26.55602 |
| 2 | 0.2381 | 54.14684 | 1.73357 | 500 | 20 | 25 | 0.40581 | 0.33436 | 17.60652 |
| 2 | 0.02381 | 541.4684 | 2.73357 | 500 | 20 | 25 | 0.32064 | 0.27844 | 13.16237 |
| 2 | 95.2381 | 2.16587 | 0.33563 | 500 | 80 | 6.25 | 1.72478 | 1.59622 | 7.45372 |
| 2 | 9.52381 | 21.65873 | 1.33563 | 500 | 80 | 6.25 | 0.70214 | 0.88054 | -25.40868 |
| 2 | 0.95238 | 216.5874 | 2.33563 | 500 | 80 | 6.25 | 0.46028 | 0.65558 | -42.43079 |
| 2 | 0.09524 | 2165.873 | 3.33563 | 500 | 80 | 6.25 | 0.68555 | 0.62958 | 8.16413 |
| 2 | 35.71429 | 0.8122 | -0.09034 | 500 | 30 | 16.66667 | 1.89988 | 1.63678 | 13.84837 |
| 2 | 3.57143 | 8.12203 | 0.90966 | 500 | 30 | 16.66667 | 0.87302 | 0.76375 | 12.51611 |
| 2 | 0.35714 | 81.22026 | 1.90966 | 500 | 30 | 16.66667 | 0.39913 | 0.39871 | 0.1057 |
| 2 | 0.03571 | 812.2026 | 2.90966 | 500 | 30 | 16.66667 | 0.36482 | 0.35257 | 3.35802 |
| 2 | 47.61905 | 1.08294 | 0.0346 | 400 | 40 | 10 | 1.88185 | 1.63337 | 13.2041 |
| 2 | 4.7619 | 10.82937 | 1.0346 | 400 | 40 | 10 | 0.94969 | 0.8253 | 13.09831 |
| 2 | 0.47619 | 108.2937 | 2.0346 | 400 | 40 | 10 | 0.44235 | 0.51483 | -16.38486 |
| 2 | 0.04762 | 1082.937 | 3.0346 | 400 | 40 | 10 | 0.45238 | 0.47664 | -5.36315 |
| 2 | 47.61905 | 1.08294 | 0.0346 | 200 | 40 | 5 | 1.90698 | 1.692 | 11.27328 |
| 2 | 4.7619 | 10.82937 | 1.0346 | 200 | 40 | 5 | 1.43857 | 1.01316 | 29.57194 |

| 2 | 0.47619 | 108.2937 | 2.0346 | 200 | 40 | 5 | 0.68923 | 0.75234 | -9.15648 |
| 2 | 0.04762 | 1082.937 | 3.0346 | 200 | 40 | 5 | 0.64682 | 0.72026 | -11.35393 |

**Table A4.1:** Training data set (blue colored cells) and testing data set (pink-colored cells)
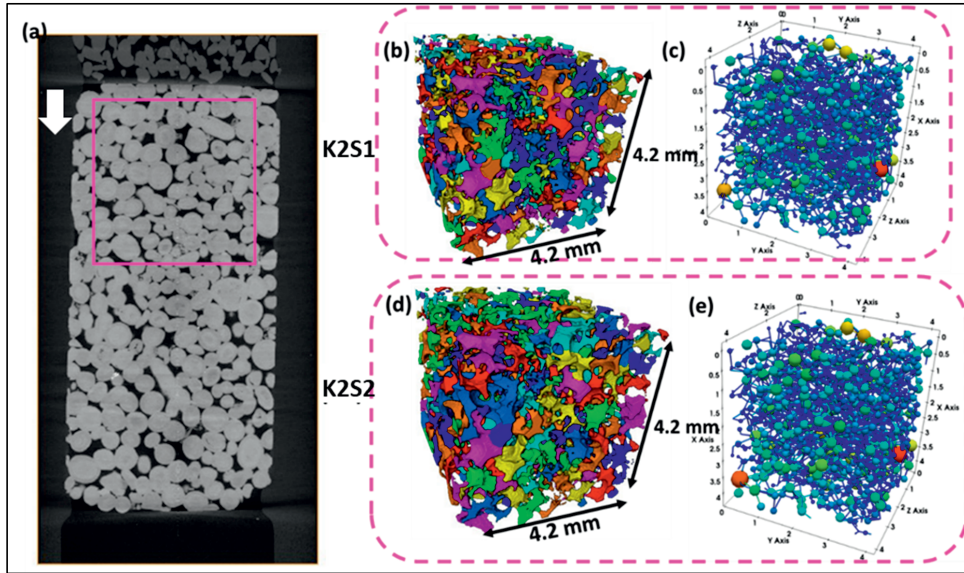
**Figure A4.1:** Vertical slice from the micro-CT volume of the sample K2 showing position and sizes of the extracted subsets K2S1, K2S2 (magenta colored square). The white-colored arrow shows the flow direction (image is rotated 180° compared to experimental position, where flow was upward). Panels (b) and (d) are the digital subsets, namely, K2S1 and K2S2, respectively. Panels (c) and (e) are the pore networks extracted from subsets K2S1 and K2S2, respectively.

| Species | The initial solution inside the pore network model | Injecting Solution – Sol.#1 (mol m$^{-3}$) | Injecting Solution – Sol. #2 (mol m$^{-3}$) | Injecting Solution – Sol. #3 (mol m$^{-3}$) |
|---|---|---|---|---|
| H$^+$ | $2.96 \times 10^{-7}$ | $1.22 \times 10^{2}$ | $1.00$ | $1.00 \times 10^{-2}$ |
| OH$^-$ | $3.40 \times 10^{-2}$ | $1.35 \times 10^{-10}$ | $1.01 \times 10^{-8}$ | $1.02 \times 10^{-6}$ |
| CO$_2$(aq) | $2.19 \times 10^{-5}$ | $1.09 \times 10^{-2}$ | $1.12 \times 10^{-2}$ | $1.13 \times 10^{-2}$ |
| HCO$_3^-$ | $3.29 \times 10^{-2}$ | $6.43 \times 10^{-8}$ | $4.99 \times 10^{-6}$ | $5.03 \times 10^{-4}$ |
| CO$_3^{2-}$ | $5.21 \times 10^{-3}$ | $6.45 \times 10^{-17}$ | $2.34 \times 10^{-13}$ | $2.39 \times 10^{-9}$ |
| Ca$^{2+}$ | $7.11 \times 10^{-1}$ | 0 | 0 | 0 |
| CO$_2$(g) | $6.45 \times 10^{-4}$ | $3.31 \times 10^{-1}$ | $3.31 \times 10^{-1}$ | $3.31 \times 10^{-1}$ |
| pH | 9.53 | 1.0 | 3.0 | 5.0 |

**Table A4.2:** Composition of the injected solution for the pore network simulations
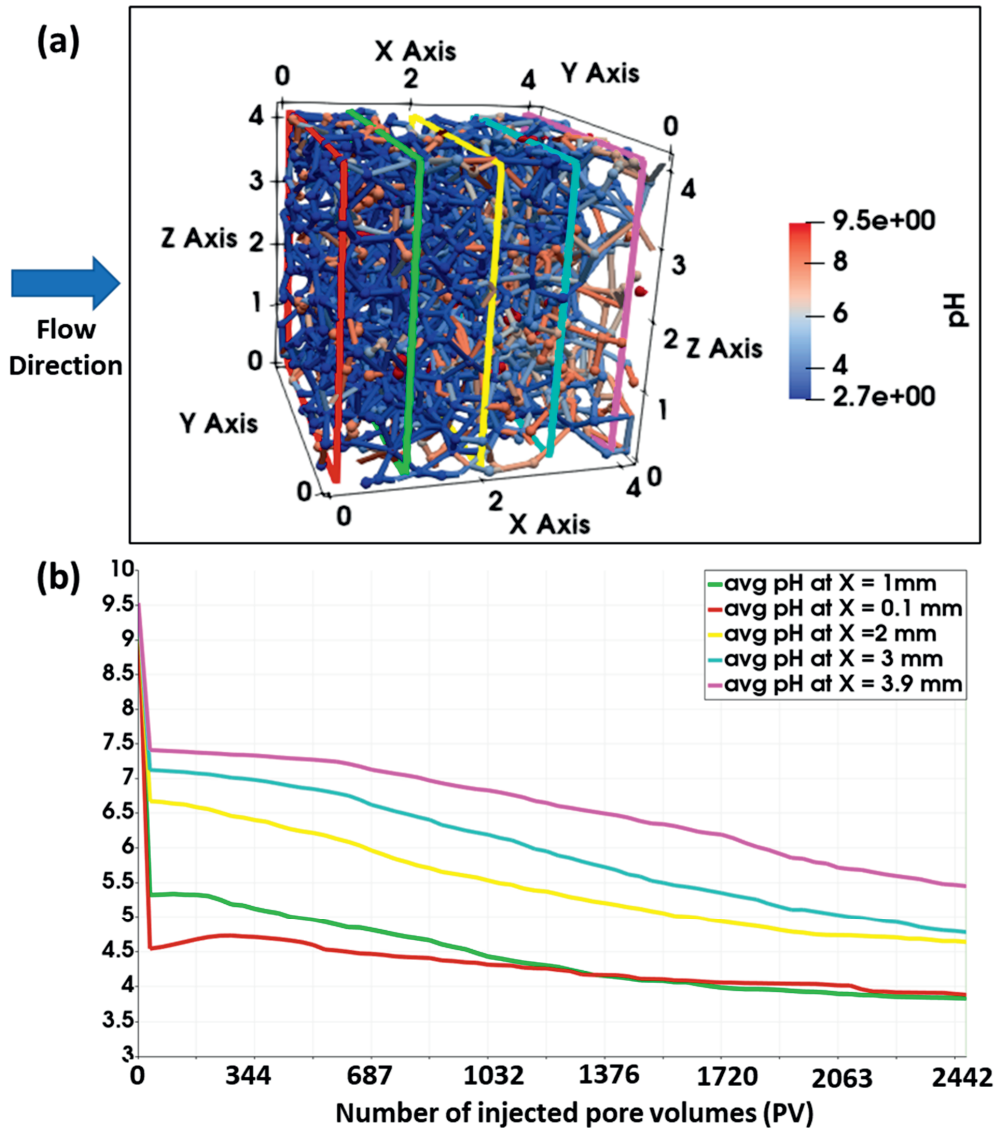
**Figure A4.2:** For the pore network model corresponding to the experiment E1-HQ, (b) 1D average pH calculated at five locations inside the pore network as highlighted with a different color in (a) as a function of injected pore volumes.
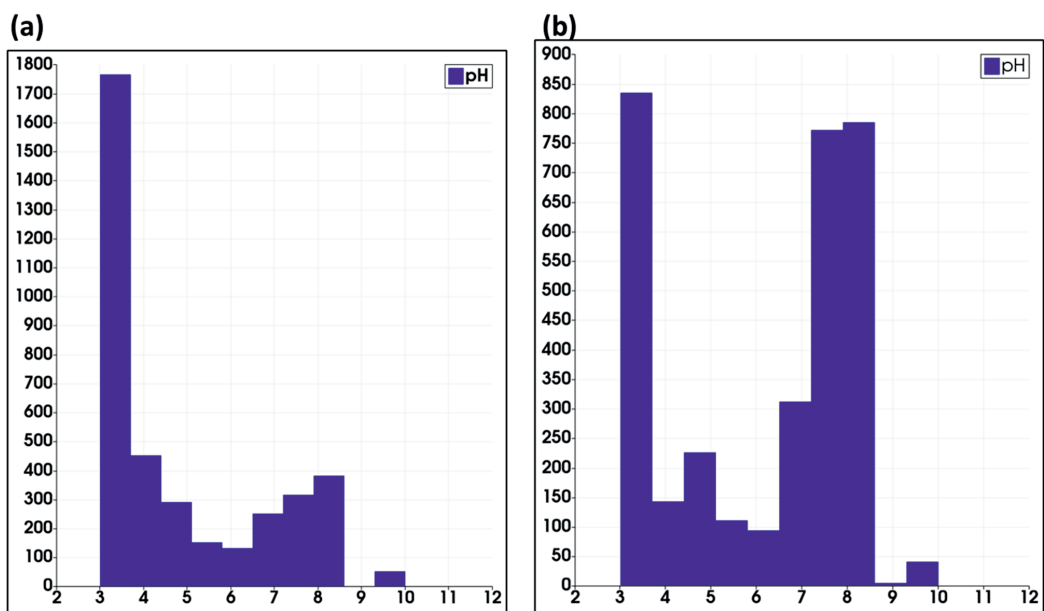
**Figure A4.3:** Frequency distribution plot of the pH of solutions inside the throat for (a) model corresponding to the experiment E1-HQ, after injection of 2442 pore volumes and (b) model corresponding to the experiment E2-LQ, after injection of 1996 pore volumes.
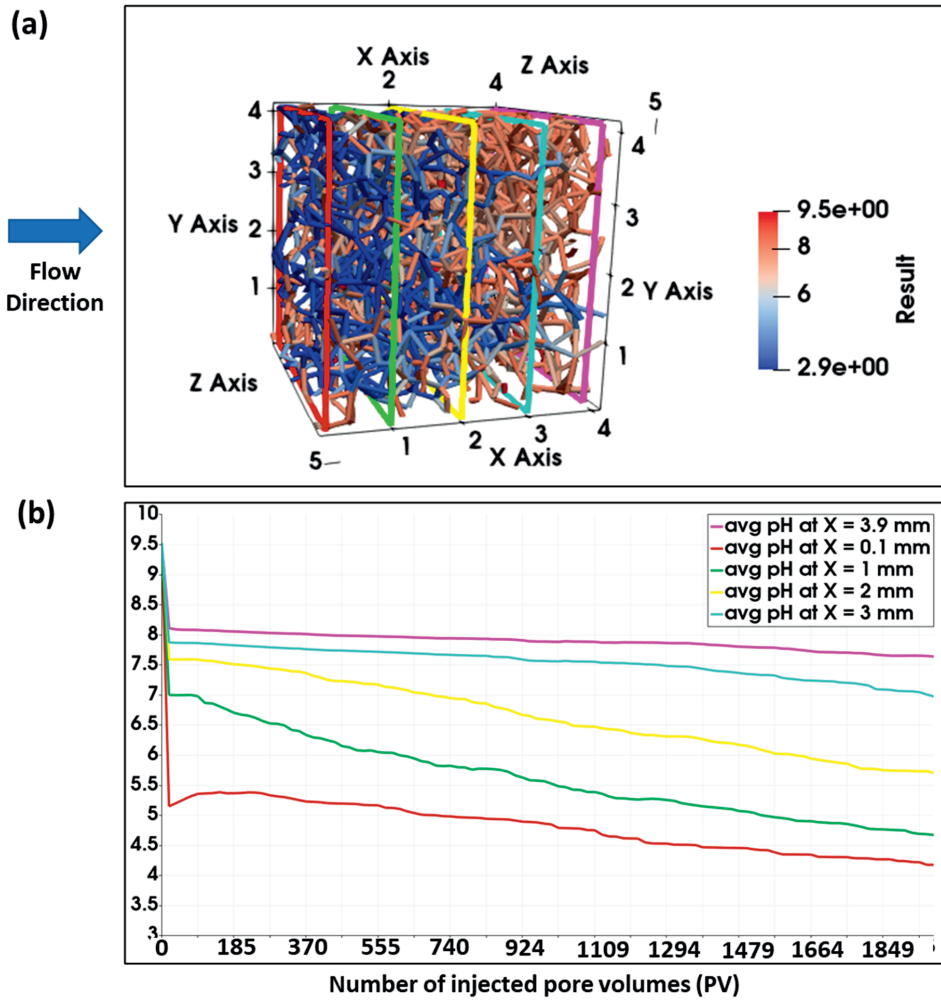
**Figure A4.4:** For the pore network model corresponding to the experiment E2-LQ, (b) 1D average pH calculated at five locations inside the pore network as highlighted with a different color in (a) as a function of injected pore volumes.
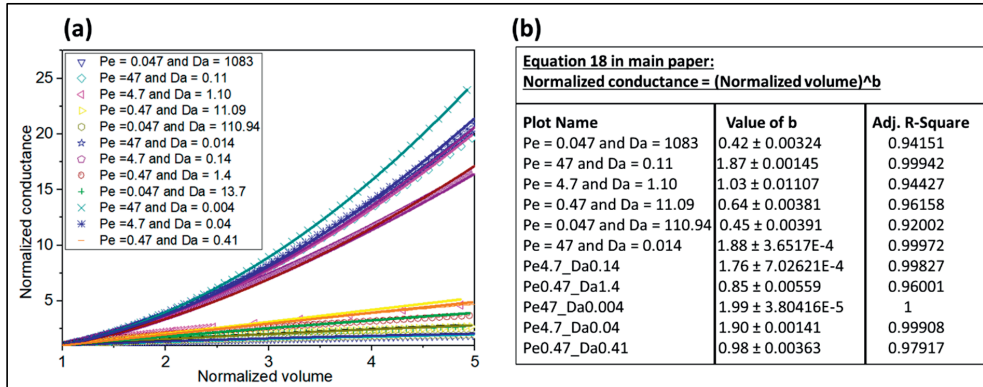
**Figure A4.5:** (a) Normalized conductance of a throat as a function of normalized volume of the throat for some of the simulated flow and reaction regimes while length and initial radius of the throat is fixed at $500 \times 10^{-6}$ m and at $40 \times 10^{-6}$ m, respectively. For each dataset, open colored symbols represent the data points and solid lines in the same color represent the fitted curves (b) fitted exponent b and fitness statistics expressed as value of R-square

## A4.1 Conductance model fitting parameter and statistics of fitness of the model

For the derivation of fitting parameters, out of the total simulated models, 47 data points are utilized. This training dataset covered Pe number range from 0.047 – 47, Da number range from 0.004 – 1082 i.e., corresponding to injecting a solution with pH values of 2, 3, or 5, throat length of 50, 100, 250, or 500 μm and throat radius of the magnitude of 20 or 80 μm (Table A4.2). For the sensitivity test of the fitting parameters, 12 data points corresponding to Pe number range from 0.047 – 47, injecting a solution with a pH value of 2, throat length of the magnitude of 200 and 400, and throat radius of the magnitude of 30 are utilized. Table A4.2 provides details of training and testing data sets. Statistics of fitting parameters are shown in figure 7a. Standard errors of each fitting parameter are lower than the respective value of the fitting parameters, which are justifiable for the training data set. Next, we provide statistics from the t-test of the fitted parameter i.e., t-Value and Prob>|t|. This test informs about the importance of each of the fitting parameters in the model. t-Value is calculated by dividing the value of the fitted parameter with the respective value of standard error. A high t-value compared to the confidence interval based critical t-Value i.e., 5%, tells that the particular fitting parameter is required in the model. Similarly, the low value of Prob>|t| indicates that each fitted parameter is important in the model. The dependency value calculated from the variance-covariance matrix tells about the correlation of fitting parameters among each other. A dependency value lower than one suggests that no parameters in the proposed model are correlated.

**(a)**

|  |  | Value | Standard Error | t-Value | Prob>\|t\| | Dependency |
|---|---|---|---|---|---|---|
| b | p1 | 1.88628 | 0.08903 | 21.18816 | 2.21365E-24 | 0.52004 |
|  | p2 | 0.60118 | 0.04981 | 12.06933 | 2.12849E-15 | 0.58126 |
|  | p3 | 0.71201 | 0.10884 | 6.54202 | 5.94686E-8 | 0.17741 |
|  | p4 | 0.31298 | 0.06757 | 4.63171 | 3.34824E-5 | 0.02068 |

**(b)**

|  | b |
|---|---|
| Number of Points | 47 |
| Degrees of Freedom | 43 |
| Reduced Chi-Sqr | 0.02048 |
| Residual Sum of Squares | 0.88062 |
| R-Square (COD) | 0.94337 |
| Adj. R-Square | 0.93942 |
| Fit Status | Succeeded(100) |

**Figure A4.6:** (a) Values of fitting parameters and related statistics of each parameter (b) Statistics related to the fitness of the model.
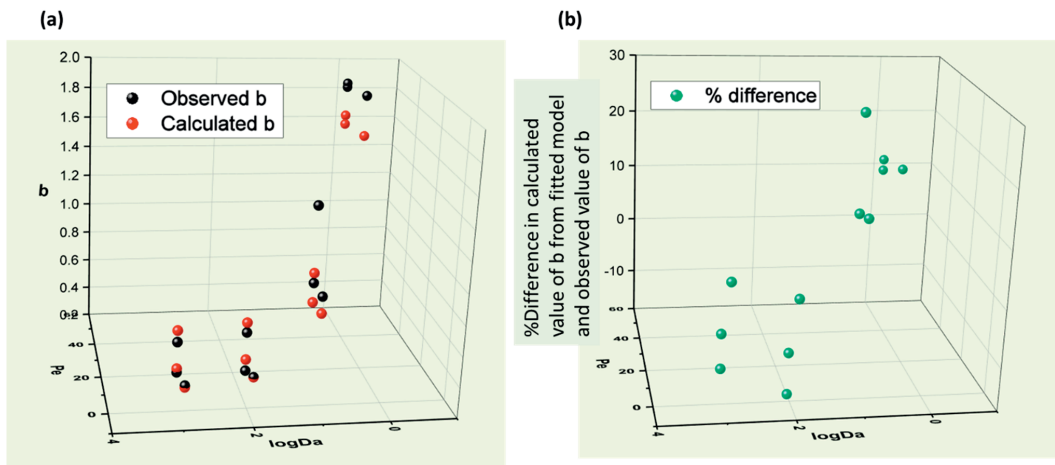


**Figure A4.7:** For testing data set (a) observed b vs calculated value of exponent b (b) %difference between the observed value of b and the calculated value of b

345
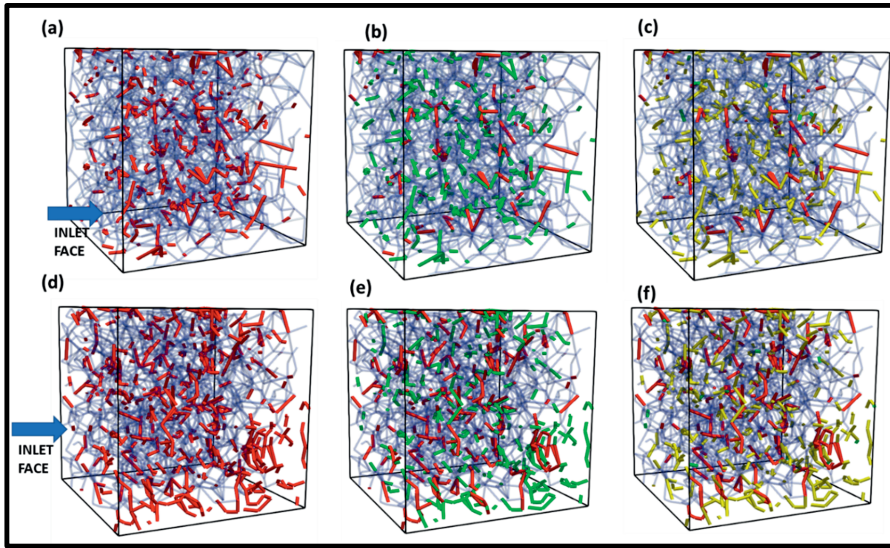
**Figure A4.8:** Panels (a)-(c) and (d)-(e) corresponds to the pore network models of the experiments E1-HQ and E2-LQ, respectively, where diffusion dominated throats (Pe<1) are shown by red, reaction dominated throats (Da>1) by marked by green, and throats with b <1.5 are shown by yellow color.
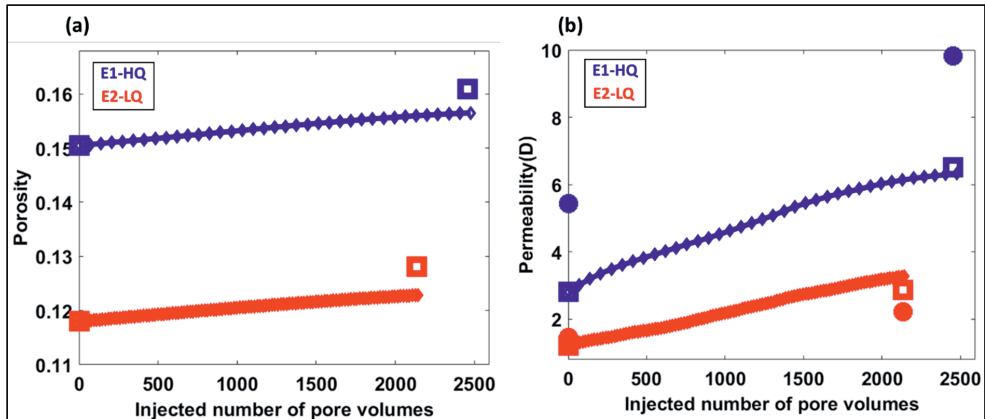


**Figure A4.9:** (a) Porosity evolution and (b) permeability evolution against the injected number of pore volumes for experiments E1-HQ (high flow rate) and E2-LQ (low flow rate). Diamond markers correspond to rtPNM and solid lines correspond to nrtPNM. Circle and squares show results of flow only simulations performed on the 3D image of the samples from the beginning and end of the experiments: circle show results from DNS and squares show results from foPNM simulations.
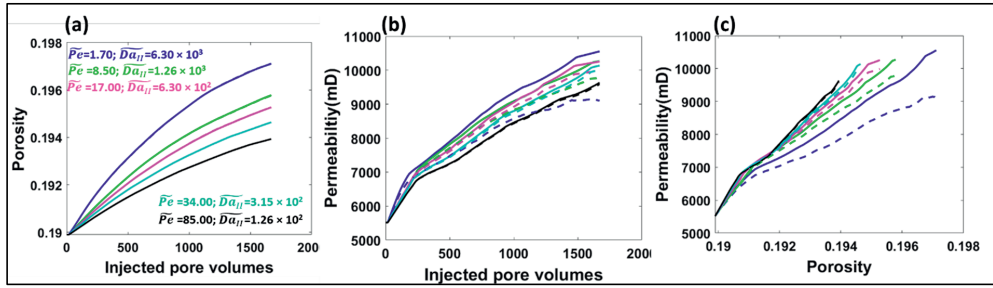
**Figure A4.10:** Evolution of porosity and permeability due to the injection of a solution with a pH value of 3.0 at five different Darcy velocities from rtPNM (solid lines) and nrtPNM (dotted lines). Note that the legend provided in panel a, is color coordinated with the plotted line colors and applicable for panels b and c, as well.
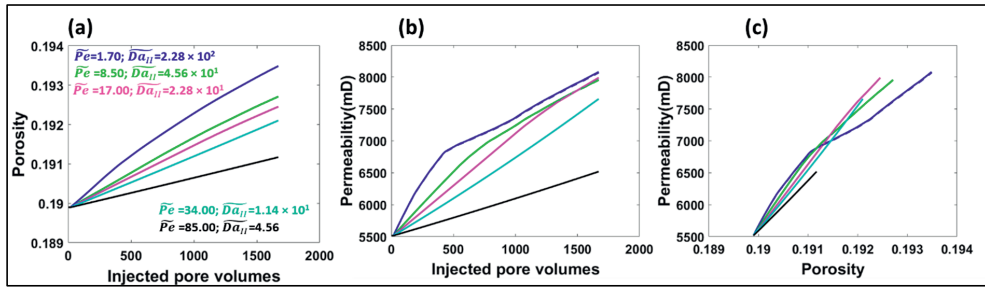


**Figure A4. 11:** Evolution of porosity and permeability due to the injection of a solution with a pH value of 5.0 at five different Darcy velocities from rtPNM (solid lines) and nrtPNM (dotted lines).

| $\widetilde{Pe}$ | $\widetilde{Da_{II}}$ | % fractions of pore throats which have a value of b<1.5 | %difference in the evolved permeability, at the end of the simulation, from rtPNM and nrtPNM models |
|---|---|---|---|
| 1.70 | 6.13E+05 | 0.60443 | 27.40 |
| 8.50 | 1.23E+05 | 0.370253 | 24.72 |
| 17.00 | 6.13E+04 | 0.28481 | 21.97 |
| 34.00 | 3.07E+04 | 0.224684 | 17.80 |
| 85.00 | 1.23E+04 | 0.129747 | 11.86 |
| 1.70 | 6.30E+03 | 0.493671 | 13.72 |
| 8.50 | 1.26E+03 | 0.189873 | 4.75 |
| 17.00 | 6.30E+02 | 0.101266 | 2.65 |
| 34.00 | 3.15E+02 | 0.091772 | 1.29 |
| 85.00 | 1.26E+02 | 0.091772 | 0.47 |
| 1.70 | 2.28E+02 | 0.088608 | 0.14 |
| 8.50 | 4.56E+01 | 0.091772 | 0.03 |
| 17.00 | 2.28E+01 | 0.088608 | 0.01 |
| 34.00 | 1.14E+01 | 0.091772 | 0.00 |
| 85.00 | 4.56E+00 | 0.091772 | 0.00 |

**Table A4.3:** For all the simulated flow and reaction regimes, % fraction of throats with b < 1.5 and % permeability difference between rtPNM and nrtPNM.
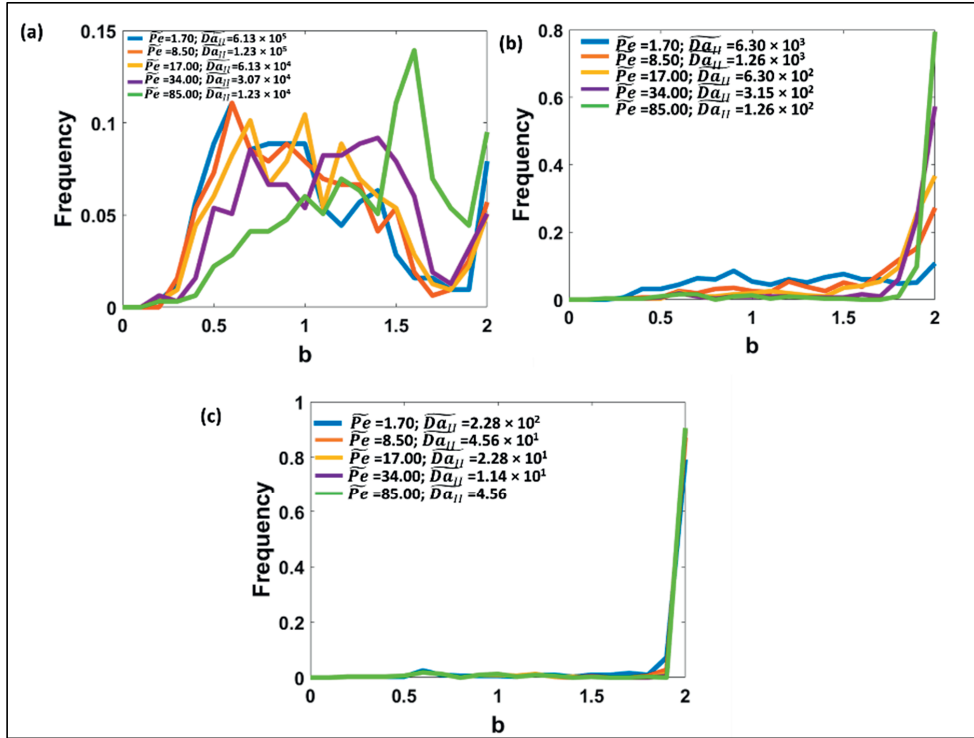


**Figure A4. 12: pore conductance parameter.** Distribution of $b$ coefficient within the sample when injecting a solution with a pH value of (a) 1.0 (b) 3.0 and (c) 5.0 using five different Darcy velocities. b.

# Chapter

# 5. Control of brine composition over reactive transport processes in dissolution of porous calcium carbonate rock

**Abstract**

We studied the impact of brine composition, mainly calcium ions and NaCl-based salinity, on the development of dissolution features in Ketton, a porous calcium carbonate rock. A laboratory XMT scanner was used to acquire time-lapse *in-situ* images of Ketton samples during dissolution experiments. A total of four flow-through experiments were performed through the injection of four different brine solutions using a flow rate of 0.26 ml min$^{-1}$. Each sample was scanned at a voxel size of 6 μm. The temporal evolution of porosity, permeability and pore structure was obtained using image analysis as well as fluid flow numerical simulations.

By varying the inflow calcium and NaCl concentration, a range of different reacting capacities of the injected solutions was achieved, resulting in different Damköhler (*Da*) numbers, with higher *Da* numbers reflecting higher reaction rates. We observed the formation of a characteristic dissolution pattern depending upon the imposed *Da* number. At the highest *Da*, we observed a significant amount of dissolution in the vicinity of the sample inlet together with the formation of many dissolution channels (wormholes). Contrastingly for low *Da* experiments, the dissolution became more focused through formation of sparsely located channels. Furthermore, at the lowest *Da* (achieved using high $Ca^{2+}$ and salinity values) uniformly disseminated dissolution was observed, with dissolution occurring mostly in the microporous realm, triggering particle detachment, displacement and local pore clogging. For each of the experiments, the relative increment in permeability correlated with the developed dissolution pattern. We observed that injection of similar number of pore volumes leads to the greatest permeability increase when solution's calcium and salinity were low, and to the least permeability increase when solution's calcium and salinity were high. In summary, different ratios of salt and calcium concentration in the injected solution led to variations in developed dissolution patterns from disseminated and microporosity dissolution to wormhole formation. These changes in dissolution patterns affect permeability and porosity systematically in such a way that it be described with an empirical porosity-permeability relationship.

## 5.1 Introduction

Carbonate formations constitute ~20% of sedimentary basins and ~60% of the world's hydrocarbon reservoirs (Morse and Mackenzie, 1990) and calcite is the dominant mineral in these reservoirs. Applications such as $CO_2$ sequestration or acid stimulation for enhanced oil and gas production from carbonate reservoirs involve the interaction of an acidic fluid with the calcite. This leads to the dissolution of calcite and the creation of secondary porosity and permeability.

Numerous studies have shown that parameters such as injection rate, the acidity of the injected solution, and initial heterogeneity of the porous medium can impact the dissolution processes and subsequent evolution of rock properties (e.g. Golfier et al., 2002; Hoefner and Fogler, 1988; Luquot and Gouze, 2009; Meile and Tuncay, 2006). In particular, dissolution kinetics along with the acid injection rate is known to be capable of inducing a characteristic dissolution pattern (e.g., Daccord et al., 1993; Elkhoury et al., 2013; Golfier et al., 2002; Hoefner et al., 1987; Hoefner and Fogler, 1988; Luquot et al., 2014; Luquot and Gouze, 2009; Maheshwari et al., 2013; Panga et al., 2005). At the pore scale, the interaction of an acid with calcite is a combination of two processes: (i) the transport rate of the aqueous ions to and from the mineral surface and (ii) the dissolution reaction at the mineral surface. Manipulation of the rate of any of these processes affects the effective dissolution rate and consequently the dissolution patterns. In general, five types of dissolution patterns have been reported, corresponding to different dissolution kinetics for a given acid injection rate (Hoefner and Fogler, 1988): 1) face

dissolution, 2) conical wormholes, 3) dominant wormholes, 4) ramified wormholes, and (5) uniform dissolution. For example, when the injected solution is highly reactive such that the transport time scale of the acid is longer than the reaction time scale of the acid, then most of the acid is consumed in the dissolution of the whole face of the rock. This leads to the development of the face dissolution pattern. Acid solutions with low reactivity, on the other hand, can penetrate uniformly into the rock, causing uniform dissolution since time scale of transport becomes smaller than the time scale of chemical reaction. In summary, with decrease in the dissolution rate, the dissolution regime changes from the face dissolution regime to the uniform dissolution regime, while passing through the intermediate regimes corresponding to the different wormhole dissolution patterns. These patterns control the required amount of acid volume that needs to flow through the sample to achieve the same permeability increment against same amount of porosity increment. For example, among the five dissolution patterns, the dominant wormholes are the most conducting channels and require the least amount of acid pore volumes to flow through to enhance the permeability by a certain amount.

One way of controlling which dissolution regime is achieved in reactive-transport dissolution is by addition of dissolution-inhibiting or -enhancing compounds. Examples are the addition of microemulsion (Hoefner et al., 1987), through the amount of $CO_2$ (Luquot et al., 2014) or the amount of $SO_4^{2-}$ ions in the injected acid (Garcia-Rios et al., 2015). Luquot et al., 2014 showed that high $pCO_2$ developed preferential flow paths while lower $pCO_2$ resulted in uniform dissolution. Garcia-Rios et al., 2015 observed the inhibitory effect of $SO_4^{2-}$ ions on calcite dissolution rates while observing no significant effect on the dissolution patterns.

The impact of salinity and dissolution-inhibiting or -enhancing ions and compounds present in formation water on pore geometry evolution during dissolution of porous carbonate rocks is less well-known. Hanor (1994) reported that the salinities of pore waters in subsurface basins span over five orders of magnitude i.e., from few mg $l^{-1}$ in shallow meteoric systems to over 400000 mg $l^{-1}$ in evaporite-rich sedimentary basin such as Michigan Basin, USA. Moreover, in the formation brines, $Ca^{2+}$ is the second most abundant cation after $Na^+$. The concentration of $Ca^{2+}$ can even exceed the $Na^+$ concentration in formation waters with salinities higher than 300000 mg $l^{-1}$ (Gledhill and Morse, 2006). Therefore, understanding the geochemistry of high salinity and $Ca^{2+}$ rich formation waters is important in the assessment of (the permeability evolution in) sedimentary basins for applications such as $CO_2$ sequestration or acid stimulation for enhanced oil production.

Several bulk experiments have examined the influence of the salinity of the solution and $Ca^{2+}$ concentration on the calcite dissolution rates (Anabaraonye et al., 2019; Buhmann and Dreybrodt, 1987; Finneran and Morse, 2009; Gledhill and Morse, 2006; Gutjahr et al., 1996b; Pokrovsky et al., 2005; Sjöberg and Rickard, 1985). For transport-controlled dissolution region, no impact of the NaCl-based ionic strength on dissolution rates is observed when I <1M (Pokrovsky et.al., 2005), while strong inhibition of dissolution rates is observed with NaCl-salinity >1M (Gledhill and Morse, 2006). The impact of $Ca^{2+}$ ions in solution on the dissolution rate is contested in literature. Some authors found that calcium inhibits calcite dissolution in neutral to basic conditions only (Sjoberg and Rickard,1985), while others found that calcium ions enhance calcite dissolutions rates (Gutjahr et al. 1996b; Gledhill and Morse 2006).

While there is a clear, albeit incoherent, impact of calcium and salinity on calcium carbonate dissolution rates, the implication of this influence on the development of secondary porosity and permeability in carbonate rocks during dissolution is unknown. We are not aware of any reactive flow experimental studies that have explored the control of NaCl and $Ca^{2+}$ concentration on the dissolution patterns.

This study examines the influence of the amount of NaCl and $Ca^{2+}$ ions in the injected solution over the dissolution kinetics and dissolution patterns in Ketton samples. We present the results of four flow experiments which were realized with the injection of four different acidic solutions with constant flow rate into four samples of oolitic limestone. The composition of these solutions, i.e. amount of salt and $Ca^{2+}$ ions, was chosen to cover a wide range of dissolution kinetics. X-ray microtomography (XMT) image analysis and effluent analysis were used to calculate the removed mass of calcite and consequent changes in the porosity of the samples. Further, time-lapse XMT data of the sample enabled the temporal characterization of the dissolution patterns in each experiment. The link between dissolution and permeability enhancement of the samples was investigated using single-phase flow simulations on the pore network extracted from the XMT images of the sample. Finally, for each experiment, development in permeability was related to the modified porosity of the sample.

## 5.2 Material and Methods

For this study, we have utilized a relatively homogeneous carbonate rock type: Ketton limestone. This oolitic limestone is a part of the Lincolnshire Formation, which was deposited around 165 million years ago. Four cylindrical samples named K1, K2, K3, and K4, of 6 mm in diameter and ~12mm in length were drilled side by side out of a limestone block. These samples were saturated with calcite-equilibrated water under vacuum conditions, for around 48 hours. To impose the radial fluid injection conditions, an inert porous sintered glass plug (Robu glass por 0 filter) was placed in front of the inlet side of the carbonate plug. Both plugs were inserted into a Viton sleeve, placed in a custom-built Hassler-type flow cell made from X-ray transparent PEEK. A confining pressure of ~20 bar was applied on the sleeve to avoid fluid bypassing the sample. Note that flow was established from bottom to top of the sample while all presented images in the subsequent sections are upside down.

### 5.2.1 Chemical composition of injecting solutions

Four solutions with the same HCl concentration of 0.001 mol dm$^{-3}$ and different salinity and $Ca^{2+}$ concentration were prepared in atmospheric conditions. The first solution had an ionic strength of 0.2 mol dm$^{-3}$, without calcium ions (referred to as "no calcium low salinity solution" or NCLS). A second solution had a similar ionic strength but contained $1 \times 10^{-3}$ mol dm$^{-3}$ of $Ca^{2+}$ ions (low calcium low salinity solution -LCLS). The third type of solution had an ionic strength of $1200 \times 10^{-3}$ mol dm$^{-3}$, without calcium ions (no calcium high salinity solution - NCHS). Finally, the fourth solution had a similar ionic strength as the third but contained $335 \times 10^{-3}$ mol dm$^{-3}$ of $Ca^{2+}$ ions (high calcium high salinity solution -HCHS). All solutions were prepared by adding the appropriate amount of the reagents $CaCl_2$, NaCl, and HCl to deionized water under atmospheric conditions. For all four experiments, acidic solutions were injected with a constant flow rate of $4.16 \times 10^{-9}$ m$^3$s$^{-1}$ (i.e. Q = 0.26 ml min$^{-1}$).

The concentration of $Ca^{2+}$ ions in inflow and outflow solutions was measured with the ICP-OES method. This method can measure $Ca^{2+}$ concentration within a range of $0.5-5 \times 10^{-3}$ mol dm$^{-3}$. Therefore, most of the solutions were diluted using 0.7M HNO$_3$ acid, to a dilution ratio of 1:100, while some of the solutions related to experiment HCHS were diluted by a ratio of 1:1000. The pH of the inflow and outflow solutions was measured with a pH 3110 portable pH meter and pH electrode SenTix™. The solution composition of all inflow solutions was calculated using PHREEQC (Parkhurst and Appelo, 2013) with the Pitzer database. These calculations showed that the activity coefficient of H$^+$ is close to unity for all solutions (Table S1). For inflow solutions NCLS and LCLS, the measured value of pH matched with the calculated value of pH. It should be noted that the measured pH values for the NCHS and the HCHS are impacted by the non-compatibility of the utilized electrode with the high number of

ions in the solutions. As a consequence, the measured value of pH of these solutions differed from the calculated value of pH. Table 1 summarizes experimental details related to flow and solution chemistry.

## 5.2.2 Data acquisition and processing

In-situ imaging of the sample was performed using a laboratory-based environmental micro-CT scanner built at Ghent University (Bultreys et al., 2016). The starting step of each experiment was the saturation of the sample with calcite-equilibrated water, followed by scanning of the sample. The scanning was performed with an X-ray beam energy of 110kV and an exposure time of 80ms. A total of 2200 projections, covering a 360° rotation of the scanner, were obtained in 15 minutes. The reconstructed voxel size of the images was 6 µm per voxel and three stacks were required to cover the full length of the sample. Such full sample length scanning was performed at the beginning and the end of the experiment. During acid injection, the scanner was fixed near the inlet of the sample; therefore, time-lapse scans correspond to a ~6 mm high part of the sample. Hereafter, these time-lapse scans are referred as half-length sample volumes. The following processing steps were subsequently performed on both types of scans:

1. Reconstruction of the 2D radiographs to obtain a 3D dataset using the filtered back-projection method in Octopus software (Vlassenbroeck et al., 2007).
2. Filtering of 3D data set using the non-local means filter (Buades et al., 2005) in Avizo module 9.5 (Avizo 9.5.0, Thermo Fischer Scientific).
3. Registration of the filtered dataset of each time step with respect to the first scan of the time series and subsequent resampling of registered datasets, using normalized mutual information metric in Avizo (Studholme et al., 1999).
4. Segmentation of resampled datasets using the Watershed segmentation method. Resultant segmented images and subsequent quantification from these images are sensitive to the choice of threshold grey-value used in marking of different phases. Therefore, for a single experiment, this value is chosen manually and maintained across the all-time series. The fact that the segmented, image-based macroporosity of the Ketton samples determined here falls within the range of reported XMT-image based porosity values of this rock suggests that the segmentation is of a similar order to previously published work and contains the same (unavoidable) offset from the true bulk porosity value (Table 3 in Menke et.al., 2017).

Figure A5.1 presents the workflow of image processing through a 2D slice from the 3D dataset of sample K1.

In order to avoid boundary effects, the segmented datasets of the sample were cropped out at ~1.5 mm from the inlet and at ~1.8mm from the outlet sides (Figure A5.2). The sizes of both full and cropped 3D volumes are provided in Table 5.1.  Hereafter cropped 3D volumes are referred as cropped length sample volumes. Quantification of the segmented dataset was performed through the following three ways, where the first and second approach was used for cropped length sample and the third approach was used for both cropped length sample and half-length sample:

1. Applying a pore separation process on the segmented dataset enabled the quantification of individual pores through properties such as equivalent diameter and volume of the pore.
2. Skeletons of the pore space were extracted from the segmented dataset using the XSkeleton pack extension of Avizo. This pore-based approach of skeletonization utilizes

distance ordered homotopic thinning (DOHT) algorithm in Avizo. Further details of this approach are provided in Section 5.2.3.

3.  A pore network was extracted from the segmented dataset using a maximal ball algorithm (Raeini et al., 2017). Further details of this approach are provided in Section 5.2.4.

### 5.2.3   Skeleton analysis

In this study, we used skeletonization to characterize the wormholes caused by limestone dissolution. The skeletonization is an image processing workflow converting the three-dimensional pore space into a one-dimensional object while preserving topological and geometrical features. This process of dimension reduction includes iterative removal of individual voxels from a volume until a single line of voxels (i.e., the medial axis of the volume) remains. This yields a simplified skeleton representation of the pore space, in which each voxel stores information of the original complex 3D pore space through attributes like thickness, orientation, length, etc.

To apply skeletonization for wormhole analysis, the first task in the workflow was the segregation of wormholes from the surrounding pore space. This was performed using segmented datasets of the sample, belonging to the start and end of the experiment, hereafter referred to as A and B, respectively. The following actions were performed on datasets A and B:

1.  Identifying the individual pores of the post-dissolution sample by separation and labelling of dataset B.
2.  Finding the voxels where solid calcite was dissolved during the experiment, by calculating the difference dataset i.e., B-A.
3.  Counting the amount of solid calcite voxels that were dissolved in each pore of the post-dissolution sample (by performing a label analysis of the pores in B using the difference dataset as an intensity image in Avizo).
4.  Selecting only the pores where a large amount of dissolution took place to filter out the dominant wormholes. In dataset B, pores that have at least 80% dissolved voxels and have a volume more than 0.001 mm$^3$ were selected. These criteria were selected by visual assessment.
5.  Finally, a closing operation was performed on the filtered dataset to reduce the influence of noise on the connectivity of the wormhole.

To calculate the wormhole length, we performed a skeleton analysis. First, we extract the skeleton from the segregated wormholes using the Auto Skeleton module in Avizo. This method takes a label image as input data (here, the filtered dataset), calculates distance map, applies a thinning algorithm, and yields output in the form of a collection of nodes (branching points on the skeleton) and segments. This skeleton, also referred to as a spatial graph object, stores attributes of nodes such as coordination number, spatial position, and attributes of segments such as mean radius, length and tortuosity. The analysis on this spatial graph was performed in MATLAB using the graph object-based toolbox:

1)  The start and end points of the wormhole's skeleton were detected by differentiating tips (coordination number of one) and nodes (coordination number greater than one). Start points were defined as tips in the inlet face of the image, end points as tips ending anywhere else in the image.

2)  The shortest path between each individual pair of start and end points along the skeleton was calculated using Dijkstra's shortest path algorithm (Joseph, 2020).

3) The shortest paths were classified into three length-based categories: category-1 includes channels with lengths greater than 5mm, category 2 includes channels with lengths ranging between 2 and 5 mm and category 3 includes channels with lengths smaller than 2 mm.

### 5.2.4 Pore network extraction and flow modelling

We have calculated the velocity field and permeability of the sample at a different stage of the dissolution process. For this purpose, we have utilized a pore network model because it requires less computational time than direct numerical simulation. Single phase flow was simulated on the extracted pore network. For simulating flow, the inlet face of the network is maintained at a constant value of Darcy velocity and the outlet face at an atmospheric pressure condition, after which the pressure and velocity in each pore are found by imposing mass conservation. The Darcy velocity is calculated as:

$$u_D = \frac{Q}{A} \tag{5.1}$$

where, Q is the volumetric flow rate ($m^3\ s^{-1}$) and A is the cross-section area of the sample ($m^2$).

Remaining boundaries of the network parallel to the flow direction are implemented as no-flow boundaries. Further details on the modelled equations can be found in Raoof et al. (2012).

### 5.2.5 Sample characterization prior to experiments

Characterization of the Ketton samples is based on the XMT images, FIB-SEM images, EDS analysis, XRD analysis, and properties of the extracted pore networks.

XMT images showed that Ketton is composed of spherical grains and can be considered a relatively homogeneous carbonate rock at the macroscopic scale (Figure A5.1). Electron microscopy imaging of the surface and cross-sectional view of a randomly chosen spherical grain were done using FIB-SEM imaging technique. Results showed the extent of the intra-grain porosity (Figure A5.3). SEM images of the part of the sample showed textural heterogeneity at a microscopic scale (Figure A5.4). We observed that some part of the grain was made of rhombohedral particles, which is a typical morphology of calcite. Other parts of the grain were made of needle-shaped particles, which is a typical morphology of aragonite (e.g. Nan et al., 2008). EDS analysis suggested that these particles are majorly composed of Ca, C and O (Figure A5.5).

In order to identify the particle polymorph, we conducted XRD analysis of three new samples that were extracted from the same Ketton limestone block. Figure A5.6 shows the comparison of the XRD spectra of a representative sample with the RRUFF reference of calcite, suggesting that Ketton is predominantly composed of the calcite and that the needle-shaped particles are probably the pseudomorphs i.e., aragonite converted into calcite (Figure A5.4).

Next, the petrophysical properties of the four samples i.e., K1, K2, K3 and K4 were investigated through analysis of the initial XMT images and of the extracted pore networks for the initial conditions in the samples. The initial porosity of each sample was calculated by dividing the volume of pore space by the total volume of the sample. The initial permeability of each sample was calculated from the single-phase flow simulation on extracted pore networks. A comparison of the porosity of all samples shows that K1, K2 and K3 have similar initial porosity while K4 has a different initial porosity (Table 5.1).

Figure 5.1 show the statistical distribution of some of the characteristic properties of the initial pore space of the samples. K1, K2 and K3 have similar throat radii and K2 and K3 have similar pore sizes. K4 has a slightly wider range of pore sizes and throat widths than K1-K3, while all

four samples have a similar distribution of coordination numbers. Figure 5.1e shows the frequency distribution of the normalized velocity which is obtained by normalizing the velocity value of each throat by the Darcy velocity. The Darcy velocity is obtained by dividing the flow rate with the cross-sectional area of the sample. The frequency distribution of normalized velocity indicates the probability of faster and slower velocity channels in comparison with the Darcy velocity. K2 and K4 have a somewhat greater number of fast channels as compared to K1 and K3. The observed velocity field in this study is similar to the previously reported velocity field for Ketton samples (Al-Khulaifi et al., 2017). Overall, the narrowness of the velocity channel suggests that all four samples have relatively similar initial pore structure (Figure 5.1e).
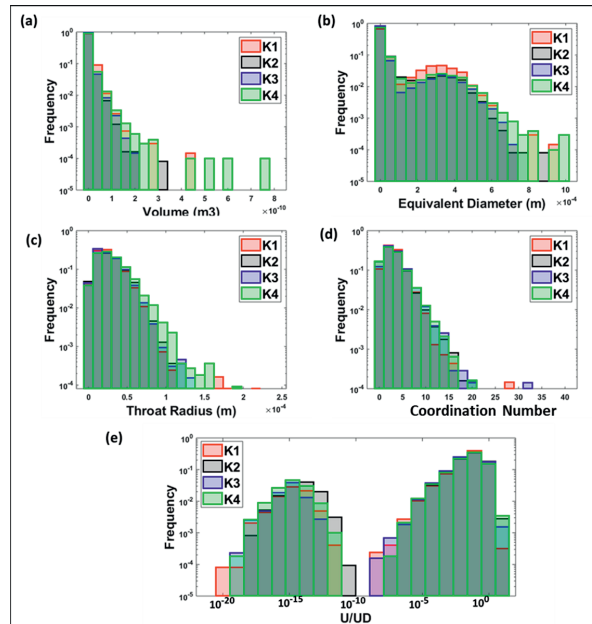


**Figure 5.1:** Statistical distribution of (a) Volume of Pores (b) Equivalent Diameter (c) Throat radius (d) Coordination Number, and (e) Velocity Field of Ketton samples. Note the log-scale based y-axis for all plots.

| Experiment | NCLS | LCLS | NCHS | HCHS | Method |
|---|---|---|---|---|---|
| Ketton sample | K1 | K2 | K3 | K4 | - |
| Flow rate ($m^3 s^{-1}$) | $4.16 \times 10^{-9}$ | $4.16 \times 10^{-9}$ | $4.16 \times 10^{-9}$ | $4.16 \times 10^{-9}$ | - |
| Darcy velocity ($m\ s^{-1}$) | $1.54 \times 10^{-4}$ | $1.54 \times 10^{-4}$ | $1.54 \times 10^{-4}$ | $1.54 \times 10^{-4}$ | - |
| Injection duration (s) | 72000 | 72000 | 43200 | 57000 | - |
| Injected pore volume | 6722 | 6977 | 3507 | 4489 | - |
| Inflow pH(Calculated) | 3.1 | 3.1 | 3.00 | 3.05 | PHREEQC Pitzer |
| Inflow pH (Measured) | 3.01 | 2.97 | 2.77 | 7.49 | pH meter |
| Inflow $Ca^{2+}$ (mol $dm^{-3}$) | - | $1 \times 10^{-3}$ | - | $335 \times 10^{-3}$ | ICP-OES |
| Inflow -salinity (mol $dm^{-3}$) | $0.2 \times 10^{-3}$ | $0.2 \times 10^{-3}$ | $1.16 \times 10^{-3}$ | $1.12 \times 10^{-3}$ | ICP-OES |
| Porosity at t = 0s (%) | 13.42 | 12.1 | 13.88 | 16.3 | XMT [a] |
| Permeability at t = 0s ($m^2$) | $9.89 \times 10^{-13}$ | $4.07 \times 10^{-13}$ | $1.41 \times 10^{-12}$ | $1.89 \times 10^{-12}$ | Flow simulation on cropped sample |
| Average equivalent diameter at t = 0s (m) | $0.89 \times 10^{-4}$ | $0.53 \times 10^{-4}$ | $0.51 \times 10^{-4}$ | $0.65 \times 10^{-4}$ | XMT [a] |
| Average volume of pores at t = 0s ($m^3$) | $0.57 \times 10^{-11}$ | $0.29 \times 10^{-11}$ | $0.31 \times 10^{-11}$ | $0.47 \times 10^{-11}$ | XMT [a] |
| Number of pores in the extracted pore network | 6832 | 6259 | 6948 | 6130 | PNM [b] |
| Number of throats in the extracted pore network | 12419 | 10915 | 12919 | 10919 | PNM [b] |
| Average pore radius at t = 0s (m) | $5.46 \times 10^{-5}$ | $4.97 \times 10^{-5}$ | $4.93 \times 10^{-5}$ | $5.31 \times 10^{-5}$ | PNM [b] |
| Average throat radius at t = 0s (m) | $2.59 \times 10^{-5}$ | $2.61 \times 10^{-5}$ | $2.59 \times 10^{-5}$ | $2.93 \times 10^{-5}$ | PNM [b] |
| Average coordination number at t = 0s | 3.64 | 3.49 | 3.72 | 3.56 | PNM [b] |
| Average pore velocity at t = 0s ($m\ s^{-1}$) | $2.43 \times 10^{-5}$ | $2.79 \times 10^{-5}$ | $2.47 \times 10^{-5}$ | $2.47 \times 10^{-5}$ | PNM [b] |
| Size of the full sample length (Voxels) | 1319×1317×2494 | 1316×1316×2418 | 1317×1319×2552 | 1317×1318×2342 | XMT Images |
| Size of the cropped sample length (Voxels) | 1319×1317×1950 | 1316×1316×1950 | 1317×1319×1950 | 1317×1318×1850 | XMT Images |
| Size of the half sample length (Voxels) | 1319×1317×818 | 1316×1316×850 | 1317×1319×850 | 1317×1318×782 | XMT Images |

**Table 5.1: Parameters for all four dissolution experiments including the skeleton (pore network) information. [a] XMT image of cropped sample length. [b] Pore Network Model of cropped sample length. It should be noted that the measured pH values for the NCHS and the HCHS are impacted by the non-compatibility of the utilized electrode with the high number of ions in the solutions.**

## 5.3 Results and Discussions

This study is based on four reactive flow experiments (Table 5.1): NCLS (No Calcium Low Salinity), LCLS (Low Calcium Low Salinity), NCHS (No Calcium High Salinity) and HCHS (High Calcium High Salinity). The analysis of effluent solution for all four experiments is provided in Section 5.3.1.1. The results are compared with the XMT image-based analysis in Section 5.3.1.2. Next, we assess the temporal evolution of bulk porosity and local porosity in Section 5.3.1.3 and corresponding effective reaction rate in Section 5.3.1.4. Further, we examine the characteristics of the dissolution structures developed in each experiment in Section 5.3.2. Finally, the impact of the dissolution structures on permeability changes is provided in Section 5.3.3.

### 5.3.1 Mass transfer analysis

### 5.3.1.1 Effluent Analysis

Figure 5.2a presents the temporal evolution of the normalized $Ca^{2+}$ concentration $\Delta cCa$, which represents the difference between outflow and inflow $Ca^{2+}$ concentration in a sampling interval. Positive values of $\Delta cCa$ for experiments NCLS, LCLS and NCHS indicates persisting dissolution throughout the experiments. From the first sampling point onwards, the experiment NCLS maintains a steady state value of outlet $Ca^{2+}$ concentration and $\Delta cCa$. Experiment LCLS, on the contrary, initially provides a lower outflow concentration compared to NCLS, which later increases towards a higher steady state value. For experiment NCHS, outflow $Ca^{2+}$ concentration shows a decreasing trend. From the saturation index of the injected solutions, we estimated the maximum amount of $Ca^{2+}$ concentration which could be dissolved before these solutions would reach equilibrium with respect to calcite. Comparison of these estimates with the measured $\Delta cCa$ suggests that the outflow solutions of experiments NCLS, LCLS and NCHS are almost in equilibrium with calcite (Figure A5.7a).

In the case of experiment HCHS, normalized $\Delta cCa$ is negative initially, followed by positive values (Figure 5.2a). As stated earlier, the inflow solution HCHS is acidic, with the measured pH value of 3.05, and undersaturated with respect to the calcite. Also, from exploring mixing calculations (i.e., PHREEQC + pitzer calculations on mixing different fractions of inflow solution HCHS with a solution in equilibrium with calcite), we did not find any ratios which can lead to a supersaturated mixture or salting-out conditions. Moreover, from the saturation index, we estimated that this solution can dissolve up to around $0.7 \times 10^{-3}$ mol dm$^{-3}$ calcite, before reaching equilibrium with respect to calcite (Figure A5.7a). Therefore, it is most likely that the initial negative $\Delta cCa$ value does not represent calcite precipitation but is caused by error accumulation during the strong dilution necessary on in- and outflow samples in preparation of ICP-OES measurements from which $\Delta cCa$ values were calculated. We suspect the calculated $Ca^{2+}$ concentrations for HCHS samples include an uncertainty larger than the standard error of 10% (SI Section A5.1, Figure A5.8).

We observed the impact of salinity and $Ca^{2+}$ concentration of the inflow solutions on the equilibrium concentrations (Figure A5.7a). As expected, inflow solutions containing $Ca^{2+}$ ions (i.e., LCLS and HCHS) require a lower amount of $Ca^{2+}$ ions to reach to the equilibrium as compared to the inflow solutions with no $Ca^{2+}$ ions (i.e., NCLS and NCHS) (Figure A5.7a). Similarly, increments in salinity lead to enhanced solubility of calcite, with more saline inflow solutions dissolving larger amounts of calcite than the inflow solutions with lower salinity (i.e., NCLS) (Figure A5.7a).

Figure 5.2b shows the measured pH of the effluent samples from all four experiments. Inflow solutions all had an approximate pH value of 3.0 (Table A5.1Table A3.1). The higher pH values measured in the outflow indicate dissolution-induced fluid buffering. The amount of fluid

buffering directly relates to the amount of $Ca^{2+}$ ions produced (Figure 5.2). Initially, experiment NCHS shows both the highest value of pH and $Ca^{2+}$ concentration at the outflow, followed by a decreasing trend (Figure 5.2). For experiment NCLS, outflow pH remains constant and for experiment LCLS, outflow pH shows an increasing trend. We observed a good agreement between the measured outflow pH and predicted outflow pH (Figure A5.7b). For the experiment HCHS, the pH of the outflow solution is calculated corresponding to the equilibrium concentration. For this experiment, we observed a higher difference between the calculated pH and the measured pH (Figure A5.7b). This is probably due to the higher uncertainty associated with the pH measurement in highly saline $Ca^{2+}$-rich outflow solution.
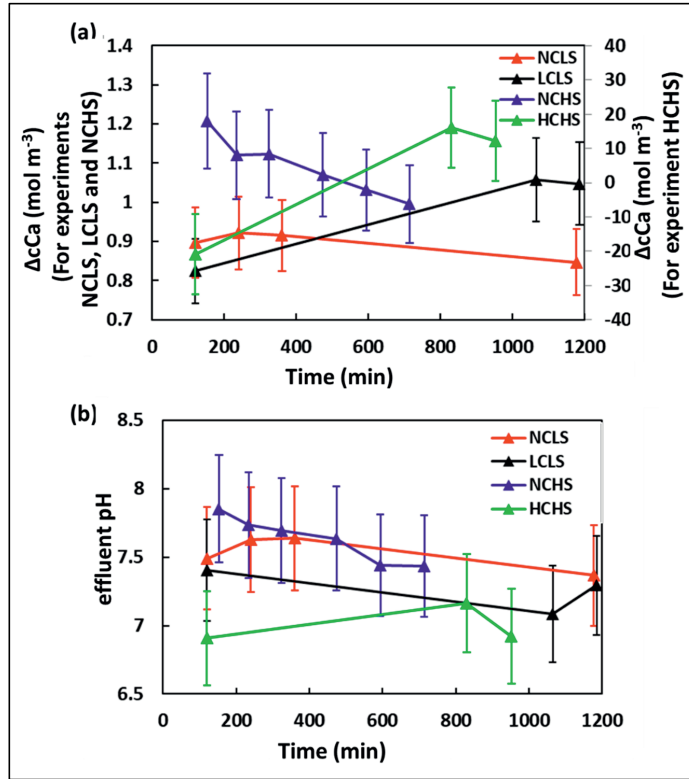


**Figure 5.2**: (a) Measured $Ca^{2+}$ concentration from effluent solution for experiments NCLS, LCLS, NCHS (left-hand vertical axis) and HCHS (right-hand vertical axis) (b) Measured pH from effluent solution for all four experiments.

**5.3.1.2 Effluent concentrations vs XMT Analysis**

Figure 5.3a shows a comparison of the dissolved volume of calcite, calculated using ΔcCa with values obtained from XMT image analysis using Equations 5.2 and 5.3, respectively. $\Delta V_{Calcite,effluent}^{n}$, the cumulative value of dissolved solid volume ($m^3$), is obtained as:

$$\Delta V_{Calcite,effluent}^{n} = \frac{Q\,M_{calcite}}{\rho_{calcite}} \sum_{i=1}^{n} \Delta cCa_{effluent}^{i}\,(t^{i} - t^{i-1}) \tag{5.2}$$

where, n is the sampling steps, $Q$ is the flow rate (m$^3$ s$^{-1}$), $\rho_{calcite}$ is the density of calcite (2710 Kg m$^{-3}$), $M_{calcite}$ is the molecular mass of calcite (0.1 Kg mol$^{-1}$) and $\Delta cCa_{effluent}$ is the outflow Ca$^{2+}$ concentration (mol m$^{-3}$).

$\Delta V_{Calcite,XMT}$, the change in the number of solid voxels of XMT images in an experiment duration denoted by time t, is given as:

$$\Delta V_{Calcite,XMT} = V_{Calcite,XMT}^t - V_{Calcite,XMT}^{t=0} \tag{5.3}$$

For experiments NCLS, LCLS and NCHS, we observed a difference of ~around 14-25% between values obtained from effluent analysis and those from XMT images (Figure 5.3a). A potential cause of this discrepancy could be resolution of imaging (voxel size 6 μm). This difference would be dependent on the length of the sample along the flow direction used in volume change calculations. Increased difference for cropped length sample-based analysis, as shown in Figure 5.3a, is due to dominance of dissolution close to the sample inlet. As discussed in Section 5.2.2, the remaining part of this study will be based on the analysis of the cropped length sample. Figure A5.2 shows the cropping position through a vertical slice of sample K1.

For experiment HCHS, the difference between effluent analysis and XMT images is more significant (Figure 5.3a). This, along with the arguments provided in Section 5.3.1.1 further suggest that the ICP-OES measurement of solutions containing a high amount of Ca$^{2+}$ ions might have inherited higher uncertainty.
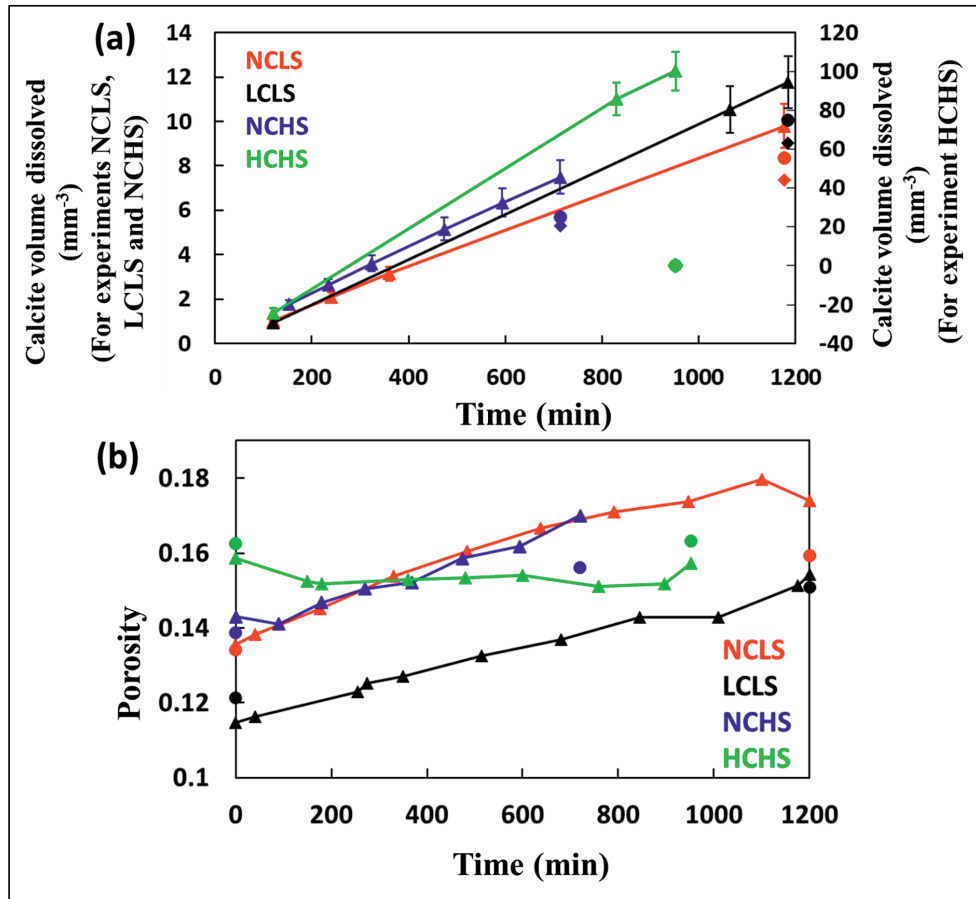
**Figure 5.3:** (a) Cumulative volume of the dissolved calcite calculated from effluent analysis (triangle) and XMT images (circle, full sample length and diamond, cropped sample length) for experiments NCLS, LCLS, NCHS (left-hand vertical axis) and HCHS (right-hand vertical axis) (b) temporal evolution of the macroporosity calculated from XMT images (circle, cropped sample length and triangle, half sample length) for all four experiments.

### 5.3.1.3 Porosity

Time-lapse imaging of the sample allowed *in-situ* tracking and analysis of the dissolution induced changes in the porosity. Figure 5.3b shows the temporal evolution of macroporosity during the four experiments calculated from XMT images. Injection of undersaturated solutions led to an increase in the macroporosity of samples for experiments NCLS, LCLS, and NCHS. Consequently, total increments in the macroporosity are of magnitudes 0.025, 0.0296 and 0.0158 for experiments NCLS, LCLS, and NCHS, respectively.

For the experiment HCHS, macroporosity of the top half of the sample first slightly decreases and then this decreased macroporosity is maintained until near the end of the experiment, where a slight increase is observed (Figure 5.3b). Luquot et al., 2014 has also observed similar decrement in the macroporosity for the acids with lower corrosiveness (i.e. less strong undersaturation). They noted that the acids with lower reactive strength attack the microporosity of the grain and resultant small particles clog the macropores. The change in

macroporosity obtained from XMT images does not resolve such changes in microporosity. Therefore, changes in the microporosity of the sample were investigated through changes in grey volume in the full samples between beginning and end of the experiment (SI Section A5.1). For this experiment, we observed that the total change in the grey volume (i.e., microporosity + macroporosity) is $3.3 \times 10^{-9}$ m$^3$ as compared to the segmented volume (i.e., macroporosity) of a value of $0.16 \times 10^{-9}$ m$^3$ (Figure A5.9: semi quantitative). This suggests that the inflow solution HCHS has dissolved more sub-resolution calcite matrix and the detached fine grains accumulated in the macropores (cf. Luquot et al., 2014).

Figure 5.4 provides a vertical profile of porosity along the direction of the flow. Each data point is obtained using a moving average of 30 consecutive 2D slices (i.e., corresponding to 0.18mm). Comparison of the vertical porosity profile of the samples from the initial and final time steps of the dissolution experiment unveils the following information:

Firstly, control of initial porosity distribution of the sample into resultant porosity distribution: For experiment NCLS, we observed a strong deviation of evolved porosity distribution along the flow path compared to initial porosity distribution whereas, for experiment LCLS and NCHS, evolved porosity distribution is similar to initial porosity distribution (Figure 5.4a). This is caused by the difference in reactive strength of the injecting fluid, as also discussed Section 5.3.2.1.

Secondly, longitudinal heterogeneity of the dissolution front, which we define as a porosity difference (new porosity (%) - old porosity (%)) of more than 3%, along the direction of flow. We observed that solution NCLS creates maximum porosity changes in the first 2 mm part of the sample whereas for solution LCLS, the effective depth of reaction front (Figure 5.4b) is around 5mm. In the case of solution NCHS, the top 3mm part of the sample experiences an average of 3% porosity change. The depth of penetration of the reaction front is related to the amount of fluid buffering. Fluid buffering is a result of a complex interplay of initial reactive strength of the injecting fluid and transport time scale (e.g., Agrawal et al., 2020; Gray et al., 2018; Molins et al., 2014). Section 5.3.1.4 explores this relationship between reaction and transport time scale for an individual experiment. For experiments NCLS, LCLS, and NCHS, the whole sample showed positive porosity changes, whereas, for experiment HCHS, the top part of the sample shows negative porosity changes (Figure 5.4b). It is worth noting that for experiment HCHS, % macroporosity difference is less than 0.5% and that dissolution in micropores played an important role.

Note that, due to the constraints with the data acquisition as mentioned in Section 5.2.2, bulk porosity for the first- and last-time steps of the experiment is calculated from the data of the full sample (Figure 5.3b). However, porosity for the intermediate time steps was calculated from the data of half-length sample i.e., part of the sample near the injection point. The difference between porosity data of these two samples size at time t= 0 denotes the initial heterogeneity of the samples (Figure 5.4a) whereas, the difference at the end of the experiment is a result of dissolution heterogeneity along the direction of flow (Figure 5.4b).
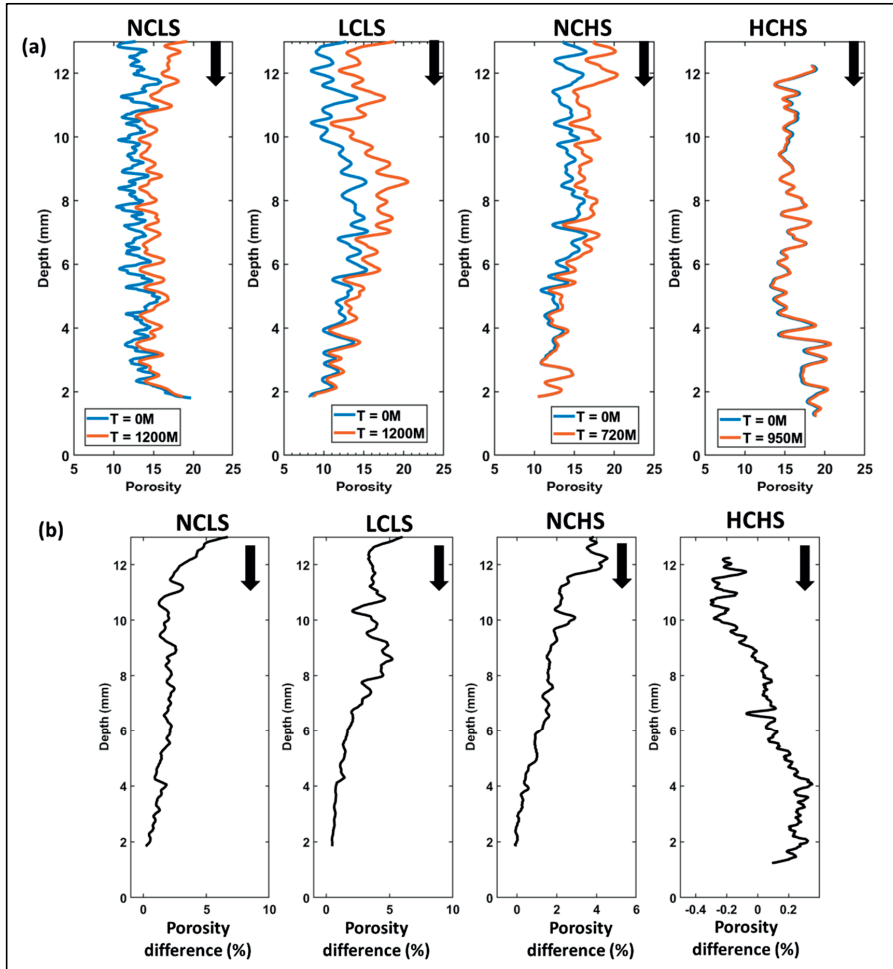
**Figure 5.4:** For all four experiments part of the vertical profiles of (a) The slice-averaged porosity values (%) and (b) difference between porosity values (%). The vertical profiles correspond to the XMT images of the cropped sample length at the beginning and the end of experiment. In order to increase the visibility, part of the vertical profile (i.e., from 1.8 till 12.5 mm) is shown here. Figure A5.11 shows full vertical profile (i.e., from 1.8 mm till 13.5 mm). Black arrow shows the flow direction. Note the different x-axis range utilized for panel (b). Note that flow was established from bottom to top of the sample and all presented images are upside down.

### 5.3.1.4 Reaction rate and dimensionless numbers

Time-lapse XMT scans of the sample provided the time-based evolution of the porosity. This porosity is utilized to obtain the dissolved mass to calculate the average reaction rate:

$$r_{calcite}(t) = \frac{\rho_{calcite}}{\Delta M_{calcite}} \frac{\Delta \emptyset_{XMT}(t)}{\Delta t} \frac{V_b}{A(t)} \tag{5.4}$$

where, $r_{calcite}(t)$ is the average reaction rate (mol m$^{-2}$ s$^{-1}$), $\Delta \emptyset_{XMT}$ (t) is the change in the macroporosity of the sample between the scan time t as compared to the initial porosity, $\Delta t$ (s)

is the acquisition time of the image and A(t) (m$^2$) is the surface area obtained by adding up the voxel faces forming the boundary between solid and pore phase and $V_b$ (m$^3$) is the total volume of the sample. Average reaction rates at different time steps of the experiment are calculated from the XMT images of the half-length sample. The average reaction rate at the beginning and at the end of the experiment is also calculated from the XMT images of the cropped length sample. Figure 5.5a shows the evolution of the average reaction rate for all four experiments.

Equation 5.4 calculates the average reaction rate from the average porosity changes. Additionally, we have calculated local reaction rate as:

$$rz_{calcite}(z,t) = \frac{\rho_{calcite}}{\Delta M_{calcite}} \frac{\Delta \emptyset_{XMT}(t,z)}{\Delta t} \tag{5.5}$$

where, $rz_{calcite}(z,t)$ is local reaction rate (mol m$^{-3}$) calculated from the change in the slice-averaged porosity of the sample (i.e., Figure 5.4b), between the scan time t and at a distance of z from the sample inlet. Figure A5.12 shows the vertical profile of the local reaction rate calculated from the XMT images of the full sample obtained at the beginning and at the end of the experiment.

We observed that the addition of the Ca$^{2+}$ ions in the inflow solution decreases the calcite dissolution rate (NCLS vs LCLS and NCHS vs HCHS in Figure 5.5a and Figure A5.12). For example, at 40 minutes, the average dissolution rate corresponding to the NCLS solution is 47.3% higher than the solution LCLS. Similarly, the solution NCHS (i.e., no Ca$^{2+}$ ions and high salinity) also showed higher average dissolution rate as compared to the solution HCHS (i.e., 337 × 10$^{-3}$ mol dm$^{-3}$ Ca$^{2+}$ ions and high salinity). In the past, several studies have shown such inhibitory impact of the Ca$^{2+}$ ions over the calcite dissolution kinetics (Buhmann and Dreybrodt, 1987; Sjöberg and Rickard, 1985).

In this study, we observed that at the sample inlet, the dissolution rate corresponding to the solution NCHS is around 54% lower than the solution NCLS (Figure A5.12). Moreover, the average dissolution rate calculated from the half sample length is lower for the experiment NCHS than the experiment NCLS (Figure 5.5a). This contrasts with the effluent analysis where the outflow Ca$^{2+}$ concentration was higher for experiment NCHS than the experiment NCLS (Figure 5.2a). This can be explained by the counter intuitive impacts of the salinity on the dissolution rate and calcite solubility. For saline solutions, on one hand dissolution rate may become reduced while on the other hand calcite solubility is increased. Therefore, the saline solution, despite showing reduced dissolution rates in the vicinity of the sample inlet, is capable of dissolving greater amounts of calcite from the whole sample length before attaining equilibrium with the calcite.

In order to understand the coupling of transport and reaction times scales, we define two dimensionless numbers i.e., Peclet number and Damköhler number.

The Peclet number (*Pe*) compares the time scale of advection to that of diffusion and is defined as:

$$Pe(t) = \frac{U_{av}(t) \, l(t)}{D} \tag{5.6}$$

where, $U_{av}$ (m s$^{-1}$) is the average pore velocity obtained by dividing Darcy velocity with the image-based porosity, $l$ is the mean pore radius calculated from the extracted pore network of the sample and $D$ is the diffusion coefficient (3.36 × 10$^{-9}$ m$^2$ s$^{-1}$).

The Damköhler number ($Da$) compares the convection time scale with the reaction time scale:

$$Da(t) = \frac{\tilde{R} \; MV_{calcite}}{U_{av}(t)} \tag{5.7}$$

where, $MV_{calcite}$ is the molar volume of calcite ($3.69 \times 10^{-5}$ m$^3$ mol$^{-1}$) and $\tilde{R}$ indicates the reactive strength of the injecting acid (mol m$^{-2}$ s$^{-1}$). This is estimated from the time-based average reaction rate of the half sample length as:

$$\tilde{R} = \left| \sum_{i=1}^{n} r_{calcite}(t_i) \right| \tag{5.8}$$

where, $r_{calcite}(t_i)$ is the average reaction rate of the half sample length at time $t_i$ and n denotes the total number of the time-lapse scans of the half sample length. The $Pe$ and $Da$ number, at different time steps is calculated from the XMT data of the half sample length, while, at the beginning and at the end of the experiment is calculated from the XMT data of the cropped sample length.

The $Pe$ number for all four experiments was greater than one, indicating advection-controlled transport regimes such that the rate of renewal of the fluid inside an individual pore of the sample was dominated by advection (Figure 5.5b). For all experiments, the $Da$ number was less than 1. This suggests that the dissolution conditions in the sample were reaction limited (Figure 5.5c) as time scale of advection is shorter than that of dissolution reaction. As the experiments progressed, the $Pe$ number decreased due to the increasing porosity of the samples (and therefore increase of pore sizes). For the studied reaction-controlled dissolution regime, this decrease of the $Pe$ number resulted in a decrease in the average dissolution rate (Figure 5.5a). This impact of the temporal evolution of the $Pe$ number over the average dissolution rate is much more clearly visible for the experiment NCLS as compared to the experiments LCLS and NCHS.
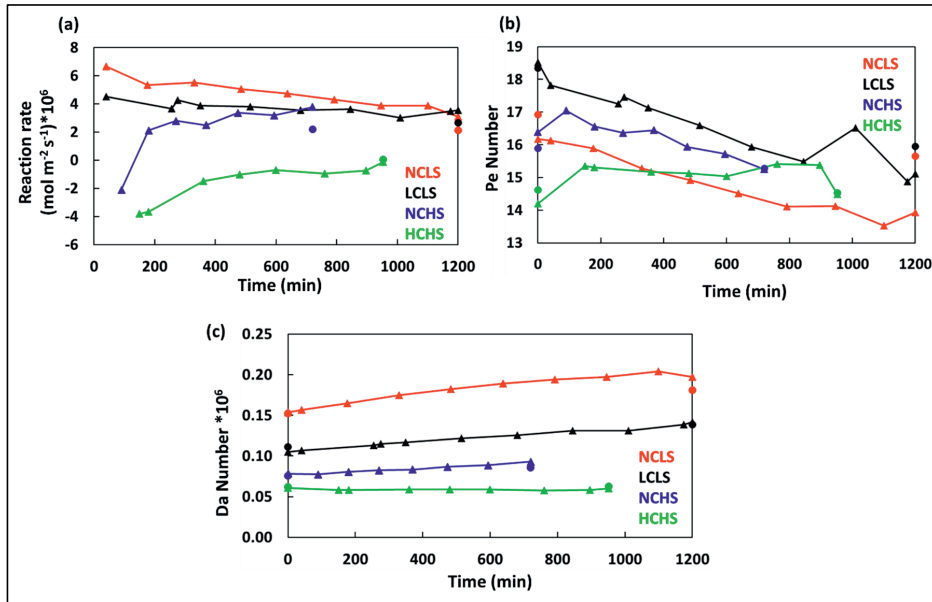
**Figure 5.5:** Temporal evolution of the (a) average reaction rate based on Equation 5.4 (b) *Pe* Number and (c) *Da* number, calculated from XMT images (circle, cropped sample length and triangle, half sample length).

## 5.3.2    Evolution of the dissolution Structure

All four experiments were performed with the same injection rate and on samples of the same rock type with very comparable pore structure (Figure 5.1). Therefore, the reactive strength of the injecting solutions was directly reflected by the *Da* number. The *Da* number is highest for experiment NCLS, then LCLS, NCHS, and HCHS. Previously, the control of the *Da* number on the dissolution patterns has been investigated through both experimental and numerical studies (e.g. Fredd and Fogler, 1998; Golfier et al., 2002; Hoefner and Fogler, 1988; Luquot et al., 2014; Maheshwari et al., 2013). In the following, we discuss the qualitative and quantitative aspects of the dissolution patterns developed in each experiment.

### 5.3.2.1 Dissolution structures in experiments NCLS, LCLS and NCHS
Experiment NCLS was performed with a solution that has low salinity, devoid of $Ca^{2+}$ ions. This injected solution initiated the dissolution with an effective reaction rate of a magnitude of $7 \times 10^{-6}$ mol m$^{-2}$ s$^{-1}$ (Figure 5.5a). Addition of a small amount $Ca^{2+}$ ions (experiment LCLS), lowered initial effective reaction rate to $4 \times 10^{-6}$ mol m$^{-2}$ s$^{-1}$ (Figure 5.5a). In the experiment NCHS, injection of a saline solution that did not contain $Ca^{2+}$ ions, caused a lower dissolution rate than in experiments NCLS and LCLS (Figure 5.5a and Figure A5.12).

Time-lapse scanning of the pore space allowed a qualitative analysis of the temporal evolution of the dissolution structures in these experiments. For the experiment NCLS, we observed that in the first 40 minutes of duration, the dissolution was very homogeneous in the radial direction (Figure 5.6a). This suggests that the starting phase of the dissolution was predominantly controlled by the acidity of the fluid rather than the initial pore structure of the sample (Figure 5.6a). Such difference between the modified porosity and the initial porosity is also clear in the vertical porosity profiles provided in Figure 5.4a. The radially homogeneous dissolution occurred in the first ~2mm of the flow path, after which selective dissolution paths continued further along the flow direction (Figure 5.6a). This development of dissolving channels was most likely guided by the initial heterogeneity and structure of the sample. In contrasts to the experiment NCLS, we observed that in both lower *Da* number-based experiments LCLS and NCHS, the development of the dissolution structure is impacted more strongly by heterogeneity in the sample's pore structure (Figure 5.6b-c, and Figure 5.4a). For example, in the experiment LCLS, after 40 minutes of acid injection, dissolution has created sparsely located flow channels (Figure 5.6b). From the scans of the half sample length, we observed that the sample's pore space evolved into several conducting channels. The trajectories and length of these channels were established within a certain experiment duration (i.e., 484 minutes in experiment NCLS, 255 minutes in experiment LCLS and 369 minutes in experiment NCHS) while the diameter of channel continued to grow (Figure 5.6 and Figure A5.13). From the scan of the full sample, which was acquired at the end of the experiment (i.e., 1200 minutes for the experiments NCLS and LCLS; 720 minutes for the experiment NCHS), we observed that most of these channels did not develop much beyond the half sample length that was scanned during the experiment (Figure 5.7). In the experiment NCLS, two of the channels extend over the full length of the sample, while in the experiments LCLS and NCHS, only one such dominant channel was formed (Figure 5.7).

Next, through skeleton analysis, we performed a quantification of the final form of the dissolution structure in these three experiments (Figure A5.14;Table A5.2). The quantification was based on attributes derived from the individual segments of the channels and side branches:

the length (sum of the segment length), radius (radius of the segments) and mean radius (average of the segment radius).

The evolution of the dissolution structures also revealed that less reactive inflow solutions (i.e., higher $Ca^{2+}$ and/or salt concentration) resulted in localization of the dissolution structure. This is evident from the decreasing number of inlet nodes (number of inlet nodes = number of unique/main channels) with the decreasing $Da$ number (Table A5.2). All the channels originating from the inlet nodes are divided into three length-based categories (Figure A5.15-Figure A5.17; Table A5.2). Figure A5.18 shows the histogram of the channel lengths for experiments NCLS, LCLS and NCHS. We observed that in the experiment NCLS, two dominant channels of a length ~14 mm were formed. As compared to this, in the experiments LCLS and NCHS, only one dominant channel of the length of 12.30 and 10.28 mm, respectively, was formed.

The impact of the reactivity of the injected solution was also observed on the starting diameter of the channel (i.e., in the vicinity of the sample inlet). For example, in the experiment NCLS, the starting diameter of two of the category 1 channels is larger than 0.6 mm while, in the experiments NCLS, the starting diameter of both of the category 1 channels is smaller than 0.4 mm (Figure A5.19a and A5.19b). Moreover, the $Da$ number also represents the buffering of fluid as it moves along the sample (Agrawal et al., 2020). This is reflected in the vertical radius profile (i.e., in the direction of flow) of the channels. In the experiments LCLS and NCHS, the vertical radius profiles of the category 1 channels are more homogeneous than the experiment NCLS (Figure A5.19).

Furthermore, in the experiment LCLS, for each category 1 channel, the number of side branches and the length of the side branches was significantly higher than the experiment NCLS (Table A5.2, Figure A5.20a-b and Figure A5.21a-b). The increased ramification of dissolution channels with decreasing $Da$ number has also been observed by Luquot et al. (2014). On the contrary, the dissolution pattern in the experiment NCHS developed with the least amount of ramification as evident from the least number of end nodes (Table A5.2, Figure A5.20c).
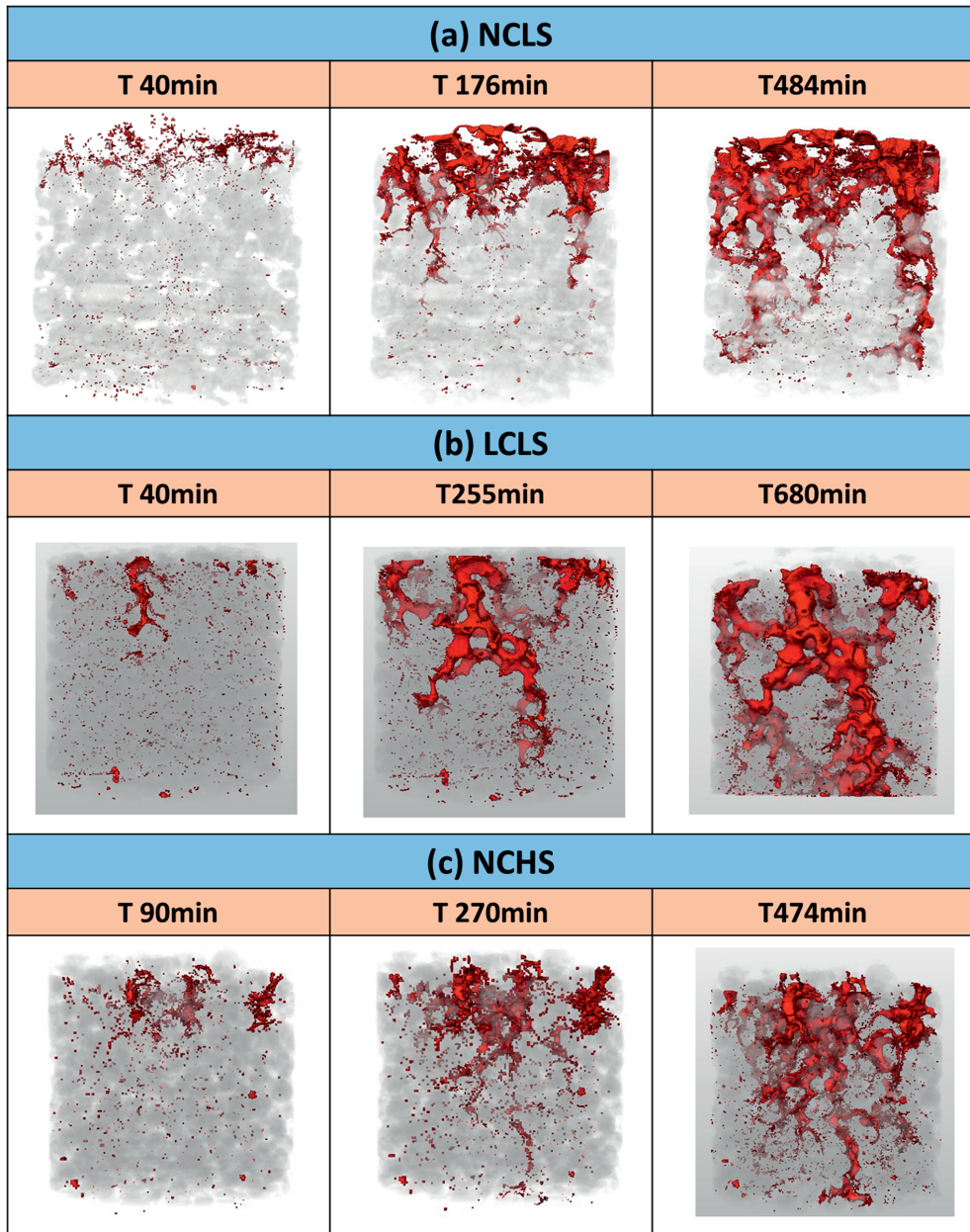
Figure 5.6: Temporal evolution of the dissolution patterns in experiment (a) NCLS, (b) LCLS and (c) NCHS. XMT images of these samples at the remaining time steps are shown in Figure A5.13.
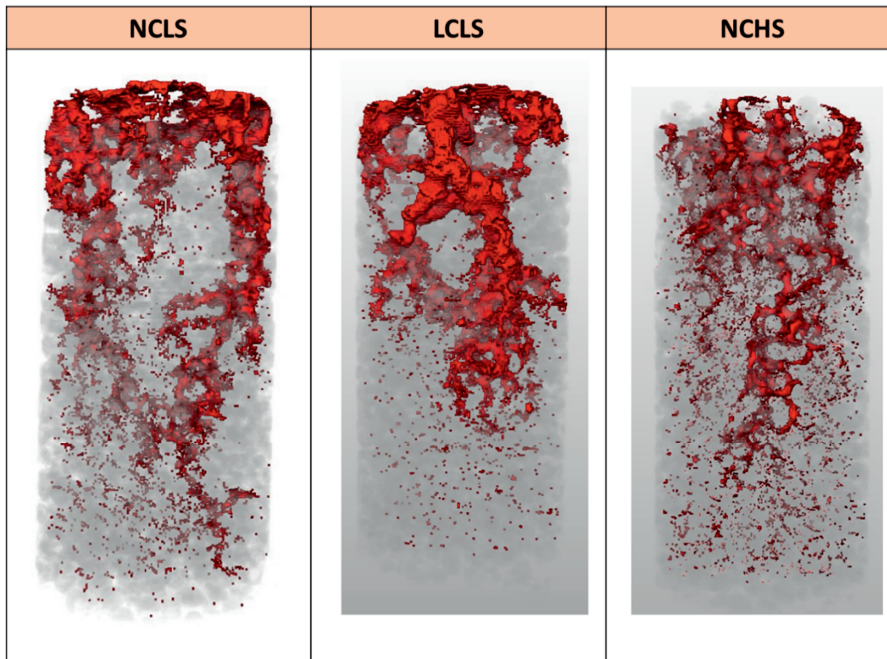
**Figure 5.7:** Final form of the dissolution patterns in experiments NCLS, LCLS and NCHS. Note that the duration of experiments NCLS, LCLS and NCHS was 1200, 1200 and 720 minutes.

### 5.3.2.2 Experiment HCHS

We observed that the presence of a high amount of $Ca^{2+}$ ions lowered the effective dissolution rate by two orders of magnitude compared to experiment NCHS (Figure 5.5a). As mentioned earlier, the macroporosity of the top part of the sample decreased throughout this experiment (Figure 5.3b and Figure 5.4). Figure 5.8 presents the temporal evolution of the pore space where the locations of removed solid mass and of added solid mass are highlighted. As explained earlier, the injected HCHS was acidic and undersaturated with respect to the calcite and mixing calculations, performed in PHREEQC with Pitzer database, showed that it is unlikely that mixing variable amounts of the HCHS solution with the equilibrated initial solution present in the sample can result in a composition that is supersaturated with respect to calcite. An alternative explanation of the accumulated solid mass in the pore space is related to the dissolution of the microporous matrix, causing solid particles to detach from the matrix and migrate through the pore space. This is described by the so-called sugar lump model (Luquot et. al., 2014). From the XMT image after 150 minutes of acid injection, we observed that small amounts of such displaced particles were uniformly distributed in the pore space (green in Figure 5.8). Dissolution of the microporous matrix was confirmed by grey value analysis of the images (Figure A5.9; semi quantitative), which showed an increase in the sum of microporosity and macroporsity. From the scan of the full sample at the end of the experiment (Figure 5.8c), we observed that the amount of clogging by displaced solid particles is higher closer to the inlet. This is consistent with most of the dissolution occurring closer to the inlet, also in the microporous domain, leading to more detachment and local displacement of particles.
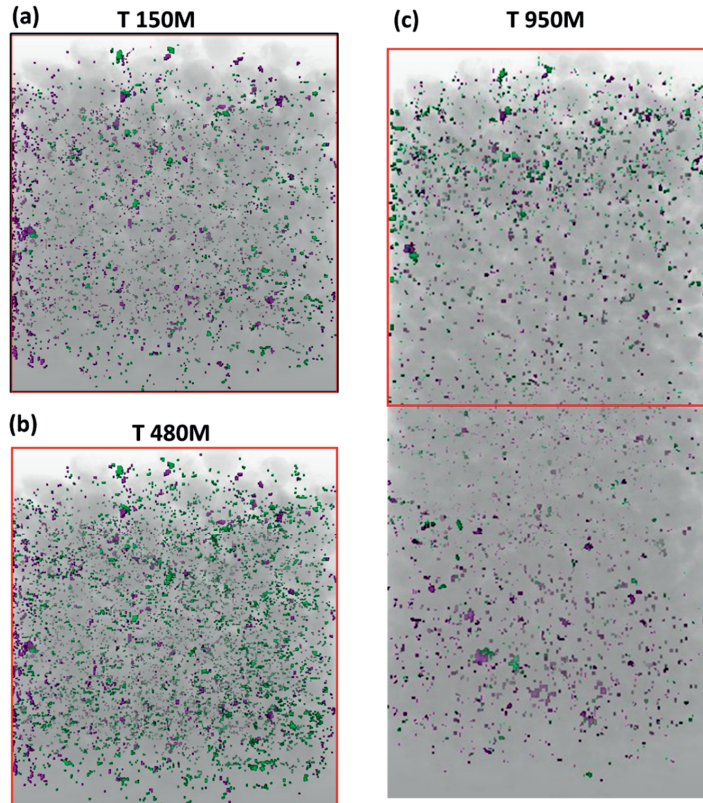
**Figure 5.8:** Temporal evolution of the pore space in the experiment HCHS. Purple colour highlights the locations from where the solid mass is removed. Green colour highlights the locations where the solid mass is added. XMT images of this sample at other time steps are shown in Figure A5.22. Note that red coloured box shown in plot (c) indicates the volume imaged in plots (a) and (b).

### 5.3.3   Evolution of transport properties

Dissolution patterns control permeability changes in the sample, and this is related to the volume of acid injection required for wormhole breakthrough ($PV_{BT}$). One of the earlier definitions of wormhole breakthrough is when the permeability of the sample increases by a factor of 100 (Fredd and Fogler, 1998). The amount of acid required for a breakthrough is a function of the dissolution pattern, and therefore of the $Pe$ and $Da$ numbers, which reflect the injection rate and the solution's corrosive nature (i.e. chemical reactivity, in the current case determined by salinity and calcium concentration). For example, face dissolution will require higher volumes of acid to attain a certain permeability increment than wormholes.

Figure A5.23 shows the temporal evolution of permeability during all four experiments. Permeability was obtained from the single-phase flow simulation of the extracted pore network for the sample. We observed a noticeable permeability increment in the experiments NCLS, LCLS and NCHS, while no significant permeability changes in experiment HCHS were observed.

If we consider the definition of breakthrough from Fredd and Fogler (1998), none of the experiments in this study led to breakthrough point (Figure A5.24). The highest permeability increment corresponding to a factor of 25 was noted for experiment LCLS. We observed that the injection of the same number of pore volumes resulted in the highest permeability increment for experiment LCLS and lowest for experiment HCHS (Figure A5.24). This indicates that the dissolution pattern formed in experiment LCLS is optimal, just as the *Da* number of this experiment is optimal among all four experiments.

The volume of acid required for breakthrough was calculated through extrapolation of permeability response curve of Figure A5.24. Figure 5.9 shows the distribution of $PV_{BT}$ as a function of *Da* number. As expected for experiment LCLS, the lowest amount of pore volumes is required to achieve an increase in permeability by a factor of 100. This suggest that the increasing amount of salinity and $Ca^{2+}$ concentration of the injecting solution results to increase in the number of acid pore volumes required for changing the permeability.
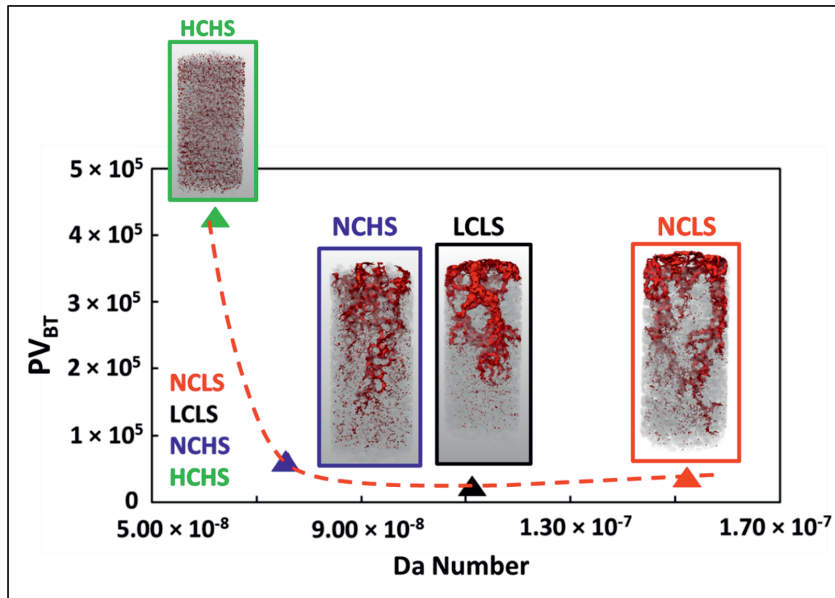


**Figure 5.9:** The expected number of pore volumes to obtain a full breakthrough curve at different *Da* number.

Figure 5.10 shows the changes in permeability as a function of porosity for all four experiments. In the past, several experimental and modelling studies have used the simplified version of Kozeny -Carman relation i.e., a power-law relation as $k \sim \phi^n$ , to relate the permeability changes with the evolving porosity of the sample (e.g. Bernabé et al., 2003; Luquot et al., 2014; Luquot and Gouze, 2009; Nogues et al., 2013; Pereira Nunes et al., 2016). The exponent n is a function of the initial porous medium properties and the processes which cause the changes in the pore structure. A higher value of n results in higher permeability change with small porosity changes. We observed that corresponding to the recorded dissolution patterns here, n ranges from 1.6 for experiment HCHS to 11 for experiment LCLS (Figure 5.10). Since the initial porous medium for the various experiments presented here was very similar (Figure 5.1), this wide range of n values does not reflect the initial porous medium properties but the composition of the injected solution, and therefore *Da* number. The presented variability in the exponent *n* suggests that precaution should be taken in generalization of a

single porosity-permeability model for a range of reservoirs containing formation water of different salinities. Potentially, the impact of $Ca^{2+}$ concentration and salinity can be implemented in derivation of porosity-permeability models to improve their predictability.
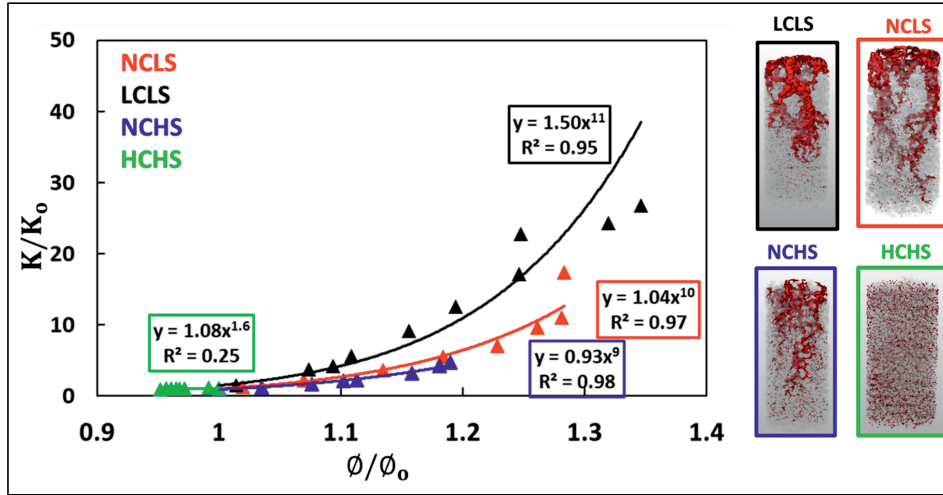


**Figure 5.10:** Permeability-porosity relationships for four experiments (triangle, half sample length).

## 5.4    Conclusions

We have imaged the dissolution of Ketton limestone at the same flow conditions and different reactive conditions, achieved through injection of different types of brine. We have observed a strong impact of the brine composition on changes in porosity and permeability. The amount of calcium ions and sodium chloride salt in the injecting solution determined the calcite dissolution rate such that both significantly inhibited the dissolution rate. We find that solutions with low salinity and no calcium ions lead to highest effective calcite dissolution rate. This highly reactive solution dissolved calcite predominantly in the vicinity of the sample inlet and relative less along the flow path. This resulted into the development of wormholes with vertically heterogeneous radius profiles. Injecting solutions containing low (1mM) calcium concentration resulted into the formation of selective dissolution paths. In this experiment, the developed wormhole had a relatively more homogeneous vertical radius profile as well as a higher amount of ramification. Similar localization of the dissolution features was observed for the higher salt, no added calcium solution. Lastly, the injecting solution with high salt and calcium concentration results in a dissolution rate around 2 orders of magnitude lower than the other experiments. For such least reactive very small amount of dissolution was recorded, distributed uniformly across the sample and predominantly within the micropore space.

Despite the initially similar porous medium properties, a wide range of exponents was obtained for the Kozeny-Carman relationship between rock permeability and porosity evolution. This wide range is due to the difference in the reactivity (corrosiveness) of the injected solutions. In summary, we observed that different combinations of salinity and $Ca^{2+}$ concentrations in the injected solution can impact dissolution and change it from disseminated and microporous regime to wormhole regime which leads to differences in the porosity-permeability relationship.

**Appendix 5**

| Species | Injected solution NCLS | | Injected solution LCLS | | Injected solution NCHS | | Injected solution HCHS | |
|---|---|---|---|---|---|---|---|---|
| | Molality (M) | Activity | Molality (M) | Activity | Molality (M) | Activity | Molality (M) | Activity |
| $H^+$ | $1 \times 10^{-3}$ | $7.9 \times 10^{-4}$ | $1 \times 10^{-3}$ | $7.9 \times 10^{-4}$ | $1 \times 10^{-3}$ | $1.0 \times 10^{-3}$ | $1 \times 10^{-3}$ | $8.9 \times 10^{-4}$ |
| $OH^-$ | $1 \times 10^{-11}$ | $1.3 \times 10^{-11}$ | $1.8 \times 10^{-11}$ | $1.3 \times 10^{-11}$ | $1.8 \times 10^{-11}$ | $9.6 \times 10^{-12}$ | $4.7 \times 10^{-11}$ | $1.1 \times 10^{-11}$ |
| $CO_2$ | $1 \times 10^{-5}$ | $1.1 \times 10^{-5}$ | $1.1 \times 10^{-5}$ | $1.1 \times 10^{-5}$ | $9.3 \times 10^{-6}$ | $1.1 \times 10^{-5}$ | $9.8 \times 10^{-6}$ | $1.1 \times 10^{-5}$ |
| $HCO_3^-$ | $7.8 \times 10^{-9}$ | $6.4 \times 10^{-9}$ | $7.8 \times 10^{-9}$ | $6.4 \times 10^{-9}$ | $9.1 \times 10^{-9}$ | $4.9 \times 10^{-6}$ | $6.3 \times 10^{-9}$ | $5.6 \times 10^{-9}$ |
| $CO3^{-2}$ | $1.6 \times 10^{-6}$ | $3.7 \times 10^{-16}$ | $1.6 \times 10^{-6}$ | $3.7 \times 10^{-16}$ | $3.3 \times 10^{-15}$ | $2.2 \times 10^{-16}$ | $1.7 \times 10^{-14}$ | $2.9 \times 10^{-16}$ |
| $Cl^-$ | $2.0 \times 10^{-1}$ | $1.4 \times 10^{-1}$ | $2.0 \times 10^{-1}$ | $1.4 \times 10^{-1}$ | $1.2$ | $7.1 \times 10^{-1}$ | $8.0 \times 10^{-1}$ | $4.8 \times 10^{-1}$ |
| $Na^+$ | $2.0 \times 10^{-1}$ | $1.5 \times 10^{-1}$ | $1.97 \times 10^{-1}$ | $1.5 \times 10^{-1}$ | $1.2$ | $8.7 \times 10^{-1}$ | | |
| $Ca^{+2}$ | | | $1 \times 10^{-4}$ | $3.05 \times 10^{-5}$ | | | 4.00E-01 | 1.00E-01 |
| pH | 3.1 | | 3.1 | | 3.00 | | 3.05 | |
| SI* | N/A | | -11.45 | | N/A | | -8.04 | |

**Table A5.1:** Composition of the injected solutions calculated from PHREEQC and Pitzer database.* saturation index *SI* with respect to calcite calculated as $(a_{Ca^{2+}} \, a_{CO_3^{2-}})/(K_{eq})$, where $K_{eq} = 10^{-8.48}$ (Plummer and Busenberg, 1982). $a_{Ca^{2+}}$ and $a_{CO_3^{2-}}$ are the activities of $Ca_{2+}$ and $CO_3^{2-}$ calculated from the respective concentrations and ionic activity coefficients using Pitzer equation.
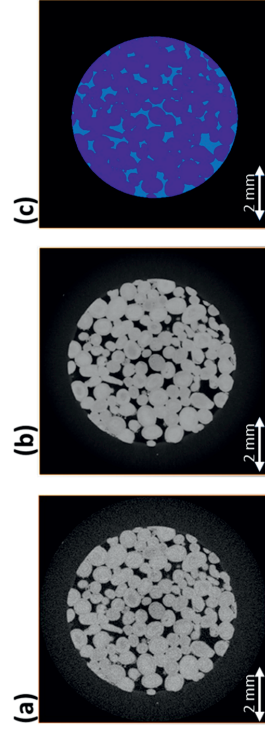


**Figure A5.1:** Workflow of the image processing starting from (a) raw image (b) filtered image and (c) segmented image.

154
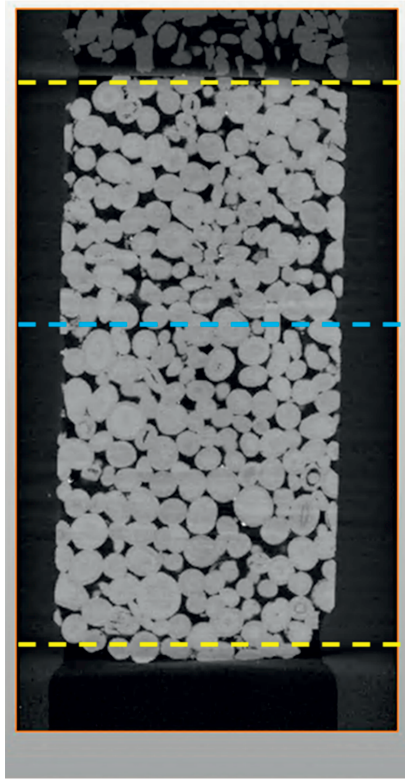
**Figure A5.2:** Three sizes are referred in the main text i.e., full sample length, cropped sample length and half sample length. Yellow lines at the top and bottom of the sample mark the size of the cropped sample length. Yellow and blue lines at the top and bottom of the sample, respectively, mark the size of the half sample length.
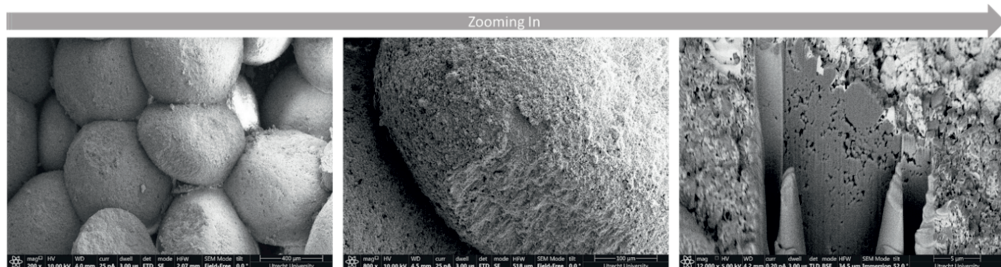


**Figure A5.3:** Example of microporosity in one of the Oolite grains in Ketton sample
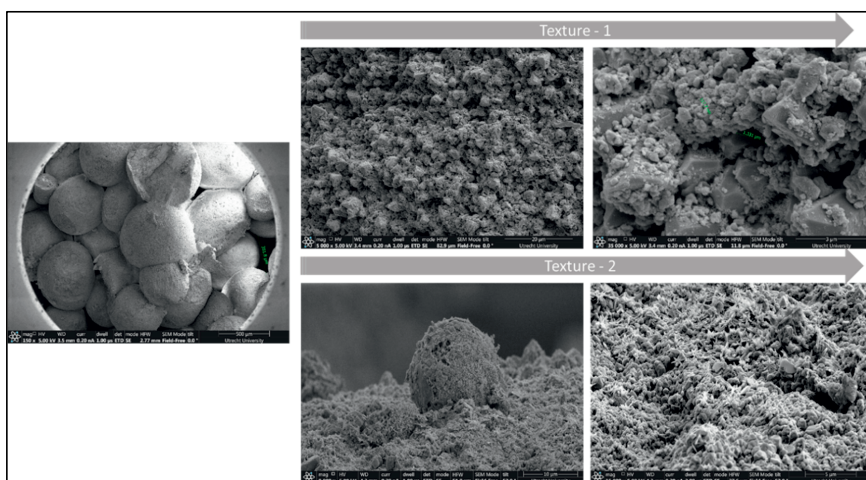
**Figure A5.4:** SEM image of the part of the Ketton sample showing textural heterogeneity.
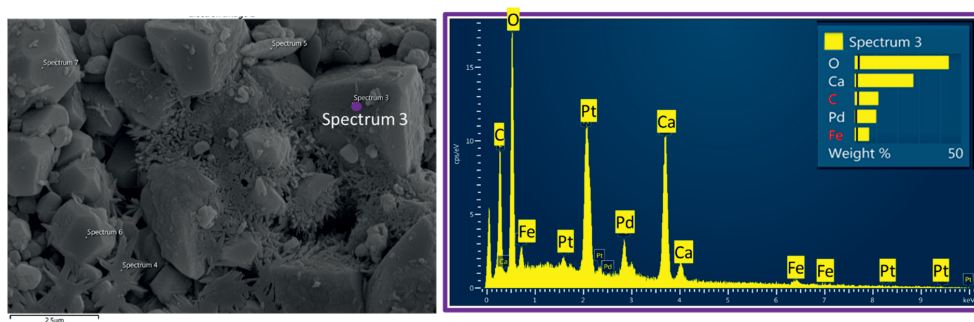


**Figure A5.5:** SEM-EDS analysis of the part of the Ketton sample. Note that Pt and Pd are measured due to the conductive coating sputtered on the sample to prevent charging by the electron beam.
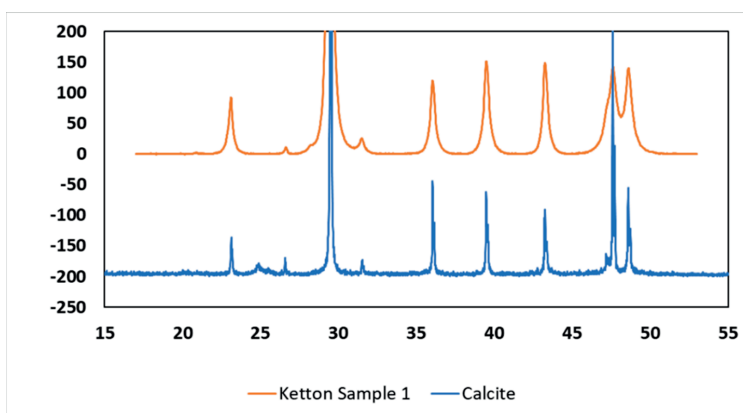


**Figure A5.6:** XRD spectra of the Ketton rock and RRUFF referenced Calcite mineral.
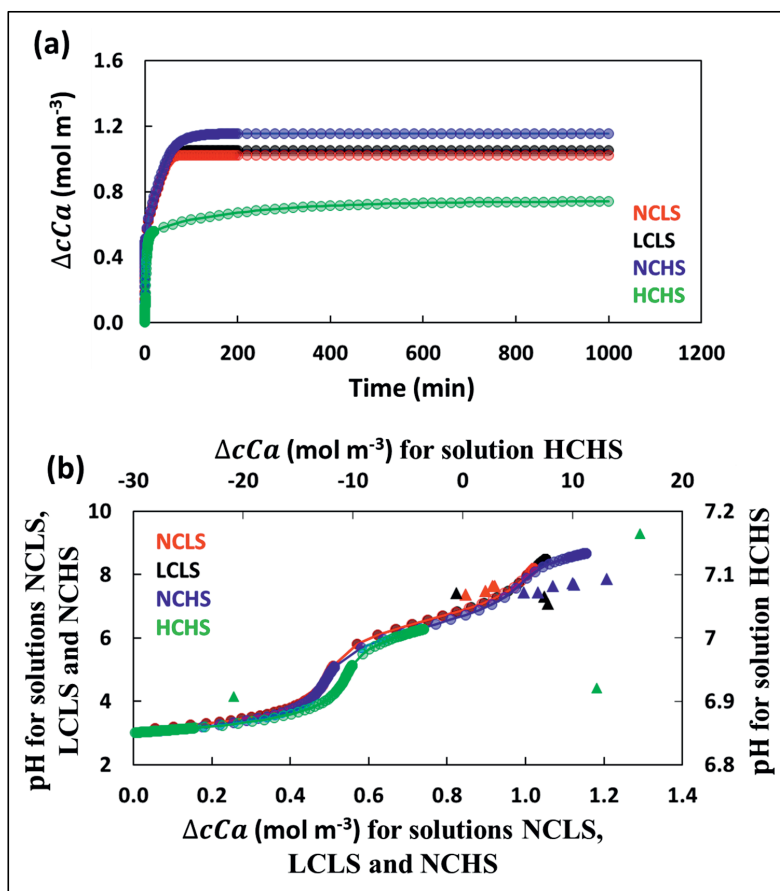
**Figure A5.7:** Corresponding to all four injected solutions, PHREEQC based (a) maximum amount of $\Delta cCa$ which can be dissolved before the solution reaches to the equilibrium (b) pH of the solution as a function of the added amount of $\Delta cCa$.

## A5.1 Experiment HCHS - Effluent Analysis VS XMT Image Analysis

*ICP-OES measurement of the inflow and outflow samples*: Each data point correponding to the experiment HCHS in Figure 5.2a utilizes an average outflow and inflow concentration based on three outflow samples and six inflow samples, respectively. Figure A5.8 shows the statistics of the measured $Ca^{2+}$ concentrations from all analyzed samples. Repeatitive anaysis showed an inconsistency of a magnitude higher than 10%.

*Grey-volume analysis:* Calculation of the dissolved rock volume from XMT images in Figure 5.3a, have utilized segmented images of the sample. Results of the segmentation procedure is sensitive to the choice of the threshold value (Shah et al., 2016). Moreover, analysis based on the segmented images does not account for the changes happened at the subresolution scale. Therefore, we have estimated the sub-resolution porosity from difference images (Ghous et al., 2007; Lin et al., 2017). For this purpose, we have utilized the grey volumes of the sample belonging to the start and end of the experiment, referred as P and Q, respectively. This calculation was performed using following steps:

- In order to match the grey scale range, both grey volumes P and Q were normalized to a range of 0-255. This means that in the resultant volumes, the voxels with a grey value of 255 are made of 100% solid and voxels with a grey value of 0 are made of 100% pore.
- These normalized grey images are subtracted from each other.
- Finally, the grey value of each of the voxel of the resultant difference is converted into the %phase change.

Figure A5.9 shows the dissolved rock volume calculated from the difference grey images and segmented images. Note that this is a semi quantitative method to estimate the changes in microporosity which is based on the assumption that intensity range of both of the grey volume of the sample (i.e., belonging to the begninning and end of the experiment) have peak to peak matching.
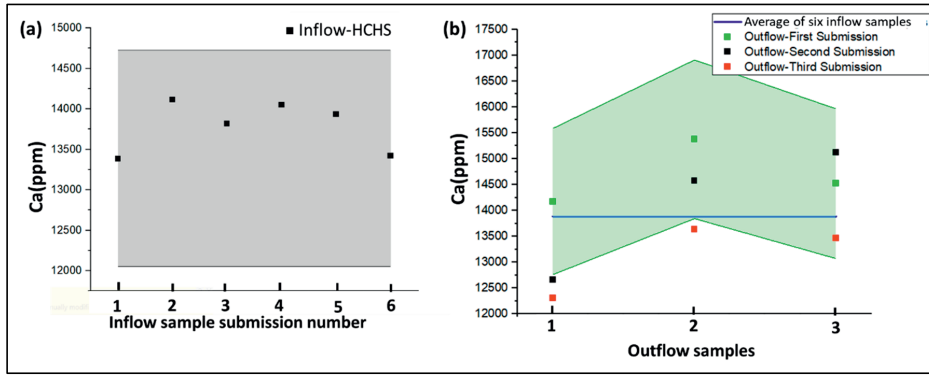


**Figure A5.8:** Statistics of the inflow and outflow measurements from experiment HCHS
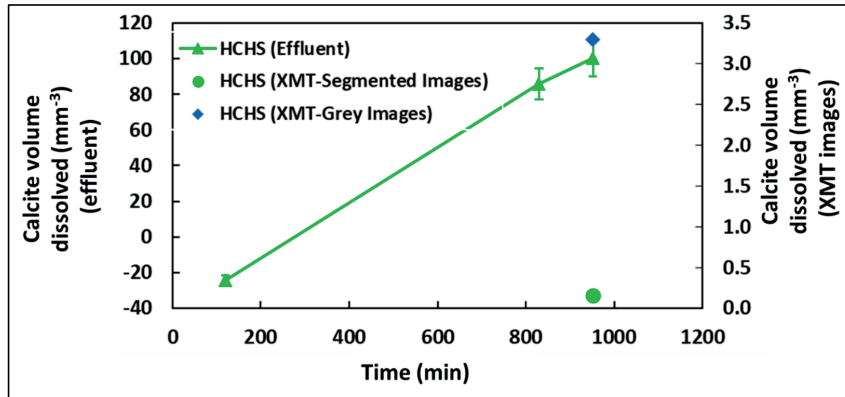


**Figure A5.9:** Comparison of the calculated volume of dissolved calcite from effluent samples, segmented images and grey images.

*3. SEM Image analysis*: SEM image of the part of the inlet face of the samples K1 and K4 are provided in Figure A5.10. We observed that the inlet face of the K1 sample (used in experiment NCLS) was smoothened as a result of the prolonged dissolution, while, the inlet face of the sample K4, which was used in HCHS, maintained the initial surface roughness caused by cutting and sample preparation.
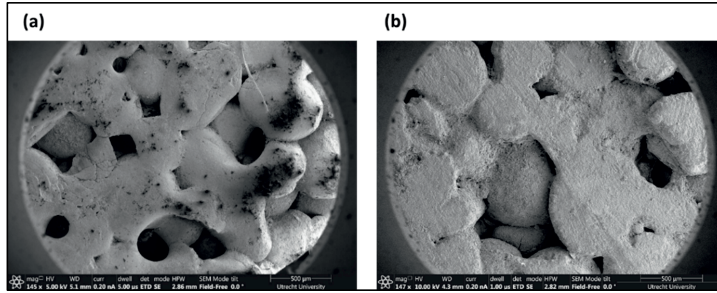
**Figure A5.10:** SEM images of the part of the inlet face of the samples belonging to the end of the experiment (a) NCLS and (b) HCHS.
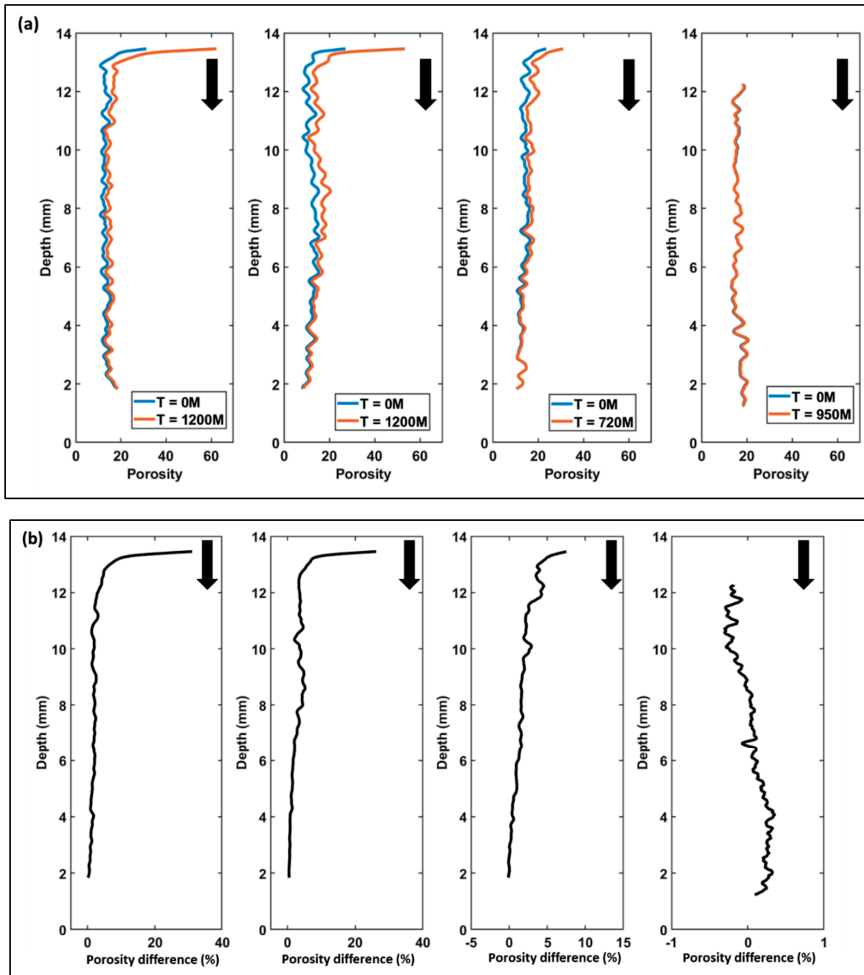


**Figure A5.11:** For all four experiments full vertical profile of (a) the slice-averaged porosity (%) and (b) porosity difference (%). The vertical profiles correspond to the XMT images of the

cropped sample length at the beginning and the end of experiment. Black arrow shows the flow direction. Note the different x-axis range utilized for panel (b).
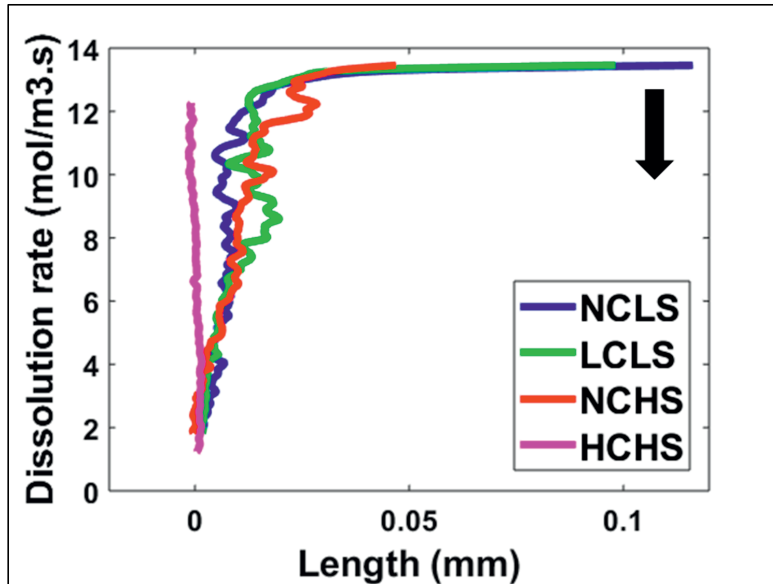


**Figure A5.12**: For all four experiments full vertical profile of slice-averaged dissolution rate calculated from Equation 5.5. Black arrow shows the flow direction.
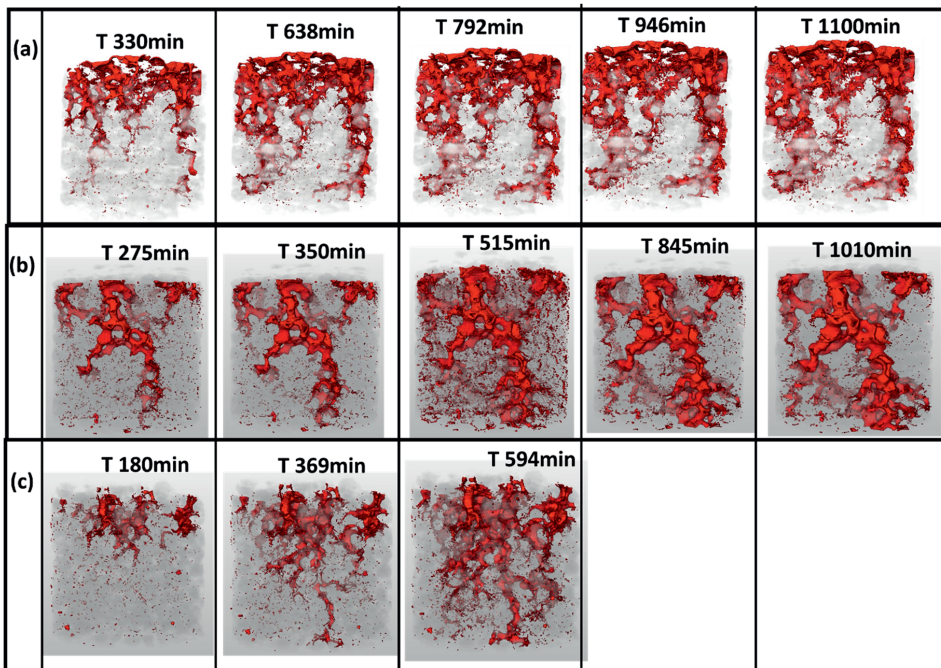
**Figure A5.13**: In addition to the Figure 5.6, XMT images of the sample at different time steps of experiments (a) NCLS, (b) LCLS and (c) NCHS.
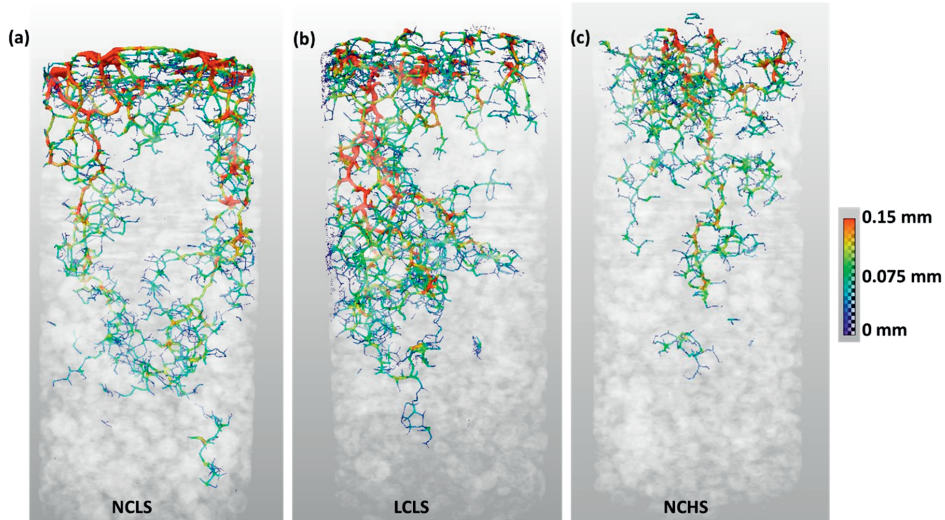


**Figure A5.14:** Extracted skeleton from the dissolution pattern of three experiment. Color of segments denote the radius of the segment.

| Experiment | Nodes | Segments | Total number of the shortest path | Inlet nodes | End nodes |
|---|---|---|---|---|---|
| NCLS | 2629 | 3137 | 1157 | 220 | 1157 |
| LCLS | 5013 | 6732 | 2018 | 200 | 2018 |
| NCHS | 1956 | 2419 | 804 | 43 | 804 |

| Experiment | Number of category 1 channels | Number of category 2 channels | Number of category 3 channels |
|---|---|---|---|
| NCLS | 3 | 8 | 209 |
| LCLS | 2 | 10 | 188 |
| NCHS | 2 | 8 | 33 |

| Experiment | Category 1 | Number of the side branches | Mean radius (mm) | Total length (mm) |
|---|---|---|---|---|
| NCLS | 1 | 306 | 0.10 | 13.61 |
| | 2 | 250 | 0.13 | 14.60 |
| | 3 | 120 | 0.14 | 7.54 |
| LCLS | 1 | 730 | 0.10 | 12.30 |
| | 2 | 342 | 0.15 | 8.36 |
| NCHS | 1 | 156 | 0.09 | 5.66 |
| | 2 | 309 | 0.11 | 10.28 |

**Table A5.2:** Statistics of the extracted skeleton for three experiments
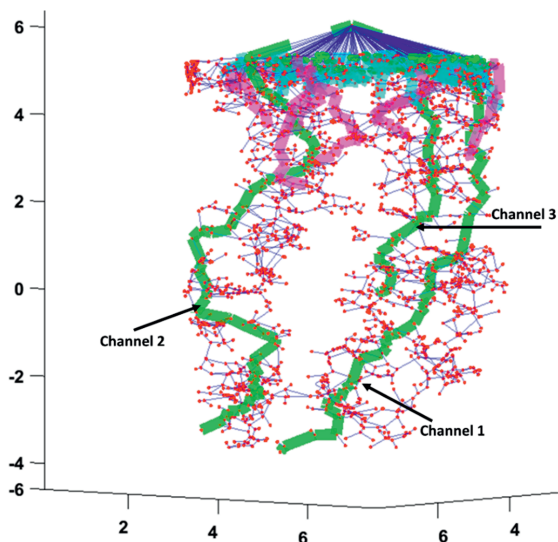
**Figure A5.15:** Skeleton analysis of the dissolution pattern of experiment NCLS. Category 1, 2 and 3 wormholes are highlighted with green, magenta and cyan color, respectively. All three category 1 channels are indicated with the black arrow.
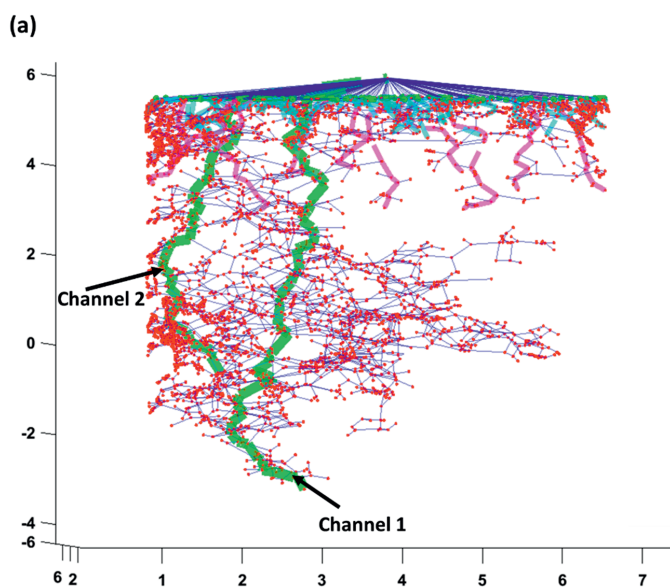


**Figure A5.16:** Skeleton analysis of the dissolution pattern of experiment LCLS. Category 1, 2 and 3 channels are highlighted with green, magenta and cyan color, respectively. Both category 1 channels are indicated with the black arrow.
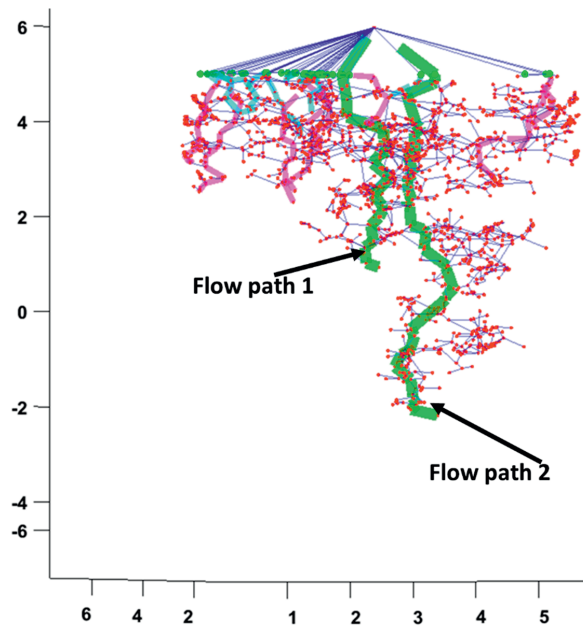
**Figure A5.17:** Skeleton analysis of the dissolution pattern of experiment NCHS. Category 1, 2 and 3 wormholes are highlighted with green, magenta and cyan color, respectively. Both category 1 channels are indicated with the black arrow.
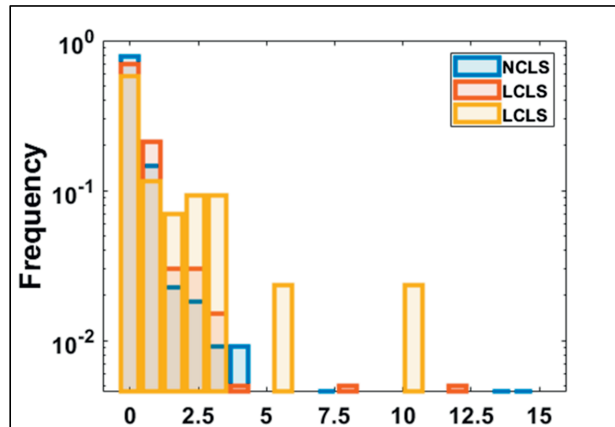


**Figure A5.18:** Frequency distribution of the total lengths of all channels corresponding to all three experiments.
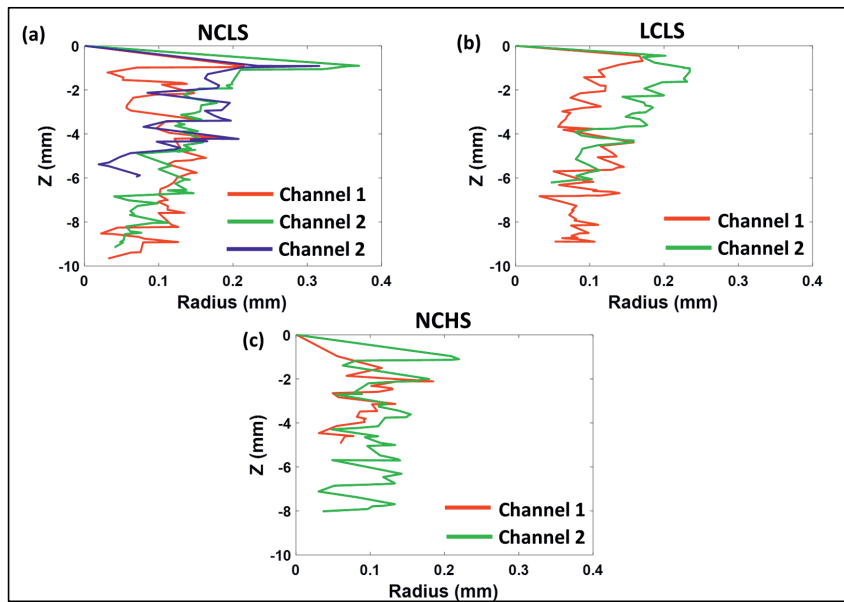
**Figure A5.19:** Vertical radius profile of the category 1 channels at the end of the experiments (a) NCLS (b) LCLS and (c) NCHS.
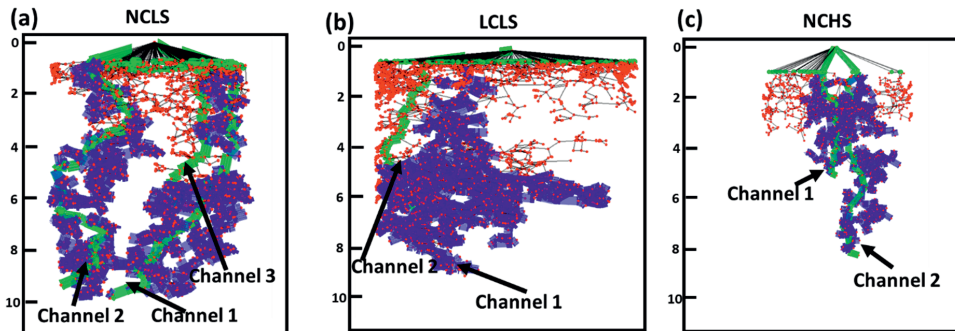


**Figure A5.20**: (a) Skeleton analysis of the dissolution pattern at the end of each experiment for (a) NCLS, (b) LCLS and (c) NCHS. Nodes and segments are highlighted with red and black colours, respectively. Category 1 channels (i.e., total length > 5mm) are highlighted with a green colour and side branches are highlighted with the blue colour.
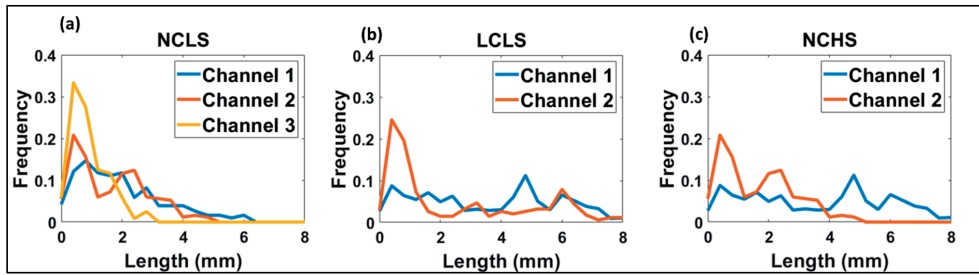
**Figure A5.21:** Frequency distribution of length of side branches for experiments (a) NCLS, (b) LCLS and (c) NCHS.
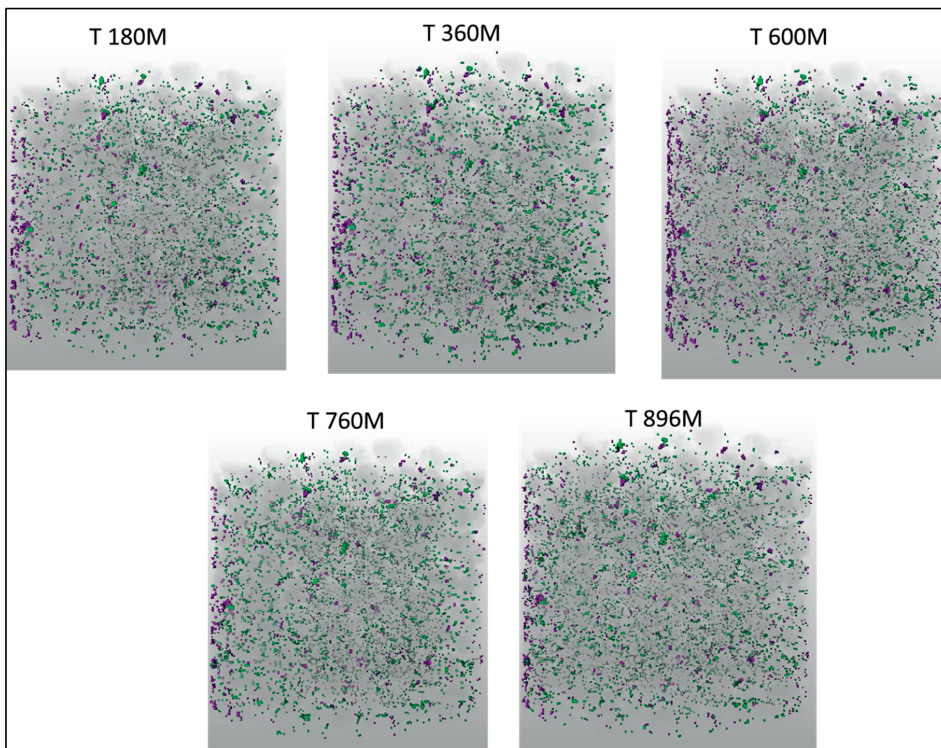


**Figure A5.22:** In addition to the Figure 5.8, XMT images of the sample at different time steps of experiment HCHS.
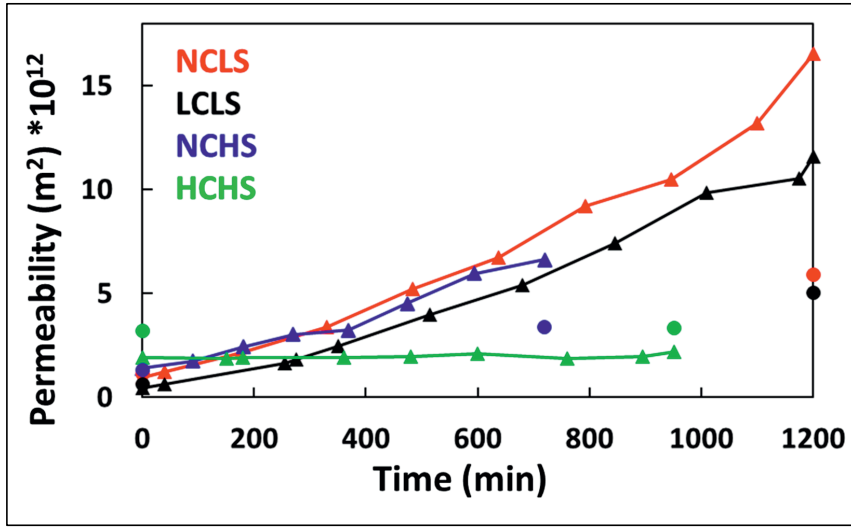
**Figure A5.23:** Temporal evolution of permeability for four experiments (circle, cropped sample length and triangle, half sample length).
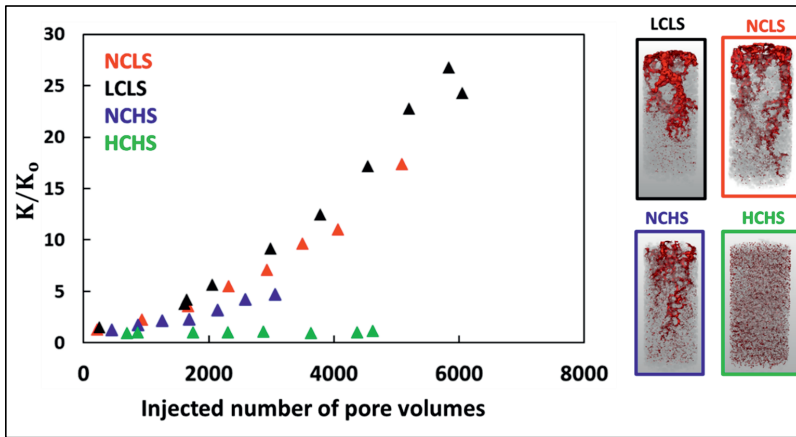


**Figure A5.24:** Permeability response as a function of injected pore volumes for four experiments (triangle, half sample length).

# Chapter
# 6. Summary and Conclusions

The focus of this research was to understand physical and chemical processes that take place during injection of $CO_2$-rich or acidic solutions into carbonate rocks. I simulated the relevant reactive transport processes using single pore scale modeling and pore network modeling and findings from the models were validated against experimental results. The pore scale model simulated calcite dissolution in an explicitly defined solid-fluid interface while the pore network model approximated the carbonate rock topology into a system of spherical pores and cylindrical throats. This research delineates the impact of the imposed reactive flow conditions on the changing geometry of the pores and throats at the microscopic scale and on the porosity-permeability relationship at the macroscopic scale. Following paragraphs further summarize the key findings of each of the chapters:

Chapter 1 first presents the motivation and scope of this study, followed by delineation of individual physical and chemical processes which define the interaction of acidic solutions with carbonate rocks. Relevant previous work regarding the calcite dissolution reactions and porosity-permeability relationships is summarized. Chapter 1 is concluded by defining the specific aims of this research.

In Chapter 2, the effect of the imposed reactive flow conditions on the evolution of the shape of the pore is investigated. The reactive transport processes were simulated using a single calcite pore and the results were validated against microfluidic experiments. The validated model was used to conduct a detailed study of the dissolution processes for a range of hydrogeological and chemical parameters. We observed that, for dissolution regimes corresponding to the lower flow rates or highly corrosive injecting solutions, a significant concentration gradient developed in the direction of flow. This resulted into transformation of the initially cylindrical pore into a non-uniform shaped pore. In contrast to this, injection at higher flow rates, preserves the initial shape of the pore during dissolution. These changes into pore shape ultimately reflect in the conductance of the pore. For a non-uniform pore, the pressure gradient does not remain constant along the pore. Therefore, the actual conductance of non-uniform pores was found to be different than the conductance value that was computed according to the PNM modeling method (assuming constant pore shape).

Chapter 3 unravels the contribution of hydrodynamic effects during surface experiments which are conducted for determining the calcite dissolution rates. We performed numerical simulations of calcite marble dissolution experiments at the scale of an entire flow-through cell. We observed that, for the simulated flow cell geometry, the commonly used flow rates (i.e., taken from the earlier surface dissolution studies) led to a considerable horizontal heterogeneity of the flow and the concentration field. Consequently, a significant discrepancy developed between the reaction rate calculated from composition of the injected fluid vs the reaction rates within the flow cell. This ultimately impacts the choice of the location for experimental investigation, given that around one order of magnitude of rate variability persists within the entire flow cell. Additionally, we investigated the hydrodynamics contribution of the microscopically rough calcite surfaces into observed rate variability (rate spectra). We observed that, at conditions corresponding to the reaction and flow regime of microscopic surface dissolution experiments, the roughness of a crystal surface (as from VSI experiments) does not influence the hydrodynamics, thus does not significantly contribute to the experimentally observed dissolution rate spectra.

Chapter 4 takes forward the findings from chapter 2 with an objective to improve the existing pore network modeling approaches for simulation of calcite dissolution processes. First, we derived new constitutive relations to update throat conductance which includes the information

of the evolving pore shape depending on the imposed flow and reaction regimes. This derivation was based on a range of numerical simulation performed on the scale of a single throat and subsequent extraction of the changes of throat conductance. For the advection dominated and reaction-controlled dissolution regimes, we showed that the Hagen-Poiseuille relation can be used for updating conductance, while for the diffusion dominated and reaction-dominated dissolution regimes, the new conductance relations are required for correct updating of the throat conductance. Next, these new conductance relations were implemented in the pore network model. The reactive transport pore network modeling predictions about permeability were compared with two sets of micro-CT experiments. These experiments utilized injection of an acidic solution with a pH value of 3.0 at two flow rates in Ketton Limestone samples. In both experiments, most of the throats maintained the cylindrical shape during the dissolution process, thus similar evolution of permeability was observed in both pore network models (i.e., one with the Hagen-Poiseuille relation and one with the new conductance relation). Finally, a sensitivity study of the new conductance relations across a range of reactive flow conditions showed that, for certain dissolution regimes, corresponding to the injection of highly acidic solution or injection at lower flow rates, utilization of the Hagen-Poiseuille relation can lead to an overestimation of 27% in the predicted permeability value and an overestimation of over 50% in the fitted exponent $\alpha$ for the porosity-permeability relationship.

Chapter 5 presents the impact of brine composition, mainly calcium ions and NaCl-based salinity, on the development of dissolution features in Ketton, a porous calcium carbonate rock. We have performed four reactive flow-through experiments which comprised of an injection of four different types of brines at a constant flow rate. Time-lapse images of the Ketton limestone were acquired using laboratory micro-CT scanner. We observed a significant impact of the amount of $Ca^{2+}$ and NaCl salt on the corrosiveness of the injecting solution and the development of dissolution patterns. Increment in the concentration of either of these two led to reduction in the corrosiveness of the solution. For a given injection rate, lesser corrosive solution dissolved the entire sample uniformly while highly corrosive solution dissolved calcite predominantly in the vicinity of the sample inlet and relative less along the flow path. In summary, we observed that varied combinations of salinity and $Ca^{2+}$ concentrations in the injected solution changed the dissolution patterns from disseminated and microporous regime to wormhole. These varied range of developed dissolution patterns control the changing permeability of the sample against similar porosity increment, suggesting a need for different porosity-permeability relations as a function of the composition of the injected brine.

This research has demonstrated the impact of several physio-chemical conditions such as flow rate, pH, pCO2 and salinity on the porosity-permeability relations. These insights are important in the context of carbonate rocks forming majority of hydrocarbon reservoirs and aquifers.

# SAMENVATTING

Geologische opslag van $CO_2$-gas wordt gezien als een mogelijke oplossing tegen opwarming van de aarde. Injectie van $CO_2$ of zure oplossingen in carbonaatgesteenten brengt een reeks fysische en chemische processen op gang. Optimalisatie van het injectieproces en veilige opslag van het geïnjecteerde gas vereisen geavanceerde modelleringstools die de grondbeginselen van de lopende processen voor een scala aan chemische en fysische omstandigheden kunnen beschrijven, zoals het injectiedebiet, de samenstelling van de geïnjecteerde oplossing en de heterogeniteit in het gesteente. Poriënschaalmodellen worden beschouwd als een veelbelovend hulpmiddel om de grondbeginselen van reactieve transportverschijnselen te begrijpen, aangezien de fysisch / chemische processen plaatsvinden op de poriënschaal. In dit proefschrift heb ik een schaalmodel met enkele poriën ontwikkeld dat een expliciet gedefinieerd grensvlak tussen vaste stof en vloeistof omvat en een volledig gekoppeld model voor simulatie van het snelheidsveld, transport van opgeloste stoffen, oppervlakte- en bulkreacties (d.w.z. omvat calcietoplossingssysteem) en een bewegend vloeistof/calciet grensvlak. Dit model werd gebruikt om de controle van de opgelegde reactieve stroomcondities op de veranderende vorm van de porie tijdens het oplossen af te bakenen. We hebben vastgesteld dat, afhankelijk van de oplossingsregimes, aanvankelijk cilindrische poriën een spectrum van porievormen kan bereiken. Deze informatie is belangrijk voor veelgebruikte porienetwerkmodellen, zodat de geleiding van de poriën correct kan worden bijgewerkt naarmate het oplossen vordert. Het poriënschaalmodel werd verder gebruikt om de hydrodynamische bijdrage van het ruwe calcietoppervlak aan de oplossnelheden van calciet te onderzoeken. Deze studie maakte gebruik van echte oppervlaktetopografische gegevens om de door ruwheid veroorzaakte variabiliteit van de reactiesnelheid voor een reeks reactie- en stroomregimes te kwantificeren. In dit onderzoek hebben we nieuwe doorlatendheidsrelaties voorgesteld voor porienetwerkmodellen die de veranderende porievorm informatie opnemen als functie van de opgelegde reactieve stromingsomstandigheden. Ten slotte onderzochten we de impact van de samenstelling van pekel, voornamelijk $Ca^{2+}$ en NaCl-zout, op de ontwikkeling van de oplossingspatronen. We ontdekten dat de verschillende verhoudingen van $Ca^{2+}$ en NaCl-zout de relatie tussen porositeit en permeabiliteit kunnen regelen.

# REFERENCES

Acharya, R.C., Van Der Zee, S.E.A.T.M., Leijnse, A., 2005. Transport modeling of nonlinearly adsorbing solutes in physically heterogeneous pore networks. Water Resour. Res. 41, 1–11. https://doi.org/10.1029/2004WR003500

Agrawal, P., Raoof, A., Iliev, O., Koskamp, J., Wolthers, M., 2017. Reactive transport modeling in carbonate rocks : Single pore model, in: Proceedings of the 2017 COMSOL Conference in Rotterdam. pp. 1–7

Agrawal, P., Raoof, A., Iliev, O., Wolthers, M., 2020. Evolution of pore-shape and its impact on pore conductivity during CO2 injection in calcite: Single pore simulations and microfluidic experiments. Adv. Water Resour. 136. https://doi.org/10.1016/j.advwatres.2019.103480

Al-Gharbi, M.S., Blunt, M.J., 2005. Dynamic network modeling of two-phase drainage in porous media. Phys. Rev. E - Stat. Nonlinear, Soft Matter Phys. 71, 1–16. https://doi.org/10.1103/PhysRevE.71.016308

Al-Khulaifi, Y., Lin, Q., Blunt, M.J., Bijeljic, B., 2017. Reaction Rates in Chemically Heterogeneous Rock: Coupled Impact of Structure and Flow Properties Studied by X-ray Microtomography. Environ. Sci. Technol. 51, 4108–4116. https://doi.org/10.1021/acs.est.6b06224

Algive, L., Bekri, S., Vizika, O., 2010. Pore-Network Modeling Dedicated to the Determination of the Petrophysical-Property Changes in the Presence of Reactive Fluid. SPE J. 15, 618–633. https://doi.org/10.2118/124305-PA

Anabaraonye, B.U., Crawshaw, J.P., Trusler, J.P.M., 2019. Brine chemistry effects in calcite dissolution kinetics at reservoir conditions. Chem. Geol. 509, 92–102. https://doi.org/10.1016/j.chemgeo.2019.01.014

André, L., Audigane, P., Azaroual, M., Menjoz, A., 2007. Numerical modeling of fluid–rock chemical interactions at the supercritical CO 2 –liquid interface during CO 2 injection into a carbonate reservoir, the Dogger aquifer (Paris Basin, France). https://doi.org/10.1016/j.enconman.2007.01.006

André, L., Azaroual, M., Menjoz, A., 2010. Numerical Simulations of the Thermal Impact of Supercritical CO 2 Injection on Chemical Reactivity in a Carbonate Saline Reservoir. Transp Porous Med 82, 247–274. https://doi.org/10.1007/s11242-009-9474-2

International Union of Pure and Applied Chemistry: Notation for states and processes, significance of the word standard in chemical thermodynamics, and remarks on commonly tabulated forms of thermodynamic functions, 1982. Pure Appl.Chem 54 (6), 1239–1250.

Arvidson, R.S., Ertan, I.E., Amonette, J.E., Luttge, A., 2003. Variation in calcite dissolution rates: A fundamental problem? Geochim. Cosmochim. Acta 67, 1623–1634. https://doi.org/10.1016/S0016-7037(02)01177-8

Aslannejad, H., Fathi, H., Hassanizadeh, S.M., Raoof, A., Tomozeiu, N., 2018. Movement of a liquid droplet within a fibrous layer: Direct pore-scale modeling and experimental observations. Chem. Eng. Sci. 191, 78–86. https://doi.org/10.1016/j.ces.2018.06.054

Bear J. and Bachmat Y. Introduction to modeling phenomena of transport in porous media Kluwer Academic publishers, Dordrecht, The Netherlands (1991).

Bedram, A., Moosavi, A., 2011. Droplet breakup in an asymmetric microfluidic T junction. Eur. Phys. J. E 34. https://doi.org/10.1140/epje/i2011-11078-7

Bekri, S., Thovert, J.F., Adler, P.M., 1995. DISSOLUTION OF POROUS MEDIA. Chem. Eng. Sci. 50, 2765–2791.

Bergfors, S.N., Schovsbo, N.H., Feilberg, K.L., 2020. Classification of and changes within formation water types in Danish North Sea Chalk: A study of the Halfdan, Dan, Kraka and Valdemar oil reservoirs. Appl. Geochemistry 122, 104702. https://doi.org/10.1016/j.apgeochem.2020.104702

Bernabé, Y., Mok, U., Evans, B., 2003. Permeability-porosity Relationships in Rocks Subjected to Various Evolution Processes. Pure Appl. Geophys. 160, 937–960. https://doi.org/10.1007/PL00012574

Berner, R.A. and Morse, J.W., 1974. Dissolution kinetics of calcium carbonate in sea water: IV. Theory of calcite dissolution. American Journal of Science, 274(2): 108-134.

Bischoff, W.D., Mackenzie, F.T. and Bishop, F.C., 1987. Stabilities of synthetic magnesian calcites in aqueous solution: Comparison with biogenic materials. Geochimica et Cosmochimica Acta, 51(6): 1413-1423.

Boudreau, B.P., 1997. Diagenetic Models and Their Implementation. Springer-Verlag, Berlin. Boudreau, B.P., 2013. Carbonate dissolution rates at the deep ocean floor. Geophysical Research Letters, 40(4): 744-748.

Boudreau, B.P. and Guinasso, N.L., Jr., 1982. The influence of a diffusive boundary layer on accretion, dissolution, and diagenesis at the sea floor. In: K.A. Fanning and F.T. Manheim (Editors), The Dynamic Environment of the Ocean Floor. Lexington Books, Lexington, pp. 115-145.

Boudreau, B.P. and Jørgensen, B.B., 2001. The Benthic Boundary Layer: Transport Processes and Biogeochemistry. Oxford University Press, Oxford.

Bibi, I., Arvidson, R., Fischer, C., Lüttge, A., 2018. Temporal Evolution of Calcite Surface Dissolution Kinetics. Minerals 8, 256. https://doi.org/10.3390/min8060256

Boever, W. De, Bultreys, T., Derluyn, H., Hoorebeke, L. Van, Cnudde, V., 2016. Science of the Total Environment Comparison between traditional laboratory tests , permeability measurements and CT-based fl uid fl ow modelling for cultural heritage applications. Sci. Total Environ. 554–555, 102–112. https://doi.org/10.1016/j.scitotenv.2016.02.195

Bollermann, T. and Fisher, C., 2020. TEMPORAL EVOLUTION OF DISSOLUTION KINETICS OF POLYCRYSTALLINE CALCITE. Am. J. Sci. 320, 53–71. https://doi.org/10.3390/min8060256

Boudreau, B.P., Sulpis, O., Mucci, A., 2020. Control of CaCO3 dissolution at the deep seafloor and its consequences. Geochim. Cosmochim. Acta 268, 90–106. https://doi.org/10.1016/j.gca.2019.09.037

Brand, A.S., Feng, P., Bullard, J.W., 2017. Calcite dissolution rate spectra measured by in situ digital holographic microscopy. Geochim. Cosmochim. Acta 213, 317–329. https://doi.org/10.1016/j.gca.2017.07.001

Buades, A., Coll, B., Morel, J., A, 2005. A review of image denoising algorithms , with a new one. Multiscale Model. Simul. 4, 490–530.

Buhmann, D., Dreybrodt, W., 1987. Calcite dissolution kinetics in the system H2O-CO2-CaCO3 with participation of foreign ions. Chem. Geol. 64, 89–102. https://doi.org/10.1016/0009-2541(87)90154-9

Bultreys, T., Boone, M.A., Boone, M.N., De Schryver, T., Masschaele, B., Van Hoorebeke, L., Cnudde, V., 2016. Fast laboratory-based micro-computed tomography for pore-scale research: Illustrative experiments and perspectives on the future. Adv. Water Resour. 95, 341–351. https://doi.org/10.1016/j.advwatres.2015.05.012

Busenberg, E., Plummer, L.N., 1986. A comparative study of the dissolution and crystal growth kinetics of calcite and aragonite. Stud. Diagenesis, U.S. Geol. Surv. Bull. 1578 139–168.

Carman, P.C.: Fluid flow through granular beds. Trans. Inst. Chem. Eng. 15, 150166 (1937)

Chen, L., Kang, Q., Carey, B., Tao, W.Q., 2014a. Pore-scale study of diffusion–reaction processes involving dissolution and precipitation using the lattice Boltzmann method. Int. J. Heat Mass Transf. 75, 483–496. https://doi.org/10.1016/j.ijheatmasstransfer.2014.03.074

Chen, L., Kang, Q., Viswanathan, H.S., Tao, W.Q., 2014b. Pore-scale study of dissolution-induced changes in hydrologic properties of rocks with binary minerals. Water Resour. Res. 50, 9343–9365. https://doi.org/10.1002/2014WR015646

Chen, L., Kang, Q., Viswanathan, H.S., Tao, W.Q., 2014c. Pore-scale study of dissolution-induced changes in hydrologic properties of rocks with binaryminerals. Water Resour. Res. 50, 5216–5234. https://doi.org/10.1002/2014WR015716

Chou, L., Garrels, R.M., Wollast, R., 1989. Comparative study of the kinetics and mechanisms of dissolution of carbonate minerals. Chem. Geol. 78, 269–282. https://doi.org/10.1016/0009-2541(89)90063-6

Daccord, G, Lenormand, R., Liétard, O., 1993. Chemical dissolution of a porous medium by a reactive fluid-I. Model for the "wormholing" phenomenon. Chem. Eng. Sci. 48, 169–178. https://doi.org/10.1016/0009-2509(93)80293-Y

Daccord, G., Liétard, O., Lenormand, R., 1993. Chemical dissolution of a porous medium by a reactive fluid-II. Convection vs reaction, behavior diagram. Chem. Eng. Sci. 48, 179–186. https://doi.org/10.1016/0009-2509(93)80294-Z

Deng, H., Molins, S., Trebotich, D., Steefel, C., DePaolo, D., 2018. Pore-scale numerical investigation of the impacts of surface roughness: Upscaling of reaction rates in rough fractures. Geochim. Cosmochim. Acta 239, 374–389. https://doi.org/10.1016/J.GCA.2018.08.005

Elkhoury, J.E., Ameli, P., Detwiler, R.L., 2013. Dissolution and deformation in fractured carbonates caused by flow of CO2-rich brine under reservoir conditions. Int. J. Greenh. Gas Control 16, S203–S215. https://doi.org/10.1016/j.ijggc.2013.02.023

Emmanuel, S., Levenson, Y., 2014. Limestone weathering rates accelerated by micron-scale grain detachment. Geology 42, 751–754. https://doi.org/10.1130/G35815.1

Finneran, D.W., Morse, J.W., 2009. Calcite dissolution kinetics in saline waters. Chem. Geol. 268, 137–146. https://doi.org/10.1016/j.chemgeo.2009.08.006

Fischer, C., Arvidson, R.S., Lüttge, A., 2012. How predictable are dissolution rates of crystalline material? Geochim. Cosmochim. Acta 98, 177–185.

References

https://doi.org/10.1016/j.gca.2012.09.011

Fischer, C., Kurganskaya, I., Luttge, A., 2018. Inherited control of crystal surface reactivity. Appl. Geochemistry 91, 140–148. https://doi.org/10.1016/j.apgeochem.2018.02.003

Fredd, C.N., Fogler, H.S., 1998. Influence of Transport and Reaction on Wormhole Formation in Porous Media. SPE J. 44, 1933–1949. https://doi.org/10.2118/56995-pa

Garcia-Rios, M., Luquot, L., Soler, J.M., Cama, J., 2015. Influence of the flow rate on dissolution and precipitation features during percolation of CO2-rich sulfate solutions through fractured limestone samples. Chem. Geol. 414, 95–108. https://doi.org/10.1016/j.chemgeo.2015.09.005

Garing, C., Gouze, P., Kassab, M., Riva, M., Guadagnini, A., 2015. Anti-correlated Porosity–Permeability Changes During the Dissolution of Carbonate Rocks: Experimental Evidences and Modeling. Transp. Porous Media 107, 595–621. https://doi.org/10.1007/s11242-015-0456-2

Gaspar Ravagnani, A.T.F.S., Ligero, E.L., Suslick, S.B., 2009. CO2 sequestration through enhanced oil recovery in a mature oil field. J. Pet. Sci. Eng. 65, 129–138. https://doi.org/10.1016/j.petrol.2008.12.015

Gasperino, D., Yeckel, A., Olmsted, B.K., Ward, M.D., Derby, J.J., 2006. Mass transfer limitations at crystallizing interfaces in an atomic force microscopy fluid cell: A finite element analysis. Langmuir 22, 6578–6586. https://doi.org/10.1021/la060592k

Ghanbarian B., Hunt A. G., D.H., 2016. Fluid flow in porous media with rough pore-solid interface. Water Resour. Res. 5, 2–2. https://doi.org/10.1111/j.1752-1688.1969.tb04897.x

Ghous, A., Senden, T.J., Sok, R.M., Sheppard, A.P., Pinczewski, V.W., Knackstedt, M.A., 2007. SPWLA Middle East Regional Symposium. 3D Characterisation Microporosity Carbonate Cores 1–11.

Giudici, G. De, 2002. Surface control vs . diffusion control during calcite dissolution : Dependence of step-edge velocity upon solution pH. Am. Mineral. 87, 1279–1285.

Gledhill, D.K., Morse, J.W., 2006. Calcite dissolution kinetics in Na-Ca-Mg-Cl brines. Geochim. Cosmochim. Acta 70, 5802–5813. https://doi.org/10.1016/j.gca.2006.03.024

Golfier, F., Bazin, B., Lenormand, R., Quintard, M., 2004. Core-scale description of porous media dissolution during acid injection – part I: Theoretical development. Comput. Appl. Math. 23, 173–194. https://doi.org/10.1590/S0101-82052004000200005

Golfier, F., Zarcone, C., Bazin, B., Lenormand, R., Lasseux, D., Quintard, M., 2002. On the ability of a Darcy-scale model to capture wormhole formation during the dissolution of a porous medium. J. Fluid Mech. 457, 213–254. https://doi.org/10.1017/S0022112002007735

Gouze, P., Luquot, L., 2011. X-ray microtomography characterization of porosity, permeability and reactive surface changes during dissolution. J. Contam. Hydrol. 120–121, 45–55. https://doi.org/10.1016/j.jconhyd.2010.07.004

Gray, F., Anabaraonye, B., Shah, S., Boek, E., Crawshaw, J., 2018. Chemical mechanisms of dissolution of calcite by HCl in porous media: Simulations and experiment. Adv. Water Resour. 121, 369–387. https://doi.org/10.1016/j.advwatres.2018.09.007

Gutjahr, A., Dabringhaus, H., Lacmann, R., 1996a. Studies of the growth and dissolution kinetics of the CaCo3 polymorphs calcite and aragonite II. The influence of divalent cation additives on the growth and dissolution rates. J. Cryst. Growth 158, 310–315. https://doi.org/10.1016/0022-0248(95)00447-5

Gutjahr, A., Dabringhaus, H., Lacmann, R., 1996b. Studies of the growth and dissolution kinetics of the CaCo3 polymorphs calcite and aragonite I. Growth and dissolution rates in water. J. Cryst. Growth 158, 296–309. https://doi.org/10.1016/0022-0248(95)00446-7

Hanor, J.S., 1994. Origin of saline fluids in sedimentary basins. Geol. Soc. Spec. Publ. 78, 151–174. https://doi.org/10.1144/GSL.SP.1994.078.01.13

Hawez, H., Ahmed, Z., 2014. Enhanced oil recovery by CO2 injection in carbonate reservoirs. WIT Trans. Ecol. Environ. 186, 547–558. https://doi.org/10.2495/ESUS140481

Hoefner, M.L., Fogler, H.S., 1988. Pore evolution and channel formation during flow and reaction in porous media. AIChE J. 34, 45–54. https://doi.org/10.1002/aic.690340107

Hoefner, M.L., Fogler, H.S., Stenius, P., Sjoblom, J., 1987. Role of Acid Diffusion in Matrix Acidizing of Carbonates. JPT, J. Pet. Technol. 39, 203–208. https://doi.org/10.2118/13564-PA

Hommel, J., Coltman, E., Class, H., 2018. Porosity–Permeability Relations for Evolving Pore Space: A Review with a Focus on (Bio-)geochemically Altered Porous Media. Transp. Porous Media. https://doi.org/10.1007/s11242-018-1086-2

Hornung U (ed.). Homogenization and Porous Media, Springer: Berlin, 1997.. https://doi.org/10.1007/978-1-4612-1920-0_1

Huber, C., Shafei, B., Parmigiani, A., 2014. A new pore-scale model for linear and non-linear heterogeneous dissolution and precipitation. Geochim. Cosmochim. Acta 124, 109–130. https://doi.org/10.1016/j.gca.2013.09.003

Izgec, O., Demiral, B., Bertin, H., Akin, S., 2008. CO2 injection into saline carbonate aquifer formations II: Comparison of numerical simulations to experiments. Transp. Porous Media 73, 57–74. https://doi.org/10.1007/s11242-007-9160-1

Janbumrung, V., Trisarn, K., 2017. Acid Stimulation of Carbonate Reservoir in Northeastern Thailand Using Developed Computer Program. Int. J. Comput. 25, 40–51.

Jeschke, A.A., Dreybrodt, W., 2002. Dissolution rates of minerals and their relation to surface morphology. Geochim. Cosmochim. Acta 66, 3055–3062. https://doi.org/10.1016/S0016-7037(02)00893-1

Joseph Kirk (2020). Dijkstra's Shortest Path Algorithm (https://www.mathworks.com/matlabcentral/fileexchange/12850-dijkstra-s-shortest-path-algorithm), MATLAB Central File Exchange.

Kahl, W.A., Yuan, T., Bollermann, T., Bach, W., Fischer, C., 2020. Crystal surface reactivity analysis using a combined approach of X-ray micro-computed tomography and vertical scanning interferometry. Am. J. Sci. 320, 27–52. https://doi.org/10.2475/01.2020.03

Kang, Q., Lichtner, P.C., Zhang, D., 2006. Lattice Boltzmann pore-scale model for multicomponent reactive transport in porous media. J. Geophys. Res. Solid Earth 111, n/a-n/a. https://doi.org/10.1029/2005JB003951

Kang, Q., Zhang, D., Chen, S., 2003. Simulation of dissolution and precipitation in porous media. J. Geophys. Res. Solid Earth 108. https://doi.org/10.1029/2003JB002504

Keeling, C.D., 1997. Climate change and carbon dioxide: An introduction. Proc. Natl. Acad. Sci. U. S. A. 94, 8273–8274. https://doi.org/10.1073/pnas.94.16.8273

Kozeny, J., 1927. Über kapillare leitung des wassers im boden (Aufstieg, Versickerung und Anwendung auf die Bewässerung). Sitzungsberichte der Wiener Akad. des Wissenschaften 136, 271–306.

Kumar, K., Van Noorden, T.L., Pop, I.S., 2011. EFFECTIVE DISPERSION EQUATIONS FOR REACTIVE FLOWS INVOLVING FREE BOUNDARIES AT THE MICROSCALE * 9, 29–58. https://doi.org/10.1137/100804553

Kumar, K., Wheeler, M.F., Thomas, W., 2013. REACTIVE FLOW AND REACTION-INDUCED BOUNDARY MOVEMENT IN A THIN CHANNEL. SIAM J. SCI. Comput. 35, B1235–B1266. https://doi.org/10.1137/130913134

Kurganskaya, I., Rohlfs, R.D., 2020. Atomistic to meso-scale modeling of mineral dissolution: Methods, challenges and prospects. Am. J. Sci. 320, 1–26. https://doi.org/10.2475/01.2020.02

Lasaga, A.C., Luttge, A., 2001. Variation of crystal dissolution rate based on a dissolution stepwave model. Science (80-.). 291, 2400–2404. https://doi.org/10.1126/science.1058173

Levenson, Y., Emmanuel, S., 2013. Pore-scale heterogeneous reaction rates on a dissolving limestone surface. Geochim. Cosmochim. Acta 119, 188–197. https://doi.org/10.1016/j.gca.2013.05.024

Levenson, Y., Schiller, M., Kreisserman, Y., Emmanuel, S., 2015. Calcite dissolution rates in texturally diverse calcareous rocks. Geol. Soc. London, Spec. Publ. 406, 81–94. https://doi.org/10.1144/SP406.14

Li, L., Peters, C.A., Celia, M.A., 2007. Reply to "Comment on upscaling geochemical reaction rates using pore-scale network modeling" by Peter C. Lichtner and Qinjun Kang. Adv. Water Resour. 30, 691–695. https://doi.org/10.1016/j.advwatres.2006.05.002

Li, L., Steefel, C.I., Yang, L., 2008. Scale dependence of mineral dissolution rates within single pores and fractures. Geochim. Cosmochim. Acta 72, 360–377. https://doi.org/10.1016/j.gca.2007.10.027

Li, X., Huang, H., Meakin, P., 2008. Level set simulation of coupled advection-diffusion and pore structure evolution due to mineral precipitation in porous media. Water Resour. Res. 44, 1–17. https://doi.org/10.1029/2007WR006742

Li, Y.H., Gregory, S., 1974. Diffusion of ions in sea water and in deep-sea sediments. Geochim. Cosmochim. Acta, 38. Pergamon Press. Printed in Northern Ireland.

Liang, Y., Baer, D.R., 1997. Anisotropic dissolution at the $CaCO_3(10\bar{1}4)$-water interface. Surf. Sci. 373, 275–287. https://doi.org/10.1016/S0039-6028(96)01155-7

Liao, X., Gao, C., Wu, P., 2012. Assessment of $CO_2$ EOR and its geo-storage potential in mature oil reservoirs, changing oil field, China. Carbon Management Technology Conference. Orlando, Florida, USA. https://doi.org/10.7122/150031-MS

Lin, Q., Bijeljic, B., Rieke, H., Blunt, M.J., 2017. Visualization and quantification of capillary drainage in the pore space of laminated sandstone by a porous plate method using differential imaging X-ray microtomography. Water Resour. Res. 53, 7457–7468. https://doi.org/10.1002/2017WR021083

Liu, C., Shang, J., Zachara, J.M., 2011. Multispecies diffusion models: A study of uranyl species diffusion. Water Resour. Res. 47, 1–16. https://doi.org/10.1029/2011WR010575

Luhmann, A.J., Kong, X.Z., Tutolo, B.M., Garapati, N., Bagley, B.C., Saar, M.O., Seyfried, W.E., 2014. Experimental dissolution of dolomite by CO2-charged brine at 100°C and 150bar: Evolution of porosity, permeability, and reactive surface area. Chem. Geol. 380, 145–160. https://doi.org/10.1016/j.chemgeo.2014.05.001

Luquot, L., Gouze, P., 2009. Experimental determination of porosity and permeability changes induced by injection of CO2 into carbonate rocks. Chem. Geol. 265, 148–159. https://doi.org/10.1016/j.chemgeo.2009.03.028

Luquot, L., Rodriguez, O., Gouze, P., 2014. Experimental Characterization of Porosity Structure and Transport Property Changes in Limestone Undergoing Different Dissolution Regimes. Transp Porous Med 101, 507–532. https://doi.org/10.1007/s11242-013-0257-4

Lüttge, A., Winkler, U., Lasaga, A.C., 2003. Interferometric study of the dolomite dissolution: A new conceptual model for mineral dissolution. Geochim. Cosmochim. Acta 67, 1099–1116. https://doi.org/10.1016/S0016-7037(02)00914-6

Maheshwari, P., Ratnakar, R.R., Kalia, N., Balakotaiah, V., 2013. 3-D simulation and analysis of reactive dissolution and wormhole formation in carbonate rocks. Chem. Eng. Sci. 90, 258–274. https://doi.org/10.1016/j.ces.2012.12.032

Mehmani, Y., Sun, T., Balhoff, M.T., Eichhubl, P., Bryant, · S, Bryant, S., 2012. Multiblock Pore-Scale Modeling and Upscaling of Reactive Transport: Application to Carbon Sequestration. Transp Porous Med 95, 305–326. https://doi.org/10.1007/s11242-012-0044-7

Meile, C., Tuncay, K., 2006. Scale dependence of reaction rates in porous media. Adv. Water Resour. 29, 62–71. https://doi.org/10.1016/j.advwatres.2005.05.007

Meldrum, F. C.; Cölfen, H. Controlling mineral morphologies and structures in biological and synthetic systems. Chem. Rev. 2008, 108, 4332– 4432.

Menke, H.P., Andrew, M.G., Blunt, M.J., Bijeljic, B., 2016. Reservoir condition imaging of reactive transport in heterogeneous carbonates using fast synchrotron tomography - Effect of initial pore structure and flow conditions. Chem. Geol. 428, 15–26. https://doi.org/10.1016/j.chemgeo.2016.02.030

Menke, H.P., Bijeljic, B., Andrew, M.G., Blunt, M.J., 2015. Dynamic three-dimensional pore-scale imaging of reaction in a carbonate at reservoir conditions. Environ. Sci. Technol. 49, 4407–4414. https://doi.org/10.1021/es505789f

Menke, H.P., Bijeljic, B., Blunt, M.J., 2017. Dynamic reservoir-condition microtomography of reactive transport in complex carbonates: Effect of initial pore structure and initial brine pH. Geochim. Cosmochim. Acta 204, 267–285. https://doi.org/10.1016/j.gca.2017.01.053

Menke, H.P., Reynolds, C.A., Andrew, M.G., Pereira Nunes, J.P., Bijeljic, B., Blunt, M.J., 2018. 4D multi-scale imaging of reactive flow in carbonates: Assessing the impact of

heterogeneity on dissolution regimes using streamlines at multiple length scales. Chem. Geol. https://doi.org/10.1016/j.chemgeo.2018.01.016

Molins, S., Trebotich, D., Yang, L., Ajo-Franklin, J.B., Ligocki, T.J., Shen, C., Steefel, C.I., 2014. Pore-scale controls on calcite dissolution rates from flow-through laboratory and numerical experiments. Environ. Sci. Technol. 48, 7453–7460. https://doi.org/10.1021/es5013438

Morse J. W. and Mackenzie F. T. 1990. Geochemistry of Sedimentary Carbonates. Elsevier, Amsterdam, 707 p.

Morse, J.W., Arvidson, R.S., 2002. The dissolution kinetics of major sedimentary carbonate minerals. Earth-Science Rev. 58, 51–84. https://doi.org/10.1016/S0012-8252(01)00083-6

Morse, J.W., Arvidson, R.S., Lüttge, A., 2007. Calcium carbonate formation and dissolution. Chem. Rev. https://doi.org/10.1021/cr050358j

Nan, Z., Shi, Z., Yan, B., Guo, R., Hou, W., 2008. A novel morphology of aragonite and an abnormal polymorph transformation from calcite to aragonite with PAM and CTAB as additives. J. Colloid Interface Sci. 317, 77–82. https://doi.org/10.1016/j.jcis.2007.09.015

Neuville, A., Renaud, L., Luu, T.T., Minde, M.W., Jettestuen, E., Vinningland, J.L., Hiorth, A., Dysthe, D.K., 2017. Xurography for microfluidics on a reactive solid. Lab Chip 17, 293–303. https://doi.org/10.1039/c6lc01253a

Nogues, J.P., Fitts, J.P., Celia, M.A., Peters, C.A., 2013. Permeability evolution due to dissolution and precipitation of carbonates using reactive transport modeling in pore networks. Water Resour. Res. 49, 6006–6021. https://doi.org/10.1002/wrcr.20486

Noiriel, C., Gouze, P., Bernard, D., 2004. Investigation of porosity and permeability effects from microstructure changes during limestone dissolution. Geophys. Res. Lett. 31, 1–4. https://doi.org/10.1029/2004GL021572

Noiriel, C., Oursin, M., Daval, D., 2020. Examination of crystal dissolution in 3D: A way to reconcile dissolution rates in the laboratory? Geochim. Cosmochim. Acta 273, 1–25. https://doi.org/10.1016/j.gca.2020.01.003

Pacala, S., Socolow, R., 2004. Stabilization wedges: solving the climate problem for the next 50 years with current technologies. Science (80-). 305, 968. https://doi.org/10.1126/science.1100103

Pandey, S.N., Chaudhuri, A., Kelkar, S., Sandeep, V.R., Rajaram, H., 2014. Investigation of permeability alteration of fractured limestone reservoir due to geothermal heat extraction using three-dimensional thermo-hydro-chemical (THC) model. Geothermics 51, 46–62. https://doi.org/10.1016/j.geothermics.2013.11.004

Pandey, S.N., Chaudhuri, A., Rajaram, H., Kelkar, S., 2015. Fracture transmissivity evolution due to silica dissolution/precipitation during geothermal heat extraction. Geothermics 57, 111–126. https://doi.org/10.1016/j.geothermics.2015.06.011

Panga, M.K.R., Ziauddin, M., Balakotaiah, V., 2005. Two-scale continuum model for simulation of wormholes in carbonate acidization. AIChE J. 51, 3231–3248. https://doi.org/10.1002/aic.10574

Parkhurst, D., Appelo, C., 2013. Description of Input and Examples for PHREEQC Version 3—A Computer Program for Speciation, Batch-Reaction, One-Dimensional Transport,

and Inverse Geochemical Calculations.

Parvan, A., Jafari, S., Rahnama, M., Norouzi apourvari, S., Raoof, A., 2020. Insight into particle retention and clogging in porous media; a pore scale study using lattice Boltzmann method. Adv. Water Resour. 138, 103530. https://doi.org/10.1016/j.advwatres.2020.103530

Pereira Nunes, J.P., Blunt, M.J., Bijeljic, B., 2016. Pore-scale simulation of carbonate dissolution in micro-CT images. J. Geophys. Res. B Solid Earth 121, 558–576. https://doi.org/10.1002/2015JB012117

Peruffo, M., Mbogoro, M.M., Adobes-Vidal, M., Unwin, P.R., 2016. Importance of Mass Transport and Spatially Heterogeneous Flux Processes for in Situ Atomic Force Microscopy Measurements of Crystal Growth and Dissolution Kinetics. J. Phys. Chem. C 120, 12100–12112. https://doi.org/10.1021/acs.jpcc.6b03560

Plummer, L. N.; Wigley, T. M. L., 1978. Parkhurst, D. L. The kinetics of calcite dissolution in CO2-water systems at 5°C to 60°C and 0.0 to 1.0 atm CO2. Am. J. Sci. 278, 179–216. https://doi.org/10.1177/1354066195001001005

Plummer, L.N., Busenberg, E., 1982. The solubilities of calcite, aragonite, and vaterite in carbon dioxide-water solutions between 0 and 90°C, and an evaluation of the aqueous model for the system calcium carbonate-carbon dioxide-water. Geochim. Cosmochim. Acta 46, 1011–1040. https://doi.org/10.1016/0016-7037(82)90056-4

Pokrovsky, O.S., Golubev, S. V., Schott, J., 2005. Dissolution kinetics of calcite, dolomite and magnesite at 25 °C and 0 to 50 atm pCO2. Chem. Geol. 217, 239–255. https://doi.org/10.1016/j.chemgeo.2004.12.012

Pokrovsky, O.S., Golubev, S. V., Schott, J., Castillo, A., 2009. Calcite, dolomite and magnesite dissolution kinetics in aqueous solutions at acid to circumneutral pH, 25 to 150 °C and 1 to 55 atm pCO2: New constraints on CO2 sequestration in sedimentary basins. Chem. Geol. 260, 317–329. https://doi.org/10.1016/j.chemgeo.2009.01.013

Raeini, A.Q., Bijeljic, B., Blunt, M.J., 2017. Generalized network modeling: Network extraction as a coarse-scale discretization of the void space of porous media. Phys. Rev. E 96, 1–17. https://doi.org/10.1103/PhysRevE.96.013312

Raoof, A., Hassanizadeh, S.M., 2012. A new formulation for pore-network modeling of two-phase flow. Water Resour. Res. 48, 1–13. https://doi.org/10.1029/2010WR010180

Raoof, A., Hassanizadeh, S.M., 2009. A new method for generating pore-network models of porous media. Transp. Porous Media 81, 391–407. https://doi.org/10.1007/s11242-009-9412-3

Raoof, A., Nick, H.M., Hassanizadeh, S.M., Spiers, C.J., 2013. PoreFlow: A complex pore-network model for simulation of reactive transport in variably saturated porous media. Comput. Geosci. 61, 160–174. https://doi.org/10.1016/j.cageo.2013.08.005

Raoof, A., Nick, H.M., Wolterbeek, T.K.T., Spiers, C.J., 2012. Pore-scale modeling of reactive transport in wellbore cement under CO2 storage conditions. Int. J. Greenh. Gas Control 11, 67–77. https://doi.org/10.1016/j.ijggc.2012.09.012

Rathnaweera, T.D., Ranjith, P.G., Perera, M.S.A., 2016. Experimental investigation of geochemical and mineralogical effects of CO 2 sequestration on flow characteristics of reservoir rock in deep saline aquifers. Nat. Publ. Gr. https://doi.org/10.1038/srep19362

References

Rickard, D.T., Sjoberg, E.L., 1983. Mixed kinetic control of calcite dissolution rates. Am. J. Sci. 283, 815–830. https://doi.org/10.2475/ajs.283.8.815

Rochelle, C. a., Czernichowski-Lauriol, I., Milodowski, a. E., 2004. The impact of chemical reactions on CO2 storage in geological formations: a brief review. Geol. Soc. London, Spec. Publ. 233, 87–106. https://doi.org/10.1144/GSL.SP.2004.233.01.07

Rötting, T.S., Luquot, L., Carrera, J., Casalinuovo, D.J., 2015. Changes in porosity, permeability, water retention curve and reactive surface area during carbonate rock dissolution. Chem. Geol. 403, 86–98. https://doi.org/10.1016/j.chemgeo.2015.03.008

Schneider, F., Potdevin, J.L., Wolf, S., Faille, I., 1996. Mechanical and chemical compaction model for sedimentary basin simulators. Tectonophysics 263, 307–317. https://doi.org/10.1016/S0040-1951(96)00027-3

Shah, S.M., Gray, F., Crawshaw, J.P., Boek, E.S., 2016. Micro-computed tomography pore-scale study of flow in porous media: Effect of voxel resolution. Adv. Water Resour. 95, 276–287. https://doi.org/10.1016/j.advwatres.2015.07.012

Shaw, J., Bachu, S., 2002. Screening, Evaluation, and Ranking of Oil Reservoirs Suitable for CO2-Flood EOR and Carbon Dioxide Sequestration. J. Can. Pet. Technol. 41. https://doi.org/10.2118/02-09-05

Shiraki, R., Rock, P.A., Casey, W.H., 2000. Dissolution kinetics of calcite in 0.1 M NaCl solution at room temperature: An atomic force microscopic (AFM) study. Aquat. Geochemistry 6, 87–108. https://doi.org/10.1023/A:1009656318574

Singurindy, O., Berkowitz, B., 2003. Evolution of hydraulic conductivity by precipitation and dissolution in carbonate rock. Water Resour. Res. 39, 1–14. https://doi.org/10.1029/2001WR001055

Sjöberg, E.L., 1978. Kinetics and mechanism of calcite dissolution in aqueous solutions at low temperatures, Stockholm University, Stockholm, 92 pp

Sjöberg, E.L. and Rickard, D.T., 1984. Calcite dissolution kinetics: Surface speciation and the origin of the variable pH dependence. Chemical Geology, 42(1-4): 119-136

Sjöberg, E.L., Rickard, D.T., 1985. The effect of added dissolved calcium on calcite dissolution kinetics in aqueous solutions at 25°C. Chem. Geol. 49, 405–413. https://doi.org/10.1016/0009-2541(85)90002-6

Smith, M.M., Sholokhova, Y., Hao, Y., Carroll, S.A., 2013. CO2-induced dissolution of low permeability carbonates. Part I: Characterization and experiments. Adv. Water Resour. 62, 370–387. https://doi.org/10.1016/j.advwatres.2013.09.008

Soulaine, C., Roman, S., Kovscek, A., Tchelepi, H.A., 2017. Mineral dissolution and wormholing from a pore-scale perspective. J. Fluid Mech. 827, 457–483. https://doi.org/10.1017/jfm.2017.499

Starchenko, V., Marra, C.J., Ladd, A.J.C., 2016. Three-dimensional simulations of fracture dissolution. J. Geophys. Res. Solid Earth 121, 6421–6444. https://doi.org/10.1002/2016JB013321

Steefel, C.I., Beckingham, L.E., Landrot, G., 2015. Micro-Continuum Approaches for Modeling Pore-Scale Geochemical Processes. Rev. Mineral. Geochemistry 80, 217–246. https://doi.org/10.2138/rmg.2015.80.07

Studholme, C., Hill, D.L.G., Hawkes, D.J., 1999. An overlap invariant entropy measure of 3D medical image alignment. Pattern Recognit. 32, 71–86. https://doi.org/10.1016/S0031-3203(98)00091-0

Stumm, W., Morgan, J.J., 1996. Aquatic chemistry : chemical equilibria and rates in natural waters. Wiley.

Tansey, J., Balhoff, M.T., 2016. Pore Network Modeling of Reactive Transport and Dissolution in Porous Media. Transp. Porous Media 113, 303–327. https://doi.org/10.1007/s11242-016-0695-x

Tartakovsky, A.M., Meakin, P., Scheibe, T.D., Eichler West, R.M., 2007. Simulations of reactive transport and precipitation with smoothed particle hydrodynamics. J. Comput. Phys. 222, 654–672. https://doi.org/10.1016/j.jcp.2006.08.013

Van Noorden, T.L., 2009. CRYSTAL PRECIPITATION AND DISSOLUTION IN A POROUS MEDIUM: EFFECTIVE EQUATIONS AND NUMERICAL EXPERIMENTS * 7, 1220–1236. https://doi.org/10.1137/080722096

van Wijngaarden, W.K., Vermolen, F.J., van Meurs, G.A.M., Vuik, C., 2013. A mathematical model for Biogrout: Bacterial placement and soil reinforcement. Comput. Geosci. 17, 463–478. https://doi.org/10.1007/s10596-012-9316-0

van Wijngaarden, W.K., Vermolen, F.J., van Meurs, G.A.M., Vuik, C., 2011. Modelling Biogrout: A New Ground Improvement Method Based on Microbial-Induced Carbonate Precipitation. Transp. Porous Media 87, 397–420. https://doi.org/10.1007/s11242-010-9691-8

Varloteaux, C., Békri, S., Adler, P.M., 2013a. Pore network modelling to determine the transport properties in presence of a reactive fluid: From pore to reservoir scale. Adv. Water Resour. 53, 87–100. https://doi.org/10.1016/j.advwatres.2012.10.004

Varloteaux, C., Vu, M.T., Békri, S., Adler, P.M., 2013b. Reactive transport in porous media: Pore-network model approach compared to pore-scale model. Phys. Rev. E 87, 023010. https://doi.org/10.1103/PhysRevE.87.023010

Vlassenbroeck, J., Dierick, M., Masschaele, B., Cnudde, V., Van Hoorebeke, L., Jacobs, P., 2007. Software tools for quantification of X-ray microtomography at the UGCT. Nucl. Instruments Methods Phys. Res. Sect. A Accel. Spectrometers, Detect. Assoc. Equip. 580, 442–445. https://doi.org/10.1016/j.nima.2007.05.073

Wolthers, M., Charlet, L., Van Cappellen, P., 2008. The surface chemistry of divalent metal carbonate minerals: A critical assessment of surface charge and potential data using the charge distribution multi-site ion complexation model. Am. J. Sci. 308, 905–941. https://doi.org/10.2475/08.2008.02

Wood, B.D., 2007. Inertial effects in dispersion in porous media. Water Resour. Res. 43, 1–16. https://doi.org/10.1029/2006WR005790

Xie, M., Mayer, K.U., Claret, F., Alt-Epping, P., Jacques, D., Steefel, C., Chiaberge, C., Simunek, J., 2015. Implementation and evaluation of permeability-porosity and tortuosity-porosity relationships linked to mineral dissolution-precipitation. Comput. Geosci. 19, 655–671. https://doi.org/10.1007/s10596-014-9458-3

Xiong, Q., Baychev, T.G., Jivkov, A.P., 2016. Review of pore network modelling of porous media: Experimental characterisations, network constructions and applications to reactive

transport. J. Contam. Hydrol. https://doi.org/10.1016/j.jconhyd.2016.07.002

Yang, Y., Patel, R.A., Churakov, S. V., Prasianakis, N.I., Kosakowski, G., Wang, M., 2018. Multiscale modeling of ion diffusion in cement paste: Electrical double layer effects. Cem. Concr. Compos. 96, 55–65. https://doi.org/10.1016/j.cemconcomp.2018.11.008

Yasuhara, H., Neupane, D., Hayashi, K., Okamura, M., 2012. Experiments and predictions of physical properties of sand cemented by enzymatically-induced carbonate precipitation. Soils Found. 52, 539–549. https://doi.org/10.1016/j.sandf.2012.05.011

Yuan, K., Starchenko, V., Lee, S.S., De Andrade, V., Gursoy, D., Sturchio, N.C., Fenter, P., 2019. Mapping Three-dimensional Dissolution Rates of Calcite Microcrystals: Effects of Surface Curvature and Dissolved Metal Ions. ACS Earth Sp. Chem. 3, 833–843. https://doi.org/10.1021/acsearthspacechem.9b00003

Zeebe, R.E., Wolf-Gladrow, D.A., 2001. CO2 in seawater : equilibrium, kinetics, isotopes.

# Acknowledgement

This Ph.D. has been truly a life-changing experience for me and it would not have been possible to do so without the support and guidance that I received from many individuals.

First and foremost, I would like to thank my supervisor Mariette Wolthers for giving me an opportunity to do research in the exciting field of computational sciences. Her immense knowledge and plentiful experience have encouraged me in all the time of my academic research and daily life. I greatly appreciate the freedom she has given me to find my own path and the guidance and support she offered when needed. Without her guidance and constant feedback this PhD would not have been achievable. Also, I would like to extend my thanks for facilitating a positive team environment where I always felt comfortable asking questions as well as sharing my own experiences.

I would also like to take a moment to thank my co-supervisor, Amir Raoof. His help in building the pore-scale model and numerical simulations has been instrumental to this Ph.D. The joy and enthusiasm he has for his research was contagious and motivational for me, even during tough times in the Ph.D. pursuit.

I am thankful to my promoters, Jack Middleburg and Nora de Leeuw for letting me under their scientific wings while giving me freedom to perform my research.

I would also like to extend my sincere thanks to Oleg Iliev whose contribution has been pivotal to the modelling work presented in chapter 2 and 3. Our discussions were always lively and although generally longer than planned, always ended too soon.

I would also like to show gratitude towards all my collaborators, Cornelius Fischer, Veerle Cnudde, Ian B. Butler, Tom Bultreys, Arjen Mascini, Hamed Aslannejad and Till Bollermann for their invaluable contributions in the research project which materialized as independent chapters in this thesis.

A good support system is important to surviving and staying sane during the long journey of PhD. I was lucky to have Janou, Sergio and Sergej as my team members who were always there to help me with the troubles of both the academic and daily world. I'll never forget the many wonderful and exceptionally long lunches we had, while having the intense discussions on totally bizarre topics.

I also want to thank all the past and current members of geochemistry and hydrogeology groups for always being so helpful and friendly.

Life in Utrecht would not have been the same, certainly not easier, without the amazing support from my friends Siddarth, Ajinkya, Sakshi, Aridaman, Abhinandan, Shamika, Sudhanshu.

Lastly, I would like to thank my family for all their love and encouragement. For my parents who raised me and supported me in all my pursuits. My hard-working parents have sacrificed their lives for my siblings and myself and provided unconditional love and care. I love them so much, and I would not have made it this far without them. My brother Pankaj and two lovely sisters, Monika and Neha, who stood like a rock to constantly motivate me through the ups and downs of this PhD journey. And most of all for my loving, supportive and encouraging husband Abhishek who patiently waited for 5 long years in India and did not let the long distance become an issue ever. He has been a true and great supporter and has unconditionally loved me during my good and bad times. He has faith in me and my intellect even when I felt like digging hole and crawling into one because I didn't have faith in myself. I truly thank Abhishek for sticking by my side, even when I was irritable and depressed. Thank you.

## CV

| | |
|---|---|
| 25 November 1990 | Born in Gangapur City, India |
| 2008-2013 | Integrated Masters, Geological Technology, Earth Science Department, Indian Institute of Technology Roorkee, India |
| 2013-2015 | Geoscientist, Samit Enterprise Private Limited, Gurgaon, India |
| 2016-2021 | Ph.D. Geochemistry group, Utrecht University, Utrecht, The Netherlands |
| Present | Computation Scientist, Shell India Market Pvt Limited, India |